THESE

présentée par

Petr Mikulík

pour obtenir le titre de

Docteur de l'Université Joseph Fourier – Grenoble I
(arrêtés ministériels du 5 juillet 1984 et du 30 mars 1992)

Spécialité : Physique

X-RAY REFLECTIVITY FROM PLANAR AND STRUCTURED MULTILAYERS

(Réflectivité des rayons X par des multicouches planaires et structurées)

(Rentgenová reflektivita rovinných a strukturovaných multivrstev)

Soutenue le 6 mars 1997

Composition du jury :

Président :	J. Lajzerowicz
Rapporteurs :	C. Malgrange
	M. Schlenker
Examinateurs :	T. Baumbach
	V. Holý
	D. Givord
	M. Brunel

Thèse préparée au sein du
Laboratoire de Magnétisme Louis Néel, CNRS,
Grenoble, France
et
Département de Physique des Solides, Faculté des Sciences, Université Masaryk,
Brno, République Tchèque

Preface to the second edition

I am very pleased that my thesis has encountered high attention by X-ray reflectivity fans; nearly one hundred copies have been distributed since March 1997 until July 1999. Since there are no more paper copies available and the microfiche version is not so much attractive, I decided to release the postscript version of the thesis on my web page so that anybody interested can print it.

This version differs from the original version from March 1997 in the following:

- the preface you are currently reading has been added,
- few typos from the first version of the thesis have been corrected (see the web page of the thesis for their list),
- abstracts on the last page have been added.

I would like to mention the following two notes here:

- The grating truncation rods are called just "truncation rods (TR)" in this thesis, while in our later publications they are called "grating truncation rods (GTR)" in order to distinguish them from "crystal truncation rods (CTR)".
- The Fresnel coefficients for rough multilayer gratings with gaussian roughness are damped by a simple exponential form similarly to those for planar multilayers — see P. Mikulík and T. Baumbach, *X-ray reflection by rough multilayer gratings: Dynamical and kinematical scattering*, *Phys. Rev. B* **59**, 7632 (1999).

Enjoy well the reading!

Petr Mikulík
Brno, November 1999

e-mail: `mikulik@physics.muni.cz`

Related web pages:
my personal page: `http://www.sci.muni.cz/~mikulik/`
web page of the thesis: `http://www.sci.muni.cz/~mikulik/Thesis/`
web page of my publications: `http://www.sci.muni.cz/~mikulik/Publications.html`

THESE

présentée par

Petr Mikulík

pour obtenir le titre de

Docteur de l'Université Joseph Fourier – Grenoble I
(arrêtés ministériels du 5 juillet 1984 et du 30 mars 1992)

Spécialité : Physique

X-RAY REFLECTIVITY FROM PLANAR AND STRUCTURED MULTILAYERS

(Réflectivité des rayons X par des multicouches planaires et structurées)

(Rentgenová reflektivita rovinných a strukturovaných multivrstev)

Soutenue le 6 mars 1997

Composition du jury :

Président :	J. Lajzerowicz
Rapporteurs :	C. Malgrange
	M. Schlenker
Examinateurs :	T. Baumbach
	V. Holý
	D. Givord
	M. Brunel

Thèse préparée au sein du
Laboratoire de Magnétisme Louis Néel, CNRS,
Grenoble, France
et
Département de Physique des Solides, Faculté des Sciences, Université Masaryk,
Brno, République Tchèque

Remerciements

Je veux remercier chaleureusement Tilo Baumbach (Fraunhofer Institut Zerstörungsfreie Prüfverfahren, Dresden), Václav Holý (katedra fyziky pevné fáze, přírodovědecká fakulta, Masarykova univerzita, Brno), et Dominique Givord (Laboratoire Louis Néel, Centre National de la Recherche Scientifique, Grenoble) pour la formation scientifique qu'ils m'ont dispensée, pour le temps qu'ils m'ont consacré ainsi que pour la liberté de mouvement et d'initiative qu'ils m'ont laissées.

Je tiens à remercier Monsieur J. Lajzerowicz, professeur à l'Université Joseph Fourier, qui m'a fait l'honneur de présider le jury de cette thèse.

Je suis particulièrement reconnaissant à mes deux rapporteurs, Madame C. Malgrange et Monsieur M. Schlenker, pour l'intérêt qu'ils ont porté à mon travail.

Je remercie Monsieur M. Brunel d'avoir accepté de faire partie de ce jury.

Je voudrais remercier mes collègues qui m'ont beaucoup aidé pendant mon travail de thèse : J. Kuběna pour les discussions sur les problèmes expérimentaux, A. Liénard pour sa disponibilité, M. Gailhanou pour les échantillons et pour sa participation amicale pendant nos manips au synchrotron à L.U.R.E., S. Jaren pour les échantillons, et Monsieur O. Litzman pour les nombreuses discussions et pour le travail sur le concept d'Ewald dans la théorie dynamique.

Je voudrais remercier toutes les personnes du Laboratoire Louis Néel, du Département de Physique des Solides à la Faculté des Sciences à l'Université Masaryk, et mes nombreux collègues à European Synchrotron Radiation Facility (E.S.R.F.) pour m'avoir permis d'effectuer à plusieurs reprises un travail scientifique dans ces endroits si efficaces et si amusants. Par souci de n'oublier personne, sans les nommer, je remercie chacun.

Je voudrais remercier toutes les autres personnes qui par leur travail ont contribué à la réalisation de ma thèse. En particulier, j'exprime ma gratitude à la communauté des programmeurs du monde entier qui distribuent leur software gratuitement.

Je remercie l'Installation Européenne de Rayonnement Synchrotron à Grenoble, le Laboratoire d'Utilisation du Rayonnement Electromagnétique à Paris, le Laboratoire de Cristallographie à Grenoble et l'Institut Laue-Langevin à Grenoble pour m'avoir permis d'effectuer les expériences chez eux.

Ma thèse a été faite dans le cadre d'une collaboration scientifique et culturelle entre la France et la République Tchèque. C'est cette collaboration scientifique internationale qui a conduit à la décision d'écrire ma thèse en anglais.

Je remercie l'Université Masaryk à Brno qui m'a permis de suivre mes études doctorales au Département de Physique des Solides. Je remercie le Ministère de la Recherche et de l'Education du Gouvernement Français de m'avoir accordé une "bourse en co-tutelle" qui m'a permis d'effectuer mes stages au Laboratoire Louis Néel à Grenoble, et donc de réaliser cette thèse pour la présenter à l'Université Joseph Fourier.

Contents

Chapter 1

Introduction

Introduction

Les progrès récents dans les techniques de croissance ont rendu possible l'élaboration de structures de faible dimensionalité telles que les films minces (multicouches planaires), les structures mésoscopiques et les nanostructures (réseaux périodiques latéralement et en multicouches, fils et points quantiques). Ces matériaux trouvent des applications en électronique et en optique.

L'optimisation des procédés de fabrication et la compréhension des propriétés physiques de ces échantillons nécessitent des méthodes d'analyse structurale non destructives. Complémentaires aux méthodes directes de sondes locales, comme la microscopie à force atomique, les techniques de diffusion élastique des rayons X permettent de sonder localement l'espace réciproque, fournissant ainsi des informations sur les propriétés statistiques des paramètres structuraux moyennés sur de grands volumes d'échantillon.

De nos jours, le développement des méthodes de diffusion des rayons X est favorisé par l'avancée technologique considérable des équipements comme les dispositifs à cristal multiple qui permettent d'obtenir une bonne précision dans l'espace réciproque. En plus des sources de rayons X conventionnelles ou à anode tournante, courantes dans les laboratoires, les nouvelles sources de radiation synchrotron très intense ont permis l'étude d'objets de basse dimensionalité à faible pouvoir de diffraction ainsi que les processus de diffusion diffuse de faible intensité. En plus du domaine dynamique accru de l'intensité mesurée et d'un faisceau très parallèle, les synchrotrons permettent aussi d'ajuster la longueur d'onde et de changer le contraste des constituants de l'échantillon.

La réflectivité des rayons X (XRR), spéculaire et non spéculaire, est une méthode pratique pour l'étude structurale des multicouches cristallisées ou amorphes. Elle est sensible à la distribution de l'indice de réfraction dans l'échantillon. La réflectivité étudie la diffusion à petits angles autour de l'angle critique de réflexion totale et fournit la carte de distribution de l'intensité diffusée au voisinage de l'origine du réseau réciproque. Ainsi la technique XRR, pour l'étude des propriétés cristallines est complémentaire des diverses méthodes de diffraction de rayons X comme la diffraction conventionnelle symétrique et asymétrique, la diffraction fortement asymétrique plus élaborée et la diffraction en incidence rasante.

Le présent travail est consacré à l'étude par réflexion des rayons X de multicouches planaires ou structurées latéralement.

En première approximation, l'intensité diffusée par un échantillon est proportionnelle au carré du module de la transformée de Fourier de la densité électronique. A partir du réseau de l'intensité mesurée, on peut déduire le profil de la densité électronique et par suite les propriétés verticales (épaisseurs de couches) ou latérales (rugosités, corrélations dans les interfaces ou structure latérale des couches) caractérisant les multicouches. Aussi la technique XRR est utilisée non seulement pour l'étude des multicouches planaires classiques, mais permet aussi de révéler les propriétés de différentes sortes d'échantillons latéralement structurés comme les réseaux ou de multicouches déposées sur des substrats inclinés ou de couches avec des structures en îlots.

J'ai développé plusieurs approches pour traiter les théories de la réflectivité des rayons X et résoudre l'équation d'onde par différentes méthodes. La principale approche s'apparente à celles de l'optique dans le visible avec pour changement un indice de réfraction voisin de 1 dans le cas des rayons X. Les autres traitements viennent de la diffraction des rayons X par les cristaux (la théorie cinématique de la diffusion) et de la mécanique quantique (l'approximation de l'onde déformée de Born).

Les théories dynamiques donnent des solutions rigoureuses aux problèmes étudiés. Cependant, elles ne sont habituellement pas bien adaptées pour une compréhension physique qualitative des résultats calculés. Pour cette raison, je développe plusieurs théories approchées de XRR

qui expliquent facilement les phénomènes de diffusion et fournissent des algorithmes de calcul rapides numériquement. Mais les régions de validité des approximations considérées doivent être déterminées.

Les théories de diffusion des rayons X étudiées dans ce travail comprennent la théorie cinématique, l'approximation de l'onde déformée de Born, la théorie dynamique et diverses approximations de la théorie dynamique, comme l'approximation à une réflexion unique, l'approximation à onde multiple et l'approximation à deux ondes.

Dans les différentes théories faites, les auteurs utilisent des notations différentes rendant ainsi difficile une comparaison directe entre les différentes approches théoriques. Aussi l'originalité de ce travail est de traiter différentes théories dans un formalisme unique qui permet, d'une manière solide et phénoménologique, l'étude, la comparaison et la discussion des régions de validité de toutes les théories traitées. Par exemple, j'ai montré que les coefficients de Fresnel, bien connus dans la réflectivité optique sur des multicouches planaires, ont leurs équivalents dans la théorie cinématique et peuvent être généralisés dans le cas de la réflectivité sur des réseaux. Je montre aussi l'avantage d'un formalisme matriciel dans les théories dynamiques. Enfin j'introduis dans la XRR le concept de la représentation graphique des phénomènes de diffusion au moyen de la construction d'Ewald.

Maintenant, je vais brièvement exposer le plan de cette thèse. Tout d'abord je fais un rappel des caractères fondamentaux de l'espace réciproque, avec les formules de correspondance entre les rotations angulaires effectuées durant les mesures et les balayages associés dans l'espace réciproque.

Ensuite, je traite la réflectivité spéculaire sur des multicouches planaires. Je développe la théorie dynamique habituelle à partir de laquelle l'approximation à une diffusion unique est déduite. La théorie cinématique est traitée ensuite par la méthode de la phase stationnaire et les coefficients de réflexion de Fresnel qui sont déduits sont comparés à ceux de la théorie dynamique. J'applique ces théories pour expliquer la courbe de réflectivité spéculaire d'une multicouche quasipériodique de Fibonacci.

Dans le chapitre suivant, j'étudie la réflectivité spéculaire et non spéculaire sur des multicouches planaires rugueuses. Les interfaces planes traitées dans le précédent chapitre dans les théories dynamique et cinématique sont reformulées de manière à tenir compte des propriétés statistiques des interfaces rugueuses de façon aléatoire. J'ai appliqué ceci pour l'ajustement des courbes expérimentales. J'ai traité aussi la diffusion diffuse en employant l'approximation de l'onde déformée de Born. Les principaux caractères de la diffusion diffuse incohérente sont brièvement présentés par des mesures.

La principale partie de ce travail est consacrée à l'étude de la réflectivité des rayons X sur des réseaux de multicouches. A l'aide du formalisme et de la notation précédemment introduits, je résouds le problème par la théorie cinématique, l'approximation de l'onde déformée de Born et la théorie dynamique exacte. Les approximations de l'onde multiple et en particulier l'approximation à deux ondes ont été déduites de la théorie dynamique. J'ai comparé ces théories de façon analytique et numérique essentiellement dans le cas de réseaux à courte période. Le but est de montrer dans quelles conditions les théories approchées de diffusion unique donnent des résultats corrects, et dans quelles régions les effets dynamiques de diffusion multiple l'emportent. Aussi l'intérêt principal d'une telle étude méthodologique est pour les théories de diffusion elles-mêmes et non pas pour l'optimisation de la structure des échantillons en vue d'applications particulières.

Enfin, j'ai traité la diffusion par des réseaux rugueux. Les imperfections de structure qui existent dans les réseaux de multicouches sont prises en compte, y comprises la rugosité des interfaces et celle des parois des réseaux. Le formalisme proposé est capable d'intégrer facilement ces effets à la fois dans les théories dynamique et cinématique.

Introduction

Recent progress in the growth techniques makes it possible to fabricate low-dimensional structures, like thin films (planar multilayers), mesoscopic structures and nanostructures (lateral surface and multilayer gratings, quantum wires and quantum dots). These elements find applications in electronic and optical devices.

Optimization of the fabrication process and the physical understanding of the samples requires non-destructive structural studies of the samples produced. Complementary to the direct local probing methods (i.e., AFM microscopy), the X-ray elastic scattering methods probe locally the reciprocal space, thus providing information about the statistical properties of the structural parameters averaged over a large volume of the sample.

Nowadays, the development of X-ray scattering methods is encouraged by advanced technical equipment being widely available, like the multiple crystal arrangements enabling good precision in reciprocal space to be obtained. Further, complementary to the conventional or rotating anode laboratory sources, new high-intensity synchrotron radiation sources are advantageously involved in studies of low-dimensional objects whose diffraction power is small, as well as in the studies of low-intensity diffuse scattering. In addition to the improved dynamical range of measured intensity and highly parallel beam, synchrotrons also provide the possibility of wavelength tuning, thus changing the contrast of the sample constituents.

X-ray reflectivity (XRR), including both the specular X-ray reflection (SXR) and non-specular X-ray reflection (NSXR), is conveniently applied for the structural studies of both crystalline and amorphous multilayer samples. It is sensitive to the distribution of the refractive index in the sample. It studies the scattering at small angles around the critical angle of total external reflection, and it maps the distribution of the scattered intensity around the origin of the reciprocal space. Thus XRR is complementary to miscellaneous X-ray diffraction methods, namely the conventional symmetric and asymmetric X-ray diffraction, the more elaborate highly asymmetric diffraction, and the grazing incidence diffraction, which study the crystalline properties.

The present work is devoted to the X-ray reflection studies of multilayered samples, either planar or laterally structured.

In a rough approximation, the intensity scattered by a sample is proportional to the square of modulus of the Fourier transform of the electron density. Thus the electron density profile can be deduced from the measured intensity pattern, and subsequently the vertical properties (layer thicknesses) as well as the lateral properties (roughnesses and correlation properties of interfaces or lateral layer structure) characterizing multilayers can be determined. Therefore XRR is now being applied not only to the usual planar multilayers, but also to reveal the properties of various kinds of laterally structured samples, for instance gratings, multilayers grown on inclined substrate surfaces or layers with random island structures.

Several approaches for treating the theories of X-ray reflectivity are developed, solving the wave equation by various methods. The main approach comes from the usual optics of visible light, which is modified for X-rays since the index of refraction is near unity. The other treatments proceed from X-ray diffraction from crystals (the kinematical theory of scattering) and from quantum mechanics (the distorted-wave Born approximation).

The dynamical theories give rigorous solutions to the studied problems. However, they are usually not well suited for a qualitative physical understanding of the calculated results. Therefore I develop several approximative theories for XRR that explain easily the scattering phenomena and provide rapid algorithms for numerical calculation. On the other hand, the regions of validity of the approximations involved have to be determined.

In particular, the X-ray scattering theories studied in this work comprise the kinematical theory, the distorted-wave Born approximation, the dynamical theory and various approximations of the dynamical theory, like the single-reflection approximation, the multiple-beam approximation and the two-beam approximation.

Apart from the use of different approximations, also different notation is used by various authors, making a direct comparison of the theoretical approaches difficult. Therefore, one particular aim of the present work is to treat different theories using a uniform formalism that will enable the regions of validity of all treated theories to be studied, compared and discussed in a consistent and methodological way. For example, I show that the Fresnel coefficients, well-known from the optical reflectivity from planar multilayers, have their counterparts in the kinematical theory, and that they can be generalized in the case of reflectivity from gratings. I also show the advantage of the matrix formalism for the dynamical theories. In addition, I introduce into XRR the concept of the graphical representation of the scattering phenomena by means of the Ewald construction.

Now I briefly outline the structure of the presented thesis. In the first part, I deal with the basic characteristics of the reciprocal space. Relations providing the connection between the angular rotations during an experiment and the appropriate scans in the reciprocal space are provided.

Further, the specular reflectivity from planar multilayers is discussed. The usual dynamical theory is developed, from which the single-reflection approximation is derived. The kinematical theory treated by the stationary-phase method is discussed afterwards and the derived kinematical Fresnel reflection coefficients compared to the dynamical ones. The theories are applied to explain the specular reflectivity curve of a quasiperiodic Fibonacci multilayer.

Specular and non-specular X-ray reflectivity from rough planar multilayers are studied in the following chapter. Both the dynamical and kinematical theories for flat interfaces treated in the previous chapter are reformulated in order to cover the statistical properties of randomly rough interfaces. The application to fitting the experimental curves is demonstrated. The diffuse scattering is dealt with as well, for which the distorted-wave Born approximation is employed. The main features of the incoherent diffuse scattering are briefly presented from the measurement.

The main part of the work is devoted to the study of X-ray reflectivity from multilayer gratings. Following the general formalism and notation introduced in the previous chapters, the problem is solved by the kinematical theory, distorted-wave Born approximation and rigorous dynamical theory. Multiple-beam approximations, mainly the two-beam approximation, are derived from the dynamical theory. These theories are compared analytically and numerically, addressing mainly the short period gratings. The aim is to show the conditions under which the approximate single-scattering theories give correct results, and which are the regions where dynamical effects of multiple scattering prevail. Therefore the main interest of such a methodological study is given to the scattering theories themselves, and not to the optimization of the sample structure for particular applications.

The scattering from rough gratings is treated afterwards. The real structural imperfections of multilayer gratings are taken into account, comprising the roughnesses of the interfaces and of the side walls of the grating shapes. The proposed unified formalism enables these effects to be easily incorporated into both the dynamical and the kinematical theories.

Chapter 2

Exploring reciprocal space

Résumé

Dans ce chapitre nous nous intéressons à la notion d'espace réciproque et à la géométrie des expériences de diffusion des rayons X. Nous définissons les angles qui décrivent l'orientation du faisceau incident et des vecteurs d'onde diffusés par rapport à l'échantillon mesuré. Au cours d'une expérience, nous faisons varier l'orientation du faisceau incident et des vecteurs d'onde diffusés par rotations de l'échantillon et du détecteur, montés sur un goniomètre. Nous donnons les formules de correspondance entre les angles et les coordonnées dans l'espace réciproque.

Nous traçons l'intensité diffusée par l'échantillon en fonction du vecteur de diffusion, différence entre le vecteur d'onde incident et le vecteur d'onde diffusé. Nous obtenons ainsi une carte dans l'espace réciproque de l'intensité diffusée.

Nous utilisons la construction d'Ewald, très utile pour une représentation des conditions de diffusion dans l'espace réciproque, pour tracer les vecteurs d'onde impliqués dans ces processus. Elle nous permet de comprendre comment la géométrie coplanaire des expériences nous limite la zone d'exploration possible de l'espace réciproque, pour une longueur d'onde donnée.

2.1 Introduction

In this chapter we deal with the notion of the reciprocal space and with the geometry of X-ray scattering experiments. We introduce the angles describing the orientation of the incident and scattered wave vectors with respect to a measured sample. Running an experiment, we change the orientation of the incident and exit wave vectors by rotating the sample and the detector on the goniometers. The reciprocal space is explored in scans related to the goniometer movements. We provide useful formulae for the transition between the angular and the reciprocal space coordinates.

We plot the intensity scattered by the sample versus the scattering vector, which is the difference of the scattered and incidence wave vectors. This gives us a reciprocal space map of the scattered intensity.

We use the Ewald construction as a very convenient tool to represent the scattering conditions in the reciprocal space by tracing the wave vectors involved in the scattering processes. It also shows how the reflection geometry of the experiment limits the accessible region of the reciprocal space that can be explored in coplanar scattering geometry by a radiation with a given wavelength.

2.2 Reciprocal space and angular representations

Let us suppose a typical X-ray scattering experiment, Fig. 2.1. An incident monochromatic plane wave propagating with the vacuum wave vector $\boldsymbol{K}_1$ irradiates the sample surface. The detector measures the intensity scattered into a direction $\boldsymbol{K}_2$. Since we suppose elastic scattering processes, the lengths of both wave vectors are the same, $|\boldsymbol{K}_1| = |\boldsymbol{K}_2| = 2\pi/\lambda$, where λ is the vacuum wavelength. For a given wavelength, the scattering process $\boldsymbol{K}_1 \rightarrow \boldsymbol{K}_2$ is characterized by the *scattering vector* (or the *wave vector transfer*) $\boldsymbol{Q} = \boldsymbol{K}_2 - \boldsymbol{K}_1$.

If we plot the wave vectors in *real space*, Fig. 2.1, then they show us the direction of propagation. We note that the dimension of the real space are metres [m], whereas the dimension of wave vectors are reciprocal metres (or more frequently for X-rays, reciprocal Angstroms [Å^{-1}]). Therefore we naturally plot wave vectors in *reciprocal space* as it is shown in Fig. 2.2. The reciprocal space drawings allow us a very illustrative and convenient graphical representation of the phenomena of the propagation of the scattered waves. The idea of the reciprocal space has been introduced by Ewald in the early stage of the dynamical theory of X-ray diffraction [CJK92].

The scattering geometry is given by the angles which the incident and exit wave vectors make with a given coordinate system. We deal with the experiments on layered and laterally large samples. Therefore we choose the coordinate system of the real space so that the axes $\hat{\boldsymbol{x}}, \hat{\boldsymbol{y}}$ are parallel to the sample surface and the axis $\hat{\boldsymbol{z}}$ is the inner surface normal, Fig. 2.1. Similarly we choose the coordinate system of the reciprocal space. The waves (i.e., the reflected and diffracted-reflected waves in our terminology) that can be experimentally measured in the reflectivity experiments (in the so-called *Bragg geometry*) propagate above the sample surface. Therefore they are scattered from the transmitted wave by the wave vector transfer $\boldsymbol{Q}$ having the negative component Q_z. For this reason we plot the reciprocal space drawings with the axis $-Q_z$ pointing up (parallel to the outward surface normal).

The coordinates of the *incident wave vector* are given by the *angle of incidence* θ_1 and the *azimuthal angle* φ_1 (Fig. 2.1)

$$\boldsymbol{K}_1 = (K_{1x}, K_{1y}, K_{1z}) = K(\cos\theta_1 \cos\varphi_1,\ \cos\theta_1 \sin\varphi_1,\ \sin\theta_1)\ . \tag{2.1a}$$

Similarly, the *outgoing wave vector* coordinates are

$$\boldsymbol{K}_2 = (K_{2x}, K_{2y}, K_{2z}) = K(\cos\theta_2 \cos\varphi_2,\ \cos\theta_2 \sin\varphi_2,\ -\sin\theta_2)\ . \tag{2.1b}$$

If the sample is laterally homogeneous, the scattering acts only in the *plane of incidence* (defined by $\boldsymbol{K}_1$ and the surface normal $\boldsymbol{n}$) and it is convenient to omit the $\hat{\boldsymbol{y}}$ components ($\varphi_1 = \varphi_2 = 0$)

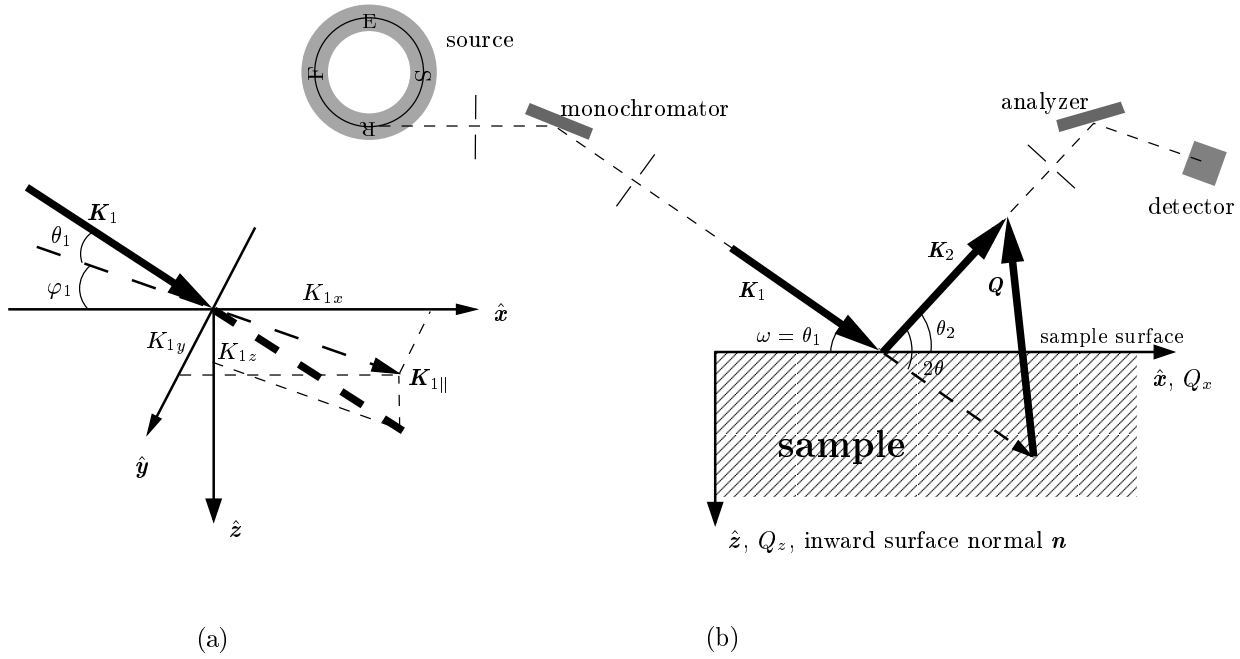

Figure 2.1. Real space representation of a scattering experiment. (a) Definition of the angle of incidence θ_1 and the azimuth φ_1 of the incident wave $\boldsymbol{K}_1$. (b) Sketch of an experimental arrangement in the coplanar geometry (here a triple-axis diffractometer). The setup of source, monochromator, slits, and the wavelength determines the direction of the incident wave $\boldsymbol{K}_1$. The setup of the slits, analyser and detector defines the direction of the exit beam $\boldsymbol{K}_2$, those intensity is measured. $\boldsymbol{Q}$ is the wave vector transfer and 2θ is the scattering angle.

which are zero. This scattering geometry is called the *coplanar geometry* and it allows us to deal with the $\hat{\boldsymbol{x}}$ and $\hat{\boldsymbol{z}}$ components only, Fig. 2.1(b),

$$\boldsymbol{K}_1 = (K_{1x}, K_{1z}) = K(\cos\theta_1,\ \sin\theta_1) \tag{2.2a}$$

$$\boldsymbol{K}_2 = (K_{2x}, K_{2z}) = K(\cos\theta_2,\ -\sin\theta_2)\ . \tag{2.2b}$$

In the most part of this report we work in the coplanar geometry because of dealing with the laterally homogeneous samples. The need of the third coordinate $\hat{\boldsymbol{y}}$ will arise in the non-coplanar reflection geometry in the study of the scattering from laterally inhomogeneous samples (gratings, Ch. 5).

The scattering vector $\boldsymbol{Q}$ of the scattering process $\boldsymbol{K}_1 \to \boldsymbol{K}_2$ is

$$\begin{aligned}\boldsymbol{Q} = \boldsymbol{K}_2 - \boldsymbol{K}_1 &= K(\cos\theta_2 - \cos\theta_1,\ \sin\theta_2 + \sin\theta_1) \\ &= 2K\sin(2\theta/2)\left(\sin\frac{\theta_1-\theta_2}{2},\ -\cos\frac{\theta_1-\theta_2}{2}\right)\end{aligned} \tag{2.3}$$

and its length is $|\boldsymbol{Q}| = 2K\sin(2\theta/2)$, where 2θ is the *scattering angle*, Fig. 2.1(b).

The scattering process is described by any pair of the variables $Q_x, Q_z, \theta_1, \theta_2$. The reversed relations transforming $\boldsymbol{Q}$ into the pair (θ_1, θ_2) are

$$\begin{aligned}\theta_1 &= \operatorname{atan}\frac{Q_x}{-Q_z} - \operatorname{asin}\frac{|\boldsymbol{Q}|}{2K} \\ \theta_2 &= \operatorname{atan}\frac{Q_x}{-Q_z} + \operatorname{asin}\frac{|\boldsymbol{Q}|}{2K}\ .\end{aligned} \tag{2.4}$$

Now we discuss which part of the reciprocal space can be explored by X-rays with a given wavelength, Fig. 2.2. We plot the end-point of the incident wave vector $\boldsymbol{K}_1$ at the origin O of the reciprocal space. The beginning point S is given by the angle of incidence and the wavelength λ. If we plot the exit wave vector from the point S, then its end-point has to lie on the *Ewald*

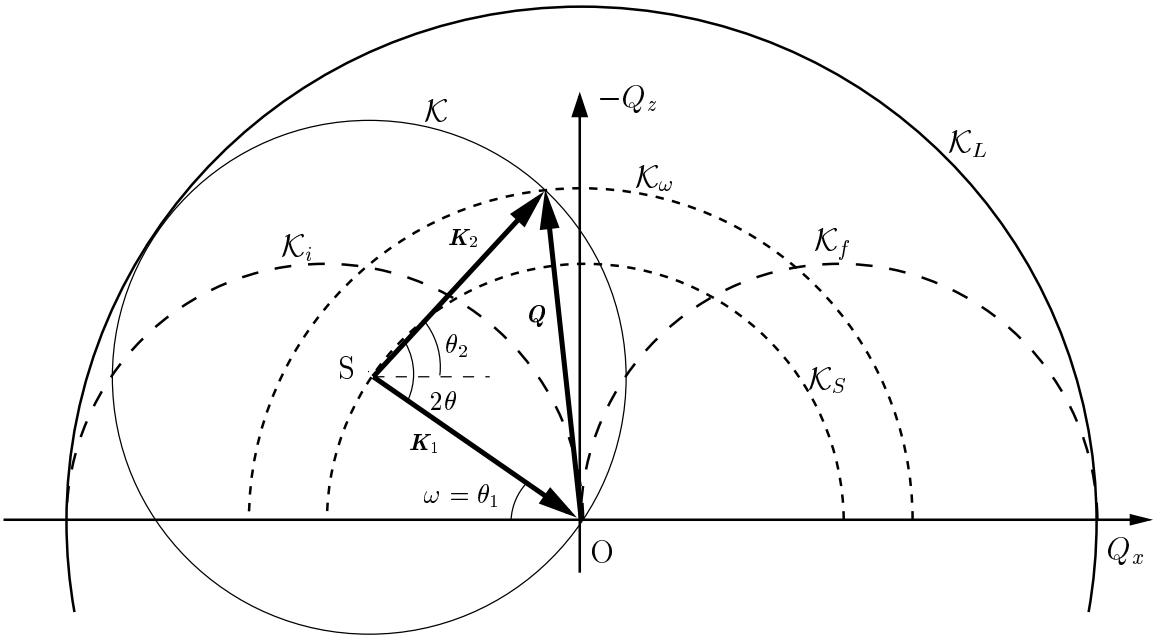

Figure 2.2. Coplanar scattering geometry drawn in a two-dimensional section of a three-dimensional reciprocal space.

sphere $\mathcal{K}$ with the radius $K = 2\pi/\lambda$. We note that the intersection of the Ewald sphere with the plane of incidence is now the "Ewald circle". However, we keep the name of the "Ewald sphere". A change of the angle of incidence moves the point S along the sphere $\mathcal{K}_S$ and the end-point of the scattering vector along $\mathcal{K}_\omega$. A change of the detector position changes the scattering angle 2θ and it moves the end-point of $\boldsymbol{K}_2$ along the Ewald sphere $\mathcal{K}$. For reflection experiments, the angles of incidence and exit have to be positive, therefore we cannot go below the *limiting Ewald spheres* $\mathcal{K}_i$ and $\mathcal{K}_f$, for which the angle of incidence and exit is zero, respectively. Further, the maximal wave vector transfer appears for $\boldsymbol{K}_2 = -\boldsymbol{K}_1$ and therefore we cannot explore the reciprocal space beyond the sphere $\mathcal{K}_L$ of the diameter $4\pi/\lambda$.

The *accessible region* of the reciprocal space that can be explored in the coplanar geometry with a radiation with fixed wavelength is shown in Fig. 2.3 by the shaded area. This is shown in a coplanar case; for a true 3d picture of $I(Q_x, Q_y, Q_z)$ we should imagine that the circles are spheres. The X-ray reflectivity method, which is studied in the present work, explores the intensity distribution around the origin O of the reciprocal space. The collected data, i.e., the intensity vs. the reciprocal space coordinates, we call *reciprocal space mapping* of the scattered intensity. In this work, these two-dimensional maps (see Figs. 4.13, 5.12, 5.23 for instance) are plotted by the program `pm3d` written by the author of this thesis.[1]

Since the index of refraction of X-rays is close to unity, X-ray reflectivity experiments take place near the origin of reciprocal space, where the angles of incidence and exit are small. The wave vector transfer is approximately

$$\boldsymbol{Q} \approx K\,(\,(\theta_1^2 - \theta_2^2)/2,\, -(\theta_1 + \theta_2)\,) = K\,(-2\theta(2\theta - 2\omega)/2, -2\theta) \tag{2.5}$$

and it is small compared to the incidence and exit wave vectors $|\boldsymbol{Q}| \ll K = |\boldsymbol{K}_1| = |\boldsymbol{K}_2|$.

The reversed relations under this small-angle approximation are

$$\begin{aligned} \theta_1 &= \frac{-Q_z}{2K} + \frac{Q_x}{-Q_z} & \qquad \omega &= \frac{-Q_z}{2K} + \frac{Q_x}{-Q_z} \\ \theta_2 &= \frac{-Q_z}{2K} - \frac{Q_x}{-Q_z} & \qquad 2\theta &= \frac{-Q_z}{K}\,. \end{aligned} \tag{2.6}$$

[1] It is available at the WWW page `http://www.sci.muni.cz/~mikulik/`. This program is free software and it is distributed under the GNU General Public License.

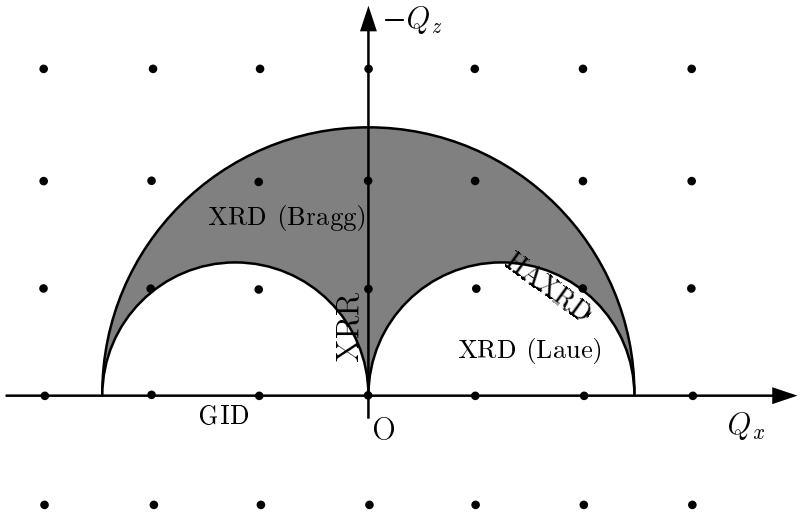

Figure 2.3. Reciprocal space of a crystalline sample. The shaded region is accessible in the coplanar geometry for a fixed wavelength. The abbreviations refer to different X-ray scattering techniques available for exploring different parts of the reciprocal space: XRR (X-ray reflectivity), XRD (X-ray diffraction), HAXRD (highly asymmetric X-ray diffraction), GID (grazing-incidence X-ray diffraction, a non-coplanar technique).

We describe the scattering geometry in the "angular space" either by the pair of the *incidence and exit angles* θ_1, θ_2 or by the pair of the *incidence and scattering angles* $\omega \equiv \theta_1, 2\theta = \theta_1 + \theta_2$. The latter pair is preferred when performing the experiments, and the incidence angle is referred to the *sample* or *rocking angle*, while the scattering angle is referred to the *detector angle* (the angle between the primary beam and the line sample—detector). Another convention employed mainly in non-coplanar scattering geometries uses the notation of α_i, α_f instead of θ_1, θ_2.

2.3 Experimental scans in the reciprocal space

When we perform an experiment, we change the diffractometer setup in order to change the angle of incidence and the scattering angle. Most of the movement is done by rotating goniometers with sample, monochromator and analyzer crystals or slits mounted on them. According to a motor movement, we drive in the reciprocal space along a one-dimensional scans, i.e., along a certain path. Fig. 2.4 shows some typical scans passing through an arbitrary point in the reciprocal space.

Running an experiment, we have direct access to the following elementary angular movements of the diffractometer setup:

ω-scan (rocking scan). We rock the sample keeping the detector position 2θ fixed. The measured points lie on the circle along the origin of the reciprocal space.

In the coplanar reflection geometry, the measured points can fill the region of $\omega \in [0; 2\theta]$. In X-ray reflectivity, this scan goes nearly parallel with the Q_x-scan. The ω-scan crosses a truncation rod Q_x (i.e., the line parallel to the axis Q_z at given Q_x) at $\omega = \frac{2\theta}{2} + \operatorname{asin} \frac{Q_x}{2K \sin(2\theta/2)}$, which approximates to $\omega = \frac{2\theta}{2} + \frac{Q_x}{K\,2\theta}$ for small angles.

2θ-scan (detector scan). We fix the sample position at ω and rotate the detector. The points on the 2θ-scan lie on inclined Ewald sphere with the origin in the beginning of the vector $\boldsymbol{K}_1$.

In the coplanar reflection geometry, this scan starts at the position $2\theta = \omega$ and ends at the intersection of the Ewald sphere $\mathcal{K}$ and the limiting Ewald sphere $\mathcal{K}_i$, Fig. 2.2.

The 2θ-scan crosses a truncation rod Q_x for $2\theta = \omega + \arccos(\cos\omega + Q_x/K)$, which approximates to $2\theta = \omega + \sqrt{\omega^2 - 2Q_x/K}$ for small angles.

ϕ-scan (azimuthal scan). We rotate the sample about its surface normal. Fig. 2.4 would be rotated about the Q_z axis.

Combining the elementary angular rotations we can perform the common reciprocal space scans:

specular scan. We change both the angle of incidence and the detector angle keeping their ratio $2\theta/\omega = 2$ fixed. This scan starts at the origin of the reciprocal space and it explores the intensity along the axis Q_z.

Q_x-scan. We change both the angle of incidence and the detector angle keeping the component Q_z of the wave vector transfer constant.

In the coplanar geometry, the starting point of this scan follows the condition $(K-|Q_x|)^2 + Q_z^2 = K^2$, therefore it starts at $Q_x = \pm\left(K - \sqrt{K^2 - Q_z^2}\right)$. In the half-space $Q_x < 0$ the angular positions of the starting point are $(\omega, 2\theta) = (0, \operatorname{asin} -Q_z/K)$, on the side $Q_x > 0$ they are $(\theta_1, \theta_2) = (\operatorname{asin} -Q_z/K, 0)$. For small angles this approximates to $(\omega, 2\theta) = (0, -Q_z/K)$ for $Q_x < 0$ and $(\omega, \theta_2) = (-Q_z/K, 0)$ for $Q_x > 0$.

Q_z-scan. We change both the angle of incidence and the detector angle while keeping Q_x of the wave vector transfer constant.

In the coplanar geometry, the starting point of this scan follows the condition $(K-|Q_x|)^2 + Q_z^2 = K^2$, therefore it starts at $|Q_z| = \sqrt{2K|Q_x| - Q_x^2}$. In the half-space $Q_x < 0$ the angular positions of the starting point are $(\omega, 2\theta) = (0, \operatorname{acos}(1 + Q_x/K))$, on the side $Q_x > 0$ they are $(\theta_1, \theta_2) = (\operatorname{acos}(1 - Q_x/K), 0)$. For small angles this approximates to $(\omega, 2\theta) = (0, \sqrt{-2Q_x/K})$ for $Q_x < 0$ and $(\omega, \theta_2) = (\sqrt{2Q_x/K}, 0)$ for $Q_x > 0$.

offset scan. This scan is a line in the reciprocal space pointing towards the origin. We perform this scan by going from an angular offset $\omega/2\theta \neq 1/2$ with the step of $\Delta\omega/\Delta 2\theta = 1/2$.

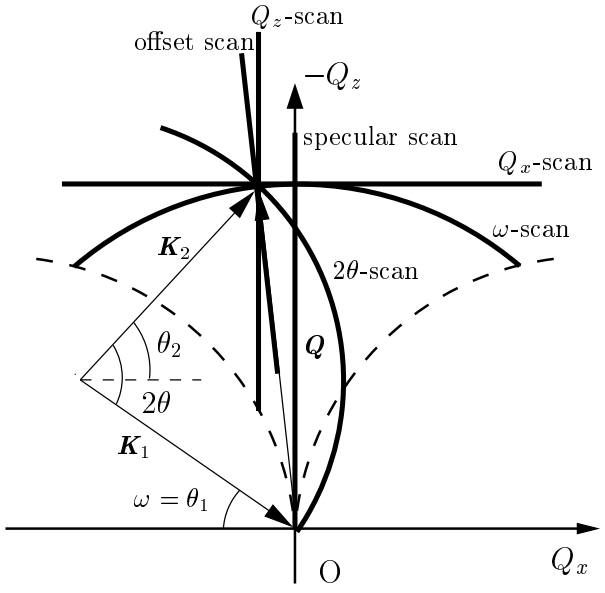

Figure 2.4. Drawing of the reciprocal space scans.

Chapter 3

X-ray reflectivity from planar multilayers

Résumé

Dans ce chapitre, nous traitons les processus fondamentaux qui interviennent dans la réflectivité spéculaire des rayons X sur des échantillons avec des interfaces parfaitement planes. En partant des équations de Maxwell, nous en déduisons l'équation d'onde, la relation de dispersion et les solutions des ondes planes. La présentation de ces résultats de base bien connus nous a permis d'établir un formalisme général que nous utiliserons dans tout ce travail pour des approches théoriques plus sophistiquées. Ensuite, nous nous intéressons à l'indice de réfraction des rayons X, paramètre du matériau qui détermine toutes les expériences de diffusion.

Dans la partie suivante, nous étudions les théories applicables au calcul de l'amplitude de la réflectivité. A partir des conditions de continuité entre les ondes à l'interface, nous obtenons les expressions des deux lois de base de l'optique : la loi de la réflexion et la loi de Snell. Nous en faisons une représentation graphique au moyen de la construction d'Ewald. La dérivation de ces formules conduit aux coefficients de Fresnel. La faible valeur négative de la susceptibilité est la principale cause de la différence existant entre l'optique X et l'optique classique (dans le visible) : la réflectivité totale externe a lieu pour tous les matériaux, les coefficients de Fresnel diminuant brutalement au-dessus de l'angle critique ; aussi l'intensité réfléchie n'est mesurable que dans le domaine des faibles angles d'incidence (mesurés par rapport à la surface des échantillons).

Nous formulons alors la théorie dynamique de la réflexion sur des matériaux en strates au moyen de formalismes de matrices et de récurrence. Nous obtenons aussi les formules des amplitudes des champs électriques de l'onde à l'intérieur de la multicouche ; nous verrons leur importance plus tard dans l'approximation de l'onde déformée de Born. Les principaux avantages du formalisme matriciel introduit dans ce chapitre seront démontrés dans l'étude de la réflectivité par des réseaux en multicouches où nous pouvons généraliser les coefficients de Fresnel, initialement définis pour la réflexion sur des interfaces planes. Nous trouvons que dans le cas où les intensités réfléchies sont faibles, la théorie dynamique peut être remplacée par l'approximation d'une réflexion simple. Cette approximation calcule l'amplitude de l'onde réfléchie comme la somme des contributions des ondes diffusées une seule fois à chaque interface, de telle sorte qu'elle calcule de façon dynamique la réflectivité à chaque interface mais néglige la diffusion multiple entre les différentes interfaces.

Dans la partie suivante, nous résolvons l'équation d'onde au moyen de la théorie cinématique habituelle dans la diffraction des rayons X. Ensuite, nous calculons la réflectivité pour des multicouches homogènes et de grandes largeurs avec une approche de calcul différente de l'approximation de Fraunhofer qui n'est pas utilisable. Cette méthode de phase stationnaire transforme l'intégrale cinématique de diffraction de volume (équivalente au principe de Huygens en optique) en une intégrale de chemin le long du parcours classique du faisceau réfléchi dans l'échantillon. Cependant, la théorie cinématique est équivalente à la première approximation de Born. Aussi, cette théorie cinématique ne tient pas compte de l'effet de la réfraction, de grande importance dans la réflectivité des rayons X. Ceci est en désaccord avec la diffraction des rayons X sur des multicouches, où la réfraction entraîne seulement un petit décalage par rapport aux positions cinématiques de Bragg.

Dans la dernière partie de ce chapitre, nous comparons ces théories au moyen de traitements analytiques et de simulations numériques. Nous réalisons la comparaison sur deux sortes d'échantillons : une multicouche périodique et une multicouche de Fibonacci. Tout d'abord, nous calculons la réflectivité sur une multicouche périodique simple. En utilisant une approche tout à fait inhabituelle pour décrire la séquence périodique des couches par la terminologie employée dans la physique des quasicristaux, nous préparons l'étape suivante du calcul de la réflectivité sur une multicouche de Fibonacci. La séquence des couches de cette multicouche est quasipériodique et une description analytique du profil de la réflectivité n'est pas facile. Aussi, nous utilisons l'approche que nous avons déjà développée pour la diffraction par des multicouches de Fibonacci et nous montrons que nous sommes capables de calculer la transformée de Fourier de la distribution de l'indice de réfraction et de trouver une formule analytique pour les positions des pics.

3.1 Introduction

In this chapter we deal with the basic phenomena of the specular X-ray reflection (SXR) from samples with perfectly flat interfaces. We start with the Maxwell equations from which we derive the wave equation, dispersion relation and the plane wave solutions. By presenting these basic and well-know results we establish a general formalism which we will keep in the whole work for more sophisticated theoretical approaches. In the second part of the general introduction we discuss the refractive index of X-rays as a material parameter determining all the scattering experiments.

In the next part we study the theories applicable to the calculation of the specular reflectivity amplitude. We apply the boundary conditions for an interface between two layers and formulate two basic laws of optics, the law of reflection and the Snell's law. We represent them graphically by means of the Ewald construction. We derive the formulae for the Fresnel coefficients. The small negative value of the susceptibility causes the main difference of X-ray optics with respect to the usual (visible) one: total external reflection of X-rays occurs for all materials, the Fresnel coefficients fall down quickly above the critical angle and therefore the reflected intensity is measurable only for small angles of incidence (measured with respect to the sample surface).

Then we formulate the dynamical theory of X-ray reflection from layered structures by means of both the matrix and recurrent formalisms. We provide formulae also for the amplitudes of the wavefields inside the multilayer, from which we will make use later in the distorted-wave Born approximation. The main advantage's of the matrix formalism introduced in the present chapter will be demonstrated mainly in the study of the reflectivity by multilayered gratings, where we can generalize the Fresnel coefficients, originally defined for the reflection from smooth interfaces. We find that for small reflected intensities the dynamical theory can be replaced by the single-reflection approximation. This approximation calculates the amplitude of the reflected wave as a sum of contributions of the waves scattered once at each interface, so that it calculates the reflectivity at each interface dynamically, but neglects the multiple scattering between different interfaces.

In the next section we solve the wave equation by means of the kinematical theory usual in X-ray diffraction. Since we calculate reflectivity from a homogeneous and laterally large multilayer, we cannot use the Fraunhofer approximation and therefore we employ a different calculation approach. This stationary phase method transforms the volume kinematical "diffraction" integral (equivalent to the Huygens principle known in optics) into the path integral along the classical path of the reflected beam in the sample. The kinematical theory is equivalent to the first Born approximation employing the vacuum plane waves as the eigenstates. It does not contain the effect of refraction, which, however, is of major importance in X-ray reflectivity. This is different to the X-ray diffraction from multilayers, where the refraction causes only a "small" shift in the Bragg position.

In the final part of this chapter we compare these theories by means of both the analytical treatment and numerical simulations. We perform the comparison for two kinds of samples: a periodic multilayer and a Fibonacci multilayer. Firstly, we calculate the reflectivity from a simple periodic multilayer. By using a quite unusual approach of describing the periodic layer sequence by the terminology of the physics of quasicrystals we prepare the next step of calculating the reflectivity from a Fibonacci multilayer. The layer sequence of this multilayer is quasiperiodic and an analytical description of the reflectivity profile is not easy. Therefore we employ an approach we developed earlier for the diffraction on Fibonacci multilayers and we show that we are able to calculate the Fourier transform of the refractive index distribution and to find an analytical formula for the peak positions.

3.2 Wave equation

X-rays are electromagnetic radiation. Their propagation can be described by the Maxwell equations, similarly to the visible optics [Kni76, BW93]. Combining the following two equations

$$\mathbf{rot}\,\boldsymbol{E} = -\frac{\partial \boldsymbol{B}}{\partial t}\,, \qquad \mathbf{rot}\,\boldsymbol{H} = \frac{\partial \boldsymbol{D}}{\partial t} \tag{3.1}$$

with the material relation

$$\boldsymbol{B} = \mu_0 \mu_r \boldsymbol{H} \tag{3.2}$$

(we note we use the SI system of units), we get

$$\mathbf{rot}\,\mathbf{rot}\,\boldsymbol{E}(\boldsymbol{r},t) = -\mu_0 \mu_r(\boldsymbol{r})\,\frac{\partial^2 \boldsymbol{D}(\boldsymbol{r},t)}{\partial t^2}\,. \tag{3.3}$$

This differential equation connects the electric field intensity $\boldsymbol{E}(\boldsymbol{r},t)$ and the electric displacement $\boldsymbol{D}(\boldsymbol{r},t)$. Since we study stationary scattering processes, the time dependence is expressed as $\boldsymbol{E}(\boldsymbol{r},t) = \boldsymbol{E}(\boldsymbol{r})e^{-i\omega t}$ and $\boldsymbol{D}(\boldsymbol{r},t) = \boldsymbol{D}(\boldsymbol{r})e^{-i\omega t}$ (this choice of the sign follows the quantum-mechanical notation). Further, using the material relation $\boldsymbol{D}(\boldsymbol{r}) = \epsilon_0 \epsilon_r(\boldsymbol{r})\boldsymbol{E}(\boldsymbol{r})$ we get

$$\mathbf{rot}\,\mathbf{rot}\,\boldsymbol{E}(\boldsymbol{r}) = K^2 \mu_r(\boldsymbol{r})\epsilon_r(\boldsymbol{r})\boldsymbol{E}(\boldsymbol{r})\,, \tag{3.4}$$

where the vacuum wave vector length is

$$K = \frac{\omega}{c} = \frac{2\pi}{\lambda}\,. \tag{3.5}$$

The fundamental of the X-ray scattering is the scattering by the individual electrons, which is kinematical (see the definition of the structure factor [AKK+74, Pin78]). The X-ray reflectivity depends on the electron density averaged over large volume, comparable to the volume of the unit cell, and therefore the wave feels only the macroscopic changes of the electric permitivity [Hol96]. This allows us to approximate $\mathrm{div}\,\boldsymbol{D} = \epsilon(\boldsymbol{r})\,\mathrm{div}\,\boldsymbol{E}(\boldsymbol{r}) \approx 0$. Let us assume that $\mu_r = 1$, which is mostly valid for the X-ray region. Then (3.4) is transformed into the *vectorial wave equation*

$$(\triangle + K^2 \epsilon_r(\boldsymbol{r}))\boldsymbol{E}(\boldsymbol{r}) = 0\,. \tag{3.6}$$

Introducing here formally the index of refraction $n(\boldsymbol{r})$ and the wave vector length in the medium $k(\boldsymbol{r})$

$$n(\boldsymbol{r}) = \sqrt{\epsilon_r(\boldsymbol{r})} \tag{3.7}$$

$$k(\boldsymbol{r}) = n(\boldsymbol{r})\,K \tag{3.8}$$

the wave equation is transformed to

$$(\triangle + k^2(\boldsymbol{r}))\boldsymbol{E}(\boldsymbol{r}) = 0\,. \tag{3.9}$$

Its solution in a homogeneous medium $\left(\epsilon_r(\boldsymbol{r}) = const\right)$ on a class of plane waves

$$\boldsymbol{E}(\boldsymbol{k},\boldsymbol{r}) = \boldsymbol{E}_0(\boldsymbol{k})\,e^{i\boldsymbol{k}(r)r} \tag{3.10}$$

provides the *dispersion relation*

$$|\boldsymbol{k}(\boldsymbol{r})|^2 = k^2(\boldsymbol{r})\,. \tag{3.11}$$

Therefore, the dispersion relation has an infinite number of solutions and the end-points of wave vectors of all allowable waves lie on the sphere $\mathcal{K}$ with diameter $k = nK$, Fig. 2.2, which we call the *Ewald sphere*.

Electromagnetic waves are transversal, i.e., the amplitude $\boldsymbol{E}_0$ is perpendicular to the direction of the propagation $\boldsymbol{k}$ [AKK$^+$74, BW93]. The sample surface defines the unique plane in the isotropic vacuum and therefore the vector $\boldsymbol{E}_0$ can be decomposed into two polarization states with respect to this plane. The component of $\boldsymbol{E}_0$ lying in the plane parallel to the sample surface is called *σ-polarization*. The perpendicular component is called *π-polarization* and it lies in the *plane of incidence* (the plane determined by the incidence wave vector and the surface normal). Bearing in mind that the sample is laterally homogeneous, then from symmetry considerations it follows that in the reflection process both components are scattered independently. There is no transition between the σ and π polarizations for $\mu_r \approx 1$ and the scattering is coplanar, i.e., the wave vector of the scattered wave lies in the plane of incidence. Then the vectorial wave equation reduces to a *scalar wave equation*. The π-polarization components of $\boldsymbol{E}_0$ after and before reflection make an angle 2θ and the amplitude of the scattered wave is diminished by $\cos(2\theta)$. The σ-polarized $\boldsymbol{E}_0$ component remains perpendicular to the plane of incidence. Studying X-ray reflectivity in the low angular region only, $\cos(2\theta) \approx 1$ and polarization effects play no role. Therefore the vectorial wave equation reduces to a scalar wave equation that is the same for both polarizations. It can be represented by any of the equivalent forms

$$\begin{aligned} &(\triangle + K^2\epsilon_r(\boldsymbol{r})\,)\; E(\boldsymbol{r}) = 0 \\ &(\triangle + K^2 n^2(\boldsymbol{r}))\; E(\boldsymbol{r}) = 0 \\ &(\triangle + k^2(\boldsymbol{r}) \quad)\; E(\boldsymbol{r}) = 0\;. \end{aligned} \tag{3.12}$$

The previous discussion on the transition from the vectorial to scalar wave equation was based on qualitative symmetry considerations. The validity of this result can be verified by means of the rigorous application of the boundary conditions for both σ (transversal electric, TE mode) and π (transversal magnetic, TM mode) polarizations separately [BW93, Hol96].

Finally, a particular *plane wave solution* in a homogeneous medium is

$$E(\boldsymbol{r}) = E_0\, e^{i\boldsymbol{k}\boldsymbol{r}}\;. \tag{3.13}$$

Therefore the total wavefield in a homogeneous medium can be expressed by a superposition of plane waves $e^{\pm i\boldsymbol{k}\boldsymbol{r}}$. In the most general case, it can be written as a superposition of transmitted (t) and reflected (r) waves

$$\begin{aligned} E(\boldsymbol{r}) &= \iint d\boldsymbol{k}_{\|}\, E(\boldsymbol{k}_{\|}, \boldsymbol{r}) = \iint d\boldsymbol{k}_{\|} \left(E_t(\boldsymbol{k})\, e^{i(\boldsymbol{k}_{\|}\boldsymbol{r}_{\|} + k_z z)} + E_r(\boldsymbol{k})\, e^{i(\boldsymbol{k}_{\|}\boldsymbol{r}_{\|} - k_z z)} \right) \\ &= \iint d\boldsymbol{k}_{\|}\, e^{i\boldsymbol{k}_{\|}\boldsymbol{r}_{\|}} \left(E_t(k_z)\, e^{ik_z z} + E_r(k_z)\, e^{-ik_z z} \right)\;. \end{aligned} \tag{3.14}$$

We made explicit use of the dispersion relation (3.11) that determines the third component $k_z = \sqrt{k^2 - k_x^2 - k_y^2}$ of the wave vector $\boldsymbol{k}^{\pm} = (k_x, k_y, \pm k_z)$ if two other components $(k_x, k_y) = \boldsymbol{k}_{\|}$ are known. According to the sample symmetry, we choose the parallel direction $\boldsymbol{r}_{\|}$ as parallel to the sample surface.

The intensity of a wave is $I(\boldsymbol{k}) = |E(\boldsymbol{k})|^2$. Then the *sample reflectivity* is defined [Pin78] as the ratio of the energy fluxes of the scattered $E(\boldsymbol{k})$ and incoming wave $E_{\rm inc}(\boldsymbol{k}^{\rm inc})$

$$\mathcal{R}(\boldsymbol{k}^{\rm inc}) = \left| \frac{E_0}{E_{\rm inc}} \right|^2 \cdot \left| \frac{k_z}{k_z^{\rm inc}} \right|\;. \tag{3.15}$$

3.3 Refractive index

In the previous section we described the propagation of an electromagnetic wave in a homogeneous medium by means of the Maxwell equations. We characterized formally the material by the index of refraction $n(\boldsymbol{r})$, see (3.7), depending on the position. However, from classical

electrodynamics [Fey64] we know that the index of refraction depends on the interaction of the medium with the electromagnetic wave and therefore it depends also on the wavelength λ of the incident wave. We can now write the relations (3.7),(3.8) explicitly including the wavelength dependence

$$k(\boldsymbol{r},\lambda) = n(\boldsymbol{r},\lambda)\,K \tag{3.16}$$

$$n^2(\boldsymbol{r},\lambda) = \epsilon_r(\boldsymbol{r},\lambda)\ . \tag{3.17}$$

The electric permittivity ϵ_r is unity in vacuum. The *electron susceptibility* (*polarizability*) $\chi(\lambda)$ is introduced [Cow75]

$$\epsilon_r(\boldsymbol{r},\lambda) = 1 + \chi(\boldsymbol{r},\lambda)\ . \tag{3.18}$$

X-ray scattering is the scattering of electromagnetic waves by electrons. The polarizability is proportional to the electron density $\rho(\boldsymbol{r})$ [Pin78]

$$\chi(\boldsymbol{r}) = -\frac{r_{el}\lambda^2}{\pi}\,\rho(\boldsymbol{r}) = -\frac{4\pi r_{el}}{K^2}\,\rho(\boldsymbol{r})\ . \tag{3.19}$$

The classical electron radius $r_{el} = \frac{1}{4\pi\epsilon_0}\frac{e^2}{m_{el}c^2} = 2.8179\cdot 10^{-15}$ m characterizes the amplitude of wave scattered by one electron in the forward direction

$$E(\boldsymbol{r},t) = \frac{r_{el}}{r}\,E_0(0,[t])\ , \tag{3.20}$$

where E_0 is the amplitude of the incoming wave and the brackets [ ] denote the retarded value. The wave scattered in the forward direction by an atom with Z electrons is

$$E([\boldsymbol{r},t]) = \frac{f\cdot r_{el}}{r}\,E_0(0,t)\ , \tag{3.21}$$

where $f = Z$ is the *atomic scattering factor*. In a crystal it equals the zeroth order Fourier transform of the electron density of the unit cell. In classical electrodynamics, the scattering factor is a real function. However, the electromagnetic waves cause atomic excitations. The Hönl dispersion corrections [Hö33] take the absorption and the inelastic scattering into account

$$f = Z + f' + if''\ . \tag{3.22}$$

These corrections are calculated by means of relativistic quantum mechanics and for the common wavelengths they are tabulated in the International Tables for X-Ray Crystallography [oC92]. A complementary source of information are the Henke tables [HGD93].[1] Henke tables cover f' and f'' for the atoms with atomic number Z between 1 and 92 in the energy region 30 eV–30 keV and they are based on a compilation of the available experimental measurements and theoretical calculations. The wavelength dependence of the dispersion correction is shown in Fig. 3.1 for As and Ga atoms.

Finally, the electron susceptibility (polarizability) of a material having M atoms in the elementary cell (volume V_{el}) is

$$\chi(\lambda) = -\frac{r_{el}\lambda^2}{\pi}\,\frac{\sum_{m=1}^{M} f_m(\lambda)}{V_{el}}\ , \quad f_m = Z_m + f'_m(\lambda) + if''_m(\lambda)\ . \tag{3.23}$$

From the above discussion follows that the scattered intensity of a crystal is wavelength dependent. Some materials (e.g., GaAs/GaInAs) have nearly the same susceptibilities for the usual X-ray tube radiation (e.g., the CuK$_\alpha$ spectral line). Measurable contrast in the reflectivity curves can be achieved using the wavelength dependence of the dispersion corrections for different

[1] They are available on the Internet at `ftp://xray1.physics.sunysb.edu`

Table 3.1. Refractive indices and critical angles for the wavelength CuKα_1 (1.540562 Å). The "AlAs on GaAs" states for an AlAs layer grown on a GaAs, where the elementary cell has tetragonal distortion. The calculation has been performed by the program `abrefr`*. This program is available at the WWW page of the author of this thesis,* `http://www.sci.muni.cz/~mikulik/` *and it is distributed under the GNU General Public License.*

material	$\delta = 1 - n = -\chi/2$	critical angle θ_C
AlAs	$1.062 \cdot 10^{-5} + i\,2.933 \cdot 10^{-7}$	0.264°
AlAs on GaAs	$1.065 \cdot 10^{-5} + i\,2.940 \cdot 10^{-7}$	0.264°
Cr	$2.120 \cdot 10^{-}5 + i\,2.176 \cdot 10^{-6}$	0.373°
Fe	$2.248 \cdot 10^{-5} + i\,2.890 \cdot 10^{-6}$	0.384°
GaAs	$1.456 \cdot 10^{-5} + i\,4.198 \cdot 10^{-7}$	0.309°
Ge	$1.454 \cdot 10^{-5} + i\,4.164 \cdot 10^{-7}$	0.309°
sapphire	$1.268 \cdot 10^{-5} + i\,1.473 \cdot 10^{-7}$	0.288°
Si	$7.577 \cdot 10^{-6} + i\,1.755 \cdot 10^{-7}$	0.223°
$TbFe_2$	$2.262 \cdot 10^{-5} + i\,3.366 \cdot 10^{-6}$	0.385°
W	$4.602 \cdot 10^{-5} + i\,3.746 \cdot 10^{-6}$	0.550°
Y_2Co_{17}	$2.158 \cdot 10^{-5} + i\,2.848 \cdot 10^{-6}$	0.376°

atoms (Fig. 3.1). Here the use of synchrotron radiation is advantageous because it enables one to tune the wavelength to the absorption edges of particular atoms.

The susceptibilities of some commonly used materials for are presented in Table 3.1 for CuKα_1 wavelength ($\lambda = 1.540562$ Å). We notice that they are of the order of 10^{-5} and therefore

$$n = \sqrt{\epsilon} = \sqrt{1+\chi} \approx 1 + \frac{\chi}{2} \,. \tag{3.24}$$

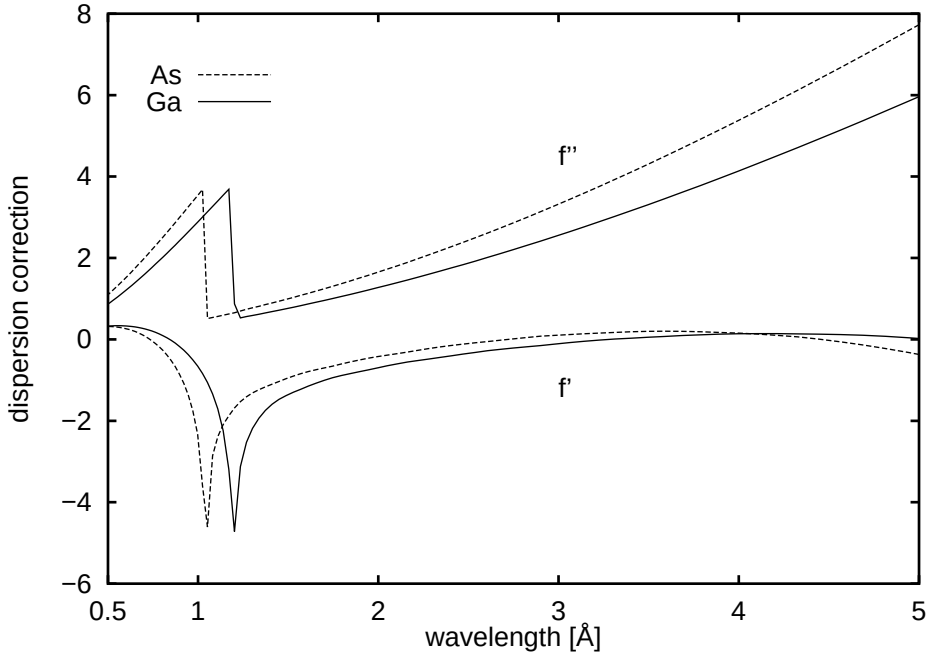

Figure 3.1. Wavelength dependence of the dispersion corrections f' and f'' for Ga and As atoms. Since $Z_{Ga} = 31$ and $Z_{As} = 33$, these corrections are of high importance near the absorption edge (at about 1 Å).

Since the phase velocity of X-ray in medium is higher than in vacuum, then the refractive index of X-rays is smaller than 1 and the susceptibility χ is negative. Introducing a deviation parameter δ

$$n = 1 - \delta \ , \quad \delta = -\frac{\chi}{2} \tag{3.25}$$

then facilitates calculations.

Finally, we make a brief note on the optical reflection of neutrons. The wave function of neutrons scattered by an atom fulfils [Sea89]

$$\psi(\boldsymbol{r}, t) = \frac{b}{r}\ \psi_0(0, [t]) \ , \tag{3.26}$$

where the neutron scattering length b is tabulated for common materials. Comparing this equation with (3.21) we find that all the relations for X-ray optical reflectivity remain valid for neutrons as well if we replace the X-ray scattering length $(f \cdot r_{el})$ by b. Contrary to X-rays, neutron scattering length b is not related to Z and it can be positive as well as negative. The main advantage of neutron reflectometry lies in the sensitivity to the magnetic properties of explored materials.

3.4 Dynamical theory of X-ray reflection

In the previous section we studied the propagation of X-rays in a homogeneous medium. Further, we will study the X-ray reflectivity from a multilayered system. A planar multilayer (Fig. 3.5) is formed by a stack of layers deposited on a thick substrate. The problem to solve now is to find the wavefields firstly in each layer and secondly on the top of the multilayer.

3.4.1 Boundary conditions

Let us study the transition of a wave through the interface j separating two adjacent layers $j, j+1$ (Fig. 3.2). The general solution of the dispersion equation (3.11) is given by (3.14). The unknown coefficients $E^j_{t,r}(k^j_z) = E_{t,r}(k_z, z)$ are constant in each homogeneous layer j. From the Maxwell equations the boundary conditions can be derived [BW93]. They provide relations to

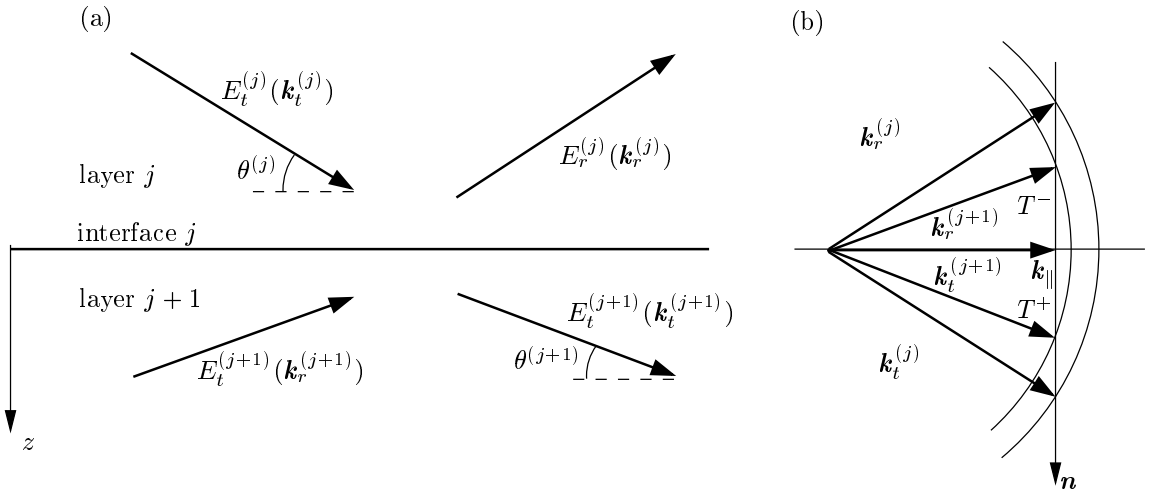

Figure 3.2. Wave vectors interacting at one interface shown in the real (a) and reciprocal (b) spaces. This geometry corresponds to angle of incidence greater than the critical angle (cf. Fig. 3.3(b)).

connect the wavefields in two adjacent layers $j, j+1$ separated by the interface j. The continuity relations of the amplitudes of electric intensity at the interface require

$$\begin{aligned}&\sum_{s=t,r} \iint d\boldsymbol{k}_{||}^{(j)\prime}\; E_s^{(j)} e^{i(\boldsymbol{k}_{||}^{(j)\prime}\boldsymbol{r}_{||} \pm k_z^{(j)\prime} z)} = \\ &\sum_{s=t,r} \iint d\boldsymbol{k}_{||}^{(j+1)\prime}\; E_s^{(j+1)} e^{i(\boldsymbol{k}_{||}^{(j+1)\prime}\boldsymbol{r}_{||} \pm k_z^{(j+1)\prime} z)}\end{aligned} \tag{3.27}$$

and the continuity of the normal derivatives

$$\begin{aligned}&\sum_{s=t,r} (\pm 1) \iint d\boldsymbol{k}_{||}^{(j)\prime}\; k_z^{(j)}\, E_s^{(j)} e^{i(\boldsymbol{k}_{||}^{(j)\prime}\boldsymbol{r}_{||} \pm k_z^{(j)\prime} z)} = \\ &\sum_{s=t,r} (\pm 1) \iint d\boldsymbol{k}_{||}^{(j+1)\prime}\; k_z^{(j+1)}\, E_s^{(j+1)} e^{i(\boldsymbol{k}_{||}^{(j+1)\prime}\boldsymbol{r}_{||} \pm k_z^{(j+1)\prime} z)}\;.\end{aligned} \tag{3.28}$$

The summation s goes over the transmitted ($(t),\ +k_z$) and reflected ($(r),\ -k_z$) waves. The two equations above can be rewritten into the equivalent form

$$\begin{aligned}&\iint d\boldsymbol{k}_{||}\, e^{i\boldsymbol{k}_{||}\boldsymbol{r}_{||}} \Big(E_t^{(j)}(k_z^{(j)}) e^{ik_z^{(j)} z} + E_r^{(j)} e^{-ik_z^{(j)} z} \\ &\qquad - E_t^{(j+1)}(k_z^{(j+1)}) e^{ik_z^{(j+1)} z} - E_r^{(j+1)}(k_z^{(j+1)}) e^{-ik_z^{(j+1)} z} \Big) = 0 \\ &\iint d\boldsymbol{k}_{||}\, e^{i\boldsymbol{k}_{||}\boldsymbol{r}_{||}} \Big(k_z^{(j)}\, E_t^{(j)}(k_z^{(j)}) e^{ik_z^{(j)} z} - k_z^{(j)}\, E_r^{(j)} e^{-ik_z^{(j)} z} \\ &\qquad - k_z^{(j+1)}\, E_t^{(j+1)}(k_z^{(j+1)}) e^{ik_z^{(j+1)} z} + k_z^{(j+1)}\, E_r^{(j+1)}(k_z^{(j+1)}) e^{-ik_z^{(j+1)} z} \Big) = 0\;.\end{aligned} \tag{3.29}$$

Since this equation has to be fulfilled at each point $\boldsymbol{r}_{||}$ of the interface, the boundary conditions separate into independent equations for each lateral component $\boldsymbol{k}_{||}$ given by the term in parenthesis, which are formally (lateral) Fourier coefficients of the wavefield $E(\boldsymbol{r}_{||}, z)$. Therefore the interface decomposes the total wavefield into separate groups of lateral Fourier components corresponding to the same lateral wave vector component $\boldsymbol{k}_{||}$. Further it shows that if at least one of the waves $E_{t,r}^{(j)}, E_{t,r}^{(j+1)}$ propagates in the medium, then it gives rise to the other three waves with the same lateral wave vector component $\boldsymbol{k}_{||}$. Thus we get the well-known law [BW93] of the *conservation of the lateral (tangential) wave vector components*

$$\boldsymbol{k}_{t,||}^{(j)} = \boldsymbol{k}_{r,||}^{(j)} = \boldsymbol{k}_{t,||}^{(j+1)} = \boldsymbol{k}_{r,||}^{(j+1)}\;, \tag{3.30}$$

which becomes for $k_y = 0$

$$k_{t,x}^{(j)} = k_{r,x}^{(j)} = k_{t,x}^{(j+1)} = k_{r,x}^{(j+1)}\;. \tag{3.31}$$

This way we formulated two principles that determine the propagation of rays in a medium: the dispersion relation (3.11) for the wave vectors in a homogeneous medium and the tangential condition (3.30) for the wave vectors at an interface. We combine both into a graphical representation in reciprocal space, similar to the *Ewald construction* used in X-ray diffraction. In particular, we draw the Ewald construction for a vacuum-layer interface (Fig. 3.3) and formulate two basic laws of the optical reflectivity [BW93].

Law of reflection

From the dispersion equation it follows that the end-points of two wave vectors drawn from the same point in reciprocal space lie on the Ewald sphere (with diameter K (nK) in vacuum (medium), respectively). The specular condition relates the lateral components of the wave vectors $\boldsymbol{k}_{||}$ of both waves $E_t\, e^{i(\boldsymbol{k}_{||}\boldsymbol{r}_{||}+k_z z)}$ and $E_r\, e^{i(\boldsymbol{k}_{||}\boldsymbol{r}_{||}-k_z z)}$ to be the same. Therefore their perpendicular wave vector components $\pm k_z$ differ in sign only and the angle of reflection equals the angle of incidence θ_1. This phenomenon is called the *law of reflection* and in Fig. 3.3(a) we represent it graphically in reciprocal space by means of the Ewald construction.

Snell's law

The tangential conditions applied to both layers give

$$\boldsymbol{k}_{||}^{(j)} = \boldsymbol{k}_{||}^{(j+1)} \ , \tag{3.32}$$

thus the wave vector components in the coplanar case are

$$\begin{aligned} k_x^{(j)} &= k_x^{(j+1)} \\ k_z^{(j+1)} &= \sqrt{(n^{(j+1)}K)^2 - |\boldsymbol{k}_{||}^{(j+1)}|^2} = \sqrt{(k_z^{(j)})^2 + ((n^{(j+1)})^2 - (n^{(j)})^2)K^2} \ . \end{aligned} \tag{3.33}$$

Since $k_x = k^{(j)}\cos\theta^{(j)} = K_x = K\cos\theta_1$, the equivalent angular condition known as *Snell's law* holds

$$n^{(j)}\cos\theta^{(j)} = n^{(j+1)}\cos\theta^{(j+1)} = \cos\theta_1 \ . \tag{3.34}$$

These two laws are known from classical optics [BW93]. Now we propose to discuss Snell's law by the Ewald construction for a vacuum-layer interface $j = 1$ ($n^{(1)} = 1$, $n^{(2)} = n < 1$), Fig. 3.3. The incoming vacuum wave $\boldsymbol{K}$ defines the origin S of the vacuum Ewald sphere $\mathcal{K}^{vac}$. Its lateral component (i.e., projection into a plane parallel to the surface) K_x has to be the same for the wave propagating in the medium n too. Because of this conservation of the lateral components, the end-point of the wave vector of the wave excited in the medium has to lie at the intersection of the surface normal drawn from the end-point of $\boldsymbol{K}$ and the Ewald sphere $\mathcal{K}$. Since $nK < K$, three distinct cases may happen:

1. Two tiepoints T^+, T^- and therefore two waves are excited in the medium n: the transmitted $\boldsymbol{k}_t$ and the reflected $\boldsymbol{k}_r$ waves, Fig. 3.3(b). Geometrical relations between the wave vectors then lead to Snell's law (3.33).

2. One tiepoint T_C is excited on the Ewald sphere $\mathcal{K}$, Fig. 3.3(c). The transmitted wave $E_t^{(2)}$ propagates parallel to the surface $k_z^{(2)} = 0$. This happens at certain vacuum incidence angle $\theta_1 = \theta_C$. The conditions

$$\cos\theta_C = n \tag{3.35a}$$

$$\theta_C \approx \sqrt{2\,\mathrm{Re}\,\delta} = \sqrt{-\,\mathrm{Re}\,\chi} \tag{3.35b}$$

$$k_C = K\sqrt{1-n^2} \approx K\sqrt{2\delta} \tag{3.35c}$$

hold and θ_C (k_C) are called the *critical angle (critical wave vector)* of total external reflection, respectively.

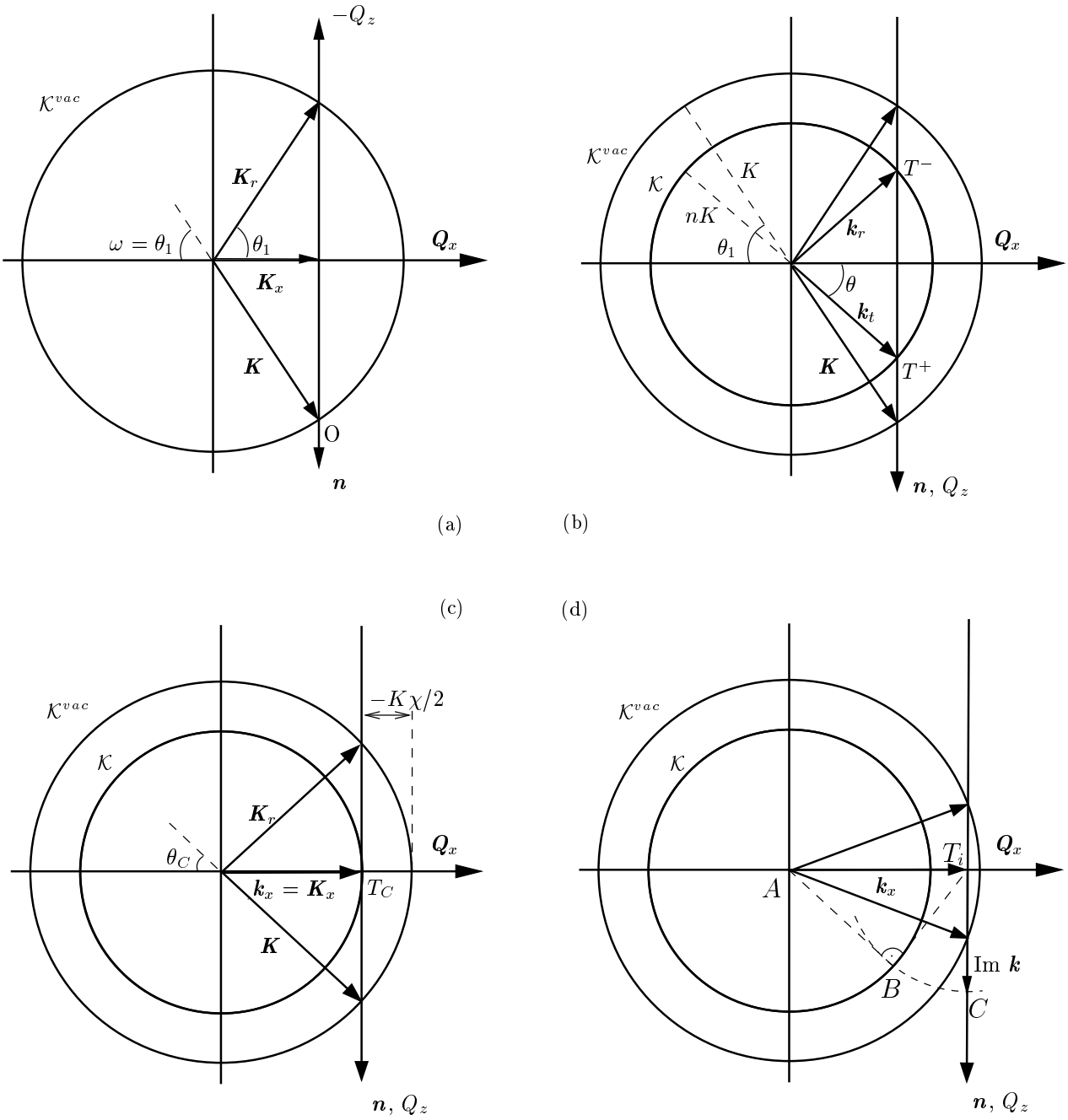

Figure 3.3. Graphical representation of the basic laws of reflectivity by means of the Ewald construction. The vacuum Ewald sphere is $\mathcal{K}^{vac}$, that of the layer with the refractive index n is $\mathcal{K}$ and $\boldsymbol{n}$ is the inner surface normal. Figure (a) represents the law of reflection. Snell's law is demonstrated in figures (b)–(d), where the angle of incidence θ_1: (b) is above the critical angle θ_C; (c) equals the critical angle; (d) is below the critical angle. In the latter case the lateral component of $\boldsymbol{k}$ is larger than the radius of the Ewald sphere of the medium and the condition $k_z^2 = (nK)^2 - k_x^2$ gives rise to the evanescent wave with purely imaginary k_z-component of the wave vector (if photoelectric absorption is neglected).

3. For angles of incidence below the critical angle the surface normal $\boldsymbol{n}$ does not cross the Ewald sphere $\mathcal{K}$ and therefore no real solution exists in the material n. The tiepoint T_i is given by the intersection of $\boldsymbol{n}$ with the Q_x axis, Fig. 3.3(d). In the medium, the lateral component k_x exceeds the admissible real wave vector length nK which gives rise to an imaginary vertical wave vector component k_z. Therefore the wave vector in the medium is complex and the condition of the conservation of the tangential components Eq. (3.32) is valid for both real and imaginary parts of wave vectors independently. The imaginary component k_z represents exponential damping of the wave in the medium in the direction perpendicular to the surface. This wave is called an *evanescent wave*.

We explain our method of plotting the imaginary part of the wave vector $\boldsymbol{k}$ in Fig. 3.3(d) in the following way. The lateral component k_x is real and it is given by the segment AT_i. The length of the wave vector in the medium is nK and therefore its end-point B lies on $\mathcal{K}$ while the beginning point is A. From the relation $k_z^2 = (nK)^2 - k_x^2$ it follows that AT_i is the hypotenuse and AB, BT_i are the other sides of the right angle triangle ABT_i. Then $|T_iB|$ is the length of the imaginary part k_z of the vertical component of the wave vector. Moving the point B into the point C on the axis Q_z we get $\operatorname{Im}\boldsymbol{k} = T_iC$.

Let us write the relation between the vacuum incidence angle $\omega = \theta_1$ and the angle $\theta = \theta^{(2)}$ and k_z in the medium explicitly. From Eq. (3.34) for the case of small angles follows

$$\theta = \sqrt{\omega^2 - 2\delta} = \sqrt{\omega^2 - \theta_C^2}\ . \tag{3.36}$$

The z component of the wave vector is

$$k_z = \sqrt{K_z^2 - 2\delta K^2} = \sqrt{K_z^2 - k_C^2}\ , \tag{3.37}$$

where in both cases the critical values θ_C and k_C are complex. Further we can see that for angles above the critical angle ($\omega \gg \theta_C$) these approximations hold:

$$\operatorname{Re}\theta \approx \omega - \frac{\theta_C^2}{2\omega} + O(\theta_C^4/\omega^3) \tag{3.38}$$

$$k_z \approx K_z + iK_z \operatorname{Im}\delta - \frac{k_C^2}{2K_z} + O(k_C^4/K_z^3)\ . \tag{3.39}$$

Therefore for larger angles of incidence the wave vector in the medium approaches the vacuum vector and refraction corrections are negligible.

3.4.2 Penetration depth

The amplitude of the plane wave propagating in a homogeneous medium (3.13) can be reexpressed

$$E(\boldsymbol{r}) = E_0\, e^{-\operatorname{Im}(k_z)z} \cdot e^{i(\boldsymbol{k}_\parallel \boldsymbol{r}_\parallel + \operatorname{Re}(k_z)\, z)} \tag{3.40}$$

and therefore the z-dependence of the intensity is

$$I(z) = |E(z)|^2 = I(0)\, e^{-2\operatorname{Im}(k_z)\, z}\ . \tag{3.41}$$

The *penetration depth* Λ is defined [BW93] as the depth at which the intensity drops $1/e$ times, $I(\Lambda) = (1/e) \cdot I(0)$, thus

$$\Lambda = \frac{1}{2\operatorname{Im}(k_z)}\ . \tag{3.42}$$

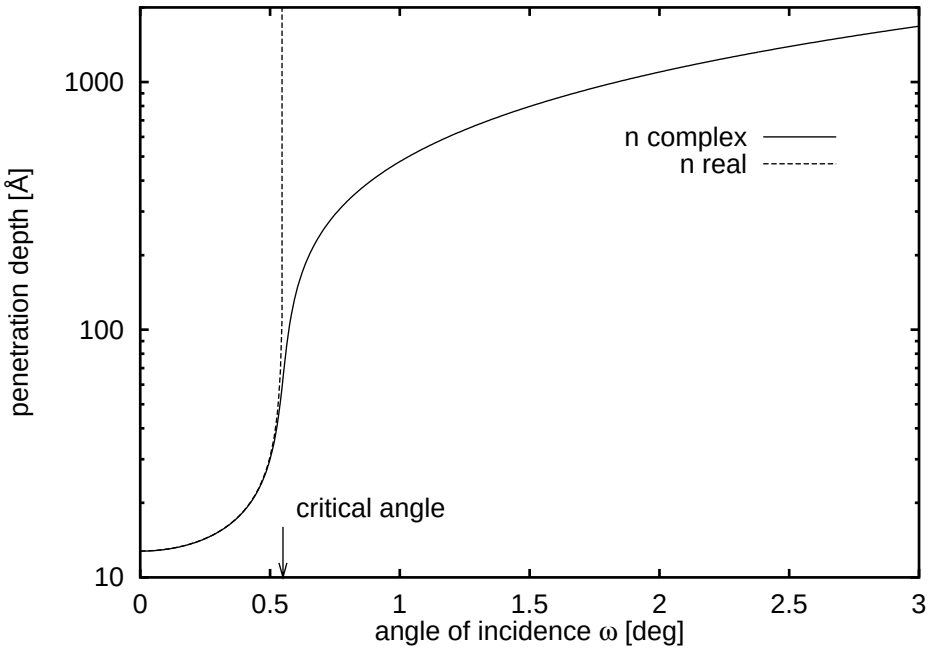

Figure 3.4. Angular dependence of the penetration depth of tungsten for the wavelength CuKα_1 (1.540562 Å). Tungsten is used as a capping layer for magnetic films [GRC+94]. Since it is a heavy element, its critical angle $\theta_C = 0.550^\circ$ is superior to the critical angle of the underlying materials. Therefore for small angles of incidence the evanescent wave propagating in a thick W layer damps substantially the intensity of the wavefield propagating in the underneath layers.

First of all we can see that for larger angles of incidence $\omega \gg \theta_C$ ($2k_z \gg k_C$) the penetration depth is inverse of the linear absorption coefficient μ

$$\Lambda(\omega \gg \theta_C) = \frac{1}{\mu} = \frac{1}{2K_z \operatorname{Im}\delta} \ . \tag{3.43}$$

Using the angular notation, the penetration depth is alternatively expressed as

$$\Lambda(\omega) = \left[2K \operatorname{Im}\left((1-\delta)\sqrt{\omega^2 - 2\delta}\right)\right]^{-1} \tag{3.44}$$

$$\Lambda(\omega \gg \theta_C) = \frac{1}{\mu} = \frac{1}{2K\omega \operatorname{Im}\delta} \ . \tag{3.45}$$

The angular dependence of the penetration depth is shown in Fig. 3.4. We note that in the non-absorbing case the penetration depth grows to infinity above θ_C. This is mostly the case of the neutron reflectivity [Sea89, Zab90].

The sensitivity of the penetration depth on the angle of incidence ω is of crucial importance for near-surface structure studies. Increasing the angle of incidence the transmitted wave penetrates more deeper and reveals information about atoms more distant from the sample surface. In addition to the X-ray optical reflectivity other X-ray scattering techniques (strongly asymmetric X-ray diffraction [Hä76, HNCM88, AM90, HBB95], X-ray fluorescence [dBLH94, Bru86] and grazing-incidence X-ray diffraction [MEC79, AAS84, BdB86, RP90, SPB95, BTPH95]) make use of this surface sensitivity.

3.4.3 Fresnel coefficients

The propagation directions of the transmitted and reflected waves in the reflection process from a single interface have been determined in the previous section. Let us now calculate the amplitudes of the corresponding wavefields at the position $z = z_j$ of an interface j separating layers j and $j+1$. The indices refer to our numbering of interfaces and layers in a multilayer,

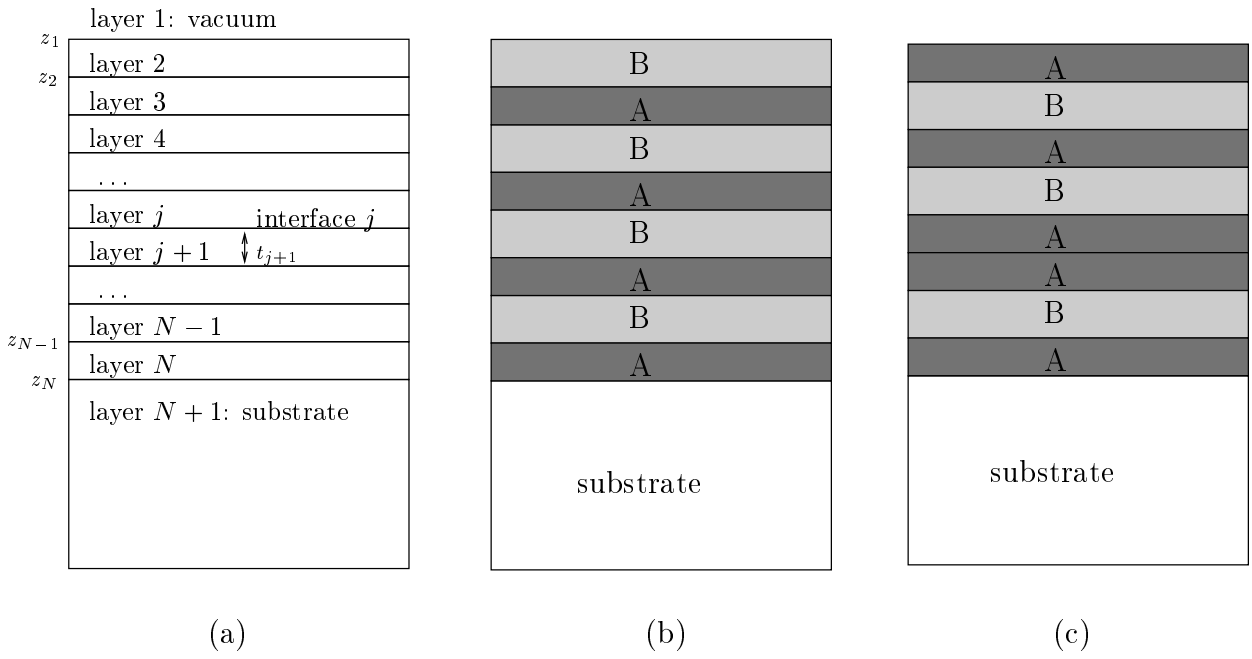

Figure 3.5. Sketch of a multilayer presenting the notation used in the text (a). Two particular examples of deterministic multilayers, a periodic multilayer with 4 periods and a quasiperiodic Fibonacci multilayer of the 5th order are shown in figures (b) and (c), respectively.

Fig. 3.5. Applying the boundary conditions ($\boldsymbol{k}_{\|}$=*const*) the integrand of (3.29) turns into the system of equations

$$\begin{aligned} E_t^{(j)} + \quad E_r^{(j)} \quad &= \quad E_t^{(j+1)} + \quad E_r^{(j+1)} \\ k_z^{(j)} E_t^{(j)} - \; k_z^{(j)} E_r^{(j)} \quad &= \; k_z^{(j+1)} E_t^{(j+1)} - \; k_z^{(j+1)} E_r^{(j+1)} \; . \end{aligned} \tag{3.46}$$

This can be expressed by means of a convenient matrix formalism (similarly to the Abèles matrix formalism [Ab50]):

$$\mathcal{P}^{(j)} \cdot \vec{E}^{(j)}(z_j) = \mathcal{P}^{(j+1)} \cdot \vec{E}^{(j+1)}(z_j) \; . \tag{3.47}$$

The *boundary matrix* of layer j is defined by

$$\mathcal{P}^{(j)} = \begin{pmatrix} 1 & 1 \\ k_z^{(j)} & -k_z^{(j)} \end{pmatrix} \; , \qquad \left(\mathcal{P}^{(j)}\right)^{-1} = \frac{1}{2k_z^{(j)}} \begin{pmatrix} k_z^{(j)} & 1 \\ k_z^{(j)} & -1 \end{pmatrix} \; , \tag{3.48}$$

and the amplitudes are represented by the column vector

$$\vec{E}^{(j)}(z) = \begin{pmatrix} E_t^{(j)}(z) \\ E_r^{(j)}(z) \end{pmatrix} = \begin{pmatrix} E_t^{(j)} \, e^{ik_z^{(j)} z} \\ E_r^{(j)} \, e^{-ik_z^{(j)} z} \end{pmatrix} \; . \tag{3.49}$$

The wavefield on the bottom side of the upper layer j is determined by the wavefield in the upper part of the layer $j+1$

$$\vec{E}^{(j)}(z_j) = \mathcal{P}_{j,j+1} \cdot \vec{E}^{(j+1)}(z_j) \tag{3.50}$$

$$\mathcal{P}_{j,j+1} = (\mathcal{P}^{(j)})^{-1} \, \mathcal{P}^{(j+1)} = \frac{1}{\mathfrak{t}_j} \begin{pmatrix} 1 & \mathfrak{r}_j \\ \mathfrak{r}_j & 1 \end{pmatrix} \; . \tag{3.51}$$

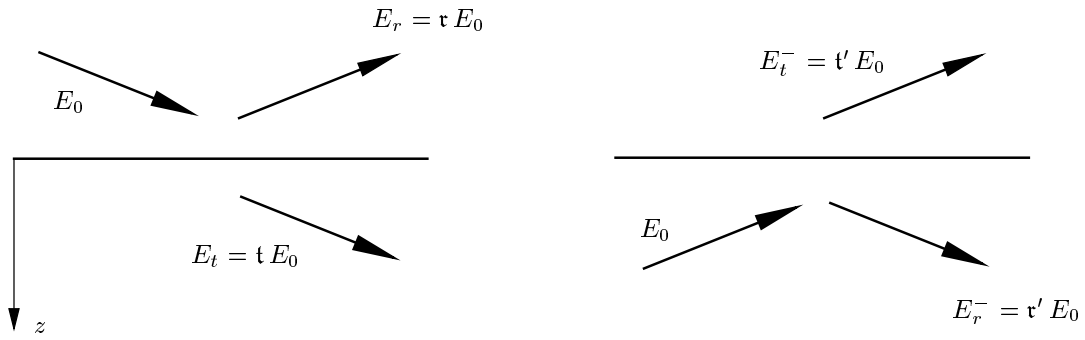

Figure 3.6. The Fresnel coefficients determine the reflection and transmission amplitudes of the waves passing through an interface. Irradiating the interface from the opposite side, they are related by $\mathfrak{r} = -\mathfrak{r}'$ *and* $1 + \mathfrak{r}\mathfrak{r}' = \mathfrak{t}\mathfrak{t}'$.

The "interface" matrix $\mathcal{P}_{j,j+1}$ describes transition through the interface separating layers j and $j+1$. Its elements are the *Fresnel reflection and transmission coefficients* [BW93]

$$\begin{aligned} \mathfrak{r}_j &= \left(\frac{E_r^{(j)}}{E_t^{(j)}}\right)_{E_r^{(j+1)}=0} = \frac{k_z^{(j)} - k_z^{(j+1)}}{k_z^{(j)} + k_z^{(j+1)}} \\ \mathfrak{t}_j &= \left(\frac{E_t^{(j+1)}}{E_t^{(j)}}\right)_{E_r^{(j+1)}=0} = \frac{2k_z^{(j)}}{k_z^{(j)} + k_z^{(j+1)}} \,. \end{aligned} \tag{3.52}$$

The graphical representation of their meaning is shown in Fig. 3.6.

In optics, the Fresnel coefficients are mostly written by the equivalent angular expressions. Within the approximation $\sin\theta \approx \theta$, adequate in X-ray optics, we write

$$\begin{aligned} \mathfrak{r}_j &= \frac{\theta^{(j)} - \theta^{(j+1)}}{\theta^{(j)} + \theta^{(j+1)}} \\ \mathfrak{t}_j &= \frac{2\theta^{(j)}}{\theta^{(j)} + \theta^{(j+1)}} \,. \end{aligned} \tag{3.53}$$

Further, for angles much larger than the critical angle the approximate formulae (3.39) give

$$\begin{aligned} \mathfrak{r}_j &\approx \frac{(k_C^{(j+1)})^2 - (k_C^{(j)})^2}{4K_z^2} = \frac{(k_C^{(j+1)})^2 - (k_C^{(j)})^2}{Q_z^2} = \frac{K^2\left(\chi^{(j)} - \chi^{(j+1)}\right)}{Q_z^2} \\ \mathfrak{t}_j &\approx 1 \,, \end{aligned} \tag{3.54}$$

where the *vacuum wave vector transfer* $\boldsymbol{Q} = \boldsymbol{K}_2 - \boldsymbol{K}_1 = (0, 0, Q_z)$, $Q_z = -2K_{1z}$. The approximate value $\mathfrak{t} = 1$ means that the transmitted wave is not diminished by the reflection process and dynamical extinction plays no role. The reflected intensity depends on the momentum transfer by the power law

$$|\mathfrak{r}|^2 \sim Q_z^{-4} \,, \tag{3.55}$$

which is similar to Porod's law in small-angle scattering [Gui63].

3.4.4 Reflection from a multilayer

In the preceding part we calculated the amplitudes of the waves acting in a reflection process by a single interface. Let us now calculate the reflection by a multilayer consisting of N interfaces, Fig. 3.5. The boundary conditions, either (3.47) or (3.50), couple the wavefields of two adjacent layers $j, j+1$ at interface j (at $z = z_j$). The wavefield inside the layer j (i.e., for $z_{j-1} \le z \le z_j$) is described by the column vector (3.49). Because both components are plane waves, the

amplitudes between the lower interface $j+1$ and the upper interface j are coupled by the phase relation

$$\vec{E}^{(j+1)}(z_j) = \mathcal{Q}^{(j+1)} \cdot \vec{E}^{(j+1)}(z_{j+1}) \tag{3.56}$$

$$\mathcal{Q}^{(j)} = \begin{pmatrix} e^{-ik_z^{(j)} t_j} & 0 \\ 0 & e^{ik_z^{(j)} t_j} \end{pmatrix} \equiv \begin{pmatrix} 1/\Phi_j & 0 \\ 0 & \Phi_j \end{pmatrix} . \tag{3.57}$$

The phase matrix $\mathcal{Q}^{(j)}$ is called *propagation matrix*, and $t_j = z_j - z_{j-1}$ is the layer thickness.

The boundary and propagation matrices allow us to describe the reflectivity from a multilayer by means of a very convenient matrix formalism. Using Eqs. (3.50) and (3.56), the wavefields calculated at the bottom interfaces of two neighbouring layers are coupled by the matrix relation

$$\vec{E}^{(j)}(z_j) = \mathcal{P}_{j,j+1}\mathcal{Q}^{(j+1)} \cdot \vec{E}^{(j+1)}(z_{j+1}) \equiv \mathcal{N}_j \cdot \vec{E}^{(j+1)}(z_{j+1}) \tag{3.58}$$

$$\mathcal{N}_j \equiv \mathcal{P}_{j,j+1}\mathcal{Q}^{(j+1)} . \tag{3.59}$$

The matrix $\mathcal{N}_j$ couples the matrices of the interface j and of the underlaying layer, i.e., it couples the wavefields on the top of interfaces j and $j+1$. Afterwards, the vacuum (index v) and the substrate (index s) wavefields are connected by the *transfer matrix of the whole multilayer* $\mathcal{M}$

$$\begin{pmatrix} T^v \\ R^v \end{pmatrix} = \mathcal{M} \cdot \begin{pmatrix} T^s \\ R^s \end{pmatrix} \tag{3.60}$$

$$\mathcal{M} = \prod_{j=1}^{N} \mathcal{N}_j \equiv \begin{pmatrix} M_{11} & M_{12} \\ M_{21} & M_{22} \end{pmatrix} , \tag{3.61}$$

where the product goes over all interfaces. The substrate has infinite thickness, therefore its reflectivity amplitude R^s is zero and its phase matrix $\mathcal{Q}^{(N+1)}$ is defined to be unity. Finally, the reflectivity amplitude of the whole multilayer is

$$R = R^v = \frac{M_{21}}{M_{11}} . \tag{3.62}$$

In this matrix arrangement we described the wavefields by connecting them via the matrices $\mathcal{N}_j$. This underlines the dominant role the interfaces play in the reflectivity. However, an equivalent calculation approach oriented to the bulk properties of the layers can be developed. We mention the bulk approach in this place not only because it is used in the X-ray diffraction, but mainly because we will make use of it later in the dynamical theory of reflectivity gratings (Ch. 5). Let us connect (3.47) and (3.56) and introduce the *transfer matrix of layer* j

$$\mathcal{M}^{(j)} = \mathcal{P}^{(j)} \cdot \mathcal{Q}^{(j)} \cdot (\mathcal{P}^{(j)})^{-1} , \tag{3.63}$$

which depends only on the parameters of layer j. Then the multilayer transfer matrix is expressed by

$$\mathcal{M} = (\mathcal{P}^v)^{-1} \cdot \mathcal{M}^{ML} \cdot \mathcal{P}^s \equiv \begin{pmatrix} M_{11} & M_{12} \\ M_{21} & M_{22} \end{pmatrix} \tag{3.64}$$

$$\mathcal{M}^{ML} = \prod_{j=2}^{N} \mathcal{M}^{(j)} , \tag{3.65}$$

where the product goes over all layers (cf. (3.61)).

However, we usually suppose that the reflection is interface-related scattering because the physical meaning is included in the matrices $\mathcal{N}$. The elements of the multilayer transfer matrix $\mathcal{M}$, given by Eq. (3.61), of the interface transfer matrices $\mathcal{N}_j$ and of any stack of $\mathcal{N}_j$ have clear

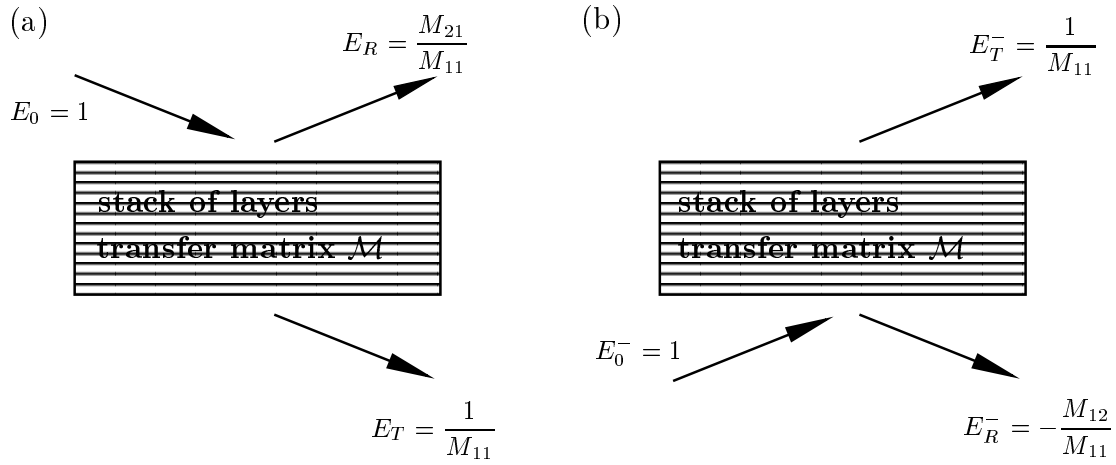

Figure 3.7. Physical meaning of the elements of a multilayer transfer matrix $\mathcal{M}$. This stack plays a role of a "generalized" interface, cf. Fig. 3.6.

physical meaning. Let us show it denoting any of the before-mentioned matrices by $\mathcal{M}$, Fig. 3.7. If an incident wave E_0 comes from above of the multilayer stack (arrangement (a)), then the wavefields on the upper and bottom sides are related by

$$\begin{pmatrix} E_0 \\ E_R \end{pmatrix} = \begin{pmatrix} M_{11} & M_{12} \\ M_{21} & M_{22} \end{pmatrix} \begin{pmatrix} E_T \\ 0 \end{pmatrix} , \tag{3.66}$$

wherefrom the *stack reflection and transmission coefficients* follow

$$\begin{aligned} R^+ &= \frac{E_R}{E_0} = \frac{M_{21}}{M_{11}} \\ T^+ &= \frac{E_T}{E_0} = \frac{1}{M_{11}} . \end{aligned} \tag{3.67}$$

If the incident wave comes from the bottom side of the stack (arrangement (b)), then

$$\begin{pmatrix} 0 \\ E_T^- \end{pmatrix} = \begin{pmatrix} M_{11} & M_{12} \\ M_{21} & M_{22} \end{pmatrix} \begin{pmatrix} E_R^- \\ E_0^- \end{pmatrix} \tag{3.68}$$

from which the *backward stack reflection and transmission coefficients* are found

$$\begin{aligned} R^- &= \frac{E_R^-}{E_0^-} = -\frac{M_{12}}{M_{11}} \\ T^- &= \frac{E_T^-}{E_0^-} = \frac{1}{M_{11}} . \end{aligned} \tag{3.69}$$

In the latter formula we made use of the equality $(\det \mathcal{M}) = 1$. If this condition is not fulfilled (in the case of rough multilayers, for instance), then $T^- = (\det \mathcal{M})/M_{11}$. The amplitudes R^+, T^+, R^-, T^- play the role of generalized Fresnel coefficients of a multilayer stack in the same manner as the Fresnel reflection and transmission coefficients act at a single interface, see Fig. 3.6. Therefore the structure and the physical meaning of those matrices are the same, and with the addition of the associativity of the matrix multiplication it means that the big multilayer matrix $\mathcal{M}$ can be calculated from whichever stack we prefer.

This is of main importance in the calculation of reflectivity from multilayers where the stacking sequence (layer arrangement) is given by a deterministic mathematical rule, see Sec. 3.6. Since the layer sequence in those multilayers is mostly given by a recurrent rule, the corresponding matrix sequence (3.61) reflects this rule in the same way. This makes the matrix approach very natural and numerically faster compared to the calculation of the whole multilayer matrix layer by layer.

It follows from the earlier discussion that the matrix approach provides the wavefield amplitudes in each layer. We will make use of it in the DWBA calculation (Sec. 4.5), where these wavefields in each layer form an eigenstate needed in the DWBA calculation. However, up to now we put the phase shifts of the waves zero at the origin of direct space (the factor $\pm ik_z z$ appears in the exponent) and it seems to be more convenient to work with amplitudes whose phase shifts are zero at the lower inner interface of the layer. Then we define $T^{(j)}, R^{(j)}$ by

$$\begin{pmatrix} E_t^{(j)}(z_j) \\ E_r^{(j)}(z_j) \end{pmatrix} = \begin{pmatrix} T^{(j)}\, e^{ik_z^{(j)}(z-z_j)} \\ R^{(j)}\, e^{-ik_z^{(j)}(z-z_j)} \end{pmatrix} \tag{3.70}$$

and we further use them in the DWBA.

Further we note that we generalize $T^{(j)}, R^{(j)}$ to the many-beam case in the dynamical theory of gratings (Ch. 5), where we present them as the coefficients of the linear combination of the independent eigenvectors of the matrix solution of the wave equation.

Single-reflection approximation—matrix approach

The dynamical theory gives exact relations for the reflectivity amplitude. However, as it is the usual case of dynamical theories, the relations are not quite transparent. Therefore we find that in the angular region, where the reflected intensity is small (compared to unity), it is possible to simplify these equations and derive a semi-kinematical-like approximation of X-ray reflectivity. We show that the physical meaning of this approximation is that it sums only the contributions of the single-reflection processes, i.e., the total reflectivity amplitude is the sum of the amplitudes of waves reflected once by each interface. This is contrary to the dynamical theory, which takes into account the interaction of the waves reflected by all the interfaces, and the reflected wave above the sample surface is in dynamical equilibrium with the wavefield below. The single-reflection approximation can be obtained from the dynamical theory supposing the back-reflection Fresnel coefficient being zero, $\mathfrak{r}' = 0$, Fig. 3.6.

The boundary matrix (3.51) can be written in the alternative matrix form

$$\mathcal{P}_{j,j+1} = \frac{1}{\mathfrak{t}_j}\left[\begin{pmatrix} 1 & 0 \\ 0 & 1 \end{pmatrix} + \mathfrak{r}_j \begin{pmatrix} 0 & 1 \\ 1 & 0 \end{pmatrix}\right] \equiv \frac{1}{\mathfrak{t}_j}\left(\hat{I} + \mathfrak{r}_j \hat{I}'\right) \ . \tag{3.71}$$

The unity and anti-unity matrices (proportional to the first and the third Pauli matrices [Dav69]) are defined

$$\hat{I} = \begin{pmatrix} 1 & 0 \\ 0 & 1 \end{pmatrix} \ , \qquad \hat{I}' = \begin{pmatrix} 0 & 1 \\ 1 & 0 \end{pmatrix} \ . \tag{3.72}$$

They follow the relations

$$\hat{I}\hat{I}' = \hat{I}'\hat{I} = \hat{I}' \ , \qquad \hat{I}'\hat{I}' = \hat{I} \ , \qquad \mathcal{Q}\hat{I}' = (\hat{I}'\mathcal{Q})^T \ , \tag{3.73}$$

where $\mathcal{Q}$ is a diagonal matrix and the superscript T denotes matrix transpose. Then it is possible to develop the multilayer matrix (3.61) in the powers of the Fresnel coefficients $\mathfrak{r}_j$. Restricting ourselves to the term linear in $\mathfrak{r}_j$ we neglect the multiple scattering processes and the transfer matrix is approximated

$$\mathcal{M}^{(j)} = \frac{1}{\prod_{j=2}^{N} \mathfrak{t}_j}\left[\prod_{j=1}^{N} \mathcal{Q}^{(j)} \cdot \hat{I} + \sum_{j=1}^{N}\prod_{m=2}^{j} \mathcal{Q}^{(m)} \cdot \mathfrak{r}_j \cdot \hat{I}' \prod_{n=j+1}^{N} \mathcal{Q}^{(n)}\right] \ . \tag{3.74}$$

In order to calculate the reflectivity amplitude (3.62), the matrix elements

$$\begin{aligned} M_{11} &= \left(\prod_{j=1}^{N} \mathcal{Q}^{(j)} \right)_{11} \\ M_{21} &= \left(\sum_{j=1}^{N} \prod_{m=2}^{j} \mathcal{Q}^{(m)} \, \mathfrak{r}_j \cdot \hat{I}' \prod_{n=j+1}^{N} \mathcal{Q}^{(n)} \right)_{21} \end{aligned} \tag{3.75}$$

need to be evaluated. Putting the explicit form of the phase matrix (3.57) into the above equations we get for the amplitude of the reflected wave

$$R = \frac{M_{21}}{M_{11}} = \left(\sum_{j=1}^{N} \prod_{m=2}^{j} \left(\mathcal{Q}^{(m)} \right)^2 \mathfrak{r}_j \cdot \hat{I}' \right)_{21} , \tag{3.76}$$

which expands into the *explicit* forms

$$R = \sum_{j=1}^{N} \mathfrak{r}_j \prod_{m=2}^{j-1} \Phi_m^2 = \sum_{j=1}^{N} \mathfrak{r}_j \prod_{m=2}^{N} e^{2ik_z^{(m)} t_m} = \sum_{j=1}^{N} \mathfrak{r}_j \prod_{m=2}^{j-1} e^{-iq_z^{(m)} t_m} \tag{3.77a}$$

$$R = \sum_{j=1}^{N} \mathfrak{r}_j \, e^{-i\phi_j} , \qquad \phi_j = \sum_{m=2}^{j-1} q_z^{(m)} t_m \tag{3.77b}$$

or into the *recurrent* form

$$R = R^{(1)} , \qquad R^{(j)} = \mathfrak{r}_j + R^{(j+1)} \, e^{-iq_z^{(j+1)} t_{j+1}} , \qquad R^{(N)} = \mathfrak{r}_N . \tag{3.77c}$$

The wave vector transfer in layer j

$$q_z^{(j)} = -2k_z^{(j)} \tag{3.78}$$

has been introduced. The phase factor $\Phi_j = e^{ik_z^{(j)} t_j}$ has been defined in (3.57).

The relations (3.77a)–(3.77c) give clear evidence why this approach is called the *single-reflection approximation* [Hol96]. The incoming wave penetrates into the sample and it passes $j-1$ layers before being reflected at the jth interface and after the reflection process it goes back. The reflection process changes the amplitude by $\mathfrak{r}_j$ and therefore the reflection by each interface is treated dynamically, applying the correct boundary conditions. The total phase shift on the passed path is $\phi_j = \sum_{m=2}^{j-1} q_z^{(m)} t_m$.

The summation in (3.77a)–(3.77c) is evaluated going from the interface nearer the vacuum towards the substrate interface, thus it is optimized for a layer sequence given by a mathematical rule determining the layers from the top of the multilayer to its bottom. In contrary, the mathematical rule determining the layer sequence can be given starting from the substrate to the vacuum (i.e., in the growth direction). Then it is useful to relate the phase shifts to the substrate

$$R = e^{-i\phi_N} \, F \tag{3.79}$$

and thus define alternative *explicit and recurrent relations* for F

$$F = \sum_{j=N}^{1} \mathfrak{r}_j \, e^{i \sum_{m=j}^{N} q_z^{(m)} t_m} \tag{3.80a}$$

$$F = F^{(j)} , \qquad F^{(j)} = \left(\mathfrak{r}_j + F^{(j+1)} \right) e^{iq_z^{(j)} t_j} , \qquad F^{(N+1)} = 0 . \tag{3.80b}$$

These formulae will be used to calculate the reflectivity by the Fibonacci multilayer in Sec. 3.6.2.

Parratt formalism

The formula (3.58) enables us to calculate dynamically the amplitudes of both the transmitted and reflected waves in each layer in the multilayer. However, in many cases the studied sample consists of a small number of layers and the primary interest is the calculation of the reflected intensity on the top of the multilayer only. Then a faster calculation procedure would be the following one. The recurrent matrix algorithm (3.58) treated earlier can be transformed into a recursion one which couples the reflectivity amplitude at the bottom layer interfaces by a single relation

$$R^{(j)} \equiv \frac{E_r^{(j)}(z_j)}{E_t^{(j)}(z_j)} = \frac{\mathfrak{r}_j + R^{(j+1)}\, e^{-iq_z^{(j+1)} t_{j+1}}}{1 + \mathfrak{r}_j R^{(j+1)}\, e^{-iq_z^{(j+1)} t_{j+1}}} \ . \tag{3.81}$$

We start the recurrent calculation procedure from the reflectivity $R^{(N)} = \mathfrak{r}_N$ of the substrate interface and after evaluating $R^{(j)}$ at all of the upper interfaces the multilayer reflectivity amplitude $R = R^{(1)}$ is known. This recurrent formula well-known in optics [Kni76] has been used first in X-ray reflectivity measurement by Parratt [Par54], together with the approximate relations (3.53).

Single-reflection approximation—Parratt formalism

Let us use the Parratt formalism and assume that the reflected intensities are weak. Then the denominator in (3.81) can be approximated by unity and the recurrent relation becomes linear

$$R^{(j)} = \mathfrak{r}_j + R^{(j+1)}\, e^{-iq_z^{(j+1)} t_{j+1}} \ . \tag{3.82}$$

We find that this equation coincides perfectly with the single-reflection approximation we derived earlier using the matrix formalism, Eq. (3.77c).

Contrary to the rule (3.81), the above linear recurrent relation can be applied efficiently to deterministic multilayers if explicit or recurrent relations for $R^{(j)}$ in (3.77c) or for the phases $\phi^{(j)}$ in (3.77b) are known. This will be demonstrated in Sec. 3.6.

3.4.5 Single layer

Let us study the reflectivity from a system of a single layer (thickness t_2) deposited on a thick substrate. The dynamical theory will be used first. The multilayer transfer matrix is

$$\mathcal{M} = (\mathcal{P}^v)^{-1}\mathcal{M}^{(2)}\mathcal{P}^s \tag{3.83}$$

$$\begin{aligned}\mathcal{M}_2 &= \mathcal{P}^{(2)} \cdot \mathcal{Q}^{(2)} \cdot (\mathcal{P}^{(2)})^{-1} = \frac{1}{2k_z^{(2)}\Phi_2} \begin{pmatrix} k_z^{(2)}(1+(\Phi_2)^2) & (1-(\Phi_2)^2) \\ (k_z^{(2)})^2(1-(\Phi_2)^2) & k_z^{(2)}(1+(\Phi_2)^2) \end{pmatrix} \\ &= \frac{1}{k_z^{(2)}} \begin{pmatrix} k_z^{(2)} \cos q_z^{(2)} t_2 & \sin q_z^{(2)} t_2 \\ i(k_z^{(2)})^2 \sin q_z^{(2)} t_2 & k_z^{(2)} \cos q_z^{(2)} t_2 \end{pmatrix} \ ,\end{aligned} \tag{3.84}$$

where $q_z^{(2)} = k_z^{(2)} t_2$ and $(\Phi_2)^2 = e^{iq_z^{(2)} t_2}$. The reflectivity curve is shown in Fig. 3.8. We can notice the periodic oscillations, known as the *thickness oscillations* or the *Kiessig fringes* [Kie31]. They are caused by the finite layer thickness, i.e., by the periodicity in the matrix $\mathcal{M}_2$; the boundary matrices of vacuum $\mathcal{P}^v$ and of the substrate $\mathcal{P}^s$ do not contribute to the phase shifts.

Calculating the reflectivity by the approach of the matrices $\mathcal{N}$ the transfer matrix is

$$\begin{aligned}\mathcal{M} = \mathcal{N}_1\mathcal{N}_2 &= \frac{1}{4k_z^{(1)}k_z^{(2)}\Phi_2} \begin{pmatrix} 1 & \mathfrak{r}_1 \\ \mathfrak{r}_1 & 1 \end{pmatrix} \begin{pmatrix} 1 & 0 \\ 0 & (\Phi_2)^2 \end{pmatrix} \begin{pmatrix} 1 & \mathfrak{r}_2 \\ \mathfrak{r}_2 & 1 \end{pmatrix} \\ &= \frac{1}{4k_z^{(1)}k_z^{(2)}\Phi_2} \begin{pmatrix} 1+\mathfrak{r}_1\mathfrak{r}_2(\Phi_2)^2 & \mathfrak{r}_2+\mathfrak{r}_1(\Phi_2)^2 \\ \mathfrak{r}_1+\mathfrak{r}_2(\Phi_2)^2 & \mathfrak{r}_1\mathfrak{r}_2+(\Phi_2)^2 \end{pmatrix} \ ,\end{aligned} \tag{3.85}$$

where the Fresnel coefficients $\mathfrak{r}_1, \mathfrak{r}_2$ apply to the vacuum-layer and layer-substrate interfaces, respectively. According to (3.62), the reflectivity amplitude is the same as provided by the second iteration of the Parratt formalism (3.81)

$$R = \frac{\mathfrak{r}_1 + \mathfrak{r}_2(\Phi_2)^2}{1 + \mathfrak{r}_1\mathfrak{r}_2(\Phi_2)^2} \ . \tag{3.86}$$

Now let us use approximative methods to calculate the reflectivity amplitude. Within the single-reflection approximation (3.77c) it is

$$R^{\mathrm{SRA}} = \mathfrak{r}_1 + \mathfrak{r}_2\,(\Phi_2)^2 = \mathfrak{r}_1 + \mathfrak{r}_2\, e^{-iq_z^{(2)}t_2} \ . \tag{3.87}$$

We find that the reflectivity coincides with that calculated by the dynamical theory (Fig. 3.8) except for a small region close to the critical angle of the layer. There the wave is still evanescent, but the imaginary part of the vertical component of the wave vector decreases and the reflected intensity is still close to unity.

The maxima of the reflectivity oscillations follow the relation

$$-q_{z,m}^{(2)} = \frac{2\pi}{t_2}\, m \tag{3.88}$$

and they are inversely proportional to the layer thickness. However, the measurement is performed in the vacuum, therefore neither the reciprocal space maxima

$$-Q_{z,m} = \sqrt{q_{z,m}^2 + 4(1-n_2^2)K^2} \approx \sqrt{q_{z,m}^2 + 8\delta_2 K^2} = \sqrt{q_{zm}^2 + 4k_C^2} \tag{3.89}$$

nor the angular distribution of maxima (angle of incidence ω_m)

$$\sqrt{\omega_m^2 - \theta_C^2} = \frac{2\pi}{2kt_2}\, m = \frac{\lambda}{2t_2}\, m \tag{3.90}$$

are equidistant due to the refraction.

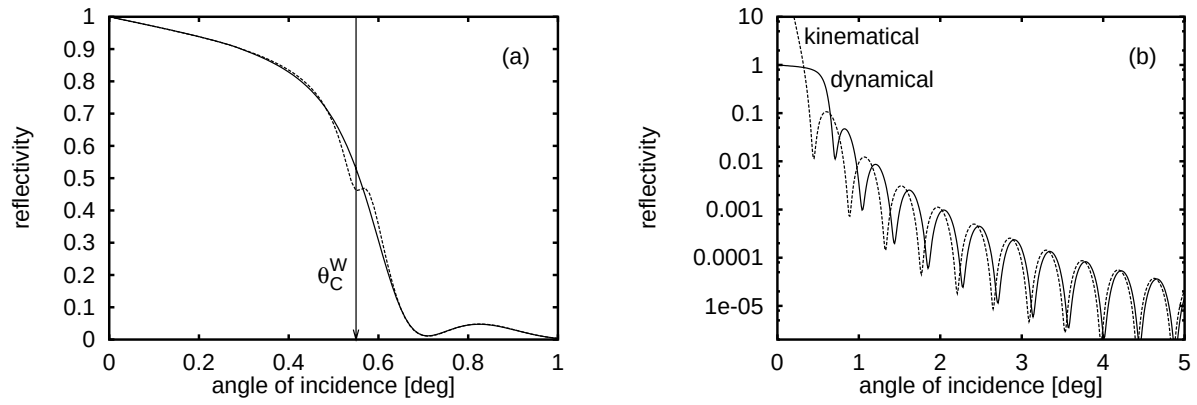

Figure 3.8. Reflectivity from a single tungsten layer (thickness 100 Å) deposited on a sapphire substrate. (a) Dynamical theory (full curve) and the single-reflection approximation (dashed curve) coincide except for the region near the critical angle of the layer. (b) Reflectivity calculated by the kinematical theory is not shifted by the critical angle, and the period of oscillations approaches that calculated dynamically as the vacuum wave vector transfer Q_z approaches that in the layer $q_z^{(2)}$.

3.5 Kinematical theory of X-ray reflection

In the previous part we treated the dynamical theory of X-ray reflection, which solved the wave equation and the boundary conditions exactly. Now we will formulate the kinematical theory, which is based on an approximate solution of the wave equation. We will show that the kinematical theory calculates the reflected field as a single reflection process (as it was the case of the single-reflection approximation of the dynamical theory), where all the waves are vacuum plane waves and not waves refracted due to the refractive index distribution in the sample.

The wave equation (3.12) in a medium can be rearranged into the form

$$(\triangle + K^2)E(\boldsymbol{r}) = V(\boldsymbol{r})\,E(\boldsymbol{r}) \tag{3.91}$$

that separates the *vacuum wave equation* (homogeneous equation)

$$(\triangle + K^2)E(\boldsymbol{r}) = 0 \tag{3.92}$$

and the contribution by a *scattering potential* in the medium

$$V(\boldsymbol{r}) = (1 - \epsilon_r(\boldsymbol{r}))K^2 = -K^2\,\chi(\boldsymbol{r})\ . \tag{3.93}$$

This differential equation can be solved by means of the method of Green functions. The Green function of the homogeneous equation (3.92) is [Dav69]

$$G(\boldsymbol{r}, \boldsymbol{r}') = -\frac{1}{4\pi}\frac{e^{i|\boldsymbol{r}-\boldsymbol{r}'|K}}{|\boldsymbol{r} - \boldsymbol{r}'|} \tag{3.94}$$

and it represents an outgoing spherical wave in vacuum. The exact solution of the wave equation (3.91) is

$$E(\boldsymbol{r}) = E_{\rm inc}(\boldsymbol{r}) + \int d\boldsymbol{r}'\, G(\boldsymbol{r}, \boldsymbol{r}')V(\boldsymbol{r}')E(\boldsymbol{r}')\ , \tag{3.95}$$

where $E_{\rm inc}(\boldsymbol{r})$ is a solution of the homogeneous equation, i.e., the incident vacuum wave

$$E_{\rm inc}(\boldsymbol{r}) = E_0\, e^{i\boldsymbol{K}\boldsymbol{r}}\ . \tag{3.96}$$

Equation (3.95) contains the true wavefield $E(\boldsymbol{r})$ on both sides and it can be solved by iterations. Let us restrict ourselves to the first iteration (*Born approximation of the first order* [Gui63, Dav69]) by replacing the true wavefield $E(\boldsymbol{r})$ under the integral by the incoming wave. Then the scattered wave is

$$E_r(\boldsymbol{r}) = \int d\boldsymbol{r}' \left(\frac{K^2\chi(\boldsymbol{r}')}{4\pi}\right)\frac{e^{i|\boldsymbol{r}-\boldsymbol{r}'|K}}{|\boldsymbol{r} - \boldsymbol{r}'|}\,E_{\rm inc}(\boldsymbol{r}')\ . \tag{3.97}$$

Using the relation

$$1 - \epsilon_r = -\chi = \frac{4\pi r_{el}}{K^2}\,\rho = 1 - n^2 \approx 2(1 - n) = 2\delta \tag{3.98}$$

the integral can be transformed into several equivalent representations, including

$$E_r(\boldsymbol{r}) = \int d\boldsymbol{r}'\ (-r_{el}\rho(\boldsymbol{r}))\,\frac{e^{i|\boldsymbol{r}-\boldsymbol{r}'|K}}{|\boldsymbol{r} - \boldsymbol{r}'|}\,E_{\rm inc}(\boldsymbol{r}')\ . \tag{3.99}$$

This integral is the well-known *diffraction integral* used frequently in X-ray diffraction [AKK+74, Cow75]. It is equivalent to the Huygens principle used in optics, which gives a clear physical interpretation of the integral: a scatterer at $\boldsymbol{r}'$ reacts to the incoming wave $E_{\rm inc}(\boldsymbol{r}')$ by the response function $T(\boldsymbol{r}') = -r_{el}\rho(\boldsymbol{r})$ by issuing a spherical wave $\frac{e^{i|\boldsymbol{r}-\boldsymbol{r}'|K}}{|\boldsymbol{r}-\boldsymbol{r}'|}$. The wave scattered by the whole crystal is a coherent sum over all the spherical waves from the individual scatterers.

In the usual kinematical theory of X-ray diffraction [Gui63, AKK$^+$74] the integral (3.99) is solved by replacing the spherical wave in the crystal by a plane wave. This *Fraunhofer approximation* is valid for crystals smaller than the first Fresnel zone [BW93], thus it cannot be applied to multilayers with lateral dimension in the order of millimetres. Therefore, we further proceed in a way similar to that used in X-ray diffraction from multilayers [Mik93a, HKA$^+$93] where the correspondence to the kinematical approximation of the Takagi-Taupin equations [Tau64, Tak69, Spe81] has been shown.

The incoming plane wave $E_{\rm inc}(\boldsymbol{r}) = E_0\, e^{i\boldsymbol{K}\boldsymbol{r}}$ impinges on a planar multilayer whose structural parameters depend on the growth direction z. Let us rearrange the integral (3.97) accordingly. The amplitude on the sample surface is

$$E_r(\boldsymbol{r}{=}0) = E_0 \int dz \left(\frac{K^2\chi(z)}{4\pi}\right) \iint dx\, dy\, \frac{1}{|\boldsymbol{r}|} e^{i(K_x x + K_y y + K_z z + K|\boldsymbol{r}|)} \,. \tag{3.100}$$

The volume integral can be separated into two parts

$$E_r(0) \;=\; E_0 \int dz\, \left(K^2\chi(z)/4\pi\right)\, e^{iK_z z}\, U(z, \boldsymbol{K}) \tag{3.101}$$

$$U(z, \boldsymbol{K}) \;=\; \iint dx\, dy\, \frac{1}{|\boldsymbol{r}|} e^{i(K_x x + K_y y + K|\boldsymbol{r}|)} \tag{3.102}$$

with $r = \sqrt{x^2 + y^2 + z^2}$. It follows from the translation invariance of the planar multilayer that the scattered plane wave is a plane wave and therefore the integral (3.102) should be solved analytically. The integral (3.102) is of the type $U(z, \boldsymbol{K}) = \iint dx\, dy\, A(x, y)\, e^{iT(x,y)}$, where the amplitude A is a slowly varying function and the phase T is a rapidly oscillating function of its

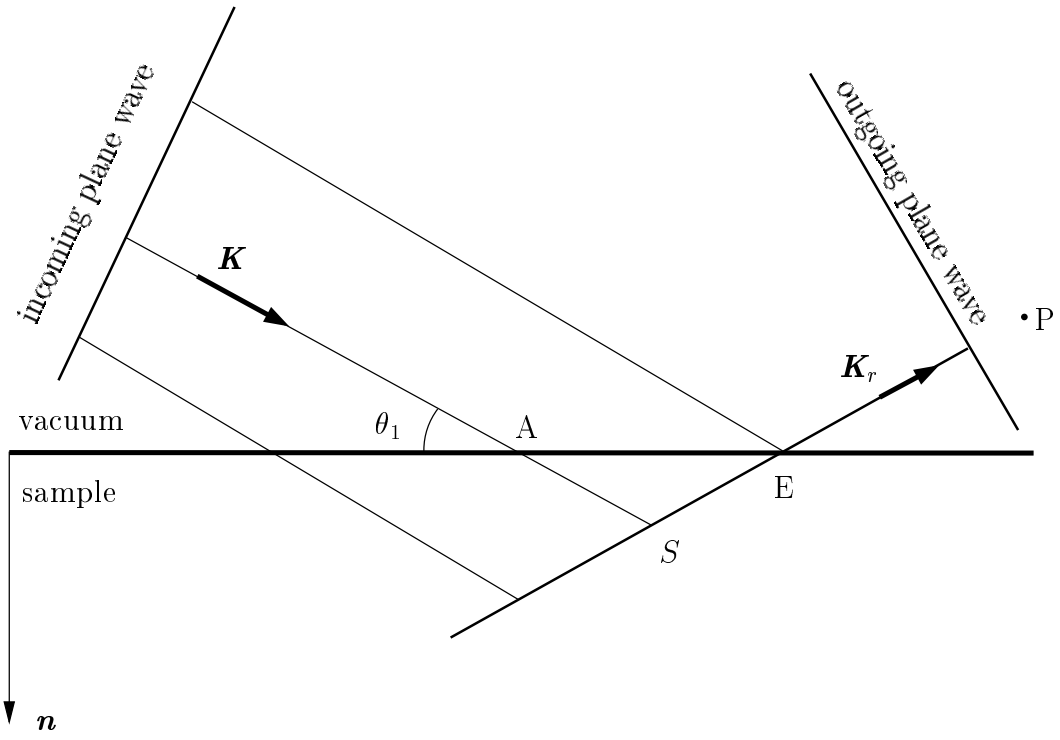

Figure 3.9. The stationary point S lies on the classical path ASE of the ray going to the observation point P. Line AS is parallel to the incoming wave vector $\boldsymbol{K}$ *and the line SE is parallel to the outgoing wave vector* $\boldsymbol{K}_r$ *while the law of reflection holds. The stationary phase method replaces the volume integral (3.100) describing the scattering from all volume elements by the integral of the contributions of the stationary points along the classical path of the outgoing wave, Eq. (3.105).*

arguments. Therefore $U(z, \boldsymbol{K})$ can be solved analytically using the two-dimensional *stationary phase method* [AKK+74]. The stationary point S is the extremal point of the phase

$$\left(\frac{\partial T}{\partial x}\right)_{[x_S,y_S]} = 0 \ , \qquad \left(\frac{\partial T}{\partial y}\right)_{[x_S,y_S]} = 0 \ .$$

Evaluated it gives

$$[x_S, y_S] = \left[-\frac{K_x}{K_z}\, z, -\frac{K_y}{K_z}\, z\right] \ . \tag{3.103}$$

We can see that the stationary point lies on the classical path of the beam in the sample (Fig. 3.9), i.e., in the intersection of the path of the incidence and the outgoing waves following the law of reflection.

Values of A, T and of the determinant of the second derivatives of T evaluated at the stationary point are

$$\begin{aligned} T[x_S, y_S] &= K_z z \\ A[x_S, y_S] &= \frac{1}{|\boldsymbol{r}_S|} = \frac{K_z}{Kz} \\ \left[\left(\frac{\partial^2 T}{\partial x^2}\right)\left(\frac{\partial^2 T}{\partial y^2}\right) - \left(\frac{\partial^2 T}{\partial x \partial y}\right)\right]_{[x_S,y_S]} &= \left(\frac{K^2 z^2}{r_S^3 K_z}\right)^2 \ . \end{aligned}$$

Therefore

$$U(z, \boldsymbol{K}) = \frac{2\pi i}{K_z}\, e^{iK_z z} \tag{3.104}$$

and the reflected wave amplitude becomes

$$E_r = E_0\, \frac{iK^2}{2K_z} \int dz\, \chi(z)\, e^{2iK_z z} = E_0\, \frac{-iK^2}{Q_z} \int dz\, \chi(z)\, e^{-iQ_z z} \ . \tag{3.105}$$

We have found that the resulting reflectivity amplitude is proportional to the Fourier transform of the susceptibility profile in the growth direction. This feature is similar to all the scattering calculations of the kinematical theory as we can see by the comparison with the kinematical theory of X-ray diffraction. However, to be more strict, the reflectivity is non-zero only at the regions where susceptibility changes (i.e., at the interfaces), because the integration method "per partes" applied to (3.105) gives

$$E_r = E_0\, \frac{-K^2}{Q_z^2} \left[\int_0^\infty dz \left(\frac{d\chi(z)}{dz}\right) e^{-iQ_z z} - \left[\chi(z)\, e^{-iQ_z z}\right]_0^\infty\right] \tag{3.106}$$

and the last term is zero.

From figure 3.9, showing the ray propagation along the classical path, and from the resulting Fourier transform we find the physical meaning of the kinematical theory. The incoming vacuum plane wave propagates through the sample without any refraction and without being absorbed. In each point it excites a reflected plane wave, so that the law of reflection holds. However, the amplitude of the incoming wave is not diminished by the reflection process and therefore the kinematical theory, as well as the single-reflection approximation, is limited only to the regions of weak reflections. If this would not be the case, then the intensity of the transmitted wave would not be constant, which could be maintained only by a higher-order Born approximation.

The stationary phase method is an approximate method that solves the integral (3.100). It approximates the amplitude $A(x, y)$ by its value in the stationary point and integrates the exponential of the phase $T(x, y)$ expanded into the first two terms of the Taylor series. However, an analytical solution can be found by means of the decomposition of the Green function (3.94)

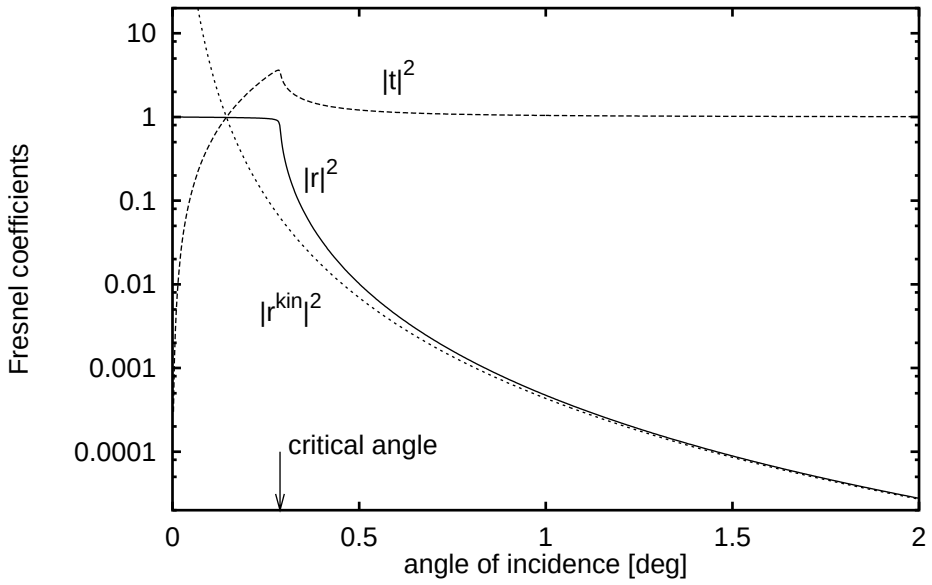

Figure 3.10. Fresnel transmission coefficient $\mathfrak{t}$ *calculated dynamically and reflection coefficients* $\mathfrak{r}$ *calculated dynamically and kinematically for a vacuum/sapphire surface and CuK*$_\alpha$ *wavelength (critical angle 0.288*$^\circ$*).*

into plane waves,[2] which leads to exactly the same result as given by Eq. (3.105) [Hol96]. To our knowledge the mathematical reason of this perfect coincidence has not yet been given.

A similar kinematical calculation approach will be used for the laterally structured multilayers (multilayered gratings) in Ch. 5. Now let us apply this kinematical approach to some simple cases.

Single interface

Let us consider the reflection from an interface separating two media 1,2 with refractive indices $n_1 = 1 + \chi_1/2,\ n_2 = 1 + \chi_2/2$. The susceptibility profile is thus

$$\chi(z) = \chi_1\, H(-z) + \chi_2\, H(z)\ , \tag{3.107}$$

where $H(z)$ is the Heaviside function (defined by $H(z{<}0) = 0$ and $H(z{>}0) = 1$) with the Fourier transform $\tilde{H}(Q_z) = \int dz\, H(z)\, e^{-iQ_z z} = 1/iQ_z$. The relative amplitude of the reflected wave, i.e., the *kinematical Fresnel reflection coefficient*, is given by the Fourier transform

$$\mathfrak{r}^{\rm kin} \equiv \frac{E_r}{E_0} = \frac{-iK^2}{Q_z} \int\limits_{-\infty}^{\infty} dz\, \chi(z)\, e^{-iQ_z z} = \frac{K^2}{Q_z^2}\,(\chi_1 - \chi_2) = \frac{k_{2C}^2 - k_{1C}^2}{Q_z^2}\ . \tag{3.108}$$

As we can see, the kinematical reflection coefficient coincides with the dynamical Fresnel coefficient calculated for large angles of incidence, see Eq. (3.54). A comparison of both the dynamical and kinematical Fresnel reflection coefficients is shown in Fig. 3.10. We observe that the kinematical one diverges for small angles of incidence and it is proportional to the difference of the scattering potentials $V_2 - V_1 = K^2(\chi_1 - \chi_2)$.

[2] The equality $\frac{e^{ikr}}{r} = \frac{i}{2\pi} \iint \frac{e^{ikr}}{k_z}\, dk_x\, dk_y$, where $k_z = \sqrt{|\boldsymbol{k}|^2 - k_x^2 - k_y^2}$, is proved by the stationary phase method in [AKK+74]. The analytical proof can be easily obtained putting $\boldsymbol{r} = (0, 0, z)$ (without loss of generality) and integrating it directly in polar coordinates. We note that the integration region covers the part where k_z is real as well as the part where k_z is imaginary.

Multilayer

The susceptibility of a multilayer is constant in each layer j, thus

$$\chi(z) = \sum_{j=2}^{N} \chi^{(j)} \cdot [H(z - z_j) - H(z - z_{j+1})] \ , \tag{3.109}$$

where j goes over all layers of the multilayer. The integral (3.105) then turns into the sum

$$R^{\mathrm{kin}} = \frac{K^2}{Q_z^2} \sum_{j=2}^{N} \chi^{(j)} \ \left[-e^{-iQ_z z_j} + e^{-iQ_z z_{j+1}}\right] = \frac{iK^2}{Q_z} \sum_{j=2}^{N} F^{(j)} \, e^{-iQ_z z_j} \ , \tag{3.110}$$

where we have defined the *structure-geometric factor* of layer j

$$F^{(j)} = \chi^{(j)} \ \frac{e^{-iQ_z z_j} - 1}{-iQ_z} \ . \tag{3.111}$$

We find this expression very close to our summation formalism of the semi-kinematical X-ray diffraction from crystals [Mik93a, Mik93b, MHKP95] derived from the Bartels *et al.* formalism [BHL86]. In the formula (3.110), the pre-factor in front of the sum is iK^2/Q_z and the contribution from each layer is proportional to its susceptibility. In symmetrical XRD, the pre-factor in front of the sum over the structure-geometric factors is $iKC/2\gamma_h = iK^2C/2K_{hz} = iK^2C/Q_{hz}$, where C is the polarization factor ($C = 1$ for the σ-polarization), and γ_h is the direction cosine of the diffracted wave. The structure-geometric factor of the diffraction from a layer is proportional to the Fourier transform of the susceptibility. Therefore both XRD and SXR express the same scattering phenomena of diffraction around a Bragg peak, which for SXR is the origin of the reciprocal space, $(hkl) = (000)$.

However, in SXR we prefer the "interface" representation of the scattering effects. By expressing the susceptibility (3.109) as a sum going over the interfaces (similarly to (3.107))

$$\chi(z) = \sum_{j=1}^{N} \left(\chi^{(j+1)} - \chi^{(j)}\right) \ H(z - z_{j+1}) \ . \tag{3.112}$$

Putting this relation into the kinematical diffraction integral (3.105) we get the reflectivity amplitude

$$R^{\mathrm{kin}} = \frac{K^2}{Q_z^2} \sum_{j=1}^{N} \chi^{(j)} \ \left[\chi^{(j)} \, e^{-iQ_z z_j} - \chi^{(j+1)} \, e^{-iQ_z z_j}\right] = \sum_{j=1}^{N} \mathfrak{r}_j^{\mathrm{kin}} \, e^{-iQ_z z_{j+1}} \ , \tag{3.113}$$

where the summation is performed over the interfaces. The *kinematical Fresnel reflection coefficient of the jth interface* reads

$$\mathfrak{r}_j^{\mathrm{kin}} = \frac{K^2}{Q_z^2} \, (\chi^{(j)} - \chi^{(j+1)}) = \frac{(k_C^{(j+1)})^2 - (k_C^{(j)})^2}{Q_z^2} \ . \tag{3.114}$$

We can see that (3.113) is formally the same relation as the single-reflection approximation of the dynamical theory of X-ray reflection, except for the absorption and refraction effects, because

- we have used the Born approximation of the first order that takes only single scattering processes into account,
- the vacuum wave vector transfer is applied instead of the actual momentum transfer in each layer—we utilized the incident vacuum plane wave (3.96) as the first estimate in the iterative solution (3.95).

A better approximation that would take into account the refraction and absorption effects would involve at least the mean refractive index of the whole multilayer. However, we show in the subsequent section that these refraction corrections are given by the single-reflection approximation. Another possibility for going beyond the first Born approximation is the calculation by the distorted-wave Born approximation, which will be employed later.

Single layer

The reflectivity amplitude (3.113) for a single-layered system (Sec. 3.4.5) gives

$$R^{\mathrm{kin}} = \mathfrak{r}_1^{\mathrm{kin}} + \mathfrak{r}_2^{\mathrm{kin}}\, e^{-iQ_z t_2} \ . \tag{3.115}$$

The kinematical reflectivity curve, Fig. 3.8(b), approaches the single-reflection approximation of the dynamical theory for $Q_z \approx q_z^{(2)}$, therefore for angles of incidence larger than the critical angle of the layer material, $\omega \gg \theta_C^{\mathrm{W}}$. Below the critical angle the kinematical Fresnel coefficient diverges and so does the kinematically calculated reflected intensity. This is because of using the vacuum plane wave (3.96) as the wave transmitted and scattered inside the sample, and not the wave with the wave vector inside the material (3.10).

3.6 Multilayers with the layer sequence given by a deterministic rule

In this section we study the reflectivity curves of multilayers whose layer sequence is constructed according to a certain mathematical rule. As particular examples we take a periodic multilayer, which is a well-known type of multilayer, and a quasiperiodic Fibonacci multilayer, whose structure is not explored so often. The construction rule of the layer sequence (i.e., the rule determining how the layers of different materials are arranged above the substrate) is quite easy for the periodic multilayer, but it is not the case of the Fibonacci multilayer [SL87, Jan92]. We will show that the reflectivity curve of the Fibonacci multilayer is self-similar and we find a rule determining the peak positions. However, in order to calculate this specular curve and the Fourier transform of a quasiperiodic lattice we will make use of the terminology of the physics of quasicrystals and for more transparency we use it for the construction of both periodic and Fibonacci multilayers.

Further, the theories of the specular reflectivity calculation presented earlier will be compared and discussed and they will be used to characterize the reflectivity curves of the proposed multilayers, mainly the peak positions.

3.6.1 Periodic multilayer

Let us treat the specular reflectivity from a periodic multilayer consisting of the periodic repetition of two building blocks A and B, the A layer being above the substrate (Fig. 3.5(b)). We derive the dynamical, single-reflection and kinematical formulae and we perform their comparison. We use the single-reflection approximation to find the peak positions and we show that they are equidistant in the reciprocal space of the averaged multilayer, but not equidistant in the vacuum (i.e., the experimental) reciprocal space.

We base our calculation approach on the physics of quasicrystals [SL87, Jan92, AG95], which will be probably found a little bit cumbersome for such a simple lattice as the periodic one is, but we will profit from this approach in the calculation of the reflectivity pattern of a quasiperiodic multilayer in the following section.

Firstly we show some mathematical rules determining the sequence of layers A, B of a periodic lattice. Let us suppose the infinite periodic lattice

$$\mathrm{P} = \mathrm{ABABABABABABAB}\ldots$$

being the limit of its orders $\mathrm{P}_m^{'}$ or of its generations P_n

$$\begin{aligned} \mathrm{P}_1 &= \mathrm{AB} & \mathrm{P}_1' &= \mathrm{AB} \\ \mathrm{P}_2 &= \mathrm{ABAB} & \mathrm{P}_2' &= \mathrm{ABAB} \\ \mathrm{P}_3 &= \mathrm{ABABABAB} & \mathrm{P}_3' &= \mathrm{ABABAB} \qquad \text{etc.} \end{aligned}$$

We can find some equivalent definitions of these lattices [Mik95]:

1. *recurrent:* P_1=AB, P_n=$\mathrm{P}_{n-1}\mathrm{P}_{n-1}$, and P'_m=$\mathrm{P}'_1\mathrm{P}'_{m-1}$=$\mathrm{P}_{2^m}$,
2. *the first analytical:* P_1=AB, P_n=$(\mathrm{P}_1)^{2^{n-1}}$ and P'_{2^m}=$(\mathrm{P}_1)^{2^m}$,
3. *deflation (substitutional):* P_1(A,B)=AB, P_n(A,B)=P_{n-1}(AB,AB),
4. *the second analytical:* P_n=$\Delta_1\Delta_2\ldots\Delta_{2^n}$ and P'_m=$\Delta_1\Delta_2\ldots\Delta_m$, where the objects Δ_j are either A or B according to

$$\Delta_j = \begin{cases} \mathrm{A} & \text{for} \quad \lfloor (j+1)/2 \rfloor - \lfloor j/2 \rfloor = 1 \ , \\ \mathrm{B} & \text{for} \quad \lfloor (j+1)/2 \rfloor - \lfloor j/2 \rfloor = 0 \ . \end{cases}$$

The function $\lfloor x \rfloor$ denotes the integer part of x.

The layer positions are $z_{An} = t_B + t_{AB}\,(n-1)$, $z_{Bn} = t_{AB}\,(n-1)$, where the lattice period is defined by $t_{AB} = t_A + t_B$.

The recursion rule 1. can be used in the dynamical calculation of the reflectivity. The matrix sequence (3.65) can be evaluated in the same way as the periodic layer sequence, thus yielding the recurrent relation

$$\mathcal{M}^{ML,n} = \mathcal{M}_{BA}\mathcal{M}^{ML,n-1} \ , \qquad \mathcal{M}^{ML,1} = \mathcal{M}_{BA} = \mathcal{M}_B\mathcal{M}_A \ . \tag{3.116}$$

If the rule 2. is used, then the explicit analytical relation is found

$$\mathcal{M}^{ML,n} = (\mathcal{M}_{BA})^n \ . \tag{3.117}$$

Within the approach of the matrices $\mathcal{N}$ the reflectivity from the vacuum and substrate interfaces have to be treated explicitly

$$\mathcal{M} = (\mathcal{P}_{vB}\mathcal{P}_{AB}^{-1})\,(\mathcal{N}_B\mathcal{N}_A)^N\mathcal{P}_{As} \ . \tag{3.118}$$

This matrix calculation method provides numerically efficient dynamical calculation which is required for thick multilayers. However, for thin layers the single-reflection approximation is acceptable and therefore we perform the corresponding calculation now. It will enable us to derive a relation for the peak positions.

The phase term in (3.77b) is a sum over the phase terms in layers above the layer j, so that

$$\phi_{jA} = n\phi_A + (n+1)\phi_B \ , \qquad \phi_{jB} = n\phi_A + n\phi_B \ , \tag{3.119}$$

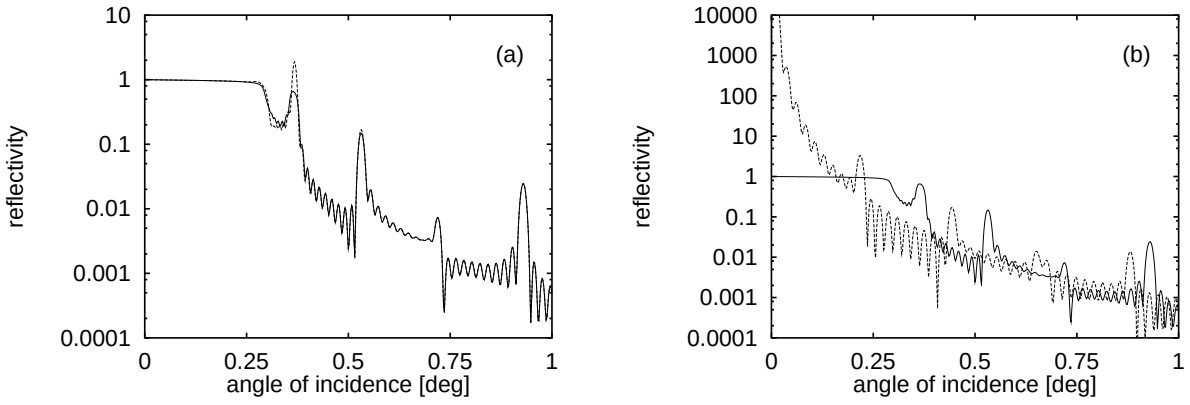

Figure 3.11. X-ray reflectivity curve of the periodic multilayer (substrate GaAs, 10 periods of 130 Å thick GaAs and 70 Å thick AlAs). The dynamical theory (full curve) is compared to the single-reflection approximation (a) and good coincidence is found except the region close to the critical angle due to the same reasons as in the case of a single-layered sample, Fig. 3.8. Comparison of the dynamical theory to the kinematical theory is shown in the figure (b).

where n is the number of periods between the vacuum and the layer j, $n = \lfloor \frac{j}{2} \rfloor$. The particular phase shifts are $\phi_A = q_{zA} t_A$ and $\phi_B = q_{zB} t_B$. It is convenient to introduce the mean momentum transfer in the multilayer

$$\langle q_z \rangle = (q_{zA} t_A + q_{zB} t_B)/t_{AB} \ . \tag{3.120}$$

Further, the periodic multilayer consisting of M periods has total thickness $t = M t_{AB}$. Then the single-reflection approximation gives the explicit formula for the reflectivity amplitude

$$\begin{aligned} R &= (\mathfrak{r}_{vB} - \mathfrak{r}_A) + \sum_{m=0}^{M-1} [\mathfrak{r}_B + \mathfrak{r}_A \, e^{i\phi_B}] e^{-im(\phi_A+\phi_B)} + \mathfrak{r}_{As} \, e^{-iM(\phi_A+\phi_B)} \\ &= (\mathfrak{r}_{vB} - \mathfrak{r}_A) + \frac{1 - e^{-i\langle q_z \rangle t}}{1 - e^{-i\langle q_z \rangle t_{AB}}} F + \mathfrak{r}_{As} \, e^{-i\langle q_z \rangle t} \ . \end{aligned} \tag{3.121}$$

We defined as $\mathfrak{r}_A$ ($\mathfrak{r}_B$) the Fresnel coefficients of the interface below the A (B) layer, respectively, and $\mathfrak{r}_{vB} = \mathfrak{r}_1$ that of the vacuum/layer B and $\mathfrak{r}_{As} = \mathfrak{r}_N$ that of the layer A/substrate interface. The structure factor of one period is

$$F = \mathfrak{r}_B + \mathfrak{r}_A \, e^{-iq_{zB} t_B} = \mathfrak{r}_A (1 - e^{-iq_{zB} t_B}) \ , \tag{3.122}$$

where we used the identity $\mathfrak{r}_{j,j+1} = -\mathfrak{r}_{j+1,j}$. From the form of the middle term in (3.121) it follows that the reflectivity maxima are distributed equidistantly in the reciprocal space of the averaged multilayer

$$\langle q_z \rangle_m = \frac{2\pi}{t_{AB}} m \ , \tag{3.123}$$

whilst they are not equidistant in the angular space

$$\sqrt{\omega_m^2 - (\theta_{1C}^2 + \theta_{2C}^2)/2} = \frac{\lambda}{2 t_{AB}} m \ . \tag{3.124}$$

The main maxima are called Bragg peaks as well, since their positions follow a condition similar to the Bragg formula in X-ray diffraction [Gui63].

The maxima of the reflectivity curve of the periodic multilayer are indexed by one integer m and the amplitude in the maximum is proportional to the number of layers M

$$\frac{1 - e^{-i\langle q_z \rangle_m t}}{1 - e^{-i\langle q_z \rangle_m t_{AB}}} = M \ . \tag{3.125}$$

Finally we note that in this section we have treated the specular reflectivity from a periodic multilayer whose main motif consisted of two building layers A, B. The generalization to the case of more building layers is straightforward, since only the structure factor (3.122) is changed by adding the phase shifts of the additional layers and the Fresnel reflection coefficients of the additional interfaces.

3.6.2 Fibonacci multilayer

A Fibonacci lattice is a well-known quasiperiodic lattice with very interesting diffraction properties [LS86, Els86]. The X-ray diffraction from the Fibonacci multilayer were frequently analyzed [MBC$^+$85, TMC$^+$86, TKO$^+$90, MHKP95], but the X-ray reflectivity has not got such attention. Therefore we perform this analysis in the present section.

The Fibonacci multilayer, shown schematically in Fig. 3.5(c), consists of two building layers A, B deposited on a substrate according to the rule of the Fibonacci lattice [Jan92]. The infinite Fibonacci lattice

F=ABAABABAABAAB ...

is the limit of its generations F_n

$$\begin{aligned} \mathrm{F}_0 &= \mathrm{B} & \mathrm{F}_3 &= \mathrm{ABA} \\ \mathrm{F}_1 &= \mathrm{A} & \mathrm{F}_4 &= \mathrm{ABAAB} \\ \mathrm{F}_2 &= \mathrm{AB} & \mathrm{F}_5 &= \mathrm{ABAABABA} \qquad \text{etc.} \end{aligned}$$

Many equivalent building rules have already been found [SL87] for Fibonacci generations F_n:

1. *recurrent:* F_0=B, F_1=A, F_n=$\mathrm{F}_{n-1}\mathrm{F}_{n-2}$,
2. *deflation (substitutional):* F_0=B, F_n(A,B)=F_{n-1}(AB,A),
3. *analytical:* F_n=$\Delta_1\Delta_2\ldots\Delta_{f_{k+2}}$ with the following definition of the objects Δ_j:

$$\Delta_j = \begin{cases} \mathrm{A} & \text{for} \quad \lfloor (j+1)\tau \rfloor - \lfloor j\tau \rfloor = 1 \ , \\ \mathrm{B} & \text{for} \quad \lfloor (j+1)\tau \rfloor - \lfloor j\tau \rfloor = 0 \ . \end{cases}$$

The formula for the Fibonacci lattice point positions is known [LS86] $z_n = t_B[n + (t_A - t_B)/t_B \cdot \lfloor \tau n \rfloor]$. The golden mean $\tau = \frac{\sqrt{5}-1}{2} \approx 0.618$ is the "magic number" of this sequence. Further, there are f_{M+1} (f_M) layers A (B) in the Mth generation, respectively, where the Fibonacci numbers are $f_M = f_{M-2} + f_{M-1}$, $f_1 = 0, f_2 = 1$.

From the recursion rule 1. immediately follows the recursion relation for the multilayer transfer matrix (3.65) for the Fibonacci multilayer of the Mth generation

$$\begin{aligned} &\mathcal{M}^{ML} = \mathcal{M}^{ML,M} \\ &\mathcal{M}^{\mathrm{Fib},M} = \mathcal{M}^{\mathrm{Fib},M-2}\mathcal{M}^{\mathrm{Fib},M-1} \\ &\mathcal{M}^{\mathrm{Fib},1} = \mathcal{M}^{A} = \mathcal{P}^{A}\mathcal{Q}^{A}\left(\mathcal{P}^{A}\right)^{-1} , \qquad \mathcal{M}^{\mathrm{Fib},2} = \mathcal{M}^{B} = \mathcal{P}^{B}\mathcal{Q}^{B}\left(\mathcal{P}^{B}\right)^{-1} , \end{aligned} \tag{3.126}$$

where $\mathcal{P}_{v,B} = \mathcal{P}_{1,2}$ and $\mathcal{P}_{A,s} = \mathcal{P}_{N,N+1}$. This matrix formalism provides a numerically rapid and still fully dynamical calculation procedure valid in the whole angular range. The reflectivity curve of the Fibonacci multilayer of the 13th generation is shown in Fig. 3.12.

The recursion relation 1. can also be applied to the calculation of the reflected amplitudes by means of the recurrent formulation of the single-reflection approximation (3.80b). If the Fibonacci generations are chained, then

$$F^{\mathrm{Fib},M} = F^{\mathrm{Fib},M-2} + F^{\mathrm{Fib},M-1}\, e^{-i\varphi^{\mathrm{Fib},M-2}} \ . \tag{3.127}$$

The phase shift over a Fibonacci stack of the Mth generation is explicitly

$$\varphi^{\mathrm{Fib},M} = f_{M+1} \cdot q_{zA} t_A + f_M \cdot q_{zB} t_B \ . \tag{3.128}$$

Finally, the calculation has to take into account the vacuum-multilayer and multilayer-substrate reflectivities separately. Then the reflectivity amplitude becomes

$$R^{\mathrm{SRA}} = (\mathfrak{r}_{v,\Delta_{M+2}} - \mathfrak{r}_{\Delta_{M+2},\Delta_{M+1}}) + F^{\mathrm{Fib},M} + \mathfrak{r}_{A,s}\, e^{-i\varphi^{\mathrm{Fib},M}} \ . \tag{3.129}$$

The objects Δ_j are defined to be A or B, thus the Fresnel coefficients are between layers A and B ($\mathfrak{r}_{A,B} = -\mathfrak{r}_{B,A}$), vacuum and layer B ($\mathfrak{r}_{v,B}$), layer A and substrate ($\mathfrak{r}_{A,s}$).

Both the dynamical (3.126) and single-reflection (3.129) expressions enable us to calculate numerically the profile of the reflectivity curve of a finite Fibonacci multilayer. Since the diffraction spectrum of a Fibonacci lattice is quasiperiodic [SL87], we expect similar properties in the specular reflectivity as well. Being interested in establishing the general properties of the reflectivity profile, mainly the peak positions, we will use the kinematical theory (Sec. 3.5) to characterize the reflectivity curve of the infinite Fibonacci multilayer. We proceed similarly to the method we used in [MHKP95]. Moreover, the kinematical wave vector transfer Q_z is a real quantity and therefore our results remain valid for both possible arrangements of the layer

sequence, which means that the stacking sequence can be parallel or antiparallel to the growth direction.

The Fibonacci lattice is self-similar and the use of the deflation building rule 2. allows the decomposition of the Fibonacci lattice F into two sublattices F_A, F_B

sublattice F_A: F = |AB|A|AB|AB|A|AB|A|AB|A|...

sublattice F_B: F = |A|BAA|BA|BAA|BAA|BA|...

The sublattice F_A is the Fibonacci lattice of groups of layers |AB| and |A|, and the sublattice F_B is the Fibonacci lattice of groups of layers |BAA| and |BA|. This represents the *self-similarity* (scale-invariance) of the Fibonacci lattice in *direct space*. Consequently, the lattice positions of the particular layers A, B are

$$z_{An} = t_A[n + t_B/t_A \cdot \lfloor \tau n \rfloor] \tag{3.130}$$

$$z_{Bn} = t_A + (t_B + t_A)[n + t_A/(t_A + t_B) \cdot \lfloor \tau n \rfloor] \tag{3.131}$$

and except for the different length scales these relations are the same as the Fibonacci lattice positions z_n. Further, we will need to evaluate the discrete Fourier transform $S(k, d_A, d_B) = \sum_n e^{-ikz_n}$, $z_n = d_B[n + (d_A - d_B)/d_B \cdot \lfloor \tau n \rfloor]$. This has already been worked out using different methods (the modulated phase method has been established by Levine and Steinhardt [LS84]), the cut and projection method by Zia and Dallas [ZD85] and Elser [Els86]. The resulting formula reads

$$S(k, d_A, d_B) = \frac{1}{t_B} \sum_{pq} \mathrm{sinc}\,\frac{\Phi_{pq}}{2}\, e^{-i\Phi_{pq}/2}\, \delta(k - k_{pq}) \ , \tag{3.132}$$

where the maxima positions are $k_{pq} = 2\pi(p/\tau + q)/d$ and the phase $\Phi_{pq} = 2\pi q - k_{pq}(d_A - d_B)$. Here p, q are integers and the lattice period is $d \equiv d_A + \tau d_B$.

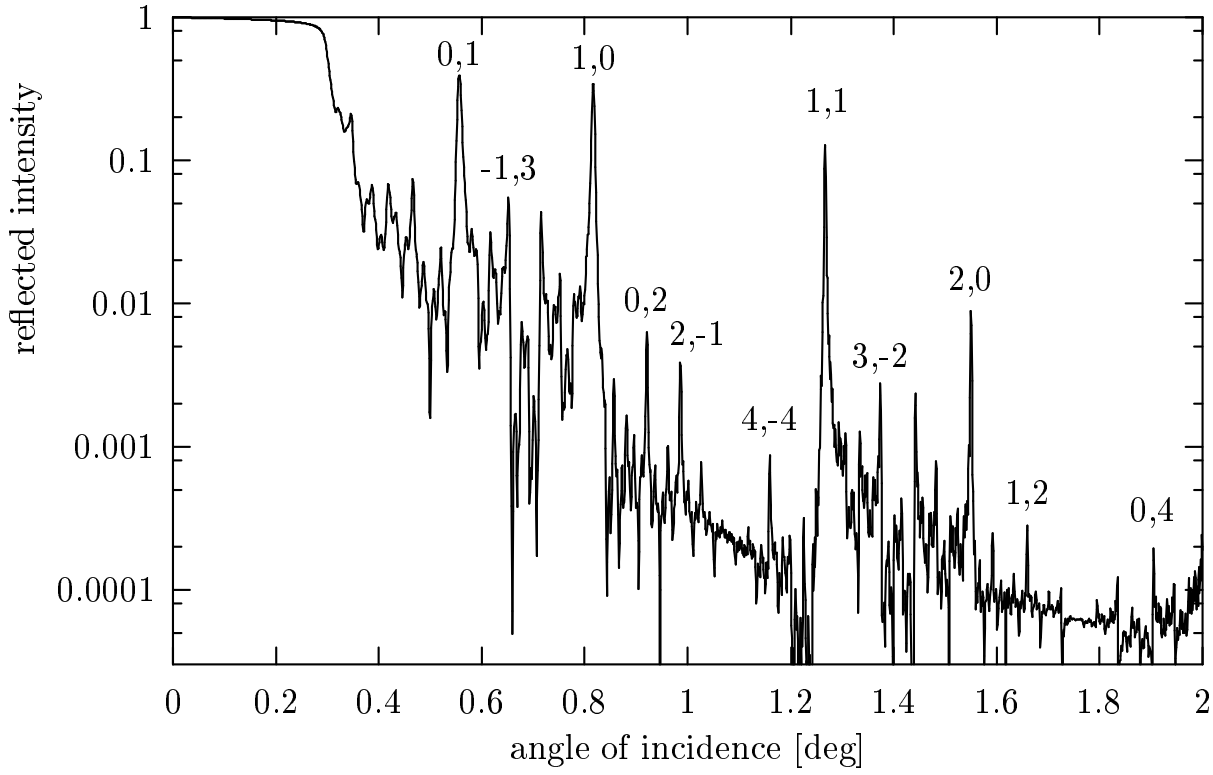

Figure 3.12. X-ray reflectivity curve of the 13th generation of the Fibonacci superlattice (substrate GaAs, layer A is 42 Å thick GaAs, layer B is 25 Å thick AlAs). The reflectivity peaks according to the formula (3.140) are labelled by two integers p, q.

Let us use the formula (3.113) and split the summation over layers A and B into separate groups

$$\begin{aligned} F^{\mathrm{Fib},\infty} &= \mathfrak{r}_A \sum_{n,\text{layers A}} e^{-iQ_z z_{An}} + \mathfrak{r}_B \sum_{n,\text{layers B}} e^{-iQ_z z_{Bn}} \\ &= \mathfrak{r}_A\, S(Q_z, t_A+t_B, t_B) + \mathfrak{r}_B\, S(Q_z, 2t_A+t_B, t_A+t_B)\, e^{-iQ_z t_A} \ . \end{aligned} \tag{3.133}$$

In other words, this decomposes the reflectivity into the reflectivity from the sublattices F_A and F_B, respectively. Applying (3.132) to both sublattices, their reciprocal space maxima

$$Q^A_{z,pq} = k_{pq}(t_A+t_B, t_A) = 2\pi(p+q\tau)/t_{AB} \tag{3.134}$$

$$Q^B_{z,pq} = k_{pq}(2t_A+t_B, t_A+t_B) = \tau Q^A_{z,pq} = Q^A_{z,q,p-q} \tag{3.135}$$

are rescaled by the golden mean τ. The period $t_{AB} = t_A + \tau t_B$. This represents the *self-similarity* of the diffraction pattern *in reciprocal space*. Since the particular phases

$$\Phi^A_{pq} = \frac{2\pi}{d}(qt_A - pt_B) \ , \qquad \Phi^B_{pq} = -\tau\Phi^A_{q,p-q} \tag{3.136}$$

are scaled by the golden mean as well, the final formula for the reflectivity amplitude (3.133) of the infinite Fibonacci multilayer reads

$$F^{\mathrm{Fib},\infty}(Q_z) = \sum_{pq} F^{\mathrm{Fib},\infty}_{pq} \cdot \delta(Q_z - Q_{z,pq}) \tag{3.137}$$

$$F^{\mathrm{Fib},\infty}_{pq} \equiv \frac{\mathfrak{r}_A(Q_{z,pq})}{t_A} \operatorname{sinc}\frac{\Phi^A_{pq}}{2} e^{-\frac{i}{2}\Phi^A_{pq}} + \frac{\mathfrak{r}_B(Q_{p+q,p}) e^{-iQ_{z,p+q,p}t_A}}{t_A+t_B} \operatorname{sinc}\frac{\tau\Phi^A_{pq}}{2} e^{\frac{i}{2}\tau\Phi^A_{pq}} . \tag{3.138}$$

Compared to the structure factor of the periodic lattice (3.122) that of the Fibonacci multilayer (3.138) exhibits a modulation by an additional periodic function $\operatorname{sinc}(x) \equiv \sin(x)/x$. The cut and projection method shows that this is caused by the projection of a periodic lattice in the higher-dimensional space (two-dimensional for the Fibonacci lattice [Els86]) into a quasiperiodic lattice in a lower-dimensional space (one-dimensional for the Fibonacci lattice).

Previously, we have found that the kinematical theory is not accurate enough near the critical angle, but a good coincidence is achieved by replacing the vacuum momentum transfer Q_z by the momentum transfer in the averaged multilayer

$$\langle q_z \rangle = \frac{q_{zA}t_A + q_{zB}t_B\tau}{t_{AB}} \ . \tag{3.139}$$

This substitution is perfectly adequate in the infinite Fibonacci multilayer as it has been demonstrated in X-ray diffraction theory using the semi-kinematical approximation [MHKP95]. Then the relation describing correctly the peak positions is

$$\langle q_z \rangle_{pq} = \frac{2\pi}{t_{AB}}\,(p+q\tau) \ . \tag{3.140}$$

Two main features revealing the quasiperiodic nature of the studied structure come out from this approach. Firstly, two indices (integers p, q) are needed to describe all peak positions and because of the irrational number τ these peaks form dense set in the reciprocal space. Secondly, the discrete Fourier transform is a sum of δ-peaks as was the case of the periodic lattice (we say that the Fourier transform of the Fibonacci sequence has *atomic spectral measure*). Further, the reflectivity of a *finite* multilayer, given by the convolution of the Fourier transform of the infinite lattice and the shape function of a finite multilayer, is proportional to the multilayer thickness. This leads to the so-called *volume-square intensity scaling*. This is another important property of quasicrystalline lattices. On the other hand, there are aperiodic lattices whose discrete Fourier transform cannot be evaluated for an infinite lattice or which is not a sum of δ-functions. Then the intensity in each reciprocal space point scales differently when the lattice size is changed

[AG95]. For example, the *Thue-Morse sequence* is automatic and not quasiperiodic, and its Fourier transform has *singular continuous measure* [Kol94, AT94, PCA95].

A dynamical calculation of the reflectivity of the Fibonacci multilayer of the 13th generation is shown in Fig. 3.12. Near the critical angle the intensity is nearly unity and the single-reflection approximation is no longer appropriate. The reflectivity curve has to be calculated dynamically and the thickness dependence of the reflected intensity of the Fibonacci multilayer can be studied. As the multilayer thickness increases, the width of all peaks decreases and new low-intensity peaks appear. The most intense peaks near the critical angle become saturated or grow very slowly, whereas the low intensity kinematical peaks grow according to thickness squared.

3.7 Conclusion

In this chapter different theories for the reflectivity calculation from planar multilayers have been dealt with. Their formulae have been presented and they were thoughtfully discussed. Therefore I hope the reader will find the enclosed "road-map" over the theories, Fig. 3.13, more useful than another textual summary.

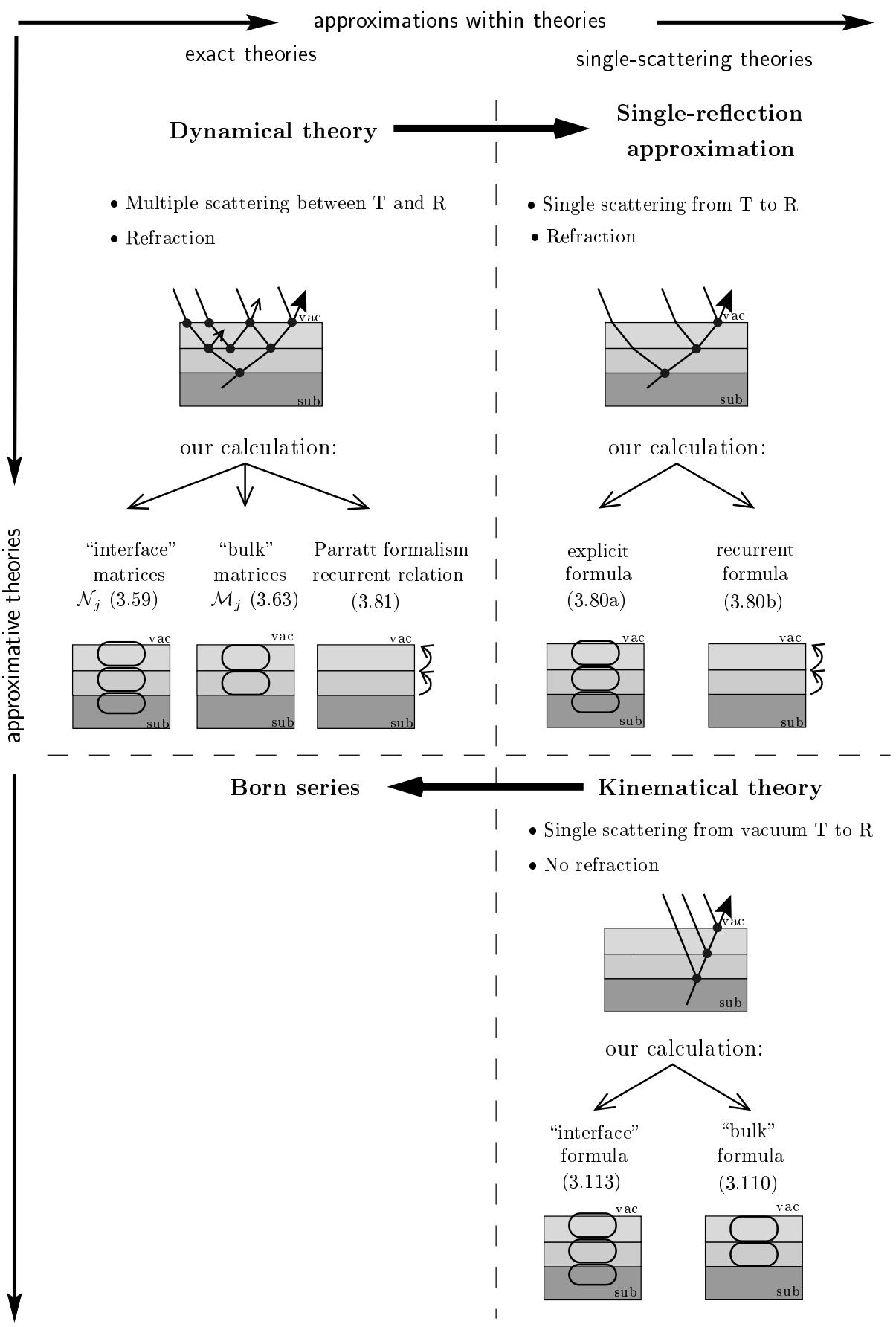

Figure 3.13. A "road-map" of our theories and their approximations for the reflection from planar multilayers. The symbols T and R stand for the transmitted and reflected wavefields, respectively.

Chapter 4

X-ray reflectivity from rough multilayers

Résumé

Dans le précédent chapitre, nous avons étudié la réflectométrie sur une multicouche à interfaces parfaitement planes. En réalité, les processus de croissance des films sont compliqués, avec un caractère aléatoire et il en résulte des imperfections structurales. Comme la réflectivité des rayons X est sensible au profil de l'indice de réfraction, nous allons considérer deux sortes d'inhomogénéités : la rugosité d'interface et l'interdiffusion.

Une interface entre deux couches est une surface mathématique entre les matériaux constituant les couches. Les atomes qui se déposent frappent au hasard la couche déjà formée. Comme leur mobilité est limitée et que beaucoup d'autres paramètres influencent la croissance des films, celle-ci n'est pas homogène sur toute la surface de la couche. En conséquence, des interfaces parfaitement planes ne peuvent pas être obtenues et la modulation de l'interface réelle entre les couches par rapport à une interface idéale se traduit comme une rugosité.

Pour ces raisons, il est indispensable d'incorporer la rugosité, c'est à dire le caractère aléatoire des interfaces, dans le calcul de la réflectivité.

La réflectivité spéculaire ne peut pas distinguer entre l'influence de la rugosité et celle de l'interdiffusion. Nous pouvons toutes les représenter par une même rugosité quadratique moyenne et une largeur d'interdiffusion moyenne. Cependant, l'interdiffusion latérale homogène ne diffuse la radiation que dans la direction spéculaire. Par contre la rugosité d'interface, aléatoire, diffuse l'onde incidente en produisant une diffusion diffuse.

Le travail préliminaire à effectuer avant le calcul de la réflectivité sur des échantillons à interfaces rugueuses est de décrire ces propriétés statistiques. Nous commençons donc ce chapitre par l'étude des propriétés statistiques d'interfaces rugueuses simples et de la corrélation entre les différentes interfaces d'une multicouche. Nous montrons comment des interfaces rugueuses modifient localement l'épaisseur d'une couche. Nous utilisons les deux théories, dynamique et cinématique, pour calculer l'intensité spéculaire sur une interface et sur une multicouche rugueuses. Nos calculs conduisent au facteur de décroissance exponentielle bien connu pour les coefficients de Fresnel. Nous utilisons ce modèle pour interpréter les courbes expérimentales de réflectivité obtenues sur des couches sandwich ou sur des multicouches périodiques.

La rugosité inhomogène latéralement et aléatoire produit une diffusion diffuse incohérente. Nous utilisons l'approximation de l'onde déformée de Born pour calculer quantitativement cette intensité diffusée. Nous démontrons les caractéristiques de la diffusion diffuse sur une carte de l'intensité mesurée dans l'espace réciproque pour une multicouche périodique.

4.1 Introduction

In the previous chapter we have studied reflection from a multilayer with flat interfaces. However, the sample growth is a complicated process with a certain amount of randomness, and therefore it introduces structural imperfections. Since the X-ray reflectivity feels the profile of the index of refraction, we will consider inhomogeneities of two kinds: interface roughness and interdiffusion.

An interface between two layers is a (mathematical) surface between the two materials constituting both layers. Deposited atoms impact randomly on the surface of the layer already grown. Since their mobility is finite and many other conditions influence the layer growth, the layer does not grow constantly in all places of the layer surface. Therefore perfectly flat interfaces cannot be achieved and the modulation of the actual interface between the layers with respect to the ideal interface is referred to as roughness.

For these reasons it is indispensable to incorporate the roughness, i.e., the random character of the interfaces, into the reflectivity calculation.

The influence of the interface roughness and of the interdiffusion is indistinguishable in the specular reflectivity. Both can be characterized by the same root mean square roughness and a mean interdiffusion width. However, a laterally homogeneous interdiffusion does not scatter the radiation into other than the specular direction. On the other hand, statistically random interface roughness produces diffuse scattering.

The preliminary task before the reflectivity calculation of samples with rough interfaces is the description of the randomness. Therefore we start this chapter by studying the statistical properties of single rough interfaces and of the correlation between different interfaces of a multilayer. We show how the rough interfaces change locally the layer thickness. We use both the dynamical and kinematical theories for calculating the specular intensity from a rough interface and from a rough multilayer. Our calculation leads to the well-known exponential diminution factors that decrease the value of the Fresnel coefficients. We use this model to fit experimental reflectivity curves of sandwich and periodic multilayers.

Laterally inhomogeneous random roughness produces diffuse (incoherent) scattering. We use a distorted-wave Born approximation to calculate quantitatively the scattered intensity. We demonstrate all the features of the diffuse scattering on the measured map of a periodic multilayer.

4.2 Statistical properties of rough interfaces

4.2.1 Description of a single rough interface

In the previous chapter we have dealt with multilayers with perfectly flat interfaces, thus having the interface coordinates constant, $z_j(\boldsymbol{r}_\parallel) = z_j$. Now let us take into account randomly rough interfaces, where $z_j(\boldsymbol{r}_\parallel)$ is no more constant. We describe the actual profile of a rough interface by the displacement $U_j(\boldsymbol{r}_\parallel)$ with respect to the mean interface (Fig. 4.1)

$$z_j(\boldsymbol{r}_\parallel) = z_j + U_j(\boldsymbol{r}_\parallel) \ . \tag{4.1}$$

The displacement U_j is random with zero mean, $\langle U_j \rangle = 0$. The random character of U_j is described by the *probability distribution function* [Hol96]

$$w_j(U) = \frac{1}{S} \int d\boldsymbol{r}_\parallel \ \delta(U_j(\boldsymbol{r}_\parallel) - U) \ , \tag{4.2}$$

which describes the probability of finding a point on the interface at the distance U from the mean interface regardless of the lateral position $\boldsymbol{r}_\parallel$ ($\delta(x)$ is the Dirac distribution, S is the area of integration). The dispersion of this function

$$\sigma_j = \sqrt{\langle U_j^2 \rangle} = \sqrt{\int dU \, w_j(U) \, U^2} \tag{4.3}$$

is called the *root mean square (rms) roughness* [CN76]. The rms roughness is a main characteristics of a rough interface. Further, the probability distribution function is related to the *mean coverage* of the plane at the distance U from the mean interface [LC84]

$$\theta_j(U) = \int_0^U dU\, w_j(U) = \frac{1}{S} \int d\boldsymbol{r}_\parallel\, H(U - U_j(\boldsymbol{r}_\parallel)) \ . \tag{4.4}$$

The Heaviside function $H(U)$ has been introduced on page 41.

Finally, we introduce the *characteristic function of the probability distribution* [Spi93]

$$\chi_{U_j}(Q) = \langle e^{-iQU_j} \rangle = \int dU\, w_j(U)\, e^{-iQU} \ , \tag{4.5}$$

which is the Fourier transform of the distribution function w_j.

It has been found that a *gaussian distribution function* satisfactory characterizes the interfaces of many samples [PC93]

$$w_j(U) = \frac{1}{\sqrt{2\pi}\,\sigma_j}\, e^{-U^2/2\sigma_j^2} \ . \tag{4.6}$$

The full-width at half maximum of this distribution is $2\sigma_j\sqrt{2\ln 2}$. The characteristic function of the gaussian probability distribution is gaussian as well

$$\chi_{U_j}(Q) = e^{-Q^2\sigma_j^2/2} \ . \tag{4.7}$$

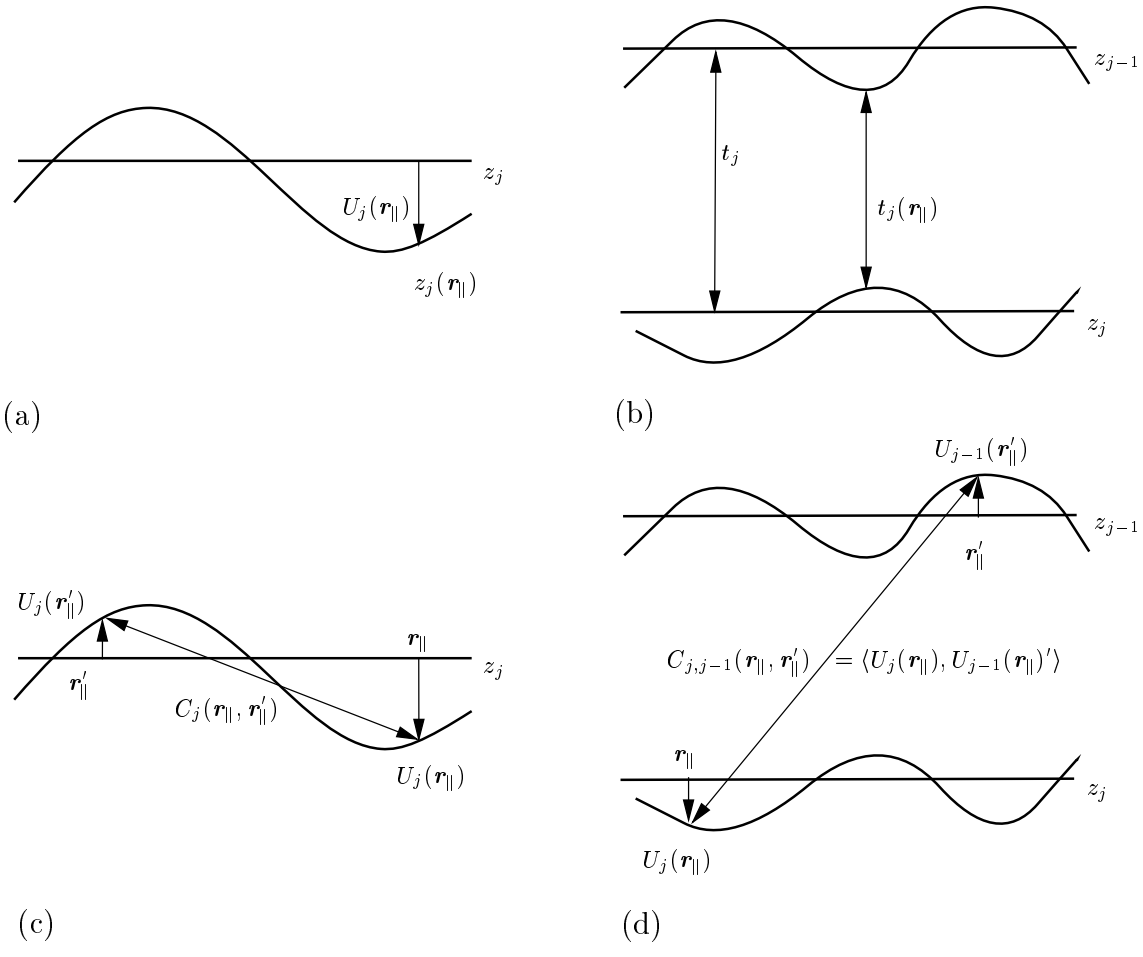

Figure 4.1. Definition of the displacement $U_j(\boldsymbol{r}_\parallel)$ of a rough interface $z_j(\boldsymbol{r}_\parallel)$ (a). Rough interfaces and the layer thickness fluctuations (b). Correlation function of a single interface (c) and a correlation function of two interfaces (d).

The probability distribution function $w_j(U)$ describes the point properties of a random interface since it does not depend on the lateral position $\boldsymbol{r}_\parallel$. A random interface (as any random function) is further characterized by the distribution functions of correlation of the heights of different points lying on the interface. Therefore we define the *pair distribution function* $w(U,U') \equiv w(U(\boldsymbol{r}_\parallel), U(\boldsymbol{r}'_\parallel))$ that determines the correlation properties between two points $U(\boldsymbol{r}_\parallel), U(\boldsymbol{r}'_\parallel)$ [Man82].[1] Let us suppose that the rough interface is homogeneous and statistically isotropic (i.e., the rough interface is described by the same set of the correlation functions over the irradiated sample area). Then the pair correlation function of two points $\boldsymbol{r}_\parallel, \boldsymbol{r}'_\parallel$ depends only on their distance $\Delta\boldsymbol{r}_\parallel = \boldsymbol{r}_\parallel - \boldsymbol{r}'_\parallel$, so that $w(U,U') = w(U(\boldsymbol{r}_\parallel), U(\boldsymbol{r}_\parallel + \Delta\boldsymbol{r}_\parallel))$ does not depend on $\boldsymbol{r}_\parallel$. The pair probability function of a gaussian interface is given by [Hol96]

$$w(U,U') = \frac{1}{2\pi\sigma^2\sqrt{1-K^2(\boldsymbol{r}_\parallel - \boldsymbol{r}'_\parallel)}} \exp\left\{-\frac{U^2 + U'^2 - 2UU'K(\boldsymbol{r}_\parallel - \boldsymbol{r}'_\parallel)}{2\sigma^2[1-K^2(\boldsymbol{r}_\parallel - \boldsymbol{r}'_\parallel)]}\right\} . \tag{4.8}$$

The dimensionless correlation coefficient $K(\boldsymbol{r}_\parallel - \boldsymbol{r}'_\parallel) = \frac{1}{\sigma^2} C(\boldsymbol{r}_\parallel - \boldsymbol{r}'_\parallel)$ is proportional to the *correlation function of the rough interface* [SSGS88]

$$C(\boldsymbol{r}_\parallel - \boldsymbol{r}'_\parallel) \equiv \langle U(\boldsymbol{r}_\parallel) U(\boldsymbol{r}'_\parallel)\rangle . \tag{4.9}$$

The characteristic function of the pair distribution function of gaussian interfaces is

$$\chi_{UU'}(Q,Q') = \langle e^{i(QU - Q'U')}\rangle = e^{-\sigma^2(Q^2+Q'^2)/2}\, e^{QQ'C(r_\parallel - r'_\parallel)} . \tag{4.10}$$

The choice of the correlation function is of crucial dependence on the sample concerned. We expect that a suitable correlation function satisfies the following two requirements: the heights U at the same point are perfectly correlated, thus $K(0) = 1$, and two points far away are not correlated, thus $K(\infty) = 0$. It has been found that the most suitable function depending on three parameters only follows from the fractal description of random surfaces [Man82], and that correlation function reads [SSGS88]

$$C_j(\boldsymbol{r}_\parallel, \boldsymbol{r}'_\parallel) = \langle U_j(\boldsymbol{r}_\parallel)\cdot U_j(\boldsymbol{r}'_\parallel)\rangle = \sigma_j^2\, e^{-\left(|\boldsymbol{r}_\parallel - \boldsymbol{r}'_\parallel|/\xi_j\right)^{2h_j}} . \tag{4.11}$$

Here ξ_j is the *in-plane correlation length* of the j-th interface and h_j is connected with the *fractal dimension* of the interface by relation $D_j = 3 - h_j$, $0 < h_j \leq 1$. Modelling the random interfaces, we see that h_j describes how smooth or jagged the interface is. Values of h_j approaching 1 produce smoothly varying interface ($h_j = 1$ for Gaussian surface), while small h_j produces very jagged interface.

4.2.2 Description of rough interfaces in a multilayer

So far we have dealt with the correlation properties of a simple interface only. A multilayer is formed by a sequence of layers that have been grown one after another. Therefore, the profile of an interface depends to a certain extent on the interface profiles of the underlaying layers. The correlation properties between different interfaces of a multilayer are discussed in this section.

Similarly to a single interface (4.8), the gaussian probability distribution function of two interfaces j,k is [Hol96]

$$w_{jk}(U,U') = \frac{1}{2\pi\sigma_j\sigma_k\sqrt{1-K_{jk}^2(\boldsymbol{r}_\parallel - \boldsymbol{r}'_\parallel)}} \exp\left\{\frac{1}{2[1-K_{jk}^2]}\left[\frac{U^2}{\sigma_j^2} + \frac{U'^2}{\sigma_k^2} - \frac{2UU'K_{jk}}{\sigma_j\sigma_k}\right]\right\} . \tag{4.12}$$

[1] The pair correlation function is required for the calculation of the mean of any function $\alpha(U,U')$: $\langle\alpha(U,U')\rangle = \langle\alpha(U(\boldsymbol{r}_\parallel), U(\boldsymbol{r}'_\parallel))\rangle = \int dU \int dU'\, \alpha(U,U')\, w(U,U')$.

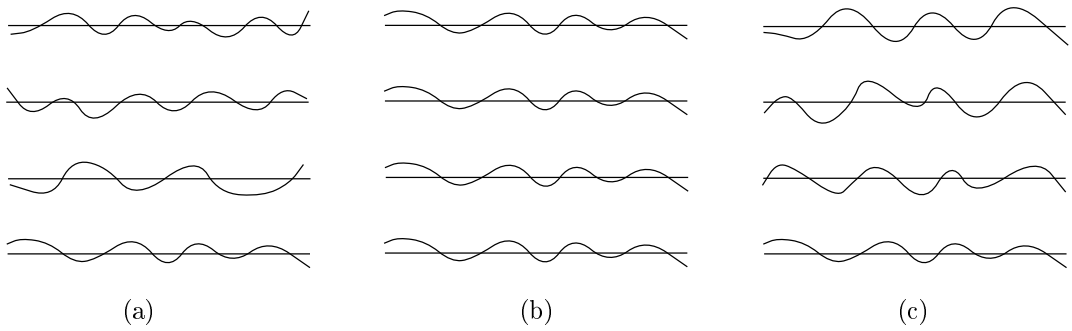

Figure 4.2. Schematic representation of interface roughness in multilayers: (a) independently rough interfaces (uncorrelated roughness), (b) perfectly correlated (identical, replicated, conformal) roughness; (c) partially correlated roughness.

The (pair) correlation function of two interfaces j,k calculated at two lateral points $\boldsymbol{r}_\parallel, \boldsymbol{r}'_\parallel$ is

$$C_{jk}(\boldsymbol{r}_\parallel - \boldsymbol{r}'_\parallel) = \sigma_j \sigma_k K_{jk}(\boldsymbol{r}_\parallel - \boldsymbol{r}'_\parallel) = \left\langle U_j(\boldsymbol{r}_\parallel) U_k(\boldsymbol{r}'_\parallel) \right\rangle \ . \tag{4.13}$$

We suppose different interfaces, $j \neq k$, since the correlation function of a single interface $C_{jj}(\boldsymbol{r}_\parallel) \equiv C_j(\boldsymbol{r}_\parallel)$ has been studied in the previous section. The correlation function depends considerably on the multilayer growth [JMP92, dBLW95].

The experimental conditions determine how each growing layer replicates the interface profile of its lower interface and how the intrinsic roughness comes out. A general formula comprising both phenomena [SSK93, Hol96] writes the interface displacement

$$U_j(\boldsymbol{r}_\parallel) = h_j(\boldsymbol{r}_\parallel) + U_{j+1}(\boldsymbol{r}_\parallel) \otimes a_j(\boldsymbol{r}_\parallel) = h_j(\boldsymbol{r}_\parallel) + \int d\boldsymbol{r}'_\parallel \ U_{j+1}(\boldsymbol{r}'_\parallel)\, a_j(\boldsymbol{r}_\parallel - \boldsymbol{r}'_\parallel) \ . \tag{4.14}$$

Here $h_j(\boldsymbol{r}_\parallel)$ is the *intrinsic roughness* of the jth interface. The *replication function* $a_j(\boldsymbol{r}_\parallel)$ corresponding to the growth of the $(j+1)$th layer can be chosen so that it covers three possible types of roughness propagation:

1. independently rough interfaces, Fig. 4.2(a): no replication is present (the growth process has "no memory"), thus $a_j(\boldsymbol{r}_\parallel) = 0$,

2. identical roughness, Fig. 4.2(b): the intrinsic roughness is zero ($h_j(\boldsymbol{r}_\parallel) = 0$) except for the substrate interface. Each interface above the substrate replicates perfectly the substrate interface profile, thus $a_j(\boldsymbol{r}_\parallel) = \delta(\boldsymbol{r}_\parallel)$. The case $a_j(\boldsymbol{r}_\parallel) \neq \delta(\boldsymbol{r}_\parallel)$ (not shown in the figure) leads to the smoothening of the substrate roughness, i.e., roughness decreases towards the free surface,

3. partial replication, Fig. 4.2(c): both the intrinsic and replicated roughness contributions are non-zero. This is the most general case given by Eq. (4.14).

4.2.3 Root mean square roughness and the thickness fluctuations

In this section we look how the fluctuations of the interface profiles (i.e., the rms roughness) and the layer thickness fluctuations are related. In a rough multilayer, the actual thickness is a local quantity (Fig. 4.1(b))

$$t_j(\boldsymbol{r}_\parallel) = z_j(\boldsymbol{r}_\parallel) - z_{j-1}(\boldsymbol{r}_\parallel) = t_j + U_j(\boldsymbol{r}_\parallel) - U_{j-1}(\boldsymbol{r}_\parallel) \ , \tag{4.15}$$

where the ideal layer thickness is $t_j = \langle z_j(\boldsymbol{r}_\parallel) - z_{j-1}(\boldsymbol{r}_\parallel) \rangle = \langle t_j(\boldsymbol{r}_\parallel) \rangle$. The root mean square fluctuation of layer thickness

$$\langle \delta t_j^2 \rangle = \langle (t_j - \langle t_j \rangle)^2 \rangle = \langle (U_j - U_{j-1})^2 \rangle = \sigma_j^2 + \sigma_{j-1}^2 - 2\, C_{j,j-1}(0) \tag{4.16}$$

depends on the root mean square roughnesses of the surrounding interfaces as well as on their vertical correlation $C_{j,j-1}(0)$.

In the case of *independently random rough interfaces*, Fig 4.2(a), the thickness fluctuations are simply

$$\langle \delta t_j^2 \rangle = \sigma_j^2 + \sigma_{j-1}^2 \ . \tag{4.17}$$

The *identical (perfectly correlated, conformal) roughness*, Fig. 4.2(b), is the other marginal case of the roughness distribution. The thickness of all layers is laterally constant in spite of the non-flat interfaces copying the rough substrate interface.

Finally, let us suppose the *intermediate case*, Fig 4.2(c), and let the layer thickness be a random quantity, $t_j(\boldsymbol{r}_\parallel) = t_j + D_j(\boldsymbol{r}_\parallel)$. The interface profile

$$z_j(\boldsymbol{r}_\parallel) = z_j + U_j(\boldsymbol{r}_\parallel) = z_{j+1}(\boldsymbol{r}_\parallel) - t_{j+1}(\boldsymbol{r}_\parallel) = z_N + U_N(\boldsymbol{r}_\parallel) - \sum_{l=N}^{j+1} t_l(\boldsymbol{r}_\parallel) \tag{4.18}$$

then gives the interface displacements

$$\begin{aligned} U_j(\boldsymbol{r}_\parallel) &= z_j(\boldsymbol{r}_\parallel) - z_j = (z_{j+1}(\boldsymbol{r}_\parallel) - z_{j+1}) - (t_{j+1}(\boldsymbol{r}_\parallel) - t_{j+1}) \\ &= U_{j+1}(\boldsymbol{r}_\parallel) - D_{j+1}(\boldsymbol{r}_\parallel) = U_N(\boldsymbol{r}_\parallel) - \sum_{l=N}^{j+1} D_j(\boldsymbol{r}_\parallel) \ . \end{aligned} \tag{4.19}$$

From this follows that the rms roughness increases from the substrate interface towards the sample surface by

$$\sigma_j^2 = \sigma_N^2 + \sum_{l=N}^{j+1} \langle D_l^2 \rangle \ . \tag{4.20}$$

For constant thickness fluctuations $\xi^2 = \langle D_l^2 \rangle$ it simplifies to the well-known relation [HB94]

$$\sigma_j^2 = \sigma_N^2 + (N-j)\xi^2 \ . \tag{4.21}$$

Both the above formulae hold for increasing roughness, where the layer thickness fluctuations increase the roughness imposed by the substrate interface σ_N, or, if the layer thickness fluctuations are zero, then the layers copy perfectly the substrate interface. The third case, when the substrate roughness is diminished by the deposited layers, is experimentally found as well.[2] The general model (4.14) describes also this case of partial replication without intrinsic roughness. It has been shown in Ref. [Hol96] that the rms roughness depends on the lateral correlation length.

4.3 Specular reflectivity from a rough multilayer

4.3.1 Dynamical calculation

Now let us calculate how the rough interfaces influence the reflected intensity. Since the roughness changes the local layer thickness, the matrix calculation procedure (3.61) requires to change the propagation matrices (3.57) accordingly. Their phase term then becomes

$$\Phi_j(\boldsymbol{r}_\parallel) = e^{ik_z^{(j)} t_j(\boldsymbol{r}_\parallel)} = \Phi_j \, e^{ik_z^{(j)}(U_j(\boldsymbol{r}_\parallel) - U_{j-1}(\boldsymbol{r}_\parallel))} \ . \tag{4.22}$$

[2] This relates to samples where the substrate roughness or that of the buffer layer is large (Sec. 4.4.3). This roughness is then smoothen by the subsequent growth.

The propagation matrix of a layer bounded by rough interfaces turns into the product of three diagonal matrices that describe the propagation through the layer with averaged thickness and through the imperfect region, respectively,

$$\mathcal{Q}^{(j)}(\boldsymbol{r}_\parallel) = \mathcal{U}_{j-1}(-k_z^{(j)}, \boldsymbol{r}_\parallel)\, \mathcal{Q}^{(j)}(k_z^{(j)})\, \mathcal{U}_j(k_z^{(j)}, \boldsymbol{r}_\parallel) \tag{4.23}$$

$$\mathcal{U}_j(k_z, \boldsymbol{r}_\parallel) \equiv \begin{pmatrix} e^{-ik_z U_j(\boldsymbol{r}_\parallel)} & 0 \\ 0 & e^{ik_z U_j(\boldsymbol{r}_\parallel)} \end{pmatrix} . \tag{4.24}$$

Further, we regroup the matrices in the sequence (3.61) so that the displacement matrices $\mathcal{U}_j$ of the same interface j are associated together with the corresponding boundary matrix $\mathcal{P}_{j,j+1}$

$$\begin{aligned} \mathcal{M}(\boldsymbol{r}_\parallel) &= \ldots \mathcal{Q}^{(j)}(\boldsymbol{r}_\parallel)\mathcal{P}^{\mathrm{id}}_{j,j+1}\mathcal{Q}^{(j+1)}(\boldsymbol{r}_\parallel)\ldots \\ &= \ldots \mathcal{U}_{j-1}(-k_z^{(j)}, \boldsymbol{r}_\parallel)\mathcal{Q}^{(j)}\mathcal{U}_j(k_z^{(j)}, \boldsymbol{r}_\parallel)\, \mathcal{P}^{\mathrm{id}}_{j,j+1}\, \mathcal{U}_j(-k_z^{(j+1)}, \boldsymbol{r}_\parallel)\mathcal{Q}^{(j+1)}\mathcal{U}_{j+1}(k_z^{(j+1)}, \boldsymbol{r}_\parallel)\ldots \\ &= \ldots \mathcal{Q}^{(j)}\mathcal{P}_{j,j+1}(\boldsymbol{r}_\parallel)\mathcal{Q}^{(j+1)} \ldots . \end{aligned} \tag{4.25}$$

After reordering, the boundary matrix describing the transition through the rough interface j became random

$$\begin{aligned} \mathcal{P}_{j,j+1}(\boldsymbol{r}_\parallel) &\equiv \mathcal{U}_j(k_z^{(j)}, \boldsymbol{r}_\parallel)\, \mathcal{P}^{\mathrm{id}}_{j,j+1}\, \mathcal{U}_j(-k_z^{(j+1)}, \boldsymbol{r}_\parallel) \\ &= \frac{1}{\mathfrak{t}_j^{\mathrm{id}}} \begin{pmatrix} e^{-i(k_z^{(j)} - k_z^{(j+1)})U_j(\boldsymbol{r}_\parallel)} & \mathfrak{t}_j^{\mathrm{id}}\, e^{-i(k_z^{(j)} + k_z^{(j+1)})U_j(\boldsymbol{r}_\parallel)} \\ \mathfrak{r}_j^{\mathrm{id}}\, e^{-i(-k_z^{(j+1)} - k_z^{(j)})U_j(\boldsymbol{r}_\parallel)} & e^{-i(k_z^{(j+1)} - k_z^{(j)})U_j(\boldsymbol{r}_\parallel)} \end{pmatrix} . \end{aligned} \tag{4.26}$$

The reflectivity amplitude of a multilayer, given by Eq. (3.62), has to be statistically averaged over the irradiated sample area, or equivalently, over the profile distribution of all interfaces. The averaged fraction of two random functions $a(x), b(x)$ can be approximated by a fraction of their means

$$\left\langle \frac{a}{b} \right\rangle = \int \frac{a(x)}{b(x)}\, w(x)\, dx = \int \frac{\langle a\rangle + \delta a(x)}{\langle b\rangle + \delta b(x)}\, w(x)\, dx \approx \frac{\langle a\rangle}{\langle b\rangle}\left[1 + \frac{\langle \delta b^2\rangle}{\langle b\rangle^2} - \frac{\langle \delta a \delta b\rangle}{\langle a\rangle\langle b\rangle}\right] , \tag{4.27}$$

where we defined $\delta a = a - \langle a\rangle$, $\delta b = b - \langle b\rangle$. In the case of small roughness we can neglect the second order contributions and approximate the reflectivity (3.62) by [PC93, Hol96]

$$R = \left\langle \frac{M_{21}}{M_{11}} \right\rangle \approx \frac{\langle M_{21}\rangle}{\langle M_{11}\rangle} . \tag{4.28}$$

Averaging the transfer matrix of the whole multilayer then separates to the averaging of the boundary matrices

$$\begin{aligned} \langle \mathcal{M}(\boldsymbol{r}_\parallel)\rangle &= \ldots \mathcal{Q}^{(j)}\, \langle \mathcal{P}_{j,j+1}(\boldsymbol{r}_\parallel)\rangle\, \mathcal{Q}^{(j+1)}\, \langle \mathcal{P}_{j+1,j+2}(\boldsymbol{r}_\parallel)\rangle \ldots \\ &= \prod_{j=1}^{N} \langle \mathcal{N}_j(\boldsymbol{r}_\parallel)\rangle = \prod_{j=1}^{N} \langle \mathcal{P}_{j,j+1}(\boldsymbol{r}_\parallel)\rangle\, \mathcal{Q}^{(j+1)} . \end{aligned} \tag{4.29}$$

The statistical averaging of the boundary matrices is straightforward and it expresses them by the characteristic function of the probability distribution

$$\langle \mathcal{P}_{j,j+1}(\boldsymbol{r}_\parallel)\rangle = \frac{1}{\mathfrak{t}_j^{\mathrm{id}}} \begin{pmatrix} \chi_{U_j}\begin{pmatrix} k_z^{(j)} - k_z^{(j+1)} \end{pmatrix} & \mathfrak{t}_j^{\mathrm{id}}\, \chi_{U_j}\begin{pmatrix} k_z^{(j)} + k_z^{(j+1)} \end{pmatrix} \\ \mathfrak{r}_j^{\mathrm{id}}\, \chi_{U_j}\begin{pmatrix} -k_z^{(j)} - k_z^{(j+1)} \end{pmatrix} & \chi_{U_j}\begin{pmatrix} k_z^{(j+1)} - k_z^{(j)} \end{pmatrix} \end{pmatrix} . \tag{4.30}$$

This matrix is symmetric for the usual case of symmetric Fourier transforms of the distribution functions and the averaged boundary matrix simplifies into the form analogous to the case with flat interfaces (3.51)

$$\mathcal{P}_{j,j+1} = \frac{1}{\mathfrak{t}_j} \begin{pmatrix} 1 & \mathfrak{r}_j \\ \mathfrak{r}_j & 1 \end{pmatrix} , \tag{4.31}$$

where the Fresnel coefficients corrected for the roughness [VV84] are

$$\begin{aligned} \mathfrak{r}_j &= \mathfrak{r}_j^{\mathrm{id}} \frac{\chi_{U_j}\left(k_z^{(j+1)}+k_z^{(j)}\right)}{\chi_{U_j}\left(k_z^{(j+1)}-k_z^{(j)}\right)} \\ \mathfrak{t}_j &= \mathfrak{t}_j^{\mathrm{id}} \frac{1}{\chi_{U_j}\left(k_z^{(j+1)}-k_z^{(j)}\right)} \; . \end{aligned} \tag{4.32}$$

Supposing a gaussian distribution function of the roughness profile we find the well-known relations (see, [CN76], for instance)

$$\begin{aligned} \mathfrak{r}_j &= \mathfrak{r}_j^{\mathrm{id}}\, e^{-2k_z^{(j)}k_z^{(j+1)}\sigma_j^2} = \mathfrak{r}_j^{\mathrm{id}}\, e^{-q_z^{(j)}q_z^{(j+1)}\sigma_j^2/2} \\ \mathfrak{t}_j &= \mathfrak{t}_j^{\mathrm{id}}\, e^{(k_z^{(j)}-k_z^{(j+1)})^2\sigma_j^2/2} \; . \end{aligned} \tag{4.33}$$

Not only the gaussian distribution functions, but also other types (e.g., symmetric exponential, pillbox) are used and their choice can lead to a better fit of a measured data [Spi93]. However, the differences are small and since we cannot verify the atom distribution directly, we will further use the gaussian distributions.

We underline that the roughness influences the specular reflectivity only by a change of the value of the Fresnel coefficients and therefore the procedure of the specular reflectivity calculation described in Sec. 3.4.4 remains still valid using the above substitution (4.32).

Since the vertical components of the wave vectors are nearly the same in all layers, the transmission is not substantially influenced by the roughness. However, the reflectivity coefficient is diminished exponentially by the rms roughness and the diminution factor is sometimes called the static Debye-Waller factor in correspondence with the form of the Debye-Waller factor in X-ray diffraction [Cow75].

The roughness can crucially change the interference between different layer stacks. If the roughnesses of two interfaces are not close, then the amplitude reflected from one interface is much stronger than the other and their interference is diminished. This explains the different sensitivity of the specular curve of a single-layered sample on the surface and interface roughnesses (i.e., on the roughnesses of the vacuum/layer and layer/substrate interfaces, respectively), Fig. 4.3. If the interface roughness is large, then this reflected wave is weak and the interference term of this wave and the wave reflected by the surface decreases, which results in smaller amplitude of the oscillations. In the opposite case, where the surface roughness is large, the amplitude of the wave reflected by the surface is weak. The amplitude of the wave reflected by the interface is decreased by the absorption of the wave transmitted through the layer and therefore the whole reflectivity curve is diminished with respect to the ideal case of perfectly flat interfaces. Similar arguments will be used later for the discussion of the reflectivity by rough gratings, Sec. 5.9.2.

4.3.2 Kinematical calculation

In the above section we calculated the specular reflectivity under the presence of rough interfaces by means of the dynamical theory. In order to be complete and show another diminution factor found in the literature, we will make use of the kinematical theory now. The kinematical Fresnel coefficient is given by the integral (3.108) and for random interface it reads

$$\begin{aligned} \mathfrak{r}_j^{\mathrm{kin}}(\boldsymbol{r}_{\|}) &= \frac{iK^2}{Q_z}\int_{-\infty}^{\infty} dU \left[\chi_j\, H(U-U_j(\boldsymbol{r}_{\|})) + \chi_{j+1}\, H(U_j(\boldsymbol{r}_{\|})-U)\right] e^{-iQ_zU} \\ &= \frac{K^2}{Q_z^2}\left(\chi_j-\chi_{j+1}\right) e^{-iQ_zU_j(\boldsymbol{r}_{\|})} = \mathfrak{r}^{\mathrm{kin,id}}\, e^{-iQ_zU_j(\boldsymbol{r}_{\|})} \; . \end{aligned} \tag{4.34}$$

Averaging this we find

$$\langle \mathfrak{r}_j^{\mathrm{kin}} \rangle = \mathfrak{r}_j^{\mathrm{kin,id}} \langle e^{-iQ_zU_j} \rangle = \mathfrak{r}_j^{\mathrm{kin,id}}\, e^{-Q_z^2\sigma_j^2/2} \; . \tag{4.35}$$

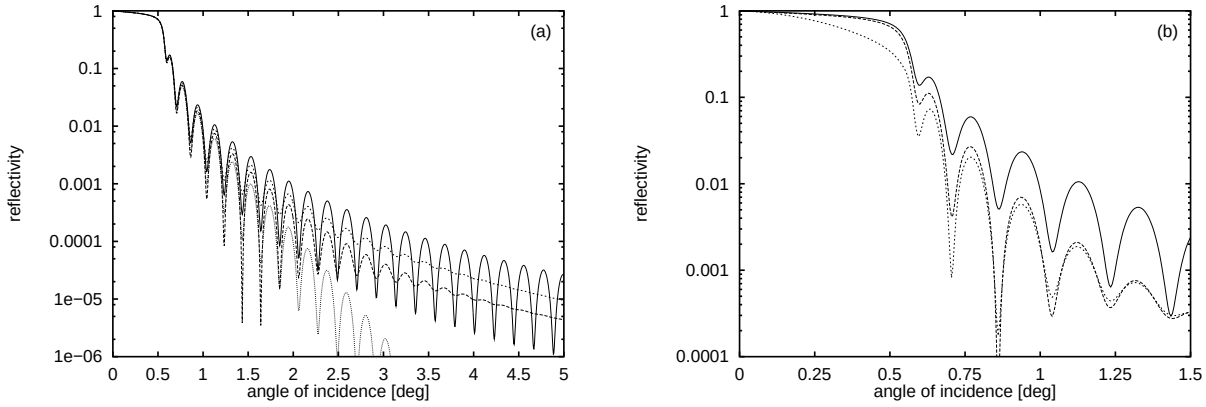

Figure 4.3. Simulation of the specular scan for different root mean square roughnesses and diminution factors (tungsten 200 Å layer on a sapphire substrate). (a) Dynamical "rapid" damping factor. From upper to lower curve: without roughness, interface roughness 5 Å, surface roughness 5 Å, both surface and interface roughnesses 5 Å. Surface roughness yields a faster decay of the reflectivity, while interface roughness attenuates the peaks. (b) Different damping factors. Surface roughness 12 Å and interface roughness 3 Å calculated for the kinematical "slow" roughness (lower curve), dynamical "rapid" roughness (middle curve) and without roughness (upper curve).

This expression is close to that found by Névot and Croce [CN76] for "slow" roughness (slowly modulated roughness with small slopes, large correlation length)

$$\langle \mathfrak{r}_j^{\mathrm{NC}} \rangle = \mathfrak{r}_j^{\mathrm{id}}\, e^{-(q_z^{(j)})^2 \sigma_j^2/2} \ . \tag{4.36}$$

We can see that the only (but important) difference encountered in the kinematical theory is the use of the vacuum wave vector transfer Q_z instead of that in the corresponding layer $q_z^{(j)}$. The "rapid" roughness reported by Névot and Croce takes the form (4.33), and it corresponds to the small correlation lengths.

Since there are two different formulae for the specular reflectivity diminution, for "slow" and "rapid" roughnesses, it is clear that there should be a connection between them depending on the lateral correlation length. This has been found by de Boer [dB94, dB95], who used the DWBA of the second order and has shown how the diminution depends on the lateral correlation length.

We plotted the reflectivity curve using both the rapid and slow diminution factors in Fig. 4.3. We find that for angles of incidence much larger than the critical angle the diminution effects are the same, but measured below the critical angle, where $q_z^{(2)}$ is purely imaginary, both dependencies considerably differ. In non-absorbing case the factor (4.36) always diminishes the specular curve, but the factor (4.33) does not influence the reflected intensity since the product $Q_z q_z^{(2)}$ is purely imaginary.

4.4 Specular reflectivity measurements

In this section we apply the theoretical formulae calculating the reflectivity curves to reveal the structural parameters of some samples from the experimental data. Firstly, we discuss the geometrical effects encountered in the specular reflectivity measurements: the intensity drop in the near-zero angular region due to the finite beam size and the smoothening effect of the beam divergence.

Then we present specular reflectivity measurements of two kinds of samples: of a multilayer with three different layers and of a periodic multilayer. In both cases we discuss the fitting of the experimental curves.

4.4.1 Instrumental factors in the specular reflectivity measurements

Effects of the instrumental functions on the measured curves affecting the measured specular reflectivity curves are found during each measurement, and therefore they are well-known (see, [DB92a, GVS93], for instance). Since we were encountering these effects during our work as well, we are going to explain them now. The first geometrical effect discussed below is employed during the sample alignment procedure. The second effect of the primary beam divergence applies mainly for thick multilayers and for divergent beams, and it does not play any role in the experimental curves of the samples discussed in Secs. 4.4.2 and 4.4.3.

Geometrical effect on the specular curve

Comparing the experimental and theoretical specular curves, a geometrical effect in the angular region close to the zero angle of incidence has to be taken into account. This effect is caused by the finite beam size b_x and sample length L_x, Fig. 4.4. For small angles of incidence ω, the whole sample surface baths in the beam and only a part of the primary intensity corresponding to the perpendicular projection of the sample surface is reflected (situation (b)). When the sample is rotated and the angle of incidence ω increases to a certain value ω_F, then the whole beam is reflected by the whole sample surface (position (c)). For the angles of incidence larger than ω_F the incoming beam illuminates the central part of the sample whose size decreases for increasing angle of incidence. From the geometry shown in the figure it follows that the *cover angle* ω_F satisfies

$$\sin\omega_F = \frac{b_x}{L_x} \ . \tag{4.37}$$

The reflected intensity below this angle is diminished with respect to the ideal reflectivity proportionally to the incidence angle

$$R(\omega{<}\omega_F) = \frac{L_-}{b_x} R^{\mathrm{id}}(\omega) = \frac{\sin\omega}{\sin\omega_F} R^{\mathrm{id}}(\omega) \approx \frac{\omega}{\omega_F} R^{\mathrm{id}}(\omega) \ . \tag{4.38}$$

The reflected intensity for angles larger than ω_F is not influenced. Graph (e) shows the situation for two cases: $\omega_F = 0.23^\circ$ and 0.69° (this corresponds to a sample length 5 mm and beam sizes of 20 μm and 60 μm, respectively).

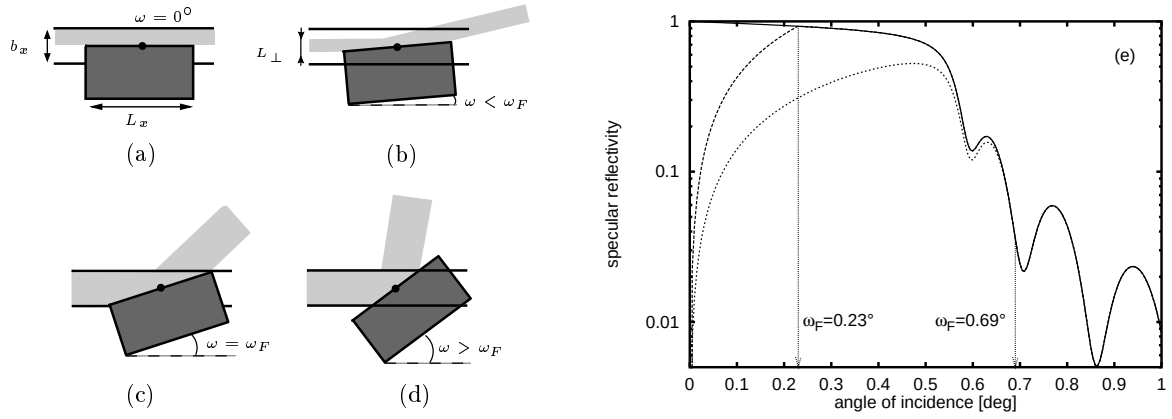

Figure 4.4. Different positions (a)–(d) of the sample (the black rectangle) in the primary beam influence the measured specular curve (e). The black circle denotes the centre of rotation (the goniometer axis). Below the cover angle ω_F, only a part (in grey) proportional to L_- of the primary beam size b_x is reflected, see (a)–(b). Above the cover angle, the whole beam is reflected, see (c)–(d). Larger beam size b_x increases the integrated primary intensity, however, in the same time the cover angle ω_F shifts to larger angles (e), which decreases the intensity measured below ω_F with respect to the ideal curve.

From the dependence (4.38) it follows that the correct geometrical arrangement as well as the primary intensity should be known even in the specular reflectivity measurement. The lack of this knowledge for the cover angle larger than the critical angle may bring uncertainty into the fitting since it would not be possible to determine whether the intensity fall (dashed curve) is due to the primary intensity lower than the actual one (this intensity drop would apply for the whole specular curve), or due to this geometrical effect (the diminution takes part only up to the cover angle).

On the other hand, the positions (a)–(c) are used in the procedure of the sample adjustment, i.e., after the sample is mounted on the goniometer head and when its correct position and zero angle have to be found. In this adjustment routine, we place the detector in the direct beam and scan the profile of the primary beam that passes above the sample surface. Then we are displacing the sample in the beam and rock it in order to find the position where the detector signal is half of the primary intensity and when rocking the sample around this zero position the detector signal decreases linearly. The position $\omega = \omega_F$ then corresponds to the position where no more intensity comes to the detector. As in the other methods of sample alignment, the correct setup has to be verified by the position of the reflected beam ($2\omega = 2\theta$ on each point of the specular curve).

Divergence of the primary beam

Let us suppose that the primary beam falling on the sample has the divergence ω_S, Fig. 4.5. This depends on the divergence after the source and the reflection curve of the monochromator and it can be cut by slits; it is measurable during the alignment procedure. The output divergence is defined by the acceptance angle of the detector window $2\theta_D$, or by the input reflection curve of an analyzer crystal if the measurement is done on a triple axis diffractometer. Let us suppose the former case, i.e., a double crystal diffractometer with large input divergence (i.e., a graphite monochromator) and an open detector preceded by a thin slit of width s_-. Then $2\theta_D = \mathrm{arctg}\, s_-/l_{SD}$, where l_{SD} is the sample-slit distance. The intensity collected by the detector is

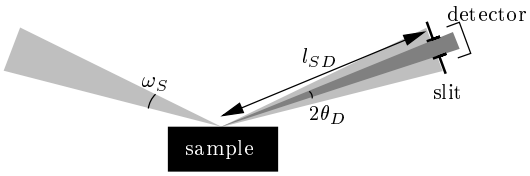

Figure 4.5.

$$\mathcal{R}(\omega) = \int_{-\theta_D}^{\theta_D} d\Delta\theta\ \mathcal{R}_1(\Delta\theta)\ \mathcal{R}(\omega + \Delta\theta)\ , \tag{4.39}$$

where $\mathcal{R}_1$ is the profile of the intensity of the primary beam and $\mathcal{R}$ is the theoretical reflectivity curve of the sample. Therefore, the effect of divergence integrates the reflectivity curve over a small region around the measured point ω thus producing smoothening of the theoretical curve.

This effect is noticeable only if the divergence is greater than the period of the thickness oscillations on the specular curve. Supposing the slit width 100 μm and the sample-slit distance 30 cm, the slit acceptance 0.019° corresponds to the thickness oscillation period for the sample thickness $t = \lambda/4\theta_D = 2300$ Å, so that the calculation of the smoothening would not be necessary for samples thinner than at about 500 Å, because the reflected intensity does not change considerably within the integration region in (4.39).

Let us note that the use of sufficiently large angular acceptance of the detector slit is desirable because it brings more intensity thus reducing the measuring time and improving the statistics of low-intensity points.

4.4.2 $TbFe_2$ sandwich multilayer

In this section we present the determination of the structural parameters of a sandwich system (see the inset in Fig. 4.6), based on the fitting of the specular reflectivity curve. The sample F19 concerned belongs to the series of samples where a thin magnetic layer, $TbFe_2$ in this

case, is deposited on a tungsten buffer layer carried by a sapphire (Al_2O_3) substrate and covered by a chrome capping layer. The samples have been prepared by laser ablation deposition (LAD, known as the pulsed laser deposition (PLD) technique as well) [Gra94] in Laboratoire Louis Néel, Grenoble, where this original method is being developed since 1992. It has been shown that this method is very successful for the epitaxial growth of multilayers consisting of transition metals and rare earths, like Fe, Gd, Cr, W [CGL$^+$93, Mik93b, Gra94, GRC$^+$94] as well as for intermetallic compounds and alloys, including Y_xCo_y [Rob95, RMC$^+$95] or $TbFe_2$. The magnetic properties of these multilayers are intensively examined, namely for the effects of magnetostriction, giant magnetoresistance and magnetic coupling. Since these properties depend considerably on the sample structure determined by the growth conditions, the sample characterization by means of non-destructive X-ray measurements is of great importance.

The reflectivity measurement of the sample F19 has been performed at the beamline BL23 in L.U.R.E. (Laboratoire d'Utilisation du Rayonnement Electromagnétique, Université Paris-Sud, Orsay), using the wavelength 1.54 Å. The measured specular scan, shown in Fig. 4.6, has been used in order to fit the layer thicknesses and interface roughnesses. In the fitting procedure, we stepped in the following way.

Using the nominal values of the layer thicknesses we estimated the reflectivity curve up to the mean critical angle because the reflectivity is not sensitive to the layer roughnesses in this angular region (this has been already discussed). Then we put in the roughnesses and fit the tail of the reflectivity curve. Afterwards, the total thickness has been estimated by means of the period of the oscillations. Finally, we tuned all the parameters in order to achieve the best coincidence of the measured and simulated curves as possible. When changing the values of the roughness of the sapphire substrate and the thickness and roughness of the tungsten layer above, we followed the results of fitting the tungsten/sapphire single-layered samples [Mik93b]. It has been found in the mentioned work, as well as in the previous studies of the sapphire substrate, that for these samples the usual sapphire substrate roughness is about 3 Å and the roughness of the deposited tungsten layer increases by about 5–6 Å per 100 Å of layer thickness. The fitted

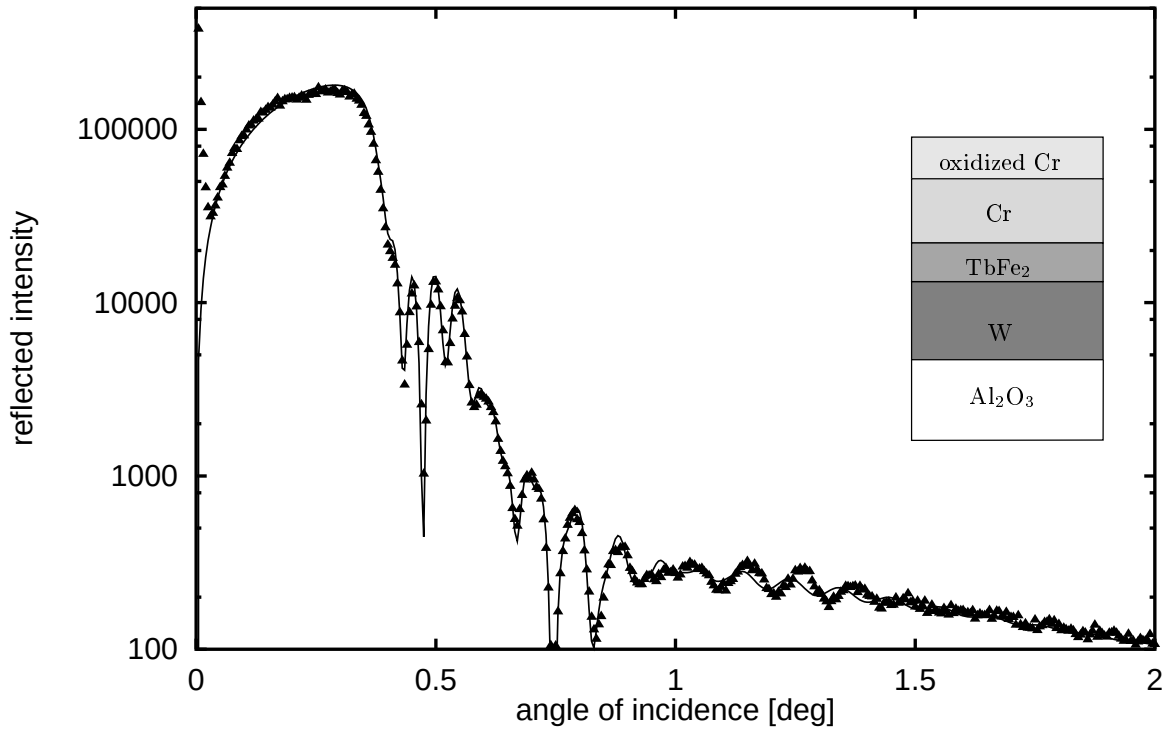

Figure 4.6. Measurement (points) and the fit (full curve) of the specular reflectivity curve of the sample F19, whose structure is schematically shown in the inset figure.

values of the F19 sample $\sigma_{sub} = 2 \pm 1$ Å, $\sigma_W = 19.7 \pm 1$ Å and the tungsten layer thickness 346 ± 4 Å coincided with our predictions. Finally, we have seen that it is not possible to fit the specular curve by supposing a stack of three layers only. A modified profile of Cr layer density near the surface had to be involved. Since we knew that Cr gets oxidized when exposed to the air, we introduced a superficial layer with the density half of the Cr density. This setup led to the fit plotted in Fig. 4.6. The thickness and the roughnesses of the $TbFe_2$ layer have been determined to be 48 ± 2 Å and 9.4 ± 1 Å, respectively, those of the chrome layer 505 ± 3 Å and 22 ± 1 Å, and the additional layer thickness was 30 Å. The thickness of the $TbFe_2$ layer has been furthermore deduced from the vibrating sample magnetometer (VSM) measurement and the values estimated by both X-ray and magnetic experiments coincided.

4.4.3 NbSi periodic multilayers

The sample discussed in the previous section was a sandwich multilayer consisting of three nominal layers only. In the present section we show a series of measurements and fits of periodic Si/Nb multilayer with 20 periods. There is a Si substrate with a very thick SiO_2 buffer layer and an aluminium layer of different thicknesses giving rise to different roughness profiles of the interfaces of the periodic multilayer deposited on it, Fig. 4.7. The sample producer (Slovak Academy of Science, Bratislava) has a main interest of growing these layers in order to study the superconducting properties. The reflectivity measurements have been performed by Dr. Kuběna (Masaryk University, Brno) using a double-crystal diffractometer (with double Ge(111) diffraction on the first crystal Ge(111)) with copper X-ray tube.

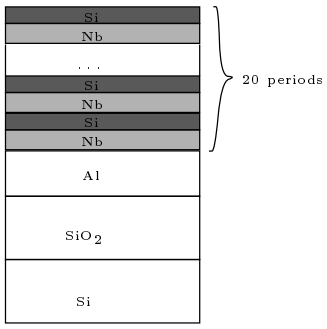

Figure 4.7.

In the fitting procedure, we stepped in the following way. Firstly, we verified that the number of periods N=20 coincide to the predicted number, since there are $N-2$=18 subsidiary maxima between two subsequent main maxima (Bragg peaks of the multilayer). However, we should stress that this rule need not be valid in each region of the reflectivity curve if roughness is taken into account, because big roughness can diminish the corresponding Fresnel coefficient in such a way that the interference between distant interfaces is destroyed. Further, the multilayer period can be established by fitting the positions of the superlattice peaks as well as by taking the position of the critical angle into account (3.124). The envelope of the main maxima is determined mainly by the ratio of the layer thicknesses. The substrate and the buffer layer roughnesses influence mainly the far tail of the reflectivity curve, whereas the roughness distribution propagating up the layers determines the peak widths. The profiles between the main maxima are sensitive to the buffer layer thickness.

The series of samples consisted of specimens with different Si and Nb layer thicknesses grown on an Al buffer layer with thickness of either 200 Å or 2000 Å. The Al layer is deposited in order to produce a rough bottom interface of the periodic Si/Nb stack and this roughness increases for thicker Al layers. The roughness distribution in the periodic multilayer can be described by two following functions. Either, we keep the roughnesses of the interfaces of Si and Nb constant (model of the constant roughnesses)

$$\sigma_j = \sigma_{\text{Nb/Si or Si/Nb}} \ ,$$

or we suppose that the roughness grows from the substrate to the vacuum by

$$\sigma_j = \sqrt{\sigma^2_{\text{Nb/Si or Si/Nb}} + n_j \, \Delta\sigma^2} \ ,$$

where n_j is the number of layers between the substrate and the jth interface (cf. Eq. (4.21)). The fit enabled us to distinguish between both roughness propagations.

The periodic sequence in sample D0B has been grown on an Al 200 Å layer. Fitting the measured curve (Fig. 4.8(a)) we have found that the constant roughness model suits better to

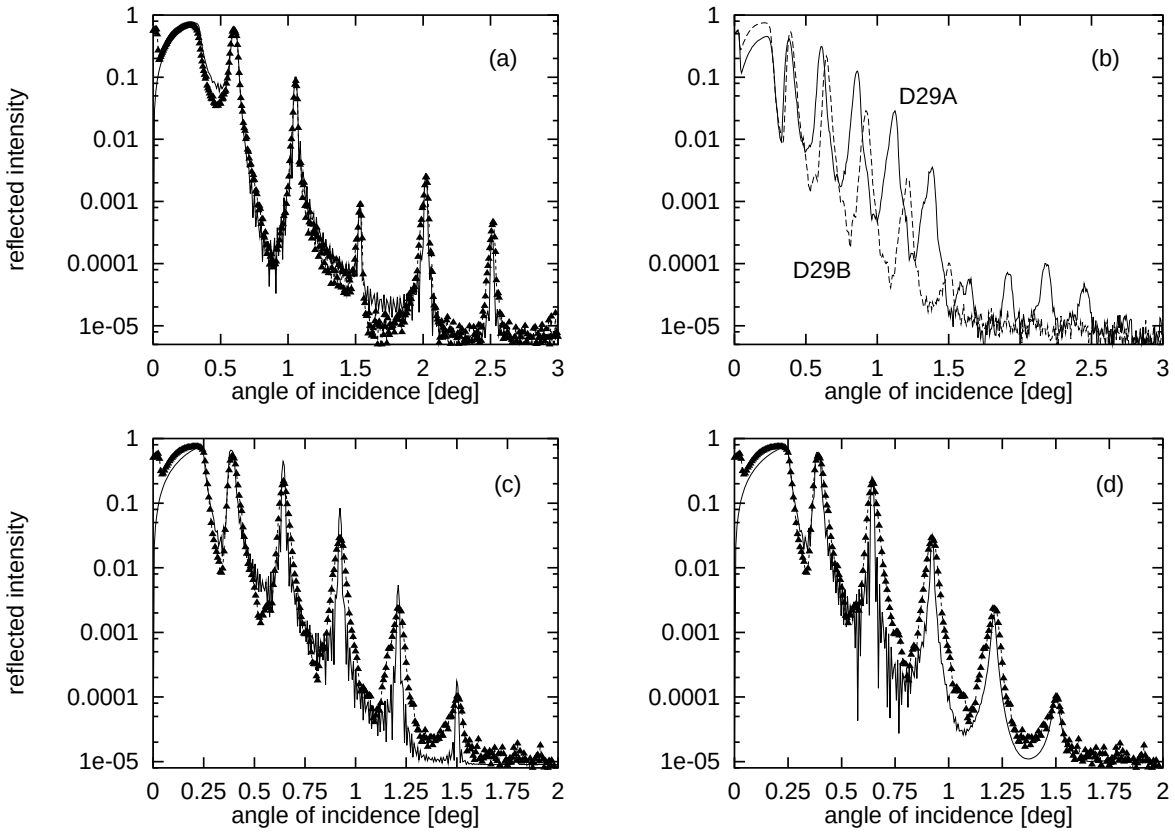

Figure 4.8. Measurements (points) and fits (full and dashed curves) of the specular reflectivity curves of the Nb/Si samples. (a) measurement and fit of the sample D0B, (b) comparison of the measurements on samples D29A and D29B. Fit of the experimental curves of the sample D29B using constant roughness (c) and increasing roughness (d) models.

this sample. The samples D29A and D29B had the same nominal Nb and Si layer thicknesses. The sample D29A is grown on a 500 Å thick Al layer and sample D29B on a 2000 Å thick layer. The comparison of the measured curves (b) shows that the period of oscillations of the sample D29B is greater than that of the other sample, thus applying the reciprocity between the real and the reciprocal (or angular) space, the period of the sample D29A is larger.

Further, the Bragg peaks of sample B are diminished after the 5th peak which expresses a big roughness introduced by the thick Al layer. Figures (c) and (d) show fits using the constant and increasing roughness models, respectively. In the case of the constant roughness model (c), all the Bragg multilayer peaks are of the same width which do not correspond to the observed situation. In the model of increasing roughness the interference in layers near the vacuum is diminished with respect to the deeper interfaces. This effect changes the peak widths and it explains well most satellites.

4.5 Incoherent scattering: Distorted-wave Born approximation calculation

In the previous sections we have calculated the specularly reflected intensity from a multilayer with rough interfaces. For the calculation we used both the dynamical and kinematical theories. In the former case, we calculated the specular reflectivity amplitude by the matrix formalism of the reflectivity from planar MLs and we averaged it over the random interface profile. A similar averaging has been used in the kinematical theory as well.

A randomly rough interface reflects the incident intensity into all directions thus producing *diffuse* or *incoherent scattering*. Calculation of the scattered wavefield is possible by both

the dynamical and kinematical theories. The dynamical theory is applied mainly in classical optics [BS63] or in the scattering of radio waves [AK83]. The Maxwell equations were used to calculate the scattering from a multilayer with slightly rough interfaces in [BW70, Ste89] or liquid surfaces [DB92b], and the solutions have been reduced to single-scattering formulae. The Born approximation of the kinematical theory has been applied as well [WB88, PSKL93]. However, this does not cover the dynamical effects, and thus it is not possible to cover the many important features found in X-ray non-specular scattering, like the enhancement of diffuse scattering near the critical angle (Yoneda wings [Yon63]) due to refraction, or resonant diffuse scattering [HB94] due to multiple scattering.

The distorted-wave Born approximation (DWBA) has been found a good compromise between the kinematical and dynamical theories which well explains most dynamical effects encountered in diffuse scattering and makes it easy to take the statistics of randomly rough interfaces into account. This scattering theory is known from quantum mechanics [Sch68, Dav69]. It has been first applied to X-ray scattering for the calculation of grazing-incidence X-ray diffraction [Vin82]. Then it was used in the calculation of X-ray reflectivity, both specular and diffuse: for a substrate with rough surface by Sinha *et al.* [SSGS88], the generalization to layered samples follow soon by Holý *et al.* [HKO$^+$93]. Then this method has been developed to scattering from multilayers with correlated interfaces [HB94, dBLW95] which explained the modulations on the diffuse scans found experimentally [Kor91]. Further it has been employed for the reflectivity from liquid surfaces [SSHO92], organic multilayers and Langmuir-Blodgett films [DB92b, PBMM94] or in neutron reflectometry [Pyn92]. Higher-order DWBA has been formulated as well. The second-order corrections have shown dependence of the diminution factor of the specular reflectivity on the lateral correlation length [dB94, dB95]. DWBA is also used for the calculation of the non-coplanar diffuse scattering measured in the new out-of-plane experimental mode [SMP94, SMPJ94].

4.5.1 Distorted-wave Born approximation

The formulation of the DWBA comes from quantum mechanics, where the scattering process is described by the differential cross-section [Dav69]. The cross-section stands for the probability of the transition between two states (incoming and outgoing wavefields). The intensity reflected by the sample is given by its integration over the acceptance window of the detector. The main advantage of the DWBA is that it can provide an approximate relation for the scattering cross-section instead of solving the wave equation exactly.

We treat scattering from a multilayer with rough interfaces as a system represented by the wave equation (3.12) in the form used already in the kinematical theory (3.91)

$$(\Delta + K^2)\, E(\boldsymbol{r}) = V(\boldsymbol{r})\, E(\boldsymbol{r}) \; . \tag{4.40}$$

The multilayer potential is according to (3.93)

$$V(\boldsymbol{r}) = K^2(1 - n^2(\boldsymbol{r})) = -K^2\chi(\boldsymbol{r}) \tag{4.41}$$

and it is random due to the interface imperfections. The scattering cross-section from the incident wave into an eigenstate of the former wave equation

$$\left(\frac{d\sigma}{d\Omega}\right) = \frac{\left\langle |T_{12}|^2 \right\rangle_{\mathrm{av}}}{16\pi^2} \tag{4.42}$$

is given in terms of the scattering matrix element T_{12}, which depends on the scattering potential $V(\boldsymbol{r})$ [Dav69]. Because of its randomness, the square of the modulus of the matrix element T_{12}

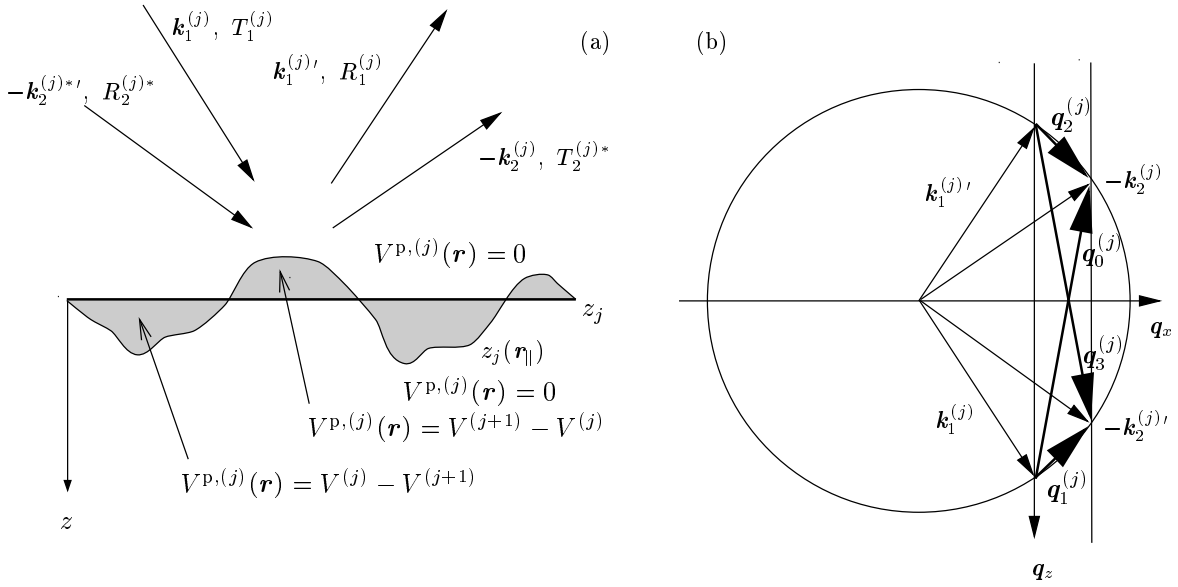

Figure 4.9. Definition of the perturbing potential $V^{\mathrm{p},(j)}$ and of the wave vectors $\boldsymbol{k}_1, \boldsymbol{k}_1', \boldsymbol{k}_2, \boldsymbol{k}_2'$ in both the real (a) and reciprocal (b) spaces. Four scattering processes encountered in the DWBA of the first order are characterized by the wave vector transfers $\boldsymbol{q}_0 = -\boldsymbol{k}_2 - \boldsymbol{k}_1$ (process T_1T_2), $\boldsymbol{q}_1 = -\boldsymbol{k}_2' - \boldsymbol{k}_1$ (T_1T_2), $\boldsymbol{q}_2 = -\boldsymbol{k}_2 - \boldsymbol{k}_1'$ (T_1T_2), $\boldsymbol{q}_3 = -\boldsymbol{k}_2' - \boldsymbol{k}_1'$ (R_1R_2) (layer indices were omitted for brevity).

has to be statistically averaged and the cross section separates into the coherent and incoherent parts [SSGS88]

$$\left(\frac{d\sigma}{d\Omega}\right) = \left(\frac{d\sigma}{d\Omega}\right)_C + \left(\frac{d\sigma}{d\Omega}\right)_I \tag{4.43}$$

$$\left(\frac{d\sigma}{d\Omega}\right)_C = \frac{|\langle T_{12}\rangle_{\mathrm{av}}|^2}{16\pi^2} \tag{4.44}$$

$$\left(\frac{d\sigma}{d\Omega}\right)_I = \frac{\left\langle \left| T_{12} - \langle T_{12}\rangle_{\mathrm{av}} \right|^2 \right\rangle_{\mathrm{av}}}{16\pi^2} = \frac{\mathcal{V}(T_{12})}{16\pi^2} \ . \tag{4.45}$$

We have defined the covariance of random quantities a, b

$$\mathcal{V}(a) \equiv \langle |a|^2\rangle_{\mathrm{av}} - |\langle a\rangle_{\mathrm{av}}|^2 \tag{4.46}$$

$$\mathcal{V}(a,b) \equiv \langle ab^*\rangle_{\mathrm{av}} - \langle a\rangle_{\mathrm{av}}\langle b^*\rangle_{\mathrm{av}} \ . \tag{4.47}$$

Therefore there are two main steps in the calculation of the cross-section. Firstly, the matrix element T_{12} has to be formed and then its statistical average and covariance have to be evaluated.

The distorted-wave Born approximation is a perturbation theory that approximates the scattering matrix element T_{12} of a system in the case when its potential $V(\boldsymbol{r})$ can be considered as a superposition of two components

$$V(\boldsymbol{r}) = V^{\mathrm{id}}(\boldsymbol{r}) + V^{\mathrm{p}}(\boldsymbol{r}) \ . \tag{4.48}$$

The ideal potential V^{id} acts as a "strong" potential, while the potential V^{p} is a weak perturbation. In the studied case of multilayers with rough interfaces, we choose V^{id} to be the potential of an ideal multilayer with perfectly flat interfaces with V^{p} being the perturbation due to the real interface profiles, see Fig. 4.9.

The ideal multilayer with V^{id} constant in each layer is described by the wave equation

$$(\Delta + K^2)E^{\mathrm{id}}(\boldsymbol{r}) = V^{\mathrm{id}}(\boldsymbol{r})E^{\mathrm{id}}(\boldsymbol{r}) \ , \tag{4.49}$$

which can be solved exactly (Sec. 3.4.4). Let us choose this ideal multilayer as the undisturbed system and employe its plane wave solutions as the eigenstates of the DWBA [SSGS88, HKO+93]. We work with the following two independent eigenstates 1, 2 of the wave equation

$$\begin{aligned} E_1^{\mathrm{id}}(\boldsymbol{r}) &= |E_1^{\mathrm{id}}\rangle = e^{i\boldsymbol{k}_{1\parallel}\boldsymbol{r}_\parallel}\left[T_1^{(j)}e^{ik_{1,z}^{(j)}(z-z_{j+1})} + R_1^{(j)}e^{-ik_{1,z}^{(j)}(z-z_{j+1})}\right] \\ E_2^{\mathrm{id}}(\boldsymbol{r}) &= \left(\langle E_2^{\mathrm{id}}|\right)^* = e^{-i\boldsymbol{k}_{2\parallel}\boldsymbol{r}_\parallel}\left[T_2^{(j)*}e^{-ik_{2,z}^{(j)*}(z-z_{j+1})} + R_2^{(j)*}e^{ik_{2,z}^{(j)*}(z-z_{j+1})}\right] . \end{aligned} \tag{4.50}$$

The eigenstate E_1^{id} is the state of the true incoming wave, Fig. 4.10. The second eigenstate E_2^{id} is chosen to be time-inverted, i.e., the primary wave with unit amplitude is emitted by the multilayer and the reflected wave is the wave incoming on it.

As we can see, each eigenstate is a superposition of two plane waves, whose particular wave vectors are

$$\begin{aligned} \boldsymbol{k}_1^{(j)} &= (\boldsymbol{k}_{1\parallel}, k_{1z}^{(j)}) \qquad \boldsymbol{k}_1^{(j)\prime} = (\boldsymbol{k}_{1\parallel}, -k_{1z}^{(j)}) \\ \boldsymbol{k}_2^{(j)} &= (\boldsymbol{k}_{2\parallel}, k_{2z}^{(j)}) \qquad \boldsymbol{k}_2^{(j)\prime} = (\boldsymbol{k}_{2\parallel}, -k_{2z}^{(j)}) . \end{aligned} \tag{4.51}$$

The parallel components are opposite and $k_{1z} > 0, k_{2z} > 0$, Fig. 4.10. An equivalent form to Eq. (4.50) is

$$\begin{aligned} |E_1^{\mathrm{id}}\rangle &= e^{i\boldsymbol{k}_1^{(j)}\boldsymbol{r}}\,T_1^{(j)}e^{-ik_{1,z}^{(j)}z_{j+1}} + e^{i\boldsymbol{k}_1^{(j)\prime}\boldsymbol{r}}\,R_1^{(j)}e^{ik_{1,z}^{(j)}z_{j+1}} \\ \langle E_2^{\mathrm{id}}| &= e^{i\boldsymbol{k}_2^{(j)}\boldsymbol{r}}\,T_2^{(j)}e^{-ik_{2,z}^{(j)}z_{j+1}} + e^{i\boldsymbol{k}_2^{(j)\prime}\boldsymbol{r}}\,R_2^{(j)}e^{ik_{2,z}^{(j)}z_{j+1}} . \end{aligned} \tag{4.52}$$

The amplitudes $T_{1,2}^{(j)}, R_{1,2}^{(j)}$ of the transmitted and the reflected beams, respectively, for the states 1 and 2, are calculated with respect to the bottom layer interfaces, Sec. 3.4.4.

Let us further denote the incoming plane wave

$$E_0(\boldsymbol{r}) = e^{i\boldsymbol{K}_0\boldsymbol{r}} . \tag{4.53}$$

The DWBA approximates the matrix element by [Sch68, SSGS88]

$$T_{12} = \langle E_2^{\mathrm{id}}|V^{\mathrm{id}}|E_0\rangle + \langle E_2^{\mathrm{id}}|V^{\mathrm{p}}|E_1^{\mathrm{id}}\rangle . \tag{4.54}$$

Therefore the calculation of the cross sections (4.44)–(4.45) requires the evaluation of the coherent and incoherent terms

$$\langle T_{12}\rangle_{\mathrm{av}} = \langle E_2^{\mathrm{id}}|V^{\mathrm{id}}|E_0\rangle + \left\langle \langle E_2^{\mathrm{id}}|V^{\mathrm{p}}|E_1^{\mathrm{id}}\rangle \right\rangle_{\mathrm{av}} \tag{4.55}$$

$$\mathcal{V}(T_{12}) = \mathcal{V}\left(\langle E_2^{\mathrm{id}}|V^{\mathrm{p}}|E_1^{\mathrm{id}}\rangle\right) . \tag{4.56}$$

This we will treat separately in the following two subsections, whereas now we express the matrix element $\langle E_2^{\mathrm{id}}|V^{\mathrm{p}}|E_1^{\mathrm{id}}\rangle$.

We can see that the perturbation potential is non-zero only near the interfaces (Fig. 4.9)

$$V^{\mathrm{p},(j)}(\boldsymbol{r}) = \begin{cases} 0 & \text{for } z < z_j(\boldsymbol{r}_\parallel) < z_j \text{ and } z_j < z_j(\boldsymbol{r}_\parallel) < z , \\ V^{(j+1)} - V^{(j)} & \text{for } z_j(\boldsymbol{r}_\parallel) < z < z_j , \\ V^{(j)} - V^{(j+1)} & \text{for } z_j(\boldsymbol{r}_\parallel) > z > z_j . \end{cases} \tag{4.57}$$

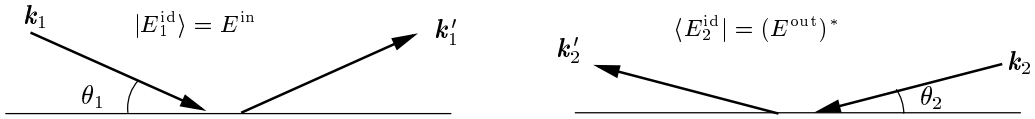

Figure 4.10. Schematic drawing of the eigenstates corresponding to the incoming and outgoing wavefields.

Thus we can decompose the perturbation over individual interfaces [HB94]

$$\langle E_2^{\mathrm{id}}|V^{\mathrm{id}}|E_1^{\mathrm{id}}\rangle = \sum_{j=1}^{N} \langle E_2^{\mathrm{id}}|V^{\mathrm{p},(j)}|E_1^{\mathrm{id}}\rangle \equiv \sum_{j=1}^{N} W_j \ . \tag{4.58}$$

Let us calculate the contribution W_j of the rough interface j. We employ the approximation [SSGS88] of replacing $E^{\mathrm{id},(j+1)}$ by $E^{\mathrm{id},(j)}$ in the region $z_j(\boldsymbol{r}_\parallel) \le z \le z_j$ and $E^{\mathrm{id},(j)}$ by $E^{\mathrm{id},(j+1)}$ in the region $z_j \le z \le z_j(\boldsymbol{r}_\parallel)$. Then

$$\begin{aligned} W_j \equiv &\langle E_2^{\mathrm{id}}|V^{\mathrm{p},(j)}|E_1^{\mathrm{id}}\rangle = \left(V^{\mathrm{p},(j)} - V^{\mathrm{p},(j+1)}\right) \times \\ &\Big[T_1^{(j)}T_2^{(j)}\mathcal{F}_-^{(j)}(-\boldsymbol{q}_0^{(j)}) + R_1^{(j)}R_2^{(j)}\mathcal{F}_-^{(j)}(-\boldsymbol{q}_3^{(j)}) + \\ &\quad T_1^{(j)}R_2^{(j)}\mathcal{F}_-^{(j)}(-\boldsymbol{q}_1^{(j)}) + R_1^{(j)}T_2^{(j)}\mathcal{F}_-^{(j)}(-\boldsymbol{q}_2^{(j)}) + \\ &T_1^{(j+1)}T_2^{(j+1)}\mathcal{F}_+^{(j)}(-\boldsymbol{q}_0^{(j+1)}) + R_1^{(j+1)}R_2^{(j+1)}\mathcal{F}_+^{(j)}(-\boldsymbol{q}_3^{(j+1)}) + \\ &\quad T_1^{(j+1)}R_2^{(j+1)}\mathcal{F}_+^{(j)}(-\boldsymbol{q}_1^{(j+1)}) + R_1^{(j+1)}T_2^{(j+1)}\mathcal{F}_+^{(j)}(-\boldsymbol{q}_2^{(j+1)})\Big] \ , \end{aligned} \tag{4.59}$$

where the Fourier transform of "hills" on particular sides is

$$\begin{aligned} \mathcal{F}_\pm^{(j)}(\boldsymbol{q}) &= \iint_S d\boldsymbol{r}_\parallel \int_0^{U_j(\boldsymbol{r}_\parallel)} dU\, e^{-i\boldsymbol{q}(\boldsymbol{r}_\parallel + U\hat{\boldsymbol{z}})}\ H\big(\pm U_j(\boldsymbol{r}_\parallel)\big) \\ &= \iint_S d\boldsymbol{r}_\parallel\, e^{-i\boldsymbol{q}_\parallel \boldsymbol{r}_\parallel}\ \frac{e^{-iq_z U}-1}{-iq_z}\ H\big(\pm U_j(\boldsymbol{r}_\parallel)\big) \ . \end{aligned} \tag{4.60}$$

Since both eigenstates consist of two plane waves, their matrix element for V^{p} decomposes into four terms containing T_1T_1, T_1R_2, R_1T_2 and R_1R_2 (Fig. 4.9). These are the four particular scattering processes with wave vector transfers $\boldsymbol{q}_l^{(j)} = (-\boldsymbol{k}_{2\parallel} - \boldsymbol{k}_{1\parallel}, q_{zl}^{(j)})$:

$$\begin{aligned} T_1T_2:\ \boldsymbol{q}_0^{(j)} &= -(\boldsymbol{k}_2^{(j)} + \boldsymbol{k}_1^{(j)}) & R_1R_2:\ \boldsymbol{q}_3^{(j)} &= -(\boldsymbol{k}_2^{(j)\prime} + \boldsymbol{k}_1^{(j)\prime}) \\ q_{0z}^{(j)} &= -q_{3z}^{(j)} = -(k_{2z}^{(j)} + k_{1z}^{(j)}) & & \\ T_1R_2:\ \boldsymbol{q}_1^{(j)} &= -(\boldsymbol{k}_2^{(j)\prime} + \boldsymbol{k}_1^{(j)}) & R_1T_2:\ \boldsymbol{q}_2^{(j)} &= -(\boldsymbol{k}_2^{(j)} + \boldsymbol{k}_1^{(j)\prime}) \\ q_{1z}^{(j)} &= -q_{2z}^{(j)} = -(k_{1z}^{(j)} - k_{2z}^{(j)}) \ , & & \end{aligned} \tag{4.61}$$

Note, that all the momentum transfers $\boldsymbol{q}_l^{(j)}$ have the same lateral component $\boldsymbol{q}_{l\parallel}^{(j)}$. Further, $q_{0z}^{(j)}$ is negative, i.e., it corresponds to the wave emerging from the layer towards the vacuum.

4.5.2 Calculation of the coherent reflectivity

The matrix element of the coherently scattered wave consists of two terms (4.55). The calculation of the first term, which describes the scattering of the vacuum plane wave by the potential of an ideal multilayer, is straightforward [SSGS88]

$$\langle E_2^{\mathrm{id}}|V^{\mathrm{id}}|E_0\rangle = 2iK_z R^{\mathrm{id}}(\boldsymbol{k}_1)\, S\, \delta_{\boldsymbol{K}_{2\parallel},\boldsymbol{K}_{0\parallel}} \ . \tag{4.62}$$

The delta function expresses the reflection law (Sec. 3.4.1). We have denoted the sample area $S = L_xL_y$, where L_x, L_y are the lateral sample dimensions. From this the amplitude of the specularly reflected wave follows

$$R = R^{\mathrm{id}} + \Big\langle \langle E_2^{\mathrm{id}}|V^{\mathrm{p}}|E_1^{\mathrm{id}}\rangle \Big\rangle_{\mathrm{av}} / 2iK_zS \ . \tag{4.63}$$

Since the reflection law holds in the specular scan, then $\boldsymbol{k}_1 = -\boldsymbol{k}_2'$, $\boldsymbol{k}_1' = -\boldsymbol{k}_2$ and thus $q_{0z} = -q_{3z} = -2k_z$, $q_{1z} = q_{2z} = 0$, and $T_1 = T_2$, $R_1 = R_2$. The perturbation matrix

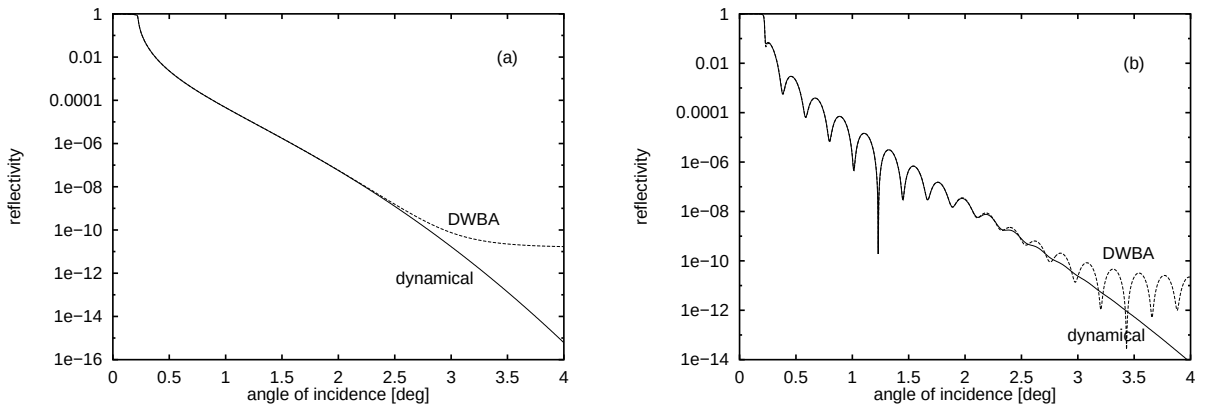

Figure 4.11. Comparison of dynamical and DWBA calculations of the specular reflectivity curves. (a) Si substrate with 8 Å surface roughness, (b) C/Si single-layer system with 10 Å/7 Å roughnesses.

element $\left\langle\langle E_2^{\rm id}|V^{\rm p}|E_1^{\rm id}\rangle\right\rangle_{\rm av}$ is calculated by averaging the relation (4.58). Terms $\langle W_j\rangle_{\rm av}$ contain the averaged Fourier transform (4.60)

$$\left\langle \mathcal{F}_\pm^{(j)}(\boldsymbol{q})\right\rangle_{\rm av} = \iint\limits_S d\boldsymbol{r}_\parallel\, e^{-i\boldsymbol{q}_\parallel \boldsymbol{r}_\parallel} \int\limits_0^\infty dU\, w_j(U)\, \frac{e^{-iq_zU}-1}{-iq_z}\, H(\pm U_j(\boldsymbol{r}_\parallel))\ . \tag{4.64}$$

The result can be written in the form [SSGS88, HKO$^+$93]

$$\left\langle \mathcal{F}_\pm^{(j)}(0)\right\rangle_{\rm av} = \mu_\pm^j\, S\, \delta_{\boldsymbol{q},0} \tag{4.65}$$

$$\left\langle \mathcal{F}_\pm^{(j)}(\boldsymbol{q})\right\rangle_{\rm av} = \frac{i}{q_z}\left[\tilde{U}_\pm^j(q_z)-\frac{1}{2}\right] S\, \delta_{\boldsymbol{q}_\parallel,0}\ , \tag{4.66}$$

where $\mu_\pm^j$ is the averaged roughness displacement on a particular side of the interface. We have defined the partial Fourier transform

$$\tilde{U}_\pm^j(q_z) = \int_{-\infty}^{\infty} dU\, e^{-iq_zU}\, w_j(U)\, H(\pm U)\ . \tag{4.67}$$

The Heaviside function has been defined on page 41.

Since we mostly work with symmetric probability distribution functions, $w(U) = w(-U)$, then $\tilde{U}_+(q_z) = \tilde{U}_-(-q_z)$. For gaussian $w(U)$ the numerical calculation of this Fourier transform is efficiently performed by the help of the Dyson function.[3]

Finally, the reflectivity amplitude of a multilayer with rough interfaces is explicitly written [HKO$^+$93]

$$\begin{aligned} R_C = R^{\rm id} + \frac{K^2}{q_z^1}\sum_{j=1}^{N}(n_j^2-n_{j+1}^2)\Big\{ &-2i\mu^j\left(T_1^{(j)}R_1^{(j)}+T_1^{(j+1)}R_1^{(j+1)}\right)\\ &+\left[(T_1^{(j)})^2U_+^{(j)}(q_z^{(j)})-(R_1^{(j)})^2U_+^{(j)*}(q_z^{(j)})\right]/q_z^{(j)}\\ &+\left[(T_1^{(j+1)})^2U_+^{(j)}(q_z^{(j+1)})-(R_1^{(j+1)})^2U_+^{(j)*}(q_z^{(j+1)})\right]/q_z^{(j+1)}\Big\}\ . \end{aligned} \tag{4.68}$$

Reflectivity curves calculated by this formula for a single surface and a single-layered system are shown in Fig. 4.11. We have compared these curves with the dynamical calculation (Sec. 4.3.1). We can see that the coincidence of both dependencies is good up to a certain angle.

[3] The Dyson function is defined by $w_D(z) = \frac{2}{\sqrt{\pi}}\int_0^\infty dz\ e^{-z^2+2icz}$. Precise rational approximation of this function can be found in mathematical tables [GR63].

For larger angles of incidence DWBA fails, since the actual wavefield in the rough multilayer differs substantially from that within the ideal layer the eigenstates of which have been used in the approximation of the matrix element.

4.5.3 Diffuse scattering

The cross section of the incoherent diffuse scattering is given by (4.45) so that the calculation of the covariance $\mathcal{V}(T^{\mathrm{p}})$ has to be performed. Using the properties of the covariance[4] we get

$$\mathcal{V}(T^{\mathrm{p}}) = \mathcal{V}\left(\sum_{j=1}^{N} W_j\right) = \sum_{j=1}^{N} \mathcal{V}(W_j) + \sum_{j>k} 2\,\mathrm{Re}\;\mathcal{V}(W_j, W_k)\ . \tag{4.69}$$

Recalling the definition $W_j = \langle E_2^{\mathrm{id}} | V^{\mathrm{p}} | E_1^{\mathrm{id}} \rangle$ we find that the diffuse scattering has two main components. The first one is the diffuse scattering created by the roughness of single interfaces and it is expressed by the first sum in the above equation. The correlation between different interfaces leads to non-zero covariancies and it gives rise to the second component of the diffuse scattering.

The form of W_j is given by Eq. (4.59), therefore it includes the covariancies

$$\begin{aligned} Q_{mn}^{jk} &\equiv Q^{jk}(\boldsymbol{q}_m^{(j+1)}, \boldsymbol{q}_n^{(k+1)}) \equiv \mathcal{V}\left(\mathcal{F}_{\pm}^{(j)}(\boldsymbol{q}_m^{(j+1)}), \mathcal{F}_{\pm}^{(k)}(\boldsymbol{q}_n^{(k+1)})\right) \\ &= \frac{S}{q_{mz}^{(j+1)} q_{nz}^{(k+1)*}} \iint d\boldsymbol{R}\, e^{-i\boldsymbol{q}_{\parallel}\boldsymbol{R}}\ \mathcal{V}\left(e^{-iq_{mz}^{(j+1)}U_j(0)}, e^{-iq_{nz}^{(k+1)}U_k(\boldsymbol{R})}\right)\ . \end{aligned} \tag{4.70}$$

The indices j, k enumerate the interfaces, m, n count the scattering processes $0 \ldots 3$. Supposing the gaussian pair probability function (4.12), this turns into

$$Q_{mn}^{jk} = \frac{S}{q_{mz}^{(j+1)} q_{nz}^{(k+1)*}}\ e^{-\frac{1}{2}[q_{mz}^2\sigma_j^2 + q_{nz}^{*2}\sigma_k^2]} \iint d\boldsymbol{R}\, e^{-i\boldsymbol{q}_{\parallel}\boldsymbol{R}} \left(e^{q_{mz}^{(j+1)} q_{nz}^{(k+1)^*} C_{jk}(\boldsymbol{R})} - 1\right) \tag{4.71}$$

Our experiments are performed without resolution in the $\hat{\boldsymbol{y}}$ direction (the detector or slit window is long in this direction). The cross section is integrated over the $\hat{\boldsymbol{y}}$ direction and we use

$$\int dy\, Q_{mn}^{jk} = \frac{2\pi S}{q_{mz}^{(j+1)} q_{nz}^{(k+1)*}}\ e^{-\frac{1}{2}[q_{mz}^2\sigma_j^2 + q_{nz}^{*2}\sigma_k^2]} \int dx\, e^{-iq_x x} \left(e^{q_{mz}^{(j+1)} q_{nz}^{(k+1)^*} C_{jk}(x)} - 1\right)\ . \tag{4.72}$$

The amount of necessary calculation can be reduced by help of the following properties. Firstly, $Q_{mn}^{jk} = Q_{mn}^{kj\,*}$. The Q_{mm}^{jj} are real. Further, for a single interface $j{=}k$ it holds $Q_{00}^{j} = Q_{33}^{j}$, $Q_{03}^{j} = Q_{30}^{j}$, $Q_{11}^{j} = Q_{22}^{j}$, $Q_{12}^{j} = Q_{21}^{j}$, $Q_{01}^{j} = Q_{32}^{j} = Q_{10}^{j*} = Q_{23}^{j*}$, $Q_{02}^{j} = Q_{31}^{j} = Q_{20}^{j*} = Q_{13}^{j*}$. For different interfaces $j \neq k$ we can find $Q_{00}^{jk} = Q_{33}^{jk}$, $Q_{03}^{jk} = Q_{30}^{jk}$, $Q_{11}^{jk} = Q_{22}^{jk}$, $Q_{12}^{jk} = Q_{21}^{jk}$, $Q_{10}^{jk} = Q_{23}^{jk}$, $Q_{01}^{jk} = Q_{32}^{jk}$, $Q_{02}^{jk} = Q_{31}^{jk}$, $Q_{20}^{jk} = Q_{13}^{jk}$.

The final formula for the covariance of a multilayer with uncorrelated rough interfaces reads

$$\begin{aligned} \mathcal{V}(W_j) =& K^4 \left|n_j^2 - n_{j+1}^2\right|^2 \Big\{ \\ & Q_{00}^{j}\left[|T_1T_2|^2 + |R_1R_2|^2\right] + Q_{11}^{j}\left[|R_1T_2|^2 + |T_1R_2|^2\right] + \\ & 2\,\mathrm{Re}\Big\{ Q_{01}^{j}\left[T_1T_2(T_1R_2)^* + R_1R_2(T_2R_1)^*\right] + Q_{02}^{j}\left[T_1T_2(T_2R_1)^* + R_1R_2(T_1R_2)^*\right] + \\ & Q_{03}^{j}\, T_1T_2(R_1R_2)^* + Q_{12}^{j}\, T_1R_2(T_2R_1)^* \Big\}\Big\}\ . \end{aligned} \tag{4.73}$$

[4] Namely $\mathcal{V}(a+b) = \mathcal{V}(a) + \mathcal{V}(b) + \mathcal{V}(a,b)$.

The upperscript of all T and R are j in the "upper"-hill approximation, $j+1$ in the "down"-hill approximation.

The calculation of the term $\sum_{j\neq k} \mathcal{V}(W_j, W_k)$ that is added in the case of correlated roughness is straightforward and it will not be shown here. It has been published for the first time in [HB94] and the detailed discussion can be found in [HBB95, Hol96].

The numerical evaluation of the integral (4.72) has to be treated carefully, since it is a Fourier transform of an oscillating and decreasing complex function. Its convergence depends considerably on the fractal coefficient h, Eq. (4.11). For two values of h, namely $h = 1$ (the gaussian profile) and $h = 0.5$, the exponential can be developed into a Taylor series and integrated analytically. For other values of h the integral has to be calculated by an adequate numerical method, where the combination of the Filon and Simpson methods [GR63] was found to be the most satisfactory.

Finally, we relate the formula for the cross-section to the measured intensity [HKO+93]

$$I(\theta_1, \theta_2) = I_{\text{inc}} \left[\int\limits_{\text{detector slit}} \left(\frac{d\sigma}{d\Omega} \right)_I d\Omega + F(\theta_1, \theta_2)\, R_{\text{spec}}(\theta_1) \right] . \tag{4.74}$$

The integration of the incoherent contribution ranges over the angular acceptance of the detector (see page 62) in the plane of incidence, and over the slit size in the $\hat{\boldsymbol{y}}$ direction with the relation (4.72) replacing (4.71). The function $F(\theta_1, \theta_2)$ describes the transmission of the coherent part of the beam into the detector staying near the specular beam. Therefore this is a trapezoidal function given by the convolution of the shape functions of the incoming beam and of the detector slit. Then

$$I(\theta_1, \theta_2) = I_{\text{inc}} \left[\frac{2\theta_D \min(L_y/L_{y,\text{beam}}, 1)}{K \max(\sin\theta_1, \omega_F)} \int dq_y \left(\frac{d\sigma(\theta_1, \theta_2)}{d\Omega} \right)_I + F(\theta_1, \theta_2)\, R_{\text{spec}}(\theta_1) \right] , \tag{4.75}$$

where ω_F is the cover angle (4.37).

The structure of the relation (4.73) seems to be quite complicated. It can be simplified if the reflectivity amplitudes R_1, R_2 are small. Then the prevailing term is that proportional to the product of the transmission function $|T_1 T_2|$ and

$$\mathcal{V}(W_j) \approx K^4 \left| n_j^2 - n_{j+1}^2 \right|^2 |T_1 T_2|^2\, Q_{00}^j . \tag{4.76}$$

Another approximation which is found adequate in the case of small roughness develops the exponential term in (4.72) into a Taylor series. Combining both approximations, we get the final formula of the covariance in the semi-kinematical approximation [SSGS88]

$$\mathcal{V}(W_j) \approx 2\pi S\; K^4 \left| n_j^2 - n_{j+1}^2 \right|^2 \left| T_1^{(j)} T_2^{(j)} \right|^2 e^{-(q_{0z}^{(j)})^2 \sigma_j^2} \int dx\, e^{-iq_x x}\, C_j(x) . \tag{4.77}$$

From this formula we can see that the diffuse intensity is proportional to the transmission function given by the product of T_1 and T_2. These transmission functions have maxima at the critical angle of total external reflection (Fig. 3.10) of the incoming and outgoing waves, respectively, which theoretically confirms the effect of the Yoneda wings found experimentally [Yon63]. Further, the scattered intensity is proportional to the Fourier transform of the correlation function $C_j(x)$ [SSGS88] as it is known in the kinematical theory of X-ray diffraction [AKK+74].

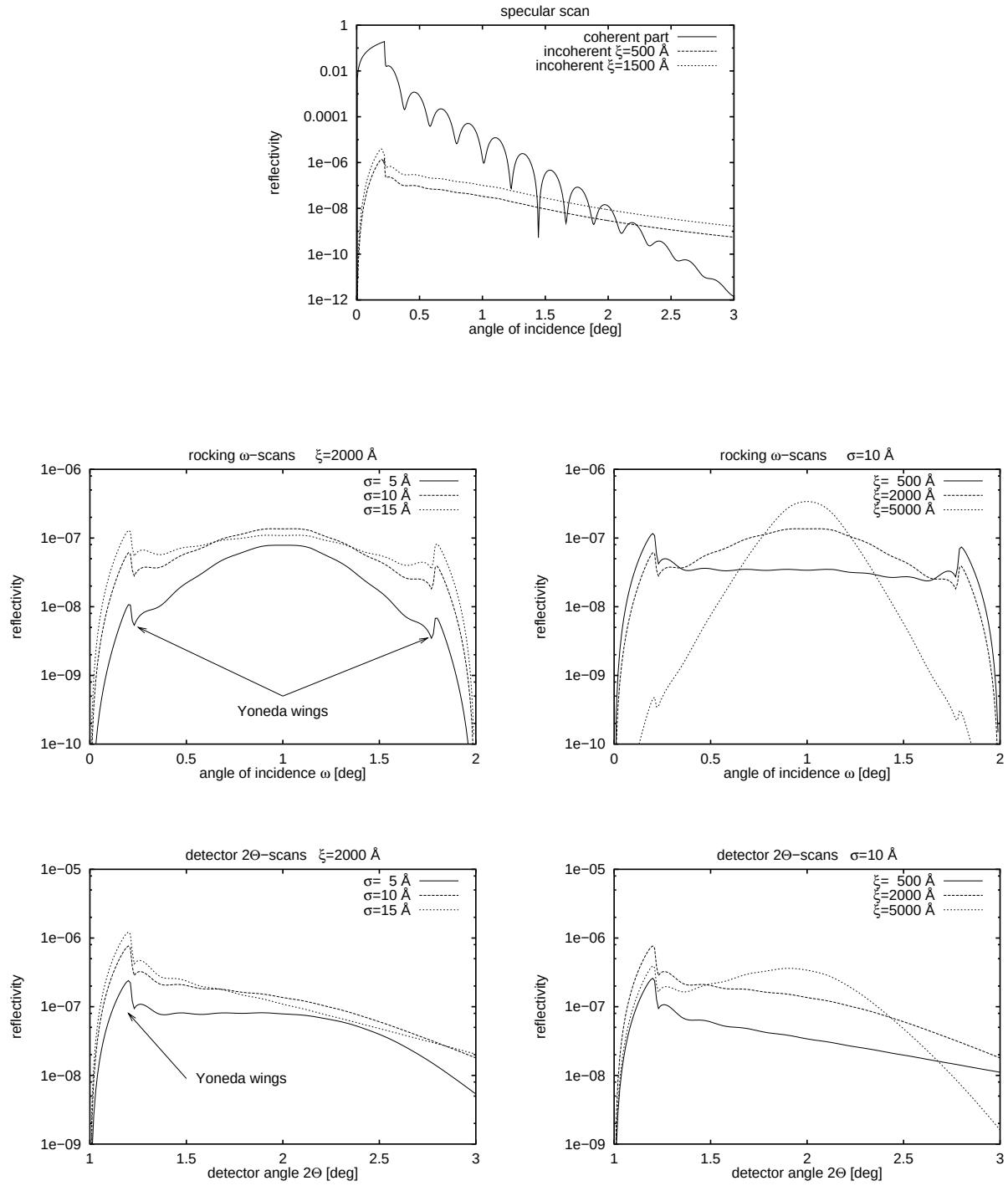

Figure 4.12. Simulations of the contribution of the diffuse scattering into the specular scan (the upper figure). Calculation of the rocking ω-scans (in the middle) and detector 2θ-scans (the lower figures) of a sample for different root mean square roughnesses and the correlation length $\xi = 2000$ Å (left) and for different lateral correlation lengths and rms roughness $\sigma = 10$ Å (right). The fractal coefficient h equals 1.

4.6 Reflectivity map of a periodic multilayer

In the previous section we worked out the theoretical treatment of specular and non-specular reflectivity from rough multilayers based on the distorted-wave Born approximation. We have shown how the interface imperfections influence the coherent specular scan and how they cause diffuse scattering, which is distributed in reciprocal space. We presented numerical simulations of the specular, rocking (ω) and detector (2θ) scans of a layered sample with uncorrelated rough interfaces. The simulations of these scans can be used to reveal the structural parameters by fitting the experimental data of a measured sample.

A good qualitative analysis comes out from the measurement of the whole reflectivity map. Therefore we present our measurement of a periodic multilayer with correlated interfaces. The sample is a periodic sequence of bilayers of Si and Nb grown $N = 10$ times on a Si substrate. A fit of the experimental data gives the bilayer period 88.5 Å and the Si/Nb thickness ratio 0.52. The high quality of the sample has been confirmed: the substrate roughness 6.7 Å is replicated by the upper interfaces and it decreases towards the free surface.

We have performed the measurement on the beamline D23 at synchrotron in LURE, Université Paris-Sud. The incoming radiation with the wavelength 1.54 Å was collimated by Si(111) double diffraction. The scattered radiation was measured by a detector installed behind a single-diffraction Ge(111) analyzing crystal. Fig. 4.13 shows both the angular and reciprocal space representation of the measured reflectivity map. Each map contains 231 ω-scans with more than 15 600 points. The maps are plotted by my program `pm3d`.

Now let us qualitatively describe the map. The bright rod at $Q_x = 0$ (or $\omega = 2\theta/2$) is the *specular scan* broadened in the Q_x-direction by the resolution function (the convolution of the finite beam with the slit width produces the function $F(\theta_1, \theta_2)$ according to (4.74)). The small intense spots on the specular scan are the *Bragg peaks* of the periodic multilayer. Less intense spots between them are the *subsidiary maxima* of the thickness oscillations.

Interface roughness gives rise to diffuse scattering, which fills the reciprocal space everywhere between the limiting Ewald spheres of the incoming and exit beams (Fig. 2.3), respectively. The correlated roughness excites the *Bragg sheets* passing through the multilayer Bragg peaks. The Bragg sheets are curved due to refraction giving them the shape and the name of "*bananas*" [HB94, HBB95].

Further, higher intensity Ewald spheres passing through each multilayer Bragg peak are distinguishable within the region of the first three Bragg sheets. This effect has a purely dynamical origin and it is explained by the concept of multiple scattering (Umweganregung) [HB94]. The spheres raise up at the maximum of either R_1 (maximum intensity of the incident transmitted plane wave) or R_2 (maximum intensity of the outgoing plane wave) in (4.73). Intense *Bragg-like peaks of resonant diffuse scattering* are found at these intersections, where both reflectivity amplitudes R_1 and R_2 are maximal.

The *Yoneda wings* [Yon63], for which the angle of incidence or exit equals the critical angle, lie on the circles inclined from the "limiting Ewald spheres" by the critical angle, thus they represent the Bragg-like peaks of the zeroth order. Since there is weak intrinsic roughness except at the substrate interface, the measurable intensity of the Yoneda wings is localized on the bananas only. The Yoneda wings corresponding to the Nb material ($\theta_C^{\mathrm{Nb}} = 0.40^\circ$) can be observed as the end-points of the bananas, whereas the Yoneda wings of the Si material ($\theta_C^{\mathrm{Si}} = 0.22^\circ$) are not resolved.

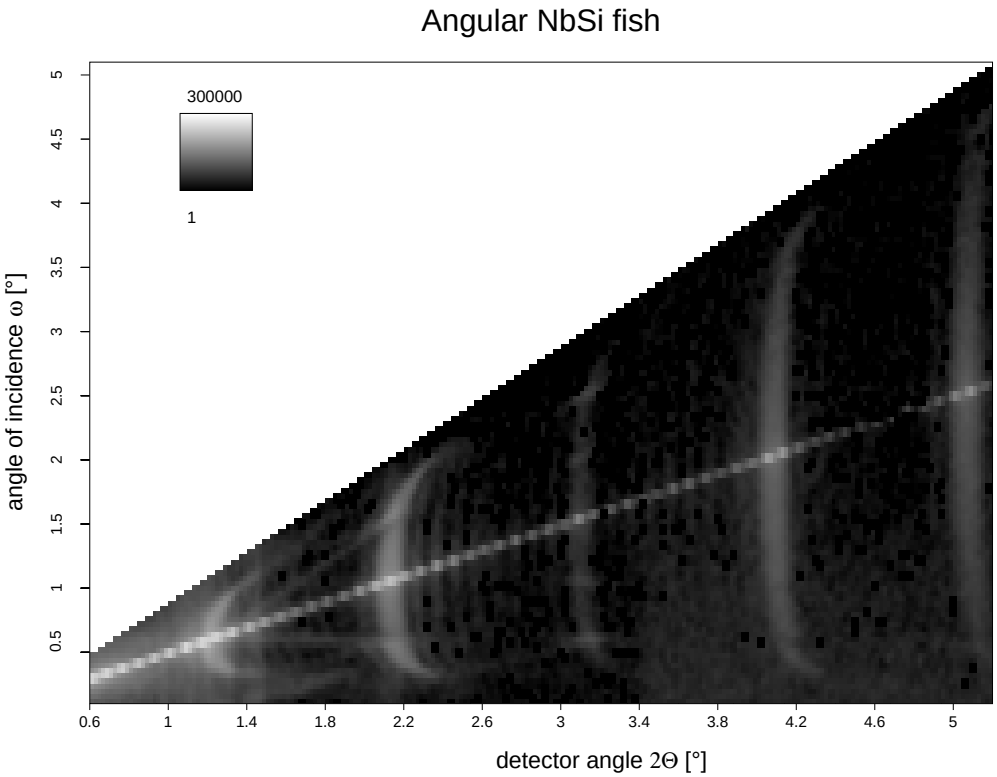

Figure 4.13. The Angular (above) and The Reciprocal (below) Space Sharks (The Reciprocal Ocean, LURE bay, Paris, 1994). X-ray fishermen have found these fishes by use of a special superlattice net and by help of the non-specular reflection of sun rays by the ocean surface. We kindly ask the reader not to touch the picture in order to avoid contamination by the diffuse scattering.

The detailed discussion and the explanation of the features we find on this measured reflectivity map is presented in Sec. 4.6.

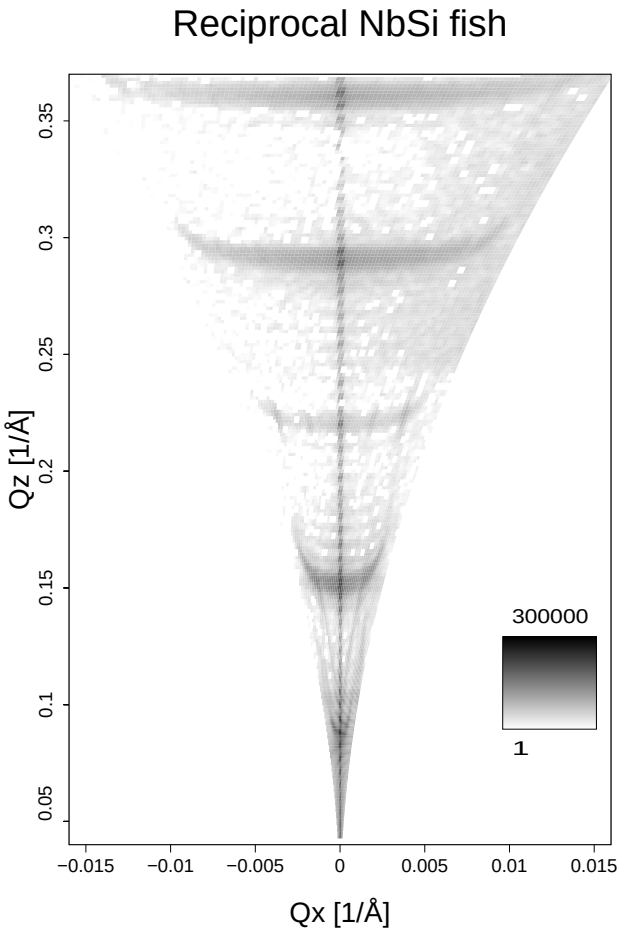

Chapter 5

X-ray reflectivity from multilayer gratings

Résumé

Dans ce chapitre nous nous intéressons à la diffusion des rayons X réfléchis sur des réseaux de multicouches (voir fig. 5.1). Ainsi, nous étudions la distribution de l'intensité diffusée au voisinage de l'origine dans l'espace réciproque pour une onde incidente rasante. La plus grande partie de ce travail concerne des réseaux latéralement périodiques. La généralisation à d'autres réseaux, avec une transformée de Fourier discrète de la structure latérale (par exemple quasipériodique), sera brièvement discutée. Par la suite nous utiliserons l'abréviation MLG (multilayer grating) à la place de "réseaux de multicouches périodiques latéralement".

Notre but est de développer plusieurs théories adaptées à ce calcul et de les comparer : la théorie cinématique, l'approximation de l'onde déformée de Born et la théorie de la diffusion dynamique. Nous indiquerons les différentes approximations qui ont été faites dans ces théories ainsi que leurs aspects communs.

La périodicité latérale uni-dimensionnelle, principale caractéristique d'un réseau de multicouches, est traitée dans ces trois théories au moyen de la transformée de Fourier de la susceptibilité. Nous résolvons l'équation d'onde dans le cas d'une périodicité latérale. Ainsi nous pouvons formuler ces théories de la même façon que celle bien connue de la diffraction des rayons X par les cristaux qui utilise, pour résoudre l'équation d'onde, l'idée similaire de la symétrie de translation tri- dimensionnelle.

Dans la première partie, nous mentionnons les publications parues sur le thème de ce chapitre. Ensuite nous traitons les caractéristiques de base des réseaux et leur réseau réciproque. Nous introduisons la notation utilisée par la suite.

Dans les paragraphes suivants, nous présentons les diverses théories en commençant par la théorie cinématique. Nous résolvons l'intégrale de diffraction cinématique par la méthode de la phase stationnaire, procédure déjà utilisée pour la réflectivité sur des multicouches planaires. La théorie cinématique ne considère que les processus à une seule diffusion et ne prend pas en compte les effets de réfraction et d'absorption. Néanmoins, les résultats obtenus montrent les principaux caractères de la diffusion par des réseaux : une onde incidente plane est dispersée en un éventail d'ondes planes. C'est un processus de diffraction, basé sur la réflexion spéculaire. Les composantes latérales des vecteurs d'onde des ondes diffusées (diffractées) diffèrent de celles de l'onde incidente par le caractère uni-dimensionnel du vecteur du réseau réciproque. Nous représentons les processus de diffusion dans l'espace réciproque au moyen de la construction d'Ewald. Nous montrons un moyen pour généraliser les coefficients cinématiques de réflexion de Fresnel.

L'approximation de l'onde déformée de Born (DWBA) sera traitée ultérieurement comme une méthode de perturbation plus élaborée. Nous avons utilisé DWBA pour le calcul de la diffusion diffuse sur des interfaces rugueuses dans des multicouches planes. On croyait jusqu'à présent que l'approximation DWBA n'était valable que dans le cas de potentiels faiblement perturbés, c'est à dire de rugosités faibles. Cependant, nous montrons que cette méthode s'applique aussi au calcul de la réflectivité sur des réseaux. Notre discussion portera essentiellement sur le domaine de validité de DWBA.

La théorie dynamique de la réflexion sur des réseaux de multicouches lamellaires a déjà été traitée par divers auteurs. Dans le paragraphe suivant, nous présentons une revue de ces travaux. Dans ce travail, nous développons une théorie dynamique de la réflexion des rayons X sur des réseaux en nous inspirant du formalisme de Darwin-Laue utilisé dans la théorie dynamique de la diffraction des rayons X par des cristaux. Notre formalisme est connu en optique ; c'est la méthode modale des valeurs propres : nous prenons comme solution à l'équation d'ondes une onde plane semblable aux ondes de Bloch à une dimension, nous résolvons la valeur propre et nous appliquons les conditions aux limites aux interfaces de MLG. Ceci sera réalisé par un

formalisme matriciel. Le principal avantage de cette présentation de notre théorie est de garder la même notation que pour la réflexion sur des multicouches planes ; ceci montre les liens existant, pour la réflectivité, entre tous les types de structures. En particulier, ce formalisme nous permet d'introduire une matrice généralisée de la matrice des coefficients de Fresnel.

Cette théorie entièrement dynamique est utilisée pour des calculs numériques. Cependant, les équations de cette théorie rigoureuse sont trop lourdes pour pouvoir être discutées de façon qualitative. Aussi, nous formulons la théorie dynamique avec des approximations de diffusion multiple. Ces approximations sont appliquées dans des régions où les effets dynamiques l'emportent. Notre approche consiste à introduire l'approximation à deux ondes, comme dans la diffraction dynamique des rayons X par les cristaux. Nous discuterons aussi le cas de la diffusion non- coplanaire quand le faisceau incident devient presque parallèle à la direction des fils des réseaux.

Dans le paragraphe suivant, nous présentons la discussion sur ces théories, les simulations numériques associées et nous les comparons sur l'exemple particulier suivant : un réseau de surface avec une largeur de fil moitié de la période (8000 Å). Nous montrons que les tiges de troncature d'ordre impair sont fortes et que la plupart des profils peuvent être expliqués par les deux théories, dynamique et DWBA. Par contre, les tiges de troncature d'ordre pair sont interdites dans toutes les théories de diffusion unique ; le calcul a besoin de tenir compte de la diffusion multiple et seulement le traitement dynamique est approprié. Nous avons fait des simulations numériques pour déterminer le nombre d'ondes nécessaire dans les approximations à ondes multiples de manière à obtenir les intensités diffusées avec une précision suffisante.

Nos théories et leur formalisme dans le cas de réseaux périodiques s'appliquent aussi bien à certains réseaux apériodiques, principalement aux réseaux dont la transformée de Fourier du profil latéral a une forme discrète. En particulier, nous étudions qualitativement la carte de réflectivité attendue pour un réseau quasi- périodique de Fibonacci. Nous discutons brièvement comment appliquer ces théories au calcul de la réflectivité par des réseaux avec des fils non rectangulaires mais trapèzoïdaux.

Les calculs ci-dessus considèrent des réseaux de multicouches parfaits. Cependant, comme dans le cas des multicouches planaires, les interfaces peuvent présenter des défauts. Nous faisons la distinction entre la rugosité sur les parois verticales des fils des réseaux et celle, horizontale, des interfaces. Nous utilisons notre formalisme matriciel de la théorie dynamique et nous montrons l'influence de ces rugosités sur l'intensité diffusée. Notre approche est ainsi une généralisation de la réflection sur des multicouches planaires rugueuses ; cependant, dans le cas des réseaux, nous n'avons pas trouvé de traitement matriciel correct dans la littérature où le plus souvent la rugosité est prise en compte par les facteurs cinématiques classiques d'atténuation exponentielle.

Dans la dernière partie de ce chapitre, nous présentons les mesures expérimentales et l'ajustement des paramètres structuraux d'une multicouche avec trois périodes et demie avec la dernière partiellement gravée en réseau.

5.1 Introduction

In this chapter we will deal with X-ray scattering from multilayer gratings (see Fig. 5.1) in reflection geometry. This means that we study the intensity distribution near the origin of the reciprocal space for grazing incidence of the incoming wave. The main part of this work is devoted to laterally periodic gratings. The generalization to other gratings with a discrete Fourier transform of the lateral structure (e.g., quasiperiodic gratings) is also briefly discussed. We further use the name of a multilayer grating (MLG) for laterally periodic multilayer gratings, if it is not explicitly stated otherwise.

Our aim is to develop and compare different theories suitable for this calculation. This comprises the kinematical theory, the distorted-wave Born approximation and the dynamical scattering theory. We point out different approximations involved in these theories as well as their common features.

The principal characteristic of a multilayer gratings, the one-dimensional lateral periodicity, is involved in all the three treatments by means of the Fourier transform of the susceptibility. We solve the wave equation for this case of lateral periodicity. Thus we can formulate the presented theories in the way of the well-known X-ray diffraction theories for crystals, which use a similar idea to solve the wave equation in the crystal with a three-dimensional translation symmetry.

In the first section, we review the work published by other authors on the topic of this chapter. Then we deal with the basic features of the gratings and their reciprocal lattice. We introduce the notation used afterwards.

In the following sections we present the theories, starting by the kinematical theory. We solve the kinematical diffraction integral by means of the stationary phase method similarly to our procedure for the reflection from planar multilayers. The kinematical theory includes only single-scattering processes and it does not include the refraction and absorption effects. Nevertheless, the results obtained show the general features of the scattering from gratings: one incoming plane wave is spread into a fan of plane waves. That is a diffraction process, based on specular reflection. The lateral components of the wave vectors of the scattered (diffracted) waves differ from that of the incoming wave by the one-dimensional reciprocal grating vector. Therefrom follows the famous grating formula. We represent the scattering process in reciprocal space by means of the conventional Ewald construction. We show a way to generalize the kinematical Fresnel reflection coefficients.

The distorted-wave Born approximation (DWBA) as a more elaborate perturbation method is treated afterwards. DWBA has been used in the X-ray reflectivity from planar multilayers for the calculation of the diffuse scattering from rough interfaces. It was believed until now that the DWBA is valid only for small perturbing potentials, e.g., small interface profile displacements (small roughnesses). However, we show the applicability of this method to the calculation of the reflectivity from gratings too. Therefore the main point of our discussion of the DWBA concerns the range of its validity.

The dynamical theory of reflection from lamellar multilayer gratings is treated by many authors. The review is presented in the following section. In this work, we develop a dynamical scattering theory of X-ray reflection from gratings, taking pattern from the Darwin-Laue formulation of the dynamical theory of X-ray diffraction from crystals. Our formulation is known in optics as the modal eigenvalue method: we find a plane wave solution of the wave equation as the one-dimensional Bloch waves, we solve the eigenvalue problem and apply the boundary conditions at the MLG interfaces. This will be performed by the matrix formalism. The main advantage of our presentation of the theory in this work is that we keep the same notation as for the reflection from planar multilayers, which depicts the links to the reflectivity from both structure types. As a particular result, this will allow us to introduce a matrix generalizing the matrix of the Fresnel coefficients.

This fully dynamical theory is used for numerical calculations. However, the equations of this rigorous theory are rather cumbersome for being discussed in a qualitative way. Therefore we formulate multiple-beam approximations of the dynamical theory. These approximation are

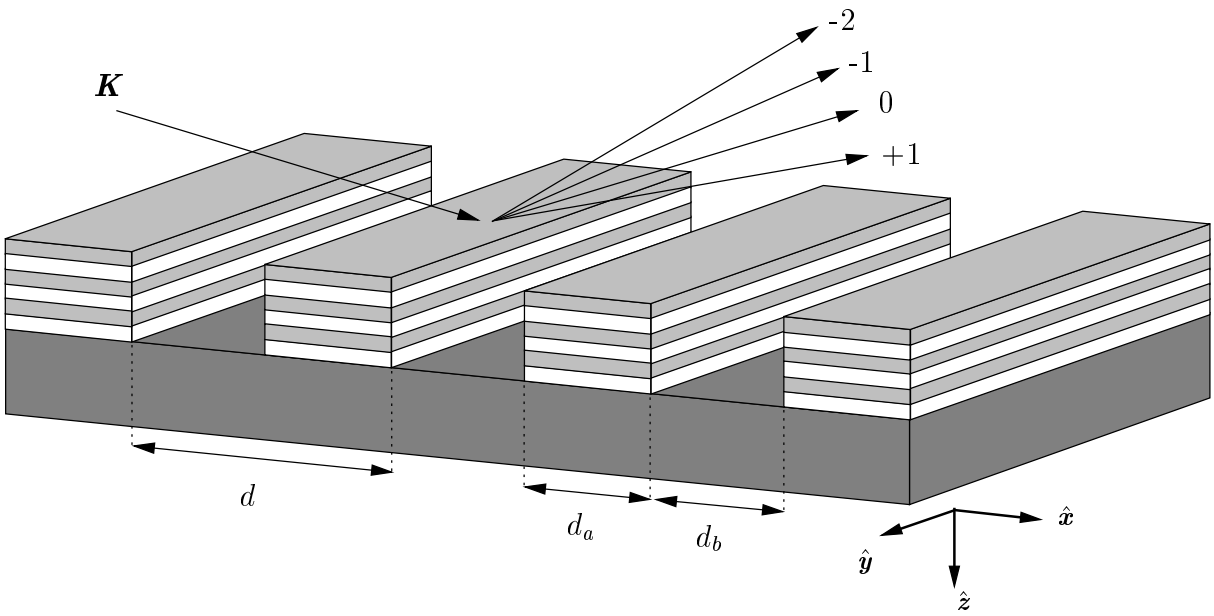

Figure 5.1. A sketch of a multilayer grating with a fan consisting of four diffracted reflected waves.

employed in the regions where the dynamical effects prevail. Our new approach consists of introducing the two-beam approximation, similarly to the two-beam case of X-ray dynamical diffraction by crystals. We discuss also non-coplanar scattering in the geometry where the incident wave falls (nearly) parallel to the wires.

The discussion of these theories, together with numerical simulations and their comparison is presented in the subsequent section. As a particular example we take a surface grating with a wire-to-period ratio 0.5 and a period of 8000 Å, which was a characteristic sample of the series of the samples we worked with. We show that the odd order truncation rods are strong, and most parts of their profile can be well explained by both the dynamical theory and the DWBA. In contrary, the even truncation rods are forbidden by all the single-scattering theories, the calculation needs to deal with a multiple scattering and thus only the dynamical treatment is appropriate. We use the numerical simulation to determine the number of interacting wavefields needed in the multiple-beam approximations in order to obtain the scattered intensities with a sufficient precision.

Our theories and their formalism for the periodic grating can be applied for certain aperiodic gratings as well, mainly to the gratings where the lateral profile has a discrete Fourier transform. In particular, we study qualitatively the expected reflectivity map of a quasiperiodic Fibonacci grating. We briefly discuss how to use the theories in order to calculate the reflectivity by gratings with non-rectangular wire shapes (trapezoidal gratings).

The calculations above considered perfect multilayer gratings. However, as it was the case of the planar multilayers, the interfaces between the materials can be imperfect. We distinguish between the side wall roughness of the grating shape and the interface roughness of the horizontal interfaces. We use our matrix formalism of the dynamical theory and we show how these roughnesses influence the scattered intensity. Thus our approach is a generalization of the reflection from rough planar multilayers; however, for the case of gratings, we have not found a correct matrix treatment in the published literature where mostly the roughness is involved by supposing the usual exponential kinematical damping factors.

In the final part of this chapter we present a measurement and fit of the structural parameters of a multilayer grating with three-and-a-half partially etched periods.

5.2 Review of the published work

Simple surface gratings and multilayer gratings have achieved scientific and practical applications mainly in optical or electronic devices. Multilayers and gratings are the microstructures used as optical elements for most of this century, mainly for the soft X-rays and ultraviolet spectral domains. Joining of these two optical microstructures to form combined microstructures greatly enhances both the throughput and the resolution attainable in soft X-ray and extreme ultraviolet optics [Bar89]. Diffraction gratings are well known for their high spectral resolution. Compared to a simple surface grating, the multilayer gratings generate higher diffraction orders, thus higher efficiencies. Optimum efficiency is obtained when the geometry for a certain grating order is such that the multilayer Bragg relation is fulfilled (the grating formula). Lamellar multilayer gratings are also applied in X-ray spectroscopy as spectral analyzers [KLC+96].

There are also interests in studies of structured multilayers, which are laterally non-periodic. The so-called Bragg-Fresnel optics have been developed recently for X-ray optics [Erk90] and stratified Fresnel linear zone plates are being used as X-ray optical elements [SA93, ASB+94]. In semiconductor physics, the quantum wires (and quantum dots as well) are partially based on layered surface gratings [WV91, TRL+92a].

The X-ray scattering techniques, being the non-destructive methods, are advantageously employed for the structural characterization of the gratings. Both X-ray reflection (XRR) and X-ray diffraction (XRD) experiments are performed, the latter for the crystalline samples.

In the theoretical approaches, X-ray diffraction applies the three-dimensional crystal lattice periodicity to the wave equation, and the additional artificial lateral periodicity is treated afterwards. In X-ray reflection this one-dimensional periodicity is the main characteristics applied directly for solving the wave equation.

Scattering theories of different complexity are involved in the calculation of the intensity scattered from multilayer gratings (MLGs), ranging from fully dynamical to simple kinematical ones. Within the XRR the kinematical and dynamical theories have been used, in XRD also the distorted-wave Born approximation (DWBA) has been applied. Let us now review these theories.

Kinematical theories

It is possible to solve the wave equation by means of the Green functions and develop the expression for the scattered wavefield into a Born series [SA93]. Cutting this series after the first iteration we get the first Born approximation or the ***kinematical theory***. The kinematical diffraction integral is mostly calculated using the Fraunhofer approximation [BTS+95, KLC+96]. However, the resulting amplitude of the scattered wave depends on the sample size as it is the case of the conventional kinematical XRD by small crystals. This leads to the simple explanation of the reflectivity map, mainly the peak positions by means of the grating formula [PdWL+91]. However, the main disadvantage of such a formulation is that the sample size has to be smaller than the first Fresnel zone, which is not fulfilled for laterally large multilayers (Sec. 3.5). This approach is also improper for comparing analytically the intensities calculated by the kinematical and dynamical theories: the intensity calculated by the kinematical theory increases quadratically with the sample dimension, whereas the dynamical theories apply the boundary conditions and use the Fourier transform for laterally infinite structures, and not for small samples. We overcome this problem by applying the stationary phase method to the calculation of the kinematical diffraction integral, which will furthermore enable us to clearly relate the obtained reflectivity coefficients to the classical Fresnel coefficients.

Dynamical theories

In 1907, Rayleigh [Ray07] studied the optical reflectivity from periodic gratings. In his theory the scattered wavefield consists of "pseudo-periodic" waves. These waves were introduced into X-ray diffraction from crystals by Ewald [CJK92], they are used in solid state physics as Bloch waves

[AM76], and they are known by mathematicians also as the solution of the Floquet theorem [SJMP91].

In a modern review Maystre [May84] presented rigorous vector theories of diffraction gratings for optics. He discussed the validity of the Rayleigh hypothesis [Ray07], i.e. the validity of the Rayleigh expansion inside the grating. For X-rays, the scalar theories are sufficient (page 21). They are also discussed in the above mentioned work. The formulae for the Rayleigh coefficients (so-called B_m) are ***integral equations***. In the X-ray region, they have been applied by Tolan *et al.* [TKB$^+$92, TVS$^+$95, TPBK95] to calculate the scattering amplitude by a trapezoidal surface grating.

Unfortunately, the integral equations have to be integrated numerically. Therefore another type of theories calculating the scattering from gratings has been developed—the ***dynamical matrix methods***. We will employ them in the rest of this work and we show how they allow us to explain the scattering phenomena.

The dynamical matrix methods calculate the Fourier components of the scattered wavefield (i.e. the Rayleigh coefficients) separately in different layers. The wavefields are then coupled at the horizontal interfaces by applying the boundary conditions. A convenient matrix formalism similar to the Abèles method [Ab50] is used for this task by all the authors.

Most of the work has been done on rectangular periodic gratings. Considering the non-periodic gratings, the dynamical matrix theory has been employed for the calculation of the reflection from stratified Bragg-Fresnel gratings [SA93]. Attention is paid also to gratings with trapezoidal and triangular wire shapes [Nev94].

We distinguish two types of dynamical matrix theories, depending on how they calculate the scattered wavefields inside the "structured" (etched, see Fig. 5.2) layer (for rectangular gratings) or along the vertical direction $\hat{\boldsymbol{z}}$ (for any grating profile):

The differential method numerically integrates the differential wave equation (e.g. by means of the Runge-Kutta method). Nevière [Nev94] used the differential method for a grating with triangular wire shapes, Erko *et al.* [EVV$^+$93] used this method also for a rectangular grating.

The modal method calculates the wavefield in the whole laterally structured layer. We distinguish two types of modal theories, depending on how they calculate the wavefield inside a structured layer:

- ***The eigenvalue method*** the periodic susceptibility in the layer is expanded into a Fourier series and the wavefield is developed into Bloch waves. The solution of the wave equation is transformed into an eigenvalue problem, which gives the wave vector components and the Fourier coefficients of the scattered waves. This method has been used for etched gratings [MVV$^+$94] as well as for multilayer mirrors modulated with a transverse acoustic wave [AEM92].

  It is this approach, the modal eigenvalue dynamical matrix method, which we will further use as the "dynamical theory" in the present work.

- ***The point matching method*** solves the wave equation inside the two homogeneous parts of the structured layer. The wavefields in both wires are coupled by applying the boundary conditions on the side walls. This leads to a transcendental dispersion equation for the wave vector components of the diffracted waves [LG85, SJMP91]. The wavefield is then Fourier transformed in order to get the Fourier coefficients of the scattered wavefield.

A comparison of the modal and differential methods for multilayer grating efficiencies has been published [MVV$^+$94]. The authors have found a good agreement of the calculated curves for gratings with lateral period between 4 and 10 μm and CuK$_\alpha$ radiation. (In the present work we are mainly interested in short period gratings with a period at about 1 μm and smaller and wavelength of about 1 Å).

However, a comparison between the modal and differential methods has not been done for the interesting case of a strong dynamical interaction. Such an interaction can be achieved when the incident beam falls parallel to the wires, see Fig. 5.4(d). In this work we present the calculation for this case (Sec. 5.7.3) by means of the eigenvalue method and we address the problem of comparing it with the point matching method for future studies.

Rough gratings

Most theoretical works about gratings consider perfect samples, whereas rough gratings have not attracted much attention. Further, all the studies of imperfect gratings were limited to the rough interfaces. They neglected the side wall roughness due to the etching process itself.

Erko *et al.* [EVV+93] assumed that the reflectivity losses are equally distributed in all the diffracted orders, therefore they empirically proposed a correction in the form of a classical kinematical Debye-Waller damping factor $\exp(-K^2\sigma^2\sin^2\theta)$ which they applied to the dynamically calculated intensity of a perfect grating. The θ is the scattering angle and σ is an effective grating roughness.

Tolan *et al.* [TPBK95] included the roughness by averaging the Rayleigh–Mayster B_m coefficients. Their damping factors were similar to the dynamical "rapid" Névot-Croce factors, cf. Eq. (4.33).

In the present work, we introduce the roughness of both the side walls of the grating shape and of the horizontal interfaces of a multilayer grating in the framework of the dynamical matrix approach as well as of the kinematical theory.

X-ray diffraction theories

This review of the published matter on the gratings would not be complete without comprising the theories of X-ray diffraction from crystalline gratings.

In general, X-ray diffraction dynamical multiple-beam scattering theories [Cha84] are rather complex, numerically difficult and they do not provide an easy relation between the formulae and the calculated map of the scattered intensity. Therefore we usually restrict the approach to multiple-beam scattering. For the region near reciprocal lattice points, the two-beam case is mostly employed. Further, Taupin [Tau64] and Takagi [Tak69] derived equations that describe diffraction by non-ideal crystals. They lead to the so-called semi-kinematical approximation, which is adequate for diffraction by multilayers [Spe81, BHL86], or periodic quantum wires [HTK+93]. The kinematical theory has been used in the calculation of diffraction by periodic gratings [TRL+92b, TRL+92a], surface gratings [TPBK94], for polystyrene films deposited on laterally structured surfaces [TVS+95] and it has been employed for a theoretical treatment of a quasiperiodic grating [Mik95]. The distorted-wave Born approximation is also used, and it is reviewed separately below. The kinematical theory with the stationary phase method has been employed for diffraction by planar multilayers as well [Mik95, Hol96] and the similarity to the semi-kinematical approximation has been addressed.

In the present work on reflection from lateral gratings, some ideas coming from the X-ray diffraction theories for crystals have been found stimulating:

- the representation of the scattering phenomena in the reciprocal space by the Ewald construction,
- developing the dynamical multiple scattering theory into a two-beam case and studying the single-scattering processes,
- making use of the kinematical theory as well as
- of the distorted-wave Born approximation.

We will show that we succeeded to reformulate the matrix eigenvalue method into the two-beam approximation, very similar to the two-beam case of the dynamical X-ray diffraction. Further,

we have achieved to calculate the scattered intensity by means of the kinematical theory using the stationary phase method.

Distorted-wave Born approximation

Perturbation theories are often involved in the scattering calculations. The *distorted-wave Born approximation (DWBA)* is successfully employed in the calculation of scattering from rough and imperfect multilayers [SSGS88, HKO+93], as we have already discussed in Sec. 4.5. On the other hand, DWBA is also found advantageous for the calculation of scattering from perfect structures [Vin82, Dos87]. It has been successfully applied to calculate grazing incidence diffraction (GID) by multilayers [HB94, BG95]. DWBA of the second order enabled to explain all features on a XRD pattern of multilayer surface gratings [GBM+93, BG95], where the authors have found the effects of a dynamical interaction of the wavefields in the partially etched grating and the underlying multilayer.

Despite these results in XRD and GID, it was believed that in the reflectivity experiments the DWBA is applicable only in the case of small roughness, and it cannot be employed to calculate the reflection from a grating, which can be considered as a big perturbation [TPBK95]. In the present work we discuss that it is possible to use the DWBA for most parts of the truncation rods, except for the known regions where the strong dynamical interaction between different truncation rods becomes important.

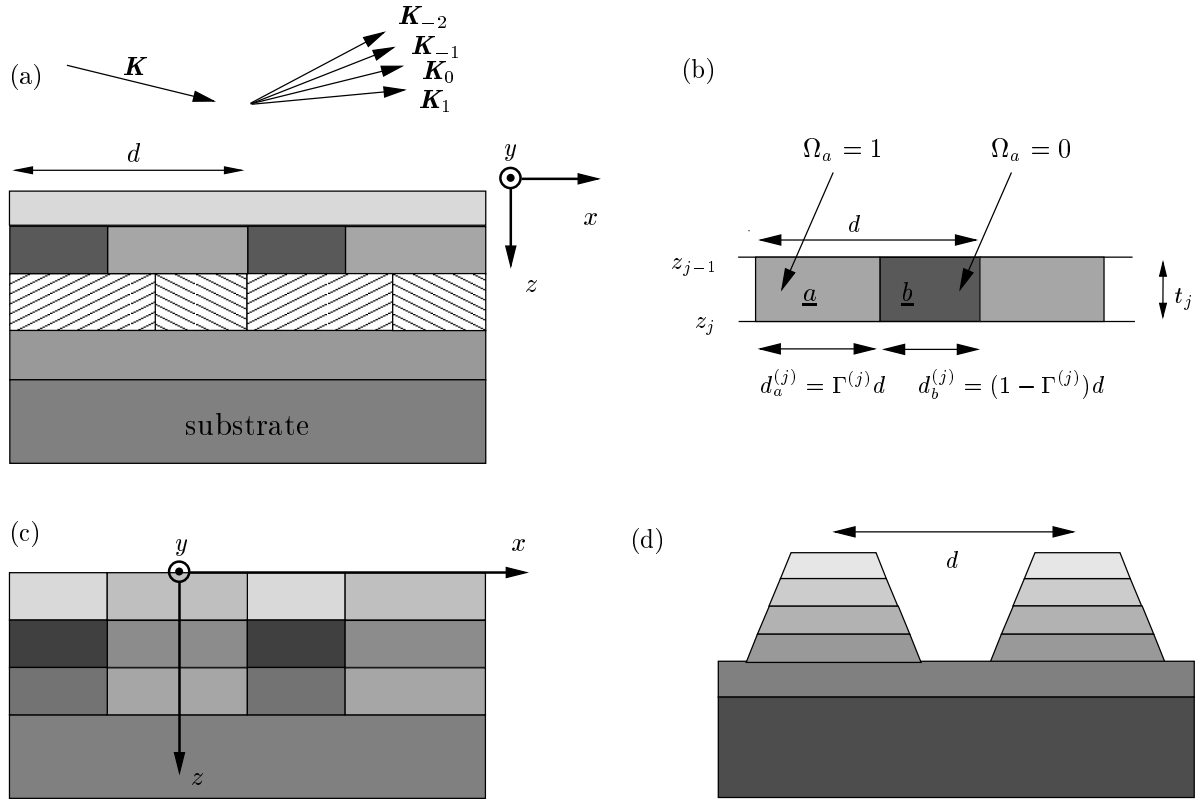

Figure 5.2. (a) Sketch of a multilayer grating. There is a homogeneous layer (e.g., a buffer layer) deposited on the substrate, covered by two structured layers and a capping layer. The system exhibits the lateral periodicity d. The incident beam $\boldsymbol{K}$ and the fan of specularly reflected ($\boldsymbol{K}_0$) and diffracted ($\boldsymbol{K}_h$) beams are schematically shown. (b) Notation of the variables describing one structured layer. (c) Sketch of a multilayer grating consisting of three layers with unique side walls. (d) Sketch of a trapezoidal multilayer grating.

5.3 General characteristics of multilayer gratings

In this section we introduce the common notation of variables and functions used in this chapter. A three-dimensional view of a rectangular multilayer grating is presented in Fig. 5.1. The whole multilayer is characterized by the lateral periodicity d in the direction $\hat{\boldsymbol{x}}$. The grating is homogeneous in the $\hat{\boldsymbol{y}}$ direction, therefore it is sufficient to draw 2d section of the gratings, Fig. 5.2. The most usual cases of the wire profiles are the rectangular (Fig. 5.2(a) and (c)) and trapezoidal (d) gratings.

The multilayer grating consists of N layers deposited on the substrate. The numbering of the layers and interfaces follows the convention introduced in Fig. 3.5. The jth layer (thickness t_j) is bounded by two interfaces j and $j+1$, the z-coordinate of the jth interface is z_j. The sample dimensions are denoted L_x and L_y and its surface area $S = L_x L_y$.

Two layer types can occur in the MLG. There are *homogeneous layers*, e.g., a buffer or a capping layer, and *structured layers*, whose structure is periodic along the axis $\hat{\boldsymbol{x}}$ with the lateral periodicity d. Each period consists of two parts (blocks, wires) $\underline{\mathrm{a}}^{(j)}$ and $\underline{\mathrm{b}}^{(j)}$. We denote their susceptibilities $\chi_a^{(j)}, \chi_b^{(j)}$ and their widths $d_a^{(j)} = \Gamma^{(j)} d$, $d_b^{(j)} = (1-\Gamma^{(j)})\, d$ with $0 \le \Gamma^{(j)} \le 1$.

The lateral periodicity d is a characteristic property of the multilayer, $\chi(\boldsymbol{r}) = \chi(\boldsymbol{r} + d\,\hat{\boldsymbol{x}})$. The reciprocal lattice of a periodic grating is shown in Fig. 5.3. It consists of truncation rods equidistantly distributed in the reciprocal space

$$\boldsymbol{h}_m = h_m\,\hat{\boldsymbol{x}}\ , \qquad h_m = \frac{2\pi}{d}\cdot m\ , \tag{5.1}$$

where m is integer.

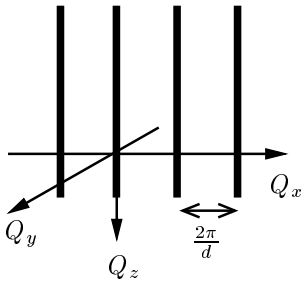

Figure 5.3. Sketch of the reciprocal lattice of a periodic grating.

Let us consider a structured layer. We develop its susceptibility into the Fourier series

$$\chi(x,z) = \sum_h \chi_h(z)\, e^{ihx} \tag{5.2}$$

$$\chi_h(z) = \frac{1}{d}\int_{-d/2}^{d/2} dx\, \chi(x,z)\, e^{-ihx}\ . \tag{5.3}$$

For brevity we omit the index j in the variables related to a layer j. Within the rectangular MLG, Fig. 5.2(c), both side walls separating the $\underline{\mathrm{a}}$ and $\underline{\mathrm{b}}$ materials are unique and $\Gamma_j = \Gamma$ for all layers j. We choose the origin or the coordinate system in the middle of the material $\underline{\mathrm{a}}$, thus χ_{-h} equals χ_h.

We introduce the *shape function* $\Omega_a(\boldsymbol{r})$ of the material $\underline{\mathrm{a}}$ in the layer. It equals unity inside the material $\underline{\mathrm{a}}$ and it is zero elsewhere, see Fig. 5.2(b). The susceptibility is

$$\chi(x,z) = \chi_a \Omega_a(x,z) + \chi_b\big(1 - \Omega_a(x,z)\big) \tag{5.4}$$

and its one-dimensional Fourier transform is

$$\chi_h(z) = \begin{cases} \frac{1}{d}\left[\chi_a d_a(z) + \chi_b d_b(z)\right] = \chi_b + (\chi_a - \chi_b)\, d_a(z)/d & \text{for } h = 0\ , \\ (\chi_a - \chi_b)\, \Omega_{ah}(z) & \text{for } h \ne 0\ . \end{cases} \tag{5.5}$$

The Fourier coefficients Ω_{ah} are calculated similarly to (5.3). We can see that $d_a(z)/d$ is the *coverage* of the material $\underline{\mathrm{a}}$ at level z.

Further we define the three-dimensional Fourier transform $\tilde{\Omega}_a(\boldsymbol{q})$ of the shape function $\Omega_a(\boldsymbol{r})$

$$\tilde{\Omega}_a(\boldsymbol{q}) = \int d\boldsymbol{r}\, \Omega_a(\boldsymbol{r})\, e^{-i\boldsymbol{q}\boldsymbol{r}}\ . \tag{5.6}$$

In comparison to the definition (5.3), we find useful to define the Fourier transform (5.6) so that it integrates over the whole layer and it is not normalized to its volume.

Since the wires a are distributed periodically, their shape function can be given as a convolution of the shape function of one period $\Omega_{a1}(\boldsymbol{r})$ (defined on the interval $-\frac{d}{2} \le x \le \frac{d}{2}$) with a periodic arrangement of δ-functions

$$\Omega_a(\boldsymbol{r}) = \Omega_{a1}(\boldsymbol{r}) \otimes \sum_n \delta(x - nd) \ . \tag{5.7}$$

The Fourier transform

$$\tilde{\Omega}_a(\boldsymbol{q}) = \frac{4\pi^2}{d}\, \tilde{\Omega}_{a1}(q_x, q_z) \cdot \sum_{h_m = \frac{2\pi}{d} m} \delta(q_x - h_m)\ \delta(q_y) = \frac{S}{d}\, \tilde{\Omega}_{a1}(q_x, q_z) \sum_{h = \frac{2\pi}{d} m} \delta_{q_x,h} \cdot \delta_{q_y,0} \tag{5.8}$$

is represented in reciprocal space as the reciprocal lattice (i.e., the truncation rods ($q_x = h_m$)) modulated by the Fourier transform of the shape function of one wire $\tilde{\Omega}_{a1}$.

With respect to the future application in multilayer gratings, the Fourier transform $\tilde{\Omega}_{a1}$ is naturally defined with respect to the lower interface of the structured layer z_j (see Fig. 3.5(a), t_j is the layer thickness)

$$\begin{aligned} \tilde{\Omega}^{(j)}_{a1}(q_x, q_z) &= \int_{z_j - t_j}^{z_j} dz \int_{-d/2}^{d/2} dx\, \Omega^{(j)}_a(\boldsymbol{r})\, e^{-i(q_x x + q_z (z - z_j))} \\ &= \int_{-t_j}^{0} dz \int_{-d/2}^{d/2} dx\, \Omega^{(j)}_a(\boldsymbol{r} - z_j \hat{\boldsymbol{z}})\, e^{-i(q_x x + q_z z)} \ . \end{aligned} \tag{5.9}$$

Therefore these Fourier coefficients in a multilayer grating will be the same for structured layers of the same type, i.e., they will not have different phases depending on the thickness of the whole multilayer.

Further, we define the area (i.e., the cross-section in the plane $(\hat{\boldsymbol{x}}, \hat{\boldsymbol{z}})$) of one period $\mathcal{V}_{ab} = dt$ ($t \equiv t_j$ is the layer thickness), and $\mathcal{V}_a = \tilde{\Omega}_{a1}(0,0) = \int_0^{t^{(j)}} dz \int_{-d/2}^{d/2} dx\, \Omega_a(\boldsymbol{r})$ gives the area of the wire a, which equals $d_a t$ for a rectangular grating. The area of the wire b is $\mathcal{V}_b = \mathcal{V}_{ab} - \mathcal{V}_a$, which becomes $d_b t$ for a rectangular grating.

We define the coverage of the layer j by the material a as $\theta^{(j)}_a \equiv \frac{\mathcal{V}^{(j)}_a}{\mathcal{V}_{ab}}$.

Explicitly for a rectangular grating, the Fourier transforms of the quantities defined above are[1]

$$\Omega_{ah_m} = \frac{d_a}{d} \operatorname{sinc} \frac{h_m d_a}{2} = \Gamma \operatorname{sinc}(\Gamma m \pi) \tag{5.10}$$

$$\tilde{\Omega}_{a1}(h_m, q_z) = d_a \operatorname{sinc} \frac{h_m d_a}{2}\, \frac{e^{iq_z t} - 1}{iq_z} = d\, \Omega_{ah_m}\, \frac{e^{iq_z t} - 1}{iq_z} \ . \tag{5.11}$$

We recall that $h_m = 2\pi/d \cdot m$ according to (5.1).

We note that the Fourier coefficient Ω_{ah_m} falls as $1/m$. Further we can see that if the ratio $1/\Gamma = d/d_a$ is integer, then the Fourier transforms are zero if m is multiple of $1/\Gamma$.

The wavefield excited by the incident plane wave $E_{\rm inc}(\boldsymbol{r}, \boldsymbol{K}) = E_0\, e^{i\boldsymbol{K}\boldsymbol{r}}$, with the vacuum wave vector $\boldsymbol{K} = (K_x, K_y, K_z)$, obeys the wave equation (3.12)

$$(\Delta + K^2)\, E(\boldsymbol{r}) = V(\boldsymbol{r})\, E(\boldsymbol{r}) \ , \qquad V(\boldsymbol{r}) = -K^2 \chi(\boldsymbol{r}) \ . \tag{5.12}$$

As in the previous chapters, the vacuum wavelength is λ and $K = 2\pi/\lambda$. The crystal polarizability χ and the potential V are zero in vacuum and complex in a medium.

The main task of our theories is to determine the intensities and directions of the scattered waves propagating above the sample surface by solving the wave equation for this case of a one-dimensional lateral periodic grating (5.2)–(5.3).

[1] $\operatorname{sinc}(x) \equiv \frac{\sin(x)}{x}$

5.4 Kinematical theory

In this section we formulate the kinematical theory for the scattering by a multilayer grating. We will make use of the results of Sec. 3.5, where we dealt with the reflectivity from planar multilayers.

There we derived the kinematical integral (3.97). In the present case of a MLG, the susceptibility is a periodic function (5.2). Therefore the reflected amplitude on the sample surface is modified to

$$E_r(\boldsymbol{r}{=}0) = \int d\boldsymbol{r}' \left(\frac{K^2}{4\pi}\right) \sum_h \chi_h(z')\, e^{ihx'}\, \frac{e^{i|\boldsymbol{r}'|K}}{|\boldsymbol{r}'|}\, E_0\, e^{i\boldsymbol{K}\boldsymbol{r}'} \ . \tag{5.13}$$

Let us join the exponential terms and introduce the lateral wave vector

$$\boldsymbol{K}_{h\|} = \boldsymbol{K}_\| + \boldsymbol{h} = (K_{hx}, K_y, 0) \ , \qquad K_{hx} = K_x + h \ . \tag{5.14}$$

Now we can separate the contribution of different Fourier components

$$E_r(\boldsymbol{r}{=}0, \boldsymbol{K}) = \sum_h E_h(\boldsymbol{K}) \tag{5.15}$$

$$E_h(\boldsymbol{K}) = \frac{K^2}{4\pi}\, E_0 \int dz\, \chi_h(z)\, e^{iK_z z}\, U_h(z, \boldsymbol{K}) \,, \tag{5.16}$$

$$U_h(z, \boldsymbol{K}) = \iint dx\, dy\, \frac{1}{|\boldsymbol{r}|}\, e^{i(K_{hx}x + K_y y + K|\boldsymbol{r}|)} = \iint d\boldsymbol{r}_\| \, \frac{1}{|\boldsymbol{r}|}\, e^{i(\boldsymbol{K}_{h\|}\boldsymbol{r}_\| + K|\boldsymbol{r}|)} \ , \tag{5.17}$$

where $|\boldsymbol{r}| = \sqrt{x^2 + y^2 + z^2}$.

The integral (5.17) is of the same form as the integral (3.102), which we have already solved exactly (i.e., without the restriction to the Fraunhofer approximation) using the *stationary phase method*. Similarly to (3.104) we get

$$U_h(z, \boldsymbol{K}) = \frac{2\pi i}{K_{hz}}\, e^{iK_{hz}z} \tag{5.18}$$

and

$$K_{hz} = \sqrt{K^2 - (K_{hx}^2 + K_y^2)} \ . \tag{5.19}$$

The latter equals the z-component of the diffracted wave vector $(\boldsymbol{K}_{h\|}, \pm K_{hz})$ with the parallel component given by (5.14) and with the length K. Thus the end-points of the diffracted wave vectors lie on the Ewald sphere (Fig. 5.5).

The diffracted-reflected waves are plane waves with the wave vector

$$\boldsymbol{K}_h = \boldsymbol{K}_{h\|} - K_{hz}\hat{\boldsymbol{z}} \tag{5.20}$$

and the amplitude

$$E_h = E_0\, \frac{iK^2}{2K_{hz}} \int dz\, \chi_h(z)\, e^{i(K_{hz} + K_z)z} = E_0\, \frac{iK^2}{2K_{hz}} \int dz\, \chi_h(z)\, e^{-iQ_{hz}z} \ . \tag{5.21}$$

The incident wave is scattered by the periodic grating into a *fan of diffracted waves*, see Fig. 5.1. The wave vector transfer of the diffraction

$$\begin{aligned} \boldsymbol{Q}_h &= \boldsymbol{K}_h - \boldsymbol{K} = \boldsymbol{h} - (K_{hz} + K_z)\hat{\boldsymbol{z}} \\ Q_{hz} &= -(K_{hz} + K_z) \end{aligned} \tag{5.22}$$

is constant over the whole MLG since we used the vacuum incoming plane wave as the eigenstate entering the Born approximation.

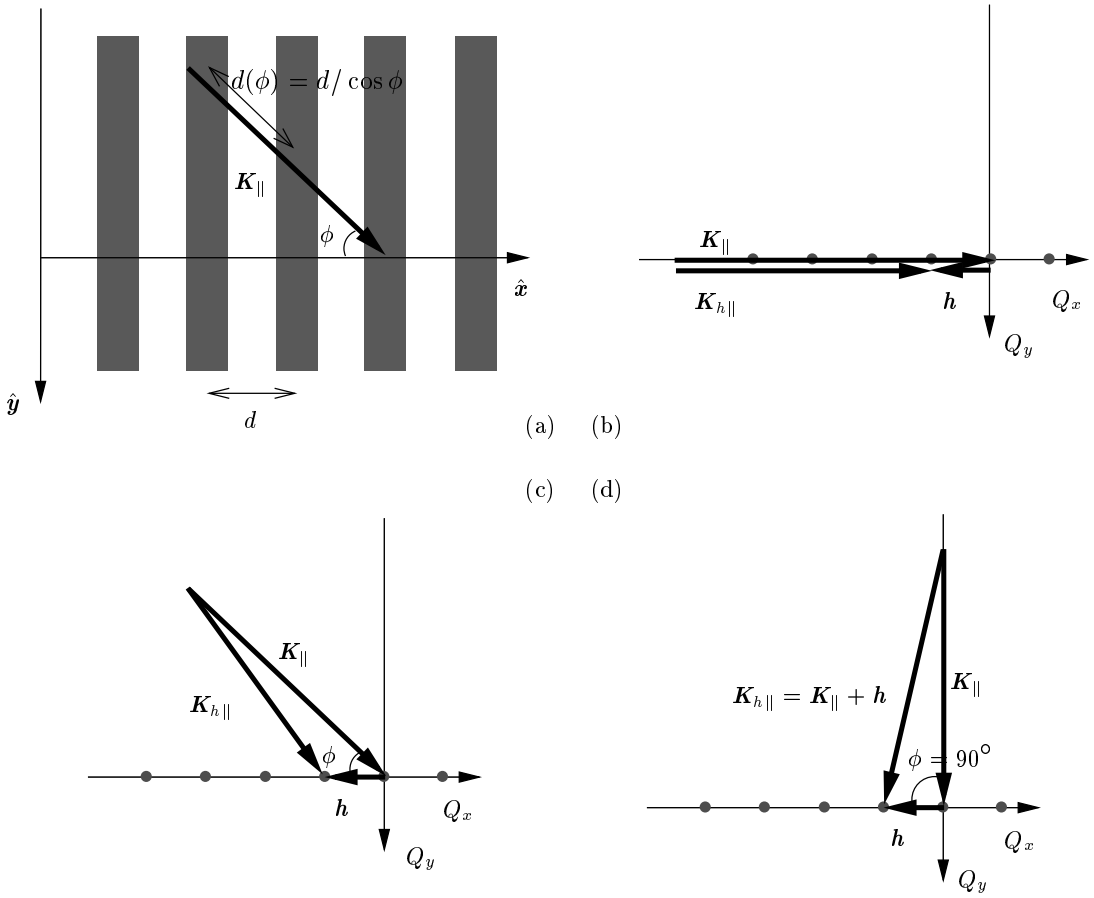

Figure 5.4. Sketch of the lateral real (a) and reciprocal (b)–(d) spaces. The azimuthal angle ϕ changes the "effective" grating period $d(\phi)$ and it diverges when the incident beam is parallel to wires. Reciprocal space drawings illustrate the (lateral) Bragg law (5.23) for different azimuths.

If we write the above equation in the parallel coordinates, we get the (lateral) Bragg law

$$\boldsymbol{K}_{h\|} = \boldsymbol{K}_{\|} + h\,\hat{\boldsymbol{x}} \tag{5.23}$$

shown schematically in Fig. 5.4. Rewritten for the coplanar geometry this leads to the conditon

$$\cos\theta_{h_m} - \cos\omega = \frac{\lambda}{d}\,m\ , \tag{5.24}$$

where θ_h is the exit angle of the diffracted-reflected wave $\boldsymbol{K}_h$ and ω is the angle of incidence. From the X-ray diffraction point of view, this grating formula is equivalent to a single Laue condition [AKK$^+$74, Pin78, SJMP91].

Considering the *specular scan* (truncation rod m=0) the kinematical integral (5.21) is the same as that in the reflectivity (3.105). Therefore the specular intensity of the MLG is exactly that of the averaged multilayer, since $\chi_0(z)$ is the laterally averaged susceptibility.

Let us now deal with the *non-zero truncation rods* (TR m, $m\neq0$, experimentally measurable as non-specular scans). Since the Fourier transform of the susceptibility is constant in each layer j (for an arbitrary wire shape), then the integral (5.21) turns into the *summation formula*

$$E_h = E_0\,\frac{iK^2}{2K_{hz}}\sum_{j=2}^{N} F_h^{(j)}\,e^{-iQ_{hz}z_j}\ . \tag{5.25}$$

We call $F_h^{(j)}$ the *structure-geometric factor* of layer j. For a rectangular grating it becomes

$$F_h^{(j)} = \chi_h^{(j)}\,\frac{e^{-iQ_{hz}t_j}-1}{-iQ_{hz}}\ . \tag{5.26}$$

The above formula is very similar to the formula of the kinematical diffraction by crystalline layers (cf. the previous discussion for planar multilayers on page 42). This is because the bulk of the grating (i.e., the lateral distribution of the susceptibility) contributes to the scattering, whereas on reflection from planar multilayers the scattering is only due to the susceptibility change at flat interfaces.

We can easily reformulate the expression (5.25) into a relation acting in the "interface" spirit of the SXR from planar multilayers, see Eq. (3.113). We put the expression (5.26) for the structure factor F into the equation (5.25) for E_h and separate the two sums

$$\begin{aligned} E_h &= E_0 \, \frac{K^2}{-2K_{hz}Q_{hz}} \sum_{j=2}^{N} \chi_h^{(j)} \left(e^{-iQ_{hz}z_{j+1}} - e^{-iQ_{hz}z_j} \right) \\ &= E_0 \, \frac{K^2}{-2K_{hz}Q_{hz}} \sum_{j=1}^{N} \left(\chi_h^{(j)} - \chi_h^{(j+1)} \right) e^{-iQ_{hz}z_{j+1}} \\ &\equiv E_0 \sum_{j=1}^{N} \mathfrak{r}_{h,j}^{\mathrm{kin}} \, e^{-iQ_{hz}z_{j+1}} \; . \end{aligned} \tag{5.27}$$

We introduced the *Fresnel reflection coefficient of kinematical diffraction* of an interface j

$$\mathfrak{r}_{h,j}^{\mathrm{kin}} \equiv \frac{K^2 \, (\chi_h^{(j)} - \chi_h^{(j+1)})}{-2K_{hz}Q_{hz}} \; . \tag{5.28}$$

For the case of specular reflection ($h = 0$, $Q_{0z} = -2K_{0z}$), this perfectly coincides with the kinematical Fresnel reflection coefficient (3.114) for the reflectivity from planar multilayers.

This generalized Fresnel coefficient for the reflection from gratings is proportional to the difference of the Fourier coefficients of the susceptibilities of the two subsequent layers, and inversely proportional to the $\hat{\boldsymbol{z}}$ component of the scattering vector and of the wave vector of the diffracted wave.

Finally, the reflectivity amplitude is $R_h = E_h/E_0$ and the sample reflectivity defined as the ratio of the energy fluxes is

$$\mathcal{R}_h = |R_h|^2 \, \frac{K_{hz}}{K_z} \; . \tag{5.29}$$

A graphical representation of this scattering phenomena by means of the Ewald construction is shown in Fig. 5.5. The diffracted wave vectors lie on the Ewald sphere $\mathcal{K}$ of the incident wave where it intersects the grating truncation rods. If a TR crosses the Ewald sphere at two points, then a pair of diffracted waves is excited. The diffracted-reflected wave propagates above the sample surface and the diffracted-transmitted wave propagates below the surface.

When we will further say that "an incident wave is scattered into a truncation rod h", then we mean that for a given incident wave there is a diffraction process characterized by the lateral wave vector transfer $\boldsymbol{h}$.

For a certain angle of incidence the Ewald sphere touches a given positive TR $m^{\max}$ in one point only ($m^{\max} = +2$ in Fig. 5.5). This is the "starting point" of a Q_z-scan, and according to page 15 this "starting angle" equals

$$\omega_{h_{m^{\max}}} = \sqrt{2h_{m^{\max}}/K} = \sqrt{2\lambda m^{\max}/d} \; . \tag{5.30}$$

We summarize that an incident plane wave creates a finite fan of diffracted (scattered) waves with real vacuum wave vectors $\boldsymbol{K}_h$, because there is a finite number of truncation rods inside the Ewald sphere of the incident wave. The TRs outside the Ewald sphere correspond to vacuum evanescent waves which cannot be measured. The condition of K_{hz} being real is expressed by the inequality

$$K^2 - (K_{hx}^2 + K_y^2) > 0 \; . \tag{5.31}$$

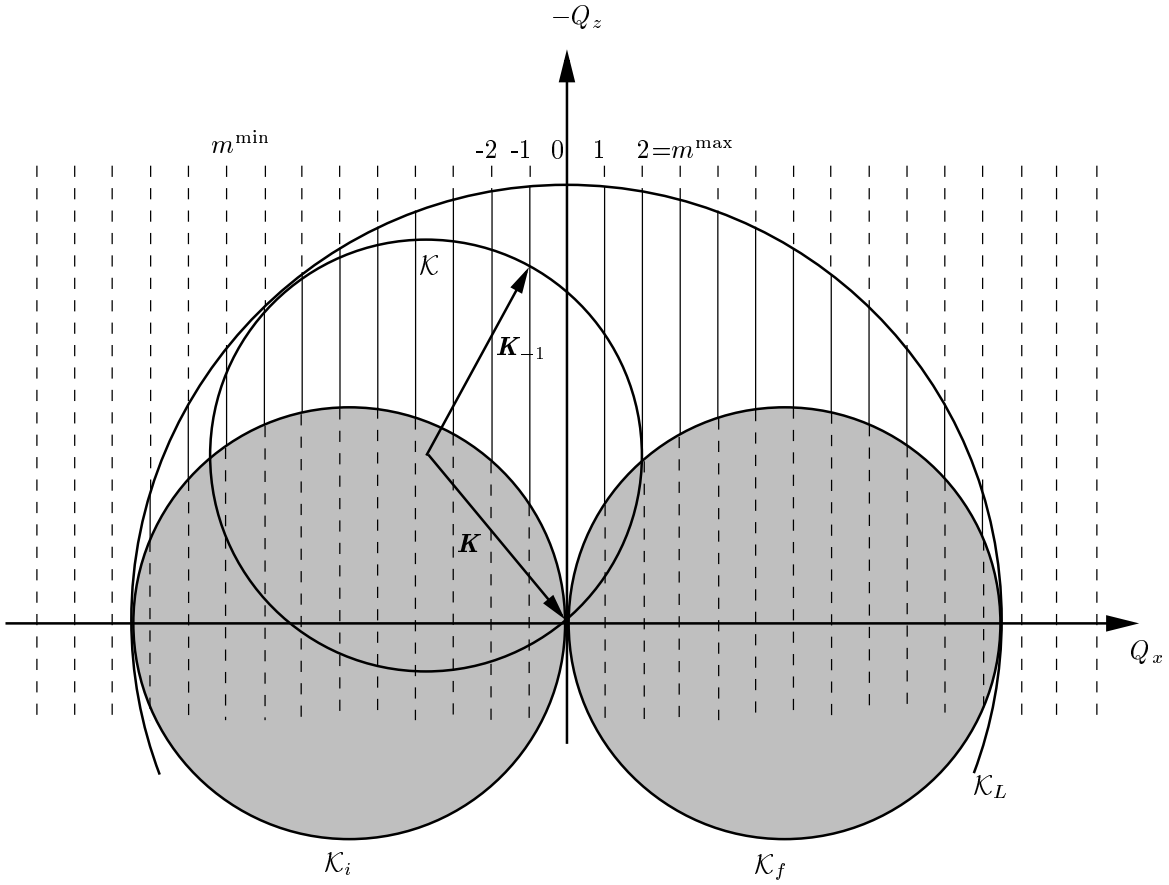

Figure 5.5. Reciprocal space representation and the Ewald construction for the scattering by a multilayer grating (coplanar geometry). The reciprocal space of the MLG consists of truncation rods distributed equidistantly along Q_x. For a given wavelength the intensity distribution along certain parts of truncation rods can be explored; the dashed parts of the truncation rods are not accessible in coplanar reflection geometry (vacuum evanescent waves). For clarity, we drawn only 24 truncation rods inside the large sphere $\mathcal{K}_L$ of diameter $2K$. In a real case, there should be thousands of them (since $2K/(2\pi/d) \approx d/\lambda \approx 10^3$) and the angle of incidence should be at about one degree.

We denote the number of excited truncation rods by $\mathcal{D}$. Since the above condition can be rewritten as

$$|K_x + h| \leq \sqrt{K^2 - K_y^2}\ , \tag{5.32}$$

then the truncation rods of the lowest and of the highest order are[2]

$$\begin{aligned} m^{\min} &= \left\lceil -\left(\sqrt{K^2 - K_y^2} + K_x\right)/d \right\rceil \\ m^{\max} &= \left\lfloor \left(\sqrt{K^2 - K_y^2} - K_x\right)/d \right\rfloor \end{aligned} \tag{5.33}$$

and the dimension

$$\mathcal{D} = m^{\min} + m^{\max} + 1\ . \tag{5.34}$$

For a rectangular grating consisting of a single layer (i.e. a surface grating) the amplitude of the wave scattered into the TR h is

$$E_{h_m} = E_0\, \frac{iK^2}{2K_{h_m z}}\, (\chi_a^{(2)} - \chi_b^{(2)})\, \Gamma\, \mathrm{sinc}\,(\Gamma m\pi)\, \frac{e^{-iQ_{h_m z} t_2} - 1}{-iQ_{h_m z}} \tag{5.35}$$

[2]Function $\lfloor x \rfloor$ returns the largest integer smaller or equal to x, and $\lceil x \rceil$ returns the smallest integer equal to or larger than x.

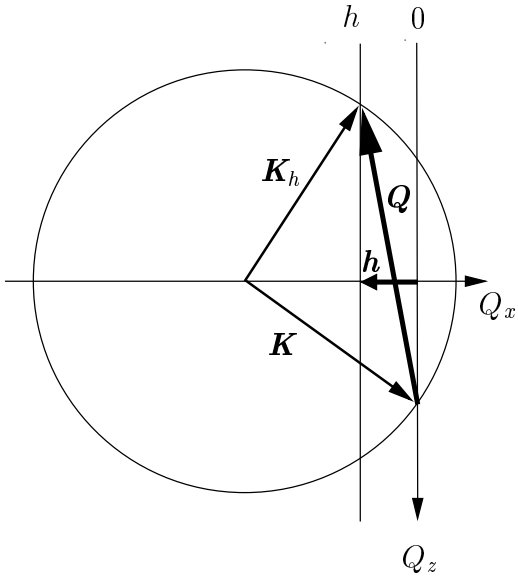

Figure 5.6. Ewald construction of the kinematical theory illustrating the scattering from the incident-transmitted to the diffracted-reflected wave. Similar figures drawn for the DWBA as well as for the two-beam approximation of the dynamical theory are drawn in Figs. 5.7 and 5.10, respectively.

and its reflectivity

$$\mathcal{R}_{h_m} = \frac{K^4 \left|\chi_a^{(2)} - \chi_b^{(2)}\right|^2}{4K_{h_m z} K_z} \, \Gamma^2 \, \mathrm{sinc}^2(\Gamma m \pi) \, (t_2)^2 \, \mathrm{sinc}^2 \, \tfrac{Q_{h_m z} t_2}{2} \; . \tag{5.36}$$

From this follows that the maxima in the Q_z direction are at the positions $Q_{z,p} = \frac{2\pi}{t} p$ (so-called *thickness oscillations*, see page 36). When this is combined with the lateral diffraction condition $\boldsymbol{Q}_{\|} = \boldsymbol{h}_m$, then peaks in the reciprocal space are expected at

$$\boldsymbol{Q}_{mp} = \frac{2\pi}{d} \, m \, \hat{\boldsymbol{x}} + \frac{2\pi}{t} \, p \, \hat{\boldsymbol{z}} \; . \tag{5.37}$$

In the coplanar geometry, the above condition provides two equations connecting the angle of incidence ω_{mp} and the exit angle of a diffracted-reflected wave θ_{mp}

$$\frac{2\pi}{\lambda} \left(\cos\theta_{mp} - \cos\omega_{mp}\right) = \frac{2\pi}{d} \, m \tag{5.38a}$$

$$\frac{2\pi}{\lambda} \left(\sin\theta_{mp} + \sin\omega_{mp}\right) = \frac{2\pi}{t} \, p \tag{5.38b}$$

which yields the *grating formula* [SJMP91, PdWL$^+$91, KLC$^+$96]

$$p \sin\omega_{mp} - m \, \frac{t}{d} \cos\omega_{mp} = \frac{\lambda}{2t} \, p^2 + \frac{\lambda t}{2d^2} \, m^2 \tag{5.39}$$

for the maxima of the angle of incidence. Similarly the maxima for the exit angle are

$$p \sin\theta_{mp} + m \, \frac{t}{d} \cos\theta_{mp} = \frac{\lambda}{2t} \, p^2 + \frac{\lambda t}{2d^2} \, m^2 \; . \tag{5.40}$$

Within the kinematical theory the peak positions are equidistant in both directions Q_x and Q_z of the reciprocal space, see Fig. 5.8(a). The kinematical theory does not take the refraction into account. In order to explain the positions of the experimentally found maxima, the kinematical theory would have to be "corrected" for this effect. This is not necessary in the dynamical theory nor in the DWBA, where the refraction is naturally involved.

5.5 Distorted-wave Born approximation

In this section we calculate the intensity scattered by a multilayer grating by means of the distorted-wave Born approximation (DWBA) of the first order. Therefore we solve the wave equation (5.12) with the periodic potential $V(\boldsymbol{r}) = V(\boldsymbol{r} + d\,\hat{\boldsymbol{x}})$. We suppose a grating with flat interfaces and walls (no roughness), and therefore the incoherent cross section (4.45) is zero. We deal with the coherent scattering term (4.44), which needs the calculation of the matrix element (4.54).

The DWBA method requires the splitting of the scattering potential into the ideal and perturbing potentials (4.48), $V(\boldsymbol{r}) = V^{\mathrm{id}}(\boldsymbol{r}) + V^{\mathrm{p}}(\boldsymbol{r})$. In homogeneous layers, including the substrate, we choose the ideal potential equal to the potential of the layer, therefore the perturbing potential is zero there. In structured layers we choose as the ideal potential V^{id} the potential of a virtual planar multilayer, where V^{id} is constant within each layer. The perturbing potential is $V^{\mathrm{p}} = V - V^{\mathrm{id}}$.

The main objection against the usage of the DWBA for the calculation of the reflectivity from gratings [TPBK95] was that the perturbing potential V^{p} is large, i.e., it is non-zero in large volume of the grating. However, in this work we will show that this is not the main obstacle and that the choice of the eigenstates determines the correct results. By comparing the DWBA to the dynamical theory and its two-beam approximation we will determine the regions of the validity of the DWBA.

The choice of V^{id} determines our set of eigenstates. Two independent eigenstates (given by (4.50) or (4.52)) are required for the DWBA calculation. They are superpositions of the transmitted (T) and the reflected (R) plane waves. We follow our convention (pages 34 and 68) concerning the phases of the transmitted $T_{1,2}^{(j)}$ and of the reflected $R_{1,2}^{(j)}$ waves to be zero at the lower interface of a layer j, $z_{j-1} \le z \le z_j$. The perpendicular wave vector components of these eigenstates follow the spherical dispersion relation (3.11)

$$k_{lz}^{(j)} = \sqrt{K^2 (n^{(j)})^2 - (k_{lx}^2 + k_{ly}^2)}\ , \qquad l = 1, 2\ . \tag{5.41}$$

This means that the wave vectors are corrected for refraction in an averaged medium.

Now we will consider some general properties of the perturbing potential

$$\begin{aligned} V^{\mathrm{p}}(\boldsymbol{r}) &= V(\boldsymbol{r}) - V^{\mathrm{id}}(\boldsymbol{r}) = (V_a - V^{\mathrm{id}})\,\Omega_a(\boldsymbol{r}) + (V_b - V^{\mathrm{id}})\,(1 - \Omega_a(\boldsymbol{r})) \\ &= (V_b - V^{\mathrm{id}}) + (V_a - V_b)\,\Omega_a(\boldsymbol{r})\ . \end{aligned} \tag{5.42}$$

The Fourier transform of the perturbing potential $\tilde{V}^{\mathrm{p}}(\boldsymbol{q})$, and the Fourier transform over one period, $\tilde{V}_1^{\mathrm{p}}(\boldsymbol{q})$, are calculated similarly to (5.8) and (5.9).

At this point we have to propose the value of the ideal potential V^{id} given by the general form (5.42). There are three natural possibilities:

1. V^{id} shall be the laterally averaged layer potential

$$V^{\mathrm{id}} = \frac{V_a \mathcal{V}_a + V_b \mathcal{V}_b}{\mathcal{V}_{ab}} = V_b + (V_a - V_b)\,\frac{\mathcal{V}_a}{\mathcal{V}_{ab}} = V_b + (V_a - V_b)\,\theta_a\ . \tag{5.43}$$

   This leads to the perturbing potential

$$V^{\mathrm{p}} = (V_a - V_b)\,[\Omega_a(\boldsymbol{r}) - \theta_a]\ . \tag{5.44}$$

2. V^{id} is equal to the potential of the material b, thus $V^{\mathrm{id}} = V_b$. This gives the perturbing potential

$$V^{\mathrm{p}} = (V_a - V_b)\,\Omega_a(\boldsymbol{r})\ . \tag{5.45}$$

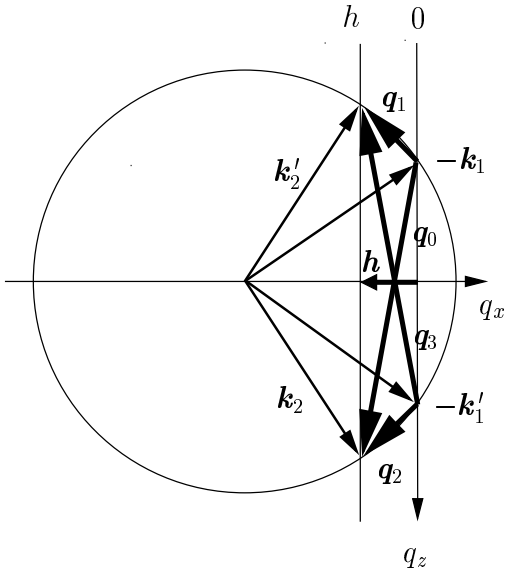

Figure 5.7. Ewald construction of the four scattering processes T_1T_2 (wave vector transfer $\boldsymbol{q}_0$), T_1R_2 ($\boldsymbol{q}_1$), R_1T_2 ($\boldsymbol{q}_2$) and R_1R_2 ($\boldsymbol{q}_3$), which are considered by the DWBA calculation. The lateral component of the wave vector transfer between the states 1, 2 equals a reciprocal grating vector $\boldsymbol{h}$ and it is the same for all four scattering processes. Similar figures drawn for the kinematical theory as well as for the two-beam approximation of the dynamical theory are drawn in Figs. 5.6 and 5.10, respectively.

3. $V^{\rm id}$ is equal to the potential of the material a, thus $V^{\rm id} = V_a$. This gives the perturbing potential

$$V^{\rm p} = -(V_a - V_b)\,\Omega_a(\boldsymbol{r}) \ . \tag{5.46}$$

Now we evaluate the matrix elements (4.54). The matrix element

$$V_{12}^{\rm id} = \langle E_2^{\rm id}|V^{\rm id}|E_0\rangle = 2iK_z \cdot R^{\rm id}(\boldsymbol{K}) \cdot S\,\delta_{\boldsymbol{K}_{2\|},\boldsymbol{K}_\|} \tag{5.47}$$

is the same as that given by (4.62), where $R^{\rm id}$ is the specular reflection amplitude by the virtual undisturbed multilayer.

The matrix element of the perturbing potential is

$$W \equiv \langle E_2^{\rm id}|V^{\rm p}|E_1^{\rm id}\rangle = \sum_{j=2}^{N} W^{(j)} \ , \tag{5.48}$$

where

$$\begin{aligned} W^{(j)} &\equiv \langle E_2^{{\rm id},(j)}|V^{{\rm p},(j)}|E_1^{{\rm id},(j)}\rangle \\ &= T_1^{(j)}T_2^{(j)}\tilde{V}^{{\rm p},(j)}(-\boldsymbol{q}_0^{(j)}) + R_1^{(j)}R_2^{(j)}\tilde{V}^{{\rm p},(j)}(-\boldsymbol{q}_3^{(j)}) + \\ &\quad T_1^{(j)}R_2^{(j)}\tilde{V}^{{\rm p},(j)}(-\boldsymbol{q}_1^{(j)}) + R_1^{(j)}T_2^{(j)}\tilde{V}^{{\rm p},(j)}(-\boldsymbol{q}_2^{(j)}) \ . \end{aligned} \tag{5.49}$$

The three-dimensional Fourier transform of the perturbing potential $\tilde{V}^{{\rm p},(j)}(-\boldsymbol{q})$ is calculated according to (5.6) or (5.8).

Finally we comment on the one-dimensional Fourier transform (5.2) of the perturbing potential. We prefer to express it by the Fourier series of the shape function. Alternatively, it can be developed into the Fourier series of the susceptibility. Both representations are equivalent and for the ideal potential being the averaged layer potential we will find

$$\begin{aligned} V^{\rm p} = -K^2(\chi(\boldsymbol{r}) - \chi_0(z)) &= -K^2 \sum_{h\neq 0} \chi_h\, e^{ihx} \\ &= -K^2(\chi_a - \chi_b) \sum_{h\neq 0} \tilde{\Omega}_{ah}\, e^{ihx} \ . \end{aligned} \tag{5.50}$$

5.5.1 Specular scan

In the specular scan it holds

$$q_{3z} = -q_{0z} \quad \text{and} \quad q_{0x} = q_{1x} = q_{2x} = q_{3x} = q_{1z} = q_{2z} = 0$$

in each layer. Then the contribution of one structured layer is

$$\begin{aligned} W^{(j)} = {} & T_1^{(j)} T_2^{(j)} \tilde{V}^{\mathrm{p},(j)}(-\boldsymbol{q}_0^{(j)}) + R_1^{(j)} R_2^{(j)} \tilde{V}^{\mathrm{p},(j)}(-\boldsymbol{q}_3^{(j)}) + \\ & T_1^{(j)} R_2^{(j)} \tilde{V}^{\mathrm{p},(j)}(0) + R_1^{(j)} T_2^{(j)} \tilde{V}^{\mathrm{p},(j)}(0) \ . \end{aligned} \tag{5.51}$$

Let us make the choice of the ideal potential V^{id} now. Firstly, let us use the perturbing potential according to the rule 1., Eq. (5.44). Then $W^{(j)}$ simplifies since

$$\tilde{V}^{\mathrm{p}}(0,0) = (V_a - V_b) \left[\int d\boldsymbol{r}\, \Omega_a(\boldsymbol{r}) - \tilde{\Omega}_a(0) \right] = 0 \tag{5.52}$$

and the scattering processes $T_1 R_2$ and $R_1 T_2$ do not contribute to the matrix element (5.51) of the specular reflectivity.

Now let us consider a rectangular grating, which is a special case of a grating with the shape function $\Omega_a(\boldsymbol{r}) = \Omega_a(x)\,\Omega_a(z)$. Here the contribution of the terms $T_1 T_2$ and $R_1 R_2$ is proportional to

$$\tilde{V}^{\mathrm{p}}(0,q_z) = (V_a - V_b) \left[\int_{-d/2}^{d/2} dx\, \Omega_a(x) - d\theta_a \right] \int dz\, \Omega_a(z) e^{-iq_z z} = 0 \ . \tag{5.53}$$

From this it follows that the choice 1. of the ideal potential corresponding to a virtual multilayer with the susceptibility averaged in the layers does not contribute to the perturbation term in the specular reflectivity, $W^{(j)} = 0$. Consequently, the specular reflectivity amplitude of the grating equals the reflectivity from the laterally averaged multilayer.

If we choose the undisturbed system according to the possibilities 2. or 3., then the Fourier transform of the perturbing potential for the specular reflectivity scattering processes is non-zero and the contributions of the four scattering processes are proportional to $(V_a - V_b)\,\tilde{\Omega}_a(0, 0 \text{ or } \pm q_z)$, and the perturbation term will influence the specular reflectivity curve. Since it is preferable to calculate the whole specular curve dynamically, we will further prefer the form (5.44) of the perturbing potential. We note that this will not influence considerably the intensity of the non-specular truncation rods, since it is proportional to the potential contrast $\pm(V_a - V_b)$ and the differences would be attributed to the eigenstates (amplitudes and phases).

Finally, making use of the choice 1., the amplitude of the specular reflectivity by a rectangular grating is

$$R^{\mathrm{spec}} = R^{\mathrm{id}}(\boldsymbol{K}) \tag{5.54}$$

and that of a general (e.g., a trapezoidal) grating is

$$\begin{aligned} R^{\mathrm{spec}} = R^{\mathrm{id}}(\boldsymbol{K}) + \frac{1}{2iK_z} \sum_{j=2}^{N} (V_a^{(j)} - V_b^{(j)}) \Bigg[& \\ & |T_1^{(j)}|^2 \left(\tilde{\Omega}_a^{(j)}(0, q_{0z}^{(j)}) - \mathcal{V}_a^{(j)} \frac{e^{-iq_{0z}^{(j)} t_j} - 1}{-iq_0^{(j)} t_j} \right) \\ & |R_1^{(j)}|^2 \left(\tilde{\Omega}_a^{(j)}(0, -q_{0z}^{(j)}) - \mathcal{V}_a^{(j)} \frac{e^{-iq_{0z}^{(j)} t_j} - 1}{-iq_0^{(j)} t_j} \right) \Bigg] \ . \end{aligned} \tag{5.55}$$

We recall that the potential contrast is proportional to the difference of the susceptibilities or the refractive indices, $V_a - V_b = -K^2(\chi_a - \chi_b) = 2K^2(\delta_a - \delta_b)$.

For most samples, the susceptibility (the index of refraction) of the averaged grating layer is higher (lower) than that of the substrate, respectively. Therefore we observe a "dip" in the specular reflectivity curve [TPBK95], see Fig. 5.20(b), at the critical angle of the averaged grating, which is between the zero angle of incidence and the critical angle of the substrate.

5.5.2 Non-specular scans

The potential contrast $(V_a - V_b)\,\Omega_a(\boldsymbol{r})$ describes the grating profile and we will treat it as a perturbation. Since the contrast is zero in homogeneous planar layers, these layers do not contribute to the non-specular reflectivity by a matrix element. Therefore we will now calculate the matrix elements of the structured layers.

The matrix element of a structured layer j is given by (5.49)

$$W^{(j)} = \frac{S}{d}(V_a - V_b)\,\delta_{q_y,0} \sum_h \delta_{q_x,h} \Big[T_1^{(j)} T_2^{(j)}\, \tilde{\Omega}_{a1}^{(j)}(-\boldsymbol{q}_0^{(j)}) + R_1^{(j)} R_2^{(j)}\, \tilde{\Omega}_{a1}^{(j)}(-\boldsymbol{q}_3^{(j)}) + T_1^{(j)} R_2^{(j)}\, \tilde{\Omega}_{a1}^{(j)}(-\boldsymbol{q}_1^{(j)}) + R_1^{(j)} T_2^{(j)}\, \tilde{\Omega}_{a1}^{(j)}(-\boldsymbol{q}_2^{(j)}) \Big] . \tag{5.56}$$

According to the discrete Fourier transform (5.8), this allows excitations of separate truncation rods m with the lateral wave vector transfer

$$\boldsymbol{Q}_{h_m,x} = (\boldsymbol{K}_2 - \boldsymbol{K}_1)_x = h_m = \frac{2\pi}{d} \cdot m\ , \qquad m \text{ integer.} \tag{5.57}$$

This is a result we have got also from kinematical theory and the stationary phase method, Eq. (5.22).

The amplitude of each scattered wave excited by the incident wave is

$$R_h = \frac{1}{2iK_{hz}\,d} \sum_{j=2}^{N} (V_a^{(j)} - V_b^{(j)}) \Big[T_1^{(j)} T_2^{(j)}\, \tilde{\Omega}_{a1}^{(j)}\big(-h, -q_{0z}^{(j)}\big) + R_1^{(j)} R_2^{(j)}\, \tilde{\Omega}_{a1}^{(j)}\big(-h, -q_{3z}^{(j)}\big) + T_1^{(j)} R_2^{(j)}\, \tilde{\Omega}_{a1}^{(j)}\big(-h, -q_{1z}^{(j)}\big) + R_1^{(j)} T_2^{(j)}\, \tilde{\Omega}_{a1}^{(j)}\big(-h, -q_{2z}^{(j)}\big) \Big] . \tag{5.58}$$

For a rectangular grating with unique side walls this takes the form

$$R_h = \frac{iK^2}{2K_{hz}}\, \Gamma\, \mathrm{sinc}(\Gamma m\pi) \sum_{j=2}^{N} \big(\chi_a^{(j)} - \chi_b^{(j)}\big) \Big[T_1^{(j)} T_2^{(j)}\, \frac{e^{-iq_{z0}^{(j)} t_j} - 1}{-iq_{z0}^{(j)}} + R_1^{(j)} R_2^{(j)}\, \frac{e^{-iq_{z3}^{(j)} t_j} - 1}{-iq_{z3}^{(j)}} + R_1^{(j)} T_2^{(j)}\, \frac{e^{-iq_{z2}^{(j)} t_j} - 1}{-iq_{z2}^{(j)}} + T_1^{(j)} R_2^{(j)}\, \frac{e^{-iq_{z1}^{(j)} t_j} - 1}{-iq_{z1}^{(j)}} \Big] . \tag{5.59}$$

The reflectivity of the grating is

$$\mathcal{R}_h = |R_h|^2\, \frac{K_{hz}}{K_z} . \tag{5.60}$$

The scattering by each layer contributes to the amplitude of the scattered wave by four terms, characterized by the pre-factors T_1T_2, R_1R_2, T_1R_2 and R_1T_2, which are weighted by the Fourier transform of the shape function, Eqs. (5.56)–(5.59). We discuss the contributions of the four elements later in Sec. 5.7. Meanwhile, we recall that the reflectivity amplitudes are mostly small and therefore we estimate that the T_1T_2 term prevails. This is the primary scattering process between $\boldsymbol{k}_1$ and $\boldsymbol{k}_2$, see Fig. 5.7. Omitting the terms proportional to the reflectivity amplitudes R_1, R_2 we get a "semi-kinematical" approximation of the scattered amplitude

$$\begin{aligned} R_h &= \sum_{j=2}^{N} \frac{(V_a^{(j)} - V_b^{(j)})}{2iK_{hz}}\, \frac{1}{d}\, \tilde{\Omega}_{a1}^{(j)}(-h, -q_{0z}^{(j)})\; T_1^{(j)} T_2^{(j)} \\ &= \sum_{j=2}^{N} \frac{(V_a^{(j)} - V_b^{(j)})}{2iK_{hz}}\, \Gamma^{(j)}\, \mathrm{sinc}(\Gamma m\pi)\; \frac{e^{-iq_{0z}^{(j)} t_j} - 1}{-iq_{0z}^{(j)}}\; T_1^{(j)} T_2^{(j)} . \end{aligned} \tag{5.61}$$

The intensity scattered by a single layered (surface) grating calculated semi-kinematically becomes

$$\mathcal{R}_h = |R_h|^2 \, \frac{K_{hz}}{K_z} = \frac{K^4 |\chi_a - \chi_b|^2}{4 K_z K_{hz}} \, \Gamma^2 \, \mathrm{sinc}^2(\Gamma m \pi) \left| \frac{e^{-i q_{0z} t} - 1}{-i q_{0z}} \right|^2 \, |T_1 T_2|^2 \; . \tag{5.62}$$

From this follows that the grating formula has to be reformulated for the interior of the averaged layer. Then the maxima are found at positions

$$-q_{0z,p} = +(k_0 z + k_{hz})_p = \frac{2\pi}{t} \cdot p \; , \tag{5.63}$$

in accordance with relation (3.88). From this also follows the necessity of correcting the grating formula for the averaged refractive index of the grating [SJMP91, PdWL$^+$91, KLC$^+$96]. This leads to the "curved" (i.e. not equidistant in Q_x vs. Q_z) peak positions as shown in Fig. 5.8(b).

The comparison of the relations (5.59) and (5.62) to both the kinematical formula and the dynamical calculation is the subject of the discussion in Sec. 5.7.

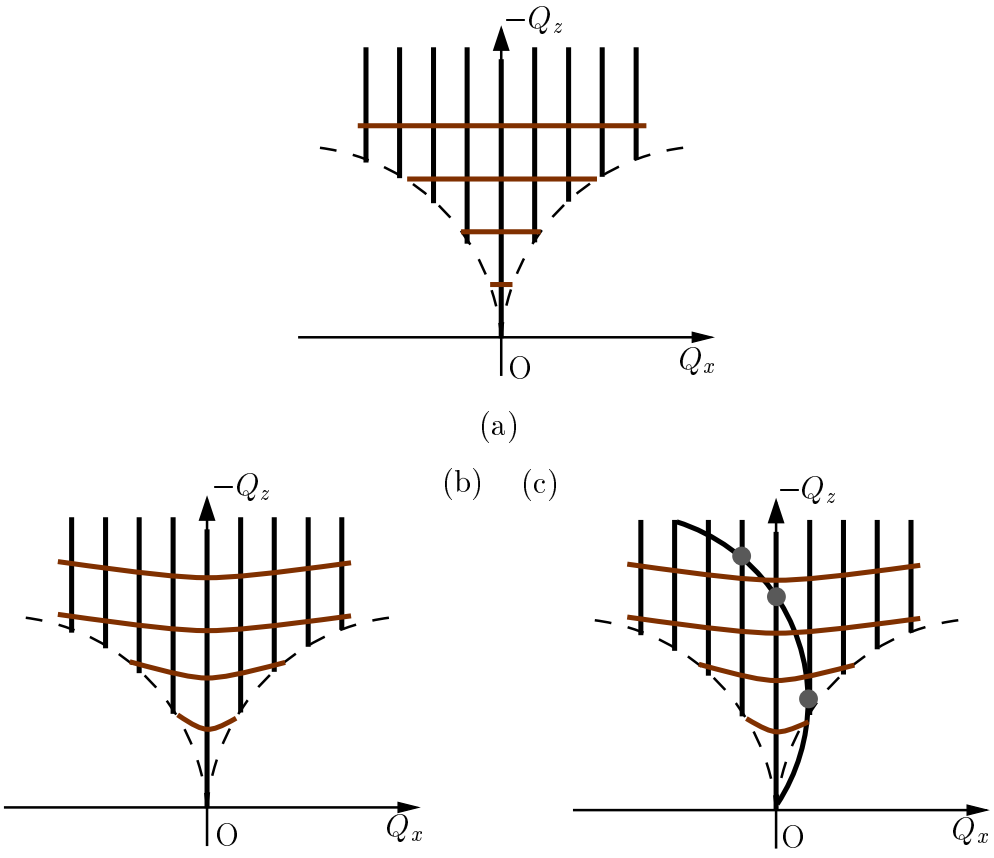

Figure 5.8. Reciprocal space maxima of a laterally periodic grating etched into a surface grating or into a periodic multilayer. The reciprocal space maxima of the grating lie on the truncation rods and that of the multilayer on sheets passing through the "Bragg peaks" or the thickness fringes on TR 0. The main reciprocal space maxima lie on the intersections. The sheets are parallel to the Q_x axis in the kinematical treatment (a), whereas they are curved in the DWBA (b) and dynamical (c) calculations due to refraction. We note that a similar phenomenon is known in diffuse scattering from correlated periodic multilayers producing "bananas" of resonant diffuse scattering [HB94]. In addition, the subfigure (c) illustrates the interaction between simultaneously excited TRs which is taken into account within the dynamical theory.

5.6 Dynamical theory

In this section we formulate the matrix dynamical theory for the scattering by a periodic multilayer grating. Firstly, we solve the wave equation within one structured layer. Then we couple the wavefields of different layers at their interfaces by means of the boundary conditions. The two-beam case, the two-beam approximation and multiple-beam approximations of the dynamical theory will be developed and their results compared.

5.6.1 Wavefields and the dispersion relation

Let us solve the wave equation in a structured medium, i.e., in a medium characterized by a lateral periodicity d. Since the susceptibility $\chi(\boldsymbol{r})$ is periodic in the direction $\hat{\boldsymbol{x}}$, its Fourier transform (5.3) is discrete and we can substitute it into the wave equation (3.12) or (5.12). We get

$$\left(\Delta + K^2\right)\, E(\boldsymbol{r}) + K^2 \sum_h \chi_h\, e^{ihx} \cdot\, E(\boldsymbol{r}) = 0 \tag{5.64}$$

or

$$\Big(\Delta + K^2(1+\chi_0)\Big) E(\boldsymbol{r}) + K^2 \sum_{h\neq 0} \chi_h\, e^{ihx} \cdot E(\boldsymbol{r}) = 0\ . \tag{5.65}$$

This procedure of using the properties of the translation symmetry from the beginning of solving the wave equation or the Schrödinger equation is known as the Ewald concept [CJK92, LMD96], because the mathematical form of the wavefield propagating in a periodic medium and fulfilling the above equation has been found by Ewald in his dynamical theory of diffraction in crystals. Later it was applied by Bloch in solid state physics (the Bloch theorem [AM76]). It is also referenced as the Floquet theorem in the case of one-dimensional periodicity [SJMP91].

This Ewald solution $E(\boldsymbol{r})$ is a superposition of plane waves

$$E(\boldsymbol{r}) \;=\; \sum_h E_h(\boldsymbol{r}) = e^{i(k_x x + k_y y)} \sum_h e^{ihx}\, E_h(z) = e^{ik_y y} \sum_h e^{ik_{hx} x}\, E_h(z)\ , \tag{5.66}$$

$$k_{hx} \;=\; k_x + h\ . \tag{5.67}$$

Introducing the variables

$$\kappa_{hz} = +\sqrt{K^2\chi_0 - (k_{hx}^2 + k_y^2)} \tag{5.68}$$

the wave equation decomposes into a set of differential equations for each Fourier component h

$$\kappa_{hz}^2\, E_h(z) + \frac{\mathrm{d}^2 E_h(z)}{\mathrm{d}z^2} + K^2 \sum_{g,g\neq h} E_g(z)\, \chi_{h-g} = 0\ . \tag{5.69}$$

We interprete κ_{hz} as the z-components of the diffracted-transmitted wave vectors $(k_{hx}, k_y, \kappa_{hz})$ which fullfill the dispersion equation (3.11) (cf. the kinematical expression (5.19)).

We solve Eq. (5.69) by choosing the particular solutions as the plane waves

$$E_{h,n}(z) = e^{ik_{zn}z}\, E_{h,n}\ , \tag{5.70}$$

where n enumerates the particular solutions. The set of equations [AEM92]

$$\left(\kappa_{hz}^2 - k_{zn}^2\right)\, E_{h,n} + K^2 \sum_{g,g\neq h} E_{g,n}\, \chi_{h-g} = 0 \tag{5.71}$$

is obtained for each component h. The above equation can be conveniently rewritten using the *matrix formalism*

$$\left[\hat{\mathrm{A}} - k_{zn}^2 \hat{\mathrm{I}}\right] \vec{E}_n = \vec{0}\ , \tag{5.72}$$

$$\hat{\mathrm{A}} = \begin{pmatrix} \ddots & & & & \\ & \kappa^2_{-h,z} & K^2\chi_{-h} & K^2\chi_{-2h} & \\ & K^2\chi_h & \kappa^2_{0z} & K^2\chi_{-h} & \\ & K^2\chi_{2h} & K^2\chi_h & \kappa^2_{hz} & \\ & & & & \ddots \end{pmatrix}, \qquad \vec{E}_n = \begin{pmatrix} \vdots \\ E_{-h,n} \\ E_{0,n} \\ E_{h,n} \\ \vdots \end{pmatrix}, \tag{5.73}$$

where $\hat{\mathrm{I}}$ is the unity matrix, $\vec{0}$ is column vector of zeros. The matrix form of (5.72) shows that the differential wave equation (3.12), (5.65) has been transformed into an eigenvalue problem.

Now let us combine the particular solutions in order to express the whole wavefield in the structured medium (structured layer). We can see that the solution of this equation gives unique amplitude $E_{h,n}$ for both $\pm k_{zn}$. Therefore we further let $k_{zn} > 0$ and get two sets of the particular solution

$$E^+_{h,n}(z) = e^{ik_{zn}z}\, E_{h,n}\ , \qquad E^-_{h,n}(z) = e^{-ik_{zn}z}\, E_{h,n}\ . \tag{5.74}$$

The physical meaning is that each diffracted wave occurs simultaneously as a pair of the diffracted-transmitted (k_{zn}) and diffracted-reflected ($-k_{zn}$) waves.

The solution of the wave equation is a linear combination of the particular solutions [SJMP91]

$$E_h(z) = \sum_n \left[T'_n\, E_{h,n}(z) + R'_n\, E^-_{h,n}(z)\right] = \sum_n \left(T'_n\, e^{ik_{zn}z} + R'_n\, e^{-ik_{zn}z}\right) E_{h,n}\ , \tag{5.75}$$

where we denoted the coefficients of the linear combination by T'_n, R'_n. Taking the simplest case of $n = 1$ we get

$$E_h(z) = T'\, e^{ik_{z,1}z}\, E_{h,1} + R'\, e^{-ik_{z,1}z}\, E_{h,1} \tag{5.76}$$

which is exactly the form (4.52), with $E_{h,1} = 1$ being the eigenvectors of (5.72). Therefore we relate the amplitudes T_n, R_n with respect to the lower layer interface and get the final form

$$E_h(z) = \sum_n \left[e^{ik_{zn}(z-z_{j+1})}\, T_n + e^{-ik_{zn}(z-z_{j+1})}\, R_n\right] E_{h,n}\ , \tag{5.77}$$

where n goes over all the particular solutions of Eq. (5.69).

Eq. (5.71) can be better understood if it is rearranged into the form

$$E_{h,n} = \frac{K^2}{k^2_{zn} - \kappa^2_{hz}} \sum_{g,g\neq h} E_{g,n}\, \chi_{h-g}\ . \tag{5.78}$$

Each component E_h (i.e., the particular wavefield corresponding to the truncation rod h) is given by the sum over contributions of the other excited waves E_g weighted by χ_{h-g}. We have shown this schematically in Fig. 5.9. The vector $h-g$ is the momentum transfer between the TRs g and h. The amplitude of $E_{h,n}$ is proportional to the *resonance factor* $\frac{K^2}{k^2_{zn}-\kappa^2_{hz}}$. Since the amplitude $E_{h,n}$ has to be finite, then $\kappa_{hz} \neq k_{zn}$. Therefore the dispersion relation for the diffracted waves is not the Ewald sphere. Such a phenomena is known in the dynamical theory of X-ray diffraction (the end-points of the wave vectors lie on the *dispersion surface* [Pin78, AEM92, MVV$^+$94]).

Since the series (5.2) and (5.66) are infinite, the dimensions of $\hat{\mathrm{A}}$ and $\vec{E}_n$ are infinite too. This cannot be handled numerically and a reasonable restriction to a finite number $\mathcal{D}$ of scattered and interacting waves has to be undertaken. We choose the number of waves in the numerical calculation so that the amplitudes E_h of the TRs of interest are approximated with a given precision.

The restriction to $\mathcal{D}$ interacting pairs of waves (each pair consists of the transmitted and reflected wave) determines the dimension $\mathcal{D}$ of the particular matrix $\hat{\mathrm{A}}$, thus the eigenvalue

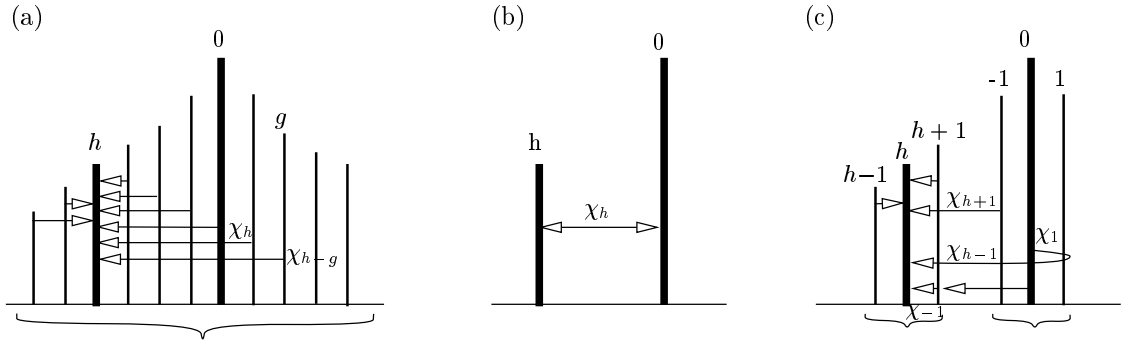

Figure 5.9. Schematic drawing of the dynamical scattering processes. In the fully dynamical theory (a), the truncation rod h is excited by the multiple scattering from all the other truncation rods, as given by (5.78). (b) In the two-beam case (and the two-beam approximation, see Sec. 5.6.4), the truncation rod h is excited by the zeroth TR, which means we calculate it as a single-scattering interaction between the incident wavefield and the wavefield diffracted to the TR h. (c) In the multiple-beam approximation only a specified set of the TRs around the TRs h and 0 contribute essentially to the amplitude of the TR h. Here the approximation of the first order is shown which calculates dynamically the scattering into the given TR h as the dynamical interaction between TRs $h-1, h, h+1$ and $-1, 0, 1$. If the Fourier coefficient $\chi_h = 0$, then the direct single-scattering process $0 \to h$ is not allowed, i.e., it does not contribute to the amplitude of the wavefield h. Then the multiple-scattering processes (we show $0 \to 1 \to h$ or $0 \to h-1 \to h$) are of decisive importance.

problem can be solved numerically. The numerical calculation is further simplified in the case $\chi_{-h} = \chi_h$. Then the matrix $\hat{\mathrm{A}}$ is symmetric, and in a non-absorbing medium it would be real.

The solution of Eq. (5.72) gives $\mathcal{D}$ wave vector components k_{zn} forming column vector $\vec{k}_z$, and $\mathcal{D}$ associated column eigenvectors $\vec{E}_n$ forming the matrix $\hat{\mathrm{E}}$. The vectors $\vec{E}_n$ are unique except for a multiplicative constant (see (5.72)), allowing us the choice $E_{n,n} = 1$ for each n.

In the following section we denote for each layer j the column vectors of T_n, R_n, k_{zn} by $\vec{T}^{(j)}$, $\vec{R}^{(j)}$, $\vec{k}_z^{(j)}$, respectively. $\hat{\mathrm{k}}_z^{(j)}$ is the diagonal matrix of the eigenvalues $k_{z,n}$ and $\hat{\mathrm{E}}^{(j)}$ is the corresponding eigenvector matrix. The dimension of these vectors and matrices is $\mathcal{D}$.

5.6.2 Boundary conditions

In the previous part we have found the form of the wavefield in a structured layer being a series of plane waves (5.66) and (5.77). In order to find the coefficients $T_n^{(j)}, R_n^{(j)}$ which determine the value of the excitation of the particular solution, we have to connect the wavefields in the layers with the wavefields in the vacuum and in the substrate. We will make use of the convenient matrix formalism similar to the Abèles method [Ab50] as it is used for this task by all the authors (see [SJMP91, Nev94] for instance).

The boundary conditions provide the relations coupling the wavefields and their derivatives at the interfaces as we have already treated in Sec. 3.4.1. Let us apply them in order to connect the wavefields of two neighbouring layers j and $j+1$ at their common interface j at $z = z_j$. In the present calculation we will closely follow the matrix formalism we used in the reflectivity calculation, see sections 3.4.3 and 3.4.4.

Since the equality between wavefield amplitudes and normal derivatives holds at each point (x, y, z_j) of each interface j, the conditions for the undetermined coefficients $T_n^{(j)}, R_n^{(j)}$ can be expressed by the matrix relation (cf. (3.47) and (3.56))

$$\mathcal{P}^{(j)} \cdot \begin{pmatrix} \vec{T}^{(j)} \\ \vec{R}^{(j)} \end{pmatrix} = \mathcal{P}^{(j+1)} \cdot \mathcal{Q}^{(j+1)} \cdot \begin{pmatrix} \vec{T}^{(j+1)} \\ \vec{R}^{(j+1)} \end{pmatrix} . \tag{5.79}$$

The *boundary matrices* $\mathcal{P}^{(j)}$ are

$$\mathcal{P}^{(j)} = \begin{pmatrix} \hat{\mathrm{E}}^{(j)} & \hat{\mathrm{E}}^{(j)} \\ \hat{\mathrm{E}}^{(j)}\,\hat{\mathrm{k}}_z^{(j)} & -\hat{\mathrm{E}}^{(j)}\,\hat{\mathrm{k}}_z^{(j)} \end{pmatrix} \tag{5.80}$$

for structured layers and

$$\mathcal{P}^{(j)} = \begin{pmatrix} \hat{\mathrm{I}} & \hat{\mathrm{I}} \\ \hat{\kappa}_z^{(j)} & -\hat{\kappa}_z^{(j)} \end{pmatrix} \tag{5.81}$$

for homogeneous layers (including both the vacuum and substrate, cf. (3.48)). The *propagation matrices* $\mathcal{Q}^{(j)}$ connect the amplitudes of the waves between the bottom and top interface of a layer (cf. (3.56) and (3.57))

$$\mathcal{Q}^{(j)} = \begin{pmatrix} \mathcal{Q}^{(j)+} & \hat{0} \\ \hat{0} & \mathcal{Q}^{(j)-} \end{pmatrix} . \tag{5.82}$$

$\mathcal{Q}^{(j)\pm}$ are diagonal matrices with the diagonal vector

$$\left(e^{\mp i k_{1,z}^{(j)} t_j}, e^{\mp i k_{2,z}^{(j)} t_j}, \ldots, e^{\mp i k_{\mathcal{D},z}^{(j)} t_j} \right) \tag{5.83}$$

for structured layers, and

$$\left(\ldots, e^{\mp i \kappa_{-1,z}^{(j)} t_j}, e^{\mp i \kappa_{0,z}^{(j)} t_j}, e^{\mp i \kappa_{1,z}^{(j)} t_j}, \ldots \right) \tag{5.84}$$

for homogeneous layers. The dimension of matrices $\mathcal{P}$ and $\mathcal{Q}$ is $2\mathcal{D}$.

Introducing the *transfer matrix of layer* j (cf. (3.63))

$$\hat{\mathrm{M}}^{(j)} = \mathcal{P}^{(j)} \cdot \mathcal{Q}^{(j)} \cdot (\mathcal{P}^{(j)})^{-1} , \tag{5.85}$$

the vacuum (index v) and the substrate (index s) waves are coupled by the transfer matrix of the whole multilayer $\hat{\mathrm{M}}$

$$\begin{aligned} &\begin{pmatrix} \vec{T}^v \\ \vec{R}^v \end{pmatrix} = \hat{\mathrm{M}} \cdot \begin{pmatrix} \vec{T}^s \\ \vec{R}^s \end{pmatrix} \\ &\hat{\mathrm{M}} = (\mathcal{P}^v)^{-1} \cdot \prod_{j=2}^{N} \hat{\mathrm{M}}^{(j)} \cdot \mathcal{P}^s \equiv \begin{pmatrix} \hat{\mathrm{M}}_{11} & \hat{\mathrm{M}}_{12} \\ \hat{\mathrm{M}}_{21} & \hat{\mathrm{M}}_{22} \end{pmatrix} . \end{aligned} \tag{5.86}$$

We employ two additional conditions. Firstly, the substrate is semi-infinite, therefore reflected waves are not excited in it ($\vec{R}^s = \vec{0}$). Secondly, there is only one beam incident on the sample, therefore $\vec{T}^v$ is zero vector except for the element corresponding to $h = 0$, which is unity, $\vec{T}^v = (0, \ldots, 0, 1, 0, \ldots, 0)$. Then the amplitudes of the reflected waves (measured in the vacuum, above the sample surface) are

$$\vec{R}^v = \hat{\mathrm{M}}_{21} \cdot \hat{\mathrm{M}}_{11}^{-1} \cdot \vec{T}^v . \tag{5.87}$$

In other words, vector $\vec{R}^v$ is the column vector of the matrix $(\hat{\mathrm{M}}_{21} \cdot \hat{\mathrm{M}}_{11}^{-1})$ corresponding to the column of $h = 0$. This can be considered as a generalization of the simple relation (3.62).

The reflected intensity of the wave h is $|R_h^v|^2$ and the reflectivity of the grating is

$$\mathcal{R}_h = |R_h^v|^2 \, \frac{K_{hz}}{K_z} . \tag{5.88}$$

In summary, we expressed the problem of the scattering from a MLG by a matrix formalism, which is very similar to the matrix formalism we used in the reflectivity calculation, Secs. 3.4.3

and 3.4.4. However, the matrices employed here are of higher order and the eigenvector matrices $\hat{\mathrm{E}}^{(j)}$ are calculated by the present procedure.

Finally, let us make a comment on the numerical implementation of the matrix calculation. In this calculation, these matrix operations are used: multiplication, eigenvalue problem and matrix inversion. Since the matrix multiplication is an algorithmically straightforward process, we can encounter only two numerically difficult points: the eigenvalue problem (5.72) and the matrix inversions (5.85) and (5.87). We have found that the solution of the eigenvalues and eigenvectors as well as the inversion of the matrix of the eigenvectors are numerically stable.[3] However, the calculation of the evanescent waves in a thick multilayer can lead to numerically singular matrix $\hat{\mathrm{M}}_{11}$. This follows from the exponential terms in (5.83) or (5.84), which are very large for imaginary k_z and thick layers (large t_j). This very large number can propagate in the matrix multiplication and cause the numbers in the corresponding column in $\hat{\mathrm{M}}_{11}$ to becomes very large compared to the other matrix elements. Then the numerical inversion will fail. We can avoid this problem by either of two methods. Firstly, we can calculate the transfer matrix of the whole multilayer from the vacuum (in $+z$ direction) and stop the calculation in the layer where the transmitted waves are sufficiently weak. Secondly, we can calculate the transfer matrix of the whole MLG and then apply the following trick. We demonstrate it for a matrix $\hat{\mathrm{M}}_{11}$, where $M_{j\mathcal{D}}$ are large numbers and M_{jk} are about unity ($1 \le k < \mathcal{D}$, $1 \le j \le \mathcal{D}$). Using the identity

$$\begin{aligned}\hat{\mathrm{M}}_{11} &\equiv \begin{pmatrix} M_{11} & M_{12} & \dots & M_{1\mathcal{D}} \\ M_{21} & M_{22} & \dots & M_{2\mathcal{D}} \\ & & \dots & \\ M_{\mathcal{D}1} & M_{\mathcal{D}2} & \dots & M_{\mathcal{D}\mathcal{D}} \end{pmatrix} \\ &= \begin{pmatrix} M_{11} & M_{12} & \dots & M_{1\mathcal{D}}/M_{\mathcal{D}\mathcal{D}} \\ M_{21} & M_{22} & \dots & M_{2\mathcal{D}}/M_{\mathcal{D}\mathcal{D}} \\ & & \dots & \\ M_{\mathcal{D}1} & M_{\mathcal{D}2} & \dots & 1 \end{pmatrix} \begin{pmatrix} 1 & 0 & \dots & 0 \\ 0 & 1 & \dots & 0 \\ & & \dots & \\ 0 & \dots & 0 & M_{\mathcal{D}\mathcal{D}} \end{pmatrix}\end{aligned} \tag{5.89}$$

the inverse matrix is

$$(\hat{\mathrm{M}}_{11})^{-1} = \begin{pmatrix} 1 & 0 & \dots & 0 \\ 0 & 1 & \dots & 0 \\ & & \dots & \\ 0 & \dots & 0 & 1/M_{\mathcal{D}\mathcal{D}} \end{pmatrix} \begin{pmatrix} M_{11} & M_{12} & \dots & M_{1\mathcal{D}}/M_{\mathcal{D}\mathcal{D}} \\ M_{21} & M_{22} & \dots & M_{2\mathcal{D}}/M_{\mathcal{D}\mathcal{D}} \\ & & \dots & \\ M_{\mathcal{D}1} & M_{\mathcal{D}2} & \dots & 1 \end{pmatrix}^{-1} . \tag{5.90}$$

The elements of the latter matrix are of the same order and the numerical inversion runs without problems.

Similar procedure can be applied in presence of more evanescent waves, i.e., for more huge columns present in $\hat{\mathrm{M}}_{11}$. Then the inversion of M_{11} is given by the product of diagonal matrix and a matrix to be inverted.

5.6.3 Relation to the Fresnel coefficients

In this section we reformulate the above matrix method based on layer transfer matrices in such a way that the new approach will make use of the matrices of the Fresnel-like coefficients. This means that we show how we can switch from the bulk-like approach of $\mathcal{M}^{(j)}$ matrices to the interface-like approach of $\mathcal{N}_j$. Later we will show the advantage of this interface-like representation for studying the reflectivity from gratings with rough interfaces. We recall that we dealt with both matrix approaches in the dynamical theory of the reflection from planar multilayers, Sec. 3.4.4.

[3] My program is written in C++. It employs the matrix libraries from the source code of program `octave`, where the `blas` and `lapack` routines are used. Program `octave` is a `Matlab`-like clone and it is free software (distributed under the GNU General Public License).

Let us reexpress Eq. (5.79) so that it includes directly the matrix of the transition through an interface j (cf. (3.50)–(3.51)) and, consequently, the $\mathcal{N}_j$ matrices (cf. (3.58)–(3.59))

$$\begin{aligned}
\begin{pmatrix} \vec{T}^{(j)} \\ \vec{R}^{(j)} \end{pmatrix} &= \mathcal{N}_j \begin{pmatrix} \vec{T}^{(j+1)} \\ \vec{R}^{(j+1)} \end{pmatrix} && (5.91)\\
\mathcal{N}_j &\equiv \mathcal{P}_{j,j+1} \cdot \mathcal{Q}^{(j+1)} && (5.92)\\
\mathcal{P}_{j,j+1} &\equiv \left(\mathcal{P}^{(j)}\right)^{-1} \mathcal{P}^{(j+1)} \ . && (5.93)
\end{aligned}$$

We rewrite the boundary matrix (5.80) so that the matrices of eigenvectors and of wave vectors are separated

$$\begin{aligned}
\mathcal{P}^{(j)} &= \begin{pmatrix} \hat{\mathrm{E}}^{(j)} & \hat{\mathrm{E}}^{(j)} \\ \hat{\mathrm{E}}^{(j)}\,\hat{\mathrm{k}}_z^{(j)} & -\hat{\mathrm{E}}^{(j)}\,\hat{\mathrm{k}}_z^{(j)} \end{pmatrix} = \begin{pmatrix} \hat{\mathrm{E}}^{(j)} & 0 \\ 0 & \hat{\mathrm{E}}^{(j)} \end{pmatrix} \begin{pmatrix} \hat{\mathrm{I}} & \hat{\mathrm{I}} \\ \hat{\mathrm{k}}_z^{(j)} & -\hat{\mathrm{k}}_z^{(j)} \end{pmatrix} && (5.94)\\
\left(\mathcal{P}^{(j)}\right)^{-1} &= \frac{1}{2} \begin{pmatrix} \hat{\mathrm{I}} & \left(\hat{\mathrm{k}}_z^{(j)}\right)^{-1} \\ \hat{\mathrm{I}} & -\left(\hat{\mathrm{k}}_z^{(j)}\right)^{-1} \end{pmatrix} \begin{pmatrix} \left(\hat{\mathrm{E}}^{(j)}\right)^{-1} & 0 \\ 0 & \left(\hat{\mathrm{E}}^{(j)}\right)^{-1} \end{pmatrix} \ . && (5.95)
\end{aligned}$$

The "interface matrix" (5.93) becomes

$$\begin{aligned}
\mathcal{P}_{j,j+1} &= \frac{1}{2} \begin{pmatrix} \hat{\mathrm{I}} & \left(\hat{\mathrm{k}}_z^{(j)}\right)^{-1} \\ \hat{\mathrm{I}} & -\left(\hat{\mathrm{k}}_z^{(j)}\right)^{-1} \end{pmatrix} \begin{pmatrix} \left(\hat{\mathrm{E}}^{(j)}\right)^{-1} & 0 \\ 0 & \left(\hat{\mathrm{E}}^{(j)}\right)^{-1} \end{pmatrix} \cdot \begin{pmatrix} \hat{\mathrm{E}}^{(j+1)} & 0 \\ 0 & \hat{\mathrm{E}}^{(j+1)} \end{pmatrix} \begin{pmatrix} \hat{\mathrm{I}} & \hat{\mathrm{I}} \\ \hat{\mathrm{k}}_z^{(j+1)} & -\hat{\mathrm{k}}_z^{(j+1)} \end{pmatrix} \\
&\equiv \begin{pmatrix} \hat{\tau}_j & \hat{\rho}_j \\ \hat{\rho}_j & \hat{\tau}_j \end{pmatrix} \ . && (5.96)
\end{aligned}$$

the form of which corresponds formally to the *"interface matrix" of the Fresnel coefficients* (3.51) for an interface of a planar multilayer.

We introduced these matrices of dimension $\mathcal{D}$

$$\begin{aligned}
\hat{\tau}_j &= \frac{1}{2}\left[\hat{\mathrm{E}}_{j,j+1} + (\hat{\mathrm{k}}_z^{(j)})^{-1}\ \hat{\mathrm{E}}_{j,j+1}\ \hat{\mathrm{k}}_z^{(j+1)}\right] \\
\hat{\rho}_j &= \frac{1}{2}\left[\hat{\mathrm{E}}_{j,j+1} - (\hat{\mathrm{k}}_z^{(j)})^{-1}\ \hat{\mathrm{E}}_{j,j+1}\ \hat{\mathrm{k}}_z^{(j+1)}\right] && (5.97)\\
\hat{\mathrm{E}}_{j,j+1} &= \left(\hat{\mathrm{E}}^{(j)}\right)^{-1}\ \hat{\mathrm{E}}^{(j+1)} \ .
\end{aligned}$$

Since the matrices $\hat{\mathrm{k}}_z$ are diagonal, the matrix elements are calculated as simply as

$$\begin{aligned}
\tau_{j,mn} &= \frac{1}{2}\,(E_{j,j+1})_{mn}\left(1 + k_{z,n}^{(j+1)}/k_{z,m}^{(j)}\right) \\
\rho_{j,mn} &= \frac{1}{2}\,(E_{j,j+1})_{mn}\left(1 - k_{z,n}^{(j+1)}/k_{z,m}^{(j)}\right) \ . && (5.98)
\end{aligned}$$

If we introduce the matrix of generalized Fresnel transmission and reflection coefficients $\hat{\mathfrak{t}}_j, \hat{\mathfrak{r}}_j$ with the elements

$$\begin{aligned}
\mathfrak{t}_{j,mn} &= \frac{2k_{z,m}^{(j)}}{k_{z,m}^{(j)} + k_{z,n}^{(j+1)}} \\
\mathfrak{r}_{j,mn} &= \frac{k_{z,m}^{(j)} - k_{z,n}^{(j+1)}}{k_{z,m}^{(j)} + k_{z,n}^{(j+1)}} && (5.99)
\end{aligned}$$

(compare (3.52)) then we can rewrite the former relations

$$\begin{aligned}
\tau_{j,mn} = (E_{j,j+1})_{mn} \cdot \frac{1}{\mathfrak{t}_{j,mn}} \quad &\longrightarrow \quad \hat{\tau}_j \equiv \hat{\mathrm{E}}_{j,j+1} \odot \frac{1}{\hat{\mathfrak{t}}_j} \\
\rho_{j,mn} = (E_{j,j+1})_{mn} \cdot \frac{\mathfrak{r}_{j,mn}}{\mathfrak{t}_{j,mn}} \quad &\longrightarrow \quad \hat{\rho}_j \equiv \hat{\mathrm{E}}_{j,j+1} \odot \frac{\hat{\mathfrak{r}}_j}{\hat{\mathfrak{t}}_j} \ . && (5.100)
\end{aligned}$$

We defined the matrix operations $\hat{\mathrm{a}} \odot \hat{\mathrm{b}}$ and $\frac{\hat{\mathrm{a}}}{\hat{\mathrm{b}}}$ as the element-by-element multiplication and division operations, respectively. The meaning of the matricial Fresnel coefficients is the following. A transmission coefficient $\tau_{j,mn}$ corresponds to the transmission of the wave $k_{z,m}^{(j)}$ (in layer j) through the interface j into the wave $k_{z,n}^{(j+1)}$ in layer j+1.

Let us consider the special case of an interface separating two homogeneous layers. There is no lateral diffraction in these layers, therefore $\hat{\mathrm{E}}^{(j)}, \hat{\mathrm{E}}^{(j+1)}$ and $\hat{\mathrm{E}}_{j,j+1}$ are unity. The matrices $\hat{\tau}_j = \hat{\mathfrak{t}}_j$ and $\hat{\rho}_j = \hat{\mathfrak{r}}_j$ are diagonal and their elements correspond to the Fresnel coefficients according to the "classical" Fresnel formulae (3.52)

$$\begin{aligned}
\hat{\mathfrak{r}}_j &= \frac{\hat{\mathrm{k}}_z^{(j)} - \hat{\mathrm{k}}_z^{(j+1)}}{\hat{\mathrm{k}}_z^{(j)} + \hat{\mathrm{k}}_z^{(j+1)}} = \begin{pmatrix} \frac{k_{z,1}^{(j)} - k_{z,1}^{(j+1)}}{k_{z,1}^{(j)} + k_{z,1}^{(j+1)}} & 0 & 0 & \dots \\ 0 & \frac{k_{z,2}^{(j)} - k_{z,2}^{(j+1)}}{k_{z,2}^{(j)} + k_{z,2}^{(j+1)}} & 0 & \dots \\ 0 & 0 & \dots & \dots \end{pmatrix} \\
\hat{\mathfrak{t}}_j &= \frac{2\hat{\mathrm{k}}_z^{(j)}}{\hat{\mathrm{k}}_z^{(j)} + \hat{\mathrm{k}}_z^{(j+1)}} = \begin{pmatrix} \frac{2k_{z,1}^{(j)}}{k_{z,1}^{(j)} + k_{z,1}^{(j+1)}} & 0 & 0 & \dots \\ 0 & \frac{2k_{z,2}^{(j)}}{k_{z,2}^{(j)} + k_{z,2}^{(j+1)}} & 0 & \dots \\ 0 & 0 & \dots & \dots \end{pmatrix} .
\end{aligned} \tag{5.101}$$

The matrices $\hat{\mathrm{k}}_z$, $\hat{\mathfrak{t}}$ and $\hat{\mathfrak{r}}$ are diagonal and therefore we have used the properties of the algebraic operations on the class of these matrices. These operations are similar to those on real numbers (commutativity of the multiplication, $\hat{\mathrm{k}}^{-1} = 1/\hat{\mathrm{k}}$, etc.).

This reformulation of the approach of the interface matrices $\mathcal{M}^{(j)}$ we dealt with in Sec. 5.6.2 turns into the formalism of the $\mathcal{N}_j = \mathcal{P}_{j,j+1}\mathcal{Q}^{(j+1)}$ matrices we preferred for planar multilayers in Sec. 3.4.4. Therefore the transfer matrix $\mathcal{M} = \prod_j \mathcal{N}_j$ of the whole multilayer grating can be computed either by means of the bulk-related formalism using the matrix $\mathcal{M}$ of Eq. (5.86), which is analogous to (3.64)–(3.65), or by the interface-related formalism using the matrices $\mathcal{N}_j$ in direct analogy to (3.61).

5.6.4 Two-beam case and multiple-beam approximations of the dynamical theory

In the fully dynamical theory formulated above, the interaction of an "infinite" number (i.e., the number of TRs intersecting the Ewald sphere) of diffracted wavefields is taken into account, Eq. (5.71). However, not all the truncation rods produce strong diffracted wavefields. For example, the diffraction orders $h \neq 0$ are weak in a surface grating for angles of incidence and exit above the critical angle. Therefore only a small number of truncation rods can be considered in the (numerical) calculation.

In this section we propose a ***two-beam approximation*** of the dynamical theory of reflection from gratings, quite similar to the so-called two-beam case of the dynamical theory of X-ray diffraction by crystals [AKK+74, Pin78]. The differences between these two methods can be found in the reciprocal space. In XRD, the usual experimental conditions are such that the Ewald sphere passes through or near only one reciprocal lattice point (Bragg peak), and the other reciprocal lattice points are so far that the case of the multiple-beam scattering can be neglected. However, in the former case the Ewald sphere always intersects many truncation rods of the reciprocal lattice of the periodic grating, see Fig. 5.5. What we can expect is that for large-period gratings the TRs are near, thus their dynamical interaction is increased, whereas for small-period gratings the TRs distances are larger and the dynamical interaction is smaller.

The two-beam approximation follows from the dynamical theory of reflection treated above. We suppose that the fan of the dynamically interacting wavefield consists of two truncation rods 0 and $h \neq 0$. We are going to show that in this case the matricial equations can be reduced into simple analytical formulae.

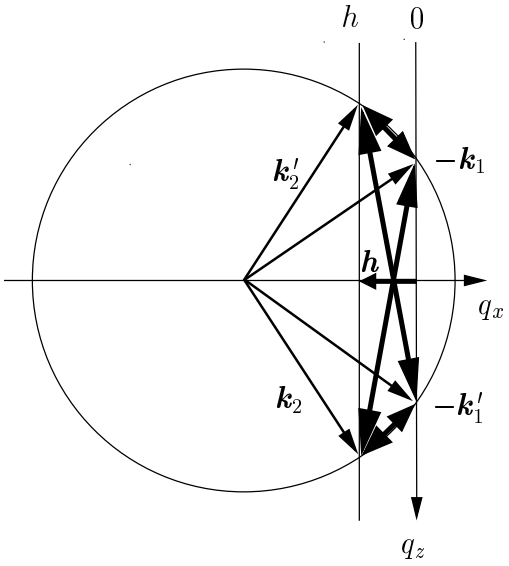

Figure 5.10. Ewald construction of the dynamical interaction acting in the two-beam approximation of the dynamical theory among the incident-transmitted, incident-reflected, diffracted-transmitted and diffracted-reflected waves. Similar figures drawn for the kinematical theory as well as for the DWBA are drawn in Figs. 5.6 and 5.7, respectively. We notice that the DWBA considers only the interaction between the incident-transmitted and incident-reflected waves and between the diffracted-transmitted and diffracted-reflected waves, and not among all four waves.

The two truncation rods 0 and $h \neq 0$ form two pairs of interacting wavefields: the transmitted and reflected incident waves ($h = 0$) and the transmitted and reflected diffracted waves ($h \neq 0$). The calculation will be therefore equivalent to the ($\mathcal{D}'$=2)-beam case of the dynamical theory.

According to (5.77), these two interacting wavefields inside the structured layer are

$$\begin{aligned} E_0(z) &= e^{ik_{z0}(z-z_j)}\, T_0 E_{0,0} + e^{-ik_{z0}(z-z_j)}\, R_0 E_{0,0} + e^{ik_{zh}(z-z_j)}\, T_h E_{0,h} + e^{-ik_{zh}(z-z_j)}\, R_h E_{0,h} \\ E_h(z) &= e^{ik_{z0}(z-z_j)}\, T_0 E_{h,0} + e^{-ik_{z0}(z-z_j)}\, R_0 E_{h,0} + e^{ik_{zh}(z-z_j)}\, T_h E_{h,h} + e^{-ik_{zh}(z-z_j)}\, R_h E_{h,h} \ , \end{aligned} \tag{5.102}$$

where we conveniently enumerated the beams by $n = 0, h$ instead of the usual enumeration of the particular solutions $n = 1, 2$ used in the dynamical theory above. Then the matrix formulation of the wave equation (5.72), supposing $\chi_h = \chi_{-h}$ for simplicity, reads

$$\begin{pmatrix} \kappa_0^2 - k_{zn}^2 & K^2\chi_h \\ K^2\chi_h & \kappa_h^2 - k_{zn}^2 \end{pmatrix} \begin{pmatrix} E_{0,n} \\ E_{h,n} \end{pmatrix} = 0 \ . \tag{5.103}$$

This leads to the *quadratic dispersion relation* for k_{zn}^2

$$(\kappa_0^2 - k_{zn}^2)(\kappa_h^2 - k_{zn}^2) - K^4\chi_h^2 = 0 \ . \tag{5.104}$$

In comparison with the similar equations of the two-beam case of the dynamical X-ray diffraction[4] the present one is mathematically more simple. The unknown wave vector components (eigenvalues) k_{zn} occur only on the matrix diagonal. This is because in the not-strongly asymmetric Bragg-case of the X-ray diffraction from crystals the net planes more or less parallel to the surface are diffracting (diffraction by $\boldsymbol{b}_{hkl}, l \neq 0$). In the present case of XRR the lateral grating diffracts the wavefields by $\boldsymbol{b}_{h0l}$, l is small. Therefore the present interpretation is closer to the grazing-incidence X-ray diffraction than to the conventional one.

[4] This dispersion equation, written in the usual notation [AKK+74, Pin78], comes from the matrix equation
$\begin{pmatrix} k^2 - k_0^2 & C\chi_{-h}k_0^2 \\ C\chi_h k_h^2 & k^2 - k_h^2 \end{pmatrix} \begin{pmatrix} D_0 \\ D_h \end{pmatrix} = 0$,
thus it is $(k^2 - k_0^2)(k^2 - k_h^2) - C^2\chi_h\chi_{-h}k_0^2k_h^2 = 0$.

We solve the dispersion relation and get

$$k^2_{\substack{z0\\zh}} = \frac{1}{2}\left[\kappa_0^2+\kappa_h^2 \pm (\kappa_0^2-\kappa_h^2)\sqrt{1+w_h^2}\right] \tag{5.105a}$$

$$\vec{E}_0 = \begin{pmatrix}1\\ E_{0h}\end{pmatrix}, \qquad \vec{E}_h = \begin{pmatrix}-E_{0h}\\ 1\end{pmatrix} \tag{5.105b}$$

$$E_{0h} = \frac{1}{w_h}\left[\sqrt{1+w_h^2}-1\right] \tag{5.105c}$$

$$w_h \equiv \frac{2K^2\chi_h}{\kappa_0^2-\kappa_h^2}\,. \tag{5.105d}$$

We note that

$$\kappa_0^2-\kappa_h^2 = h(2k_x+h) \tag{5.106}$$

and the roots k_{z0} and k_{zh} of the quadratic equation (5.105a) must have either the real part positive (real transmitted waves), or the imaginary part negative (evanescent waves).

The variable w_h depends further on the incidence wave vector component k_x, i.e., $w_h(k_x)$. Let us notice that defining $y_h = 1/w_h$ we can rewrite Eq. (5.105c) into the equivalent form

$$E_{0h} = -\left[y_h - \mathrm{sgn}\,(y_h)\sqrt{1+y_h^2}\right]\,, \tag{5.107}$$

which is similar to the well-known expression for the two-beam case of dynamical XRD for $c^{(i)} = D_h/D_0$ in the Laue case of diffraction [Pin78]. This we can understand by a simple consideration: in the present case, the lateral wave vector transfer $\boldsymbol{h}$ is much smaller than the lateral component $\boldsymbol{K}_{||}$ of the scattered wave vectors, therefore all waves are diffracted forward (see Fig. 5.4) as in the Laue case of diffraction.

The solution of the dispersion relation can be approximated if

$$|w_h| = 2K^2\,|\chi_h||\kappa_0^2-\kappa_h^2| \;\lesssim\; \frac{2K^2}{h(2k_x+h)}\frac{|\chi_a-\chi_b|\,\Gamma}{hd_a/2} \approx \frac{4K^2}{h^2d(2K_x+h)}\,|\chi_a| \tag{5.108}$$

is small. For typical values of the parameters of interest (namely $\lambda \approx 1$ Å, $d \lesssim 10^4$ Å, $|\chi_a| \lesssim 10^{-5}$), this value depends considerably on the orientation of the sample with respect to the incident beam. There can be two marginal cases:

1. The incident beam makes large angle with the wires, $K_x \approx K \gg h$, thus it can be (nearly) perpendicular to the wires (Fig. 5.4(b)–(c)). Then

$$w_h^- = \frac{2K^2}{K_x h^2 d}\,|\chi_a| \approx \frac{d}{m\lambda}\,|\chi_a| \approx 10^{-1}\,. \tag{5.109}$$

The approximate relations of the two-beam case are

$$k_{z0}^2 = \kappa_0^2 + \frac{K^4\chi_h^2}{(\kappa_0^2-\kappa_h^2)} \tag{5.110a}$$

$$k_{zh}^2 = \kappa_h^2 - \frac{K^4\chi_h^2}{(\kappa_0^2-\kappa_h^2)} \tag{5.110b}$$

$$E_{0h} = \frac{w_h}{2} = \frac{K^2}{\kappa_0^2-\kappa_h^2}\cdot\chi_h\,. \tag{5.110c}$$

2. The incident beam is (nearly) parallel to the wires (Fig. 5.4(d)), $K_x \approx h$. Then

$$w_h^{||} = \frac{4K^2}{h^3 d}\,|\chi_a| \approx \frac{d}{m\lambda}\,|\chi_a| \approx 10^{+3}\,. \tag{5.111}$$

The approximate relations of the two-beam case are

$$k_{z0}^2 = \frac{\kappa_0^2 + \kappa_h^2}{2} + K^2\chi_h \tag{5.112a}$$

$$k_{zh}^2 = \frac{\kappa_0^2 + \kappa_h^2}{2} - K^2\chi_h \tag{5.112b}$$

$$E_{0h} = \mathrm{sgn}\,(w_h) - \frac{1}{w_h} \approx \pm 1\ . \tag{5.112c}$$

In the case 1., the amplitude of the diffracted wave E_{0h} is proportional to the resonance factor and to the susceptibility. Therefore it is a small number and this wave is weak. In the case 2., both eigenvalue amplitudes E_{00} of the incident wave and E_{0h} of the diffracted wave are of the same absolute value $|\pm 1|$, therefore there is a strong dynamical interaction between them.

We can see that the value of $w_h(k_x)$ conditions the applicability of the two-beam approximation for a given truncation rod h, angle of incidence ω (and for azimuthal angle ϕ in non-coplanar geometries). For choosing the value of the threshold we can take the value $w_h = 0.01$ at which E_{0h} is 2% of E_{00}, therefore

$$|w_h(k_x)| \leq 0.01 \tag{5.113}$$

is the ***condition of the validity of the two-beam approximation (TBA)***.

Usually the strongest TRs are the TRs ± 1, therefore if this condition holds for them, it holds for the other TRs as well since w_h falls as h^{-2}. We verified numerically that this is a good choice: for the surface grating discussed in Sec. 5.7 the $w_{h_{\pm 1}}$ equals 0.012 and the single-scattering is found adequate for TRs m with $|m| \leq 3$ and for larger angles of incidence on the TRs ± 1; for the measured MLG (Sec. 5.10) the $w_{h_{\pm 1}}$ equals 0.009 and the single-scattering theories (i.e., the two-beam approximation as well as the DWBA) give the same results as the dynamical higher-order multiple-beam approximations.

The reflectivity amplitude on the top surface of a multilayer grating is obtained by applying the boundary conditions. Most easily we calculate the scattered intensity by using the matrix formalism, as described in Sec. 5.6.2, for the matrix dimension $\mathcal{D} = 2$.

We find that under the TBA validity condition, the contributions of the TRs $\pm h$ to the TR 0 cancel each other. This follows from the analysis of Eq. (5.78): χ_{+g} equals χ_{-g}, whilst the amplitudes $E_{g,0}$ are inversely proportional to g, so that $E_{g,0} = -E_{-g,0}$ and the sum of the g and $-g$ terms goes away. We can illustrate this phenomena by an "effective, mean field of the truncation rods" in reciprocal space, which causes the DWBA[5] to give the same results as the multiple-beam dynamical theory as we will show later by numerical simulations.

However, this cancelling will not occur in large period gratings where the TBA is not valid and $E_{g,n}$ are no more inversely proportional to g. We will come back to this point later in the discussion in Sec. 5.7.

For a mesoscopic grating there are thousands ($\approx d/\lambda$) of simultaneously excited TRs, Fig. 5.5. Within the two-beam approximation we calculate the intensity of all the diffracted waves as a two-beam case, i.e., as a pair interaction of the incident ($h = 0$) and the scattered ($h \neq 0$) wavefields. This is shown schematically in Fig. 5.9(b) and 5.10. The two-beam approximation is correct if the intensity of the diffracted waves is weak and when the dynamical interaction with the other diffracted waves $g \neq h$, see Eq. (5.78) and Fig. 5.9(a), is small. Therefore TBA can be used in the case 1. ($K_x \gg h$), but not in the case 2. ($K_x \approx h$), i.e., when the incident wave is nearly parallel to the wires.

[5] In our convention, the DWBA, as well as the kinematical theory and the TBA, is a single-scattering theory because of calculating the scattering between two TRs only. However, all these theories differ in the approach for choosing the eigenstates and in solving the boundary conditions at the interfaces.

The accuracy of this approximation should be numerically checked by comparing it to the fully dynamical calculation. This we will discuss for the simple case of a surface grating in Sec. 5.7.

The main advantage of the two-beam approximation is that we are able to analyze the analytical formulae of the amplitudes of the wavefields and of the wave vectors. These relations are not easy to see in the fully matricial dynamical theory. The other advantage of the two-beam approximation lies in the numerical calculation of the intensity profile of the diffracted waves. The use of TBA enables us to transform the problem of solving the dynamical theory with one matrix of order $\mathcal{D}$ into a procedure of solving $(\mathcal{D}-1)$ times the dynamical two-beam case ($\mathcal{D}'$=2), which is numerically much faster.

However, TBA fails for the calculation of the amplitudes of wavefields of the TRs with zero Fourier coefficients of the susceptibility, $\chi_h = 0$, since $E_{0h} = 0$ in this case. This is for example the case of the rectangular grating with the ratio $\Gamma = d_a/d = 1:2$ and even truncation rods (h is even). In this case the wavefield E_h is not excited directly by a single-scattering from the incident wavefield (scattering by h) since this contribution within the two-beam case is proportional to χ_h/h and thus it is zero. Now also the weak contributions of the multiple diffraction from the other excited truncation rods play a role. Mathematically, we have to take into account the terms $g \neq 0$ in (5.71) and therefore we introduce the ***multiple-beam approximations***. The *zeroth order* of this approximation is the two-beam approximation. In the higher orders p we calculate the given E_h as the dynamical interaction of the wavefields whose contribution is proportional up to $\chi_p\chi_h$. Therefore we take the wavefields of the two stripes of the truncation rods (Fig. 5.9(c)): from the TRs around 0 (their amplitude is proportional to $\chi_g/g \gtrsim \chi_p$, but the contribution is approximately $\chi_{h-g} \approx \chi_{h+1}$) and from the stripe around the TR h (their amplitudes are $\chi_g/g \approx \chi_{h+1}/h$ and their contributions are superior to χ_p).

Explicitly in the approximation of the *first order*, we calculate the given E_h as the dynamical interaction of the wavefields whose contribution is proportional up to $\chi_1\chi_h$. Therefore we use $E_{h-1}, E_h, E_{h+1}, E_{-1}, E_0$ and E_1, and this is the *six-beam approximation*. If, for example, all even χ_h are zero, then the approximation of the *second order* would take all terms up to χ_3 into account, thus the waves of TRs $h{-}3, h{-}1, h, h{+}1, h{+}3, -3, -1, 0, 1, 3$, which leads to the *ten-beam approximation*. In the graphical representation in Fig. 5.9(c), the first order approximation is drawn as the interaction of the wavefields of TRs $h-1, h, h+1$ and $-1, 0, 1$. In general, multiple-beam approximation of order p leads to the $(4p+2)$-*beam approximation*.

The accuracy and convergence of these higher-order multiple-beam approximations should be verified by the numerical calculation that compares them to the dynamical calculation, i.e., to a multiple-beam approximation of very large order.

Finally let us make a remark on the terminology used. We denoted by the "two-beam approximation" the scattering when two truncation rods 0 and h are simultaneously excited, giving rise to four waves, see Fig. 5.10. Although the names of "two-truncation-rod case" or "four-wave case" could be used, we prefer the "two-beam approximation" due to the correspondence to the X-ray diffraction theory from crystals. The latter theory uses the name of "two-beam case" for historical reasons, though in this conventional case there are two transmitted and two diffracted waves excited on both sides of the Ewald sphere for both σ and π polarisations, i.e., there are 16 waves.

5.7 Discussion of the reflectivity from a perfect rectangular surface grating

In this section we discuss the theories treated earlier and we compare the analytical formulae as well as the results obtained by a numerical simulation. We study a simple *surface grating*, i.e., a MLG with one structured layer deposited on a substrate. On a GaAs substrate ($\delta_a = 1.455 \cdot 10^{-5} + i\,4.195 \cdot 10^{-7}$) there are GaAs wires of width $d_a = 4000$ Å distributed with the lateral periodicity $d = 8000$ Å. The layer thickness is $t \equiv t_2 = 3000$ Å. The wavelength is

1.54 Å, the critical angle of GaAs is 0.309° and that of the averaged layer is $0.309^\circ/\sqrt{2} = 0.219^\circ$. The Fourier coefficients (5.3) with $\chi_b = 0$ are $\chi_h = \chi_a \Omega_{ah}$. The formula (5.10) for $\Gamma = d_a/d = 1/2$ gives the averaged layer susceptibility $\chi_0 = \frac{1}{2}\chi_a$. The odd coefficients are $\Omega_{ah_m} = (1/m\pi)(-1)^{\lfloor m/2 \rfloor}$ and the even coefficients are zero. The reciprocal grating vector is $2\pi/d = 7.85 \cdot 10^{-4}$ Å^{-1}.

The choice of the period d is given according to the series of samples we dealt with (so-called quantum wires with period around 1 μm). We stress in the beginning that these are short period gratings for which all theories we are presenting here are adequate. This will not be necessary the case of large period gratings of $d \gtrsim 10$ μm, where truncation rods are close together and the single-scattering approximations are no more valid (cf. the validity of the two-beam approximation given by the condition (5.113)).

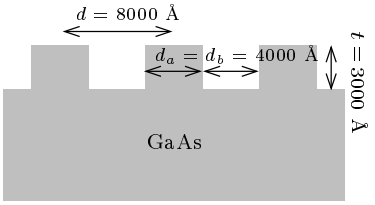

Figure 5.11. Sketch of a surface grating.

The comprehensive diffraction pattern is represented as the reciprocal space map of the scattered intensity in Fig. 5.12. It consists of the main (specular) truncation rod $m = 0$ (the specular reflectivity) around which the truncation rods of non-zero orders are distributed equidistantly in the Q_x direction. Due to the choice of $\Gamma = 1/2$ we expect that the even truncation rods (except for the zeroth TR) disappear in the calculations where only single scattering processes are considered (kinematical theory, DWBA of the first order, two-beam approximation)—we say that these TRs are *kinematically forbidden*. This feature will underline the necessity of the dynamical theory or of higher-order approximations of the dynamical theory.

5.7.1 Intensity of the diffracted waves

In this section, we discuss the properties of the non-zero truncation rods, i.e., the intensity profile measured along the non-specular TRs. We start the discussion by the odd truncation rods and we show that our theories can describe the intensity pattern under several limitations. Therefore we will determine their regions of validity, i.e., the multiple-scattering regions, illustrated in Fig. 5.12. Afterwards we show that only the dynamical theory can explain the profile of the kinematically forbidden even-order TRs because of their multiple scattering origin.

The following discussion is devoted mainly to the coplanar scattering geometry when the incident beam is perpendicular to the wires. The non-coplanar case when the incident beam is parallel to the wires is discussed separately in Sec. 5.7.3.

We note that the Q_z dependence of the intensities of the opposite TRs $+m$ and $-m$ are the same. However, the plots with respect to the angle of incidence are different. The negative TRs are every time excited because they are always crossed by the Ewald sphere of the incident wave, see Fig. 2.2. However, the positive TRs are being excited one after another when the angle of incidence increases, Fig. 5.20(b). This explains the angular shifts of the first three positive truncation rods in Fig. 5.15.

Dynamical theory and multiple-beam approximations

We start the discussion with the dynamical theory since it provides the exact solution. Firstly, let us briefly summarize how we deal with the numerical calculation. We calculate the wave vectors in the vacuum and in the homogeneous layers (substrate including) for a given incident wave. We form the matrix $\hat{\mathrm{A}}$ (5.73) and by solving the eigenvalue problem (5.72) we get the wave vectors and their relative amplitudes in the structured layers. Then the layer transfer matrices $\mathcal{M}^{(j)}$ are created (5.85) and from the transfer matrix of the whole MLG (5.86) the amplitudes of the scattered waves is obtained (5.88).

The dynamical nature of the scattering (i.e., the expression of the multiple scattering) is found in both basic equations (5.72) and (5.78) we derived from the wave equation. Firstly the matrix relation (5.72) stores together all the amplitudes in a single matrix and therefore all these amplitudes are interdependent. In the second alternative expression (5.78) we can see

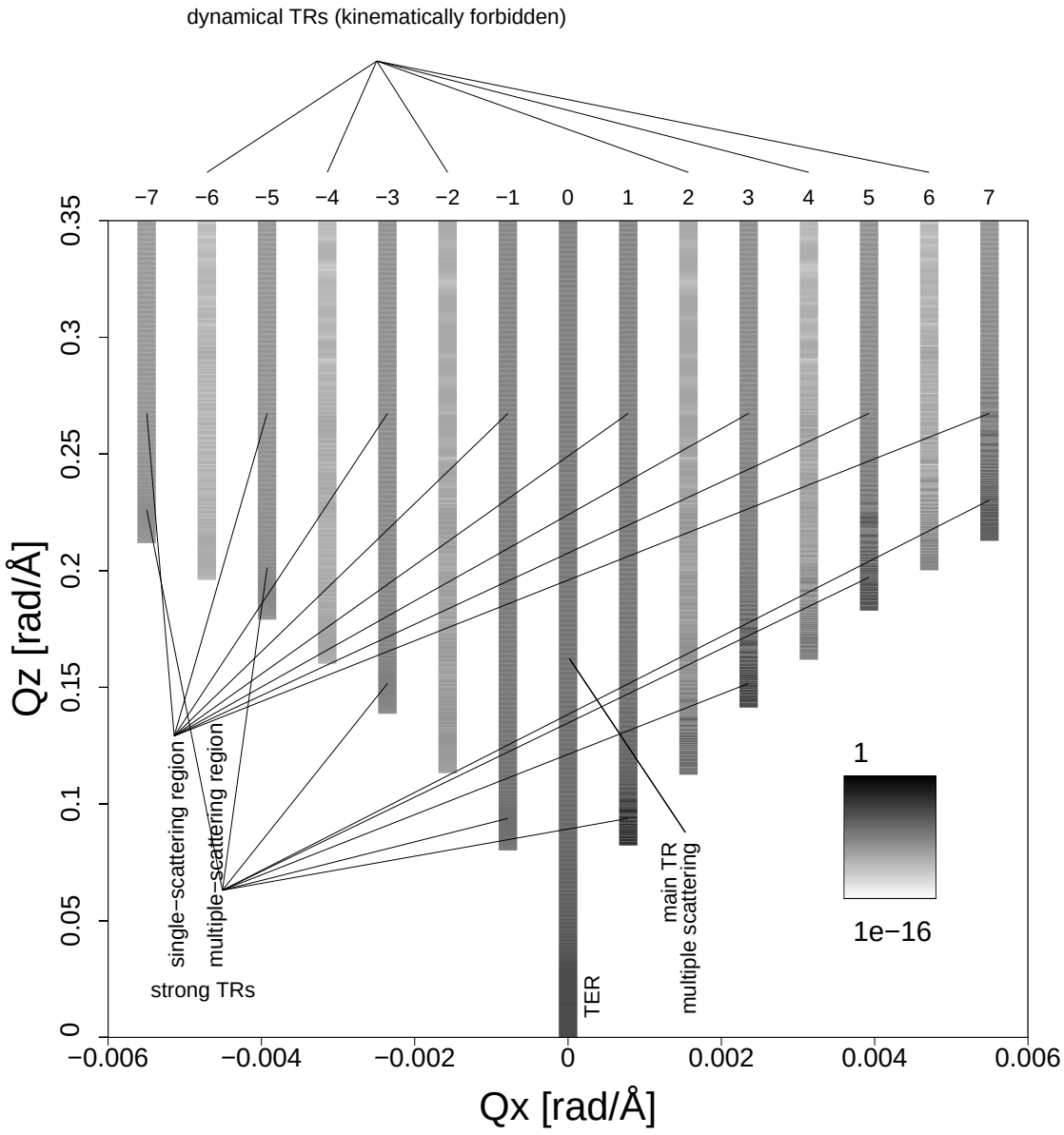

Figure 5.12. Reciprocal space map of the intensity scattered by the surface grating considered in the discussion. This comprehensive view combines the schematic reciprocal space representation of the grating truncation rods (cf. Fig. 5.5) with the intensity profile of the separate scans, Figs. 5.13–5.14 and with the annotation of regions with two-beam scattering and multiple-beam scattering. We show in the discussion that the dynamical theory and the DWBA (single-scattering "effective field" theory) can calculate the intensity of the strong truncation rods, whereas the single-scattering two-beam approximation is valid (with a given precision) above the critical angles of the grating materials of the incident and/or exit wave. The most intense is the main truncation rod 0 (the specular scan) starting in the origin of the reciprocal space by an intense plateau of the total external reflection (TER). The other truncation rods start on the Ewald sphere $\mathcal{K}_i$ and $\mathcal{K}_f$, respectively (Fig. 5.5). The odd order TRs are of high intensity and they exhibit periodic oscillations in Q_z, cf. Fig. 5.13. The "dynamical" even order TRs are of low intensity and their oscillations are no more equidistant, cf. Fig. 5.14. The coherent truncation rods (δ-function profile in the Q_x direction) have been enlarged to a certain finite width (using the so-called "truncation-rod" algorithm of my plotting program `pm3d`). In an experiment, non-zero intensity between the truncation rods would be measured because of the incoherent diffuse scattering, and further the truncation rods would be enlarged by the resolution function of the measuring diffractometer [HM96].

that each amplitude can be expressed as a sum of the contributions of the other TRs. The individual contributions are proportional to the Fourier transform of the susceptibility and it is demonstrated graphically in Fig. 5.9. The dynamical behaviour is observed in (5.78) because each amplitude on the right-hand side is again a sum of the contributions of the other waves, and so on.

The former method of (5.72) is very convenient for numerical simulations. The latter (5.78) is useful for describing the scattering by means of the excitations of truncation rods and of the wavefield propagation because the intensity of the most intense TRs can be predicted by the two-beam approximation, Sec. 5.6.4.

The Fourier transform χ_h drops with $1/h$ (Sec. 5.3), thus the contribution of distant TRs for a given TR h decreases, see (5.78). Within the TBA we have shown that E_h is proportional to χ_h/h. Therefore, there are two regions of strong contributions to E_h. The first includes the TRs around the main truncation rod 0, the other one contains the TRs around h, Fig. 5.9(c).

Let us choose one particular truncation rod $m \neq 0$ (diffraction by the lateral vector $h_m = 2\pi/d \cdot m$). The wavefield corresponding to this TR is excited through the interaction of many scattering processes (5.78). The primary scattering process is the scattering by h from the primary beam ($g = 0$) to that TR. Other scattering processes are multiple diffractions of the other diffracted waves ($g \neq 0$) as we have shown in Fig. 5.9(c). If the amplitudes of the other diffracted waves are smaller or comparable to the amplitude of the chosen TR, and they are all small with respect to the amplitude of the primary beam, then only a small number of interacting waves can affect the scattered amplitude E_h substantially. The limiting case is described by the two-beam approximation, in which the intensity of a non-specular truncation rod is determined (with a given precision) only as the interaction of the primary waves and those diffracted waves corresponding to h.

As we already stated, the dynamical theory gives exact solutions and therefore it would be preferable to use it every time. However, the applicability of the matricial dynamical theory is limited by the efficiency of the numerical calculation.[6]

The matrix order is given by the number of interacting waves $\mathcal{D}$ being proportional to d/λ. For $d/\lambda \gtrsim 1$ the numerical calculation is easy, but as in our case $d/\lambda = 8000$ Å$/1.54$ Å, the full dynamical calculation covering all the real TRs within and the evanescent TRs near the Ewald sphere of the incident wave would not be numerically possible. Fortunately, not all waves are very strong and approximations of the dynamical theory are valid in this case. Instead of taking all those thousands of TRs, only several dozens of TRs from the region near to the origin of the reciprocal space are taken into account. Their number was chosen by testing the numerical convergence required for a given precision. The computer program was written in a way, which allowed us to investigate the dynamical interaction for arbitrarily selected TRs separately.

We have already discussed the two-beam approximation (TBA) on the basis of two-beam case. We have shown that it can be applied for "nearly" coplanar scattering, i.e., $K_x \gg h$. Its validity has been further supported by the small value of the susceptibility for X-rays, $\chi_0 \approx 10^{-5}$.

The diffracted wave amplitude in the structured layer (5.110c) is approximately

$$E_h \approx \frac{K^2}{2k_x\, h}\,\chi_h = \frac{d}{\lambda}\,\frac{\chi_A}{2\pi}\,\frac{1}{m^2}\,(-1)^{\lfloor m/2 \rfloor} \ . \tag{5.114}$$

We can see that the amplitudes E_h of the diffracted waves in a layer drop as $\chi_h/h \approx h^{-2}$, thus the intensity of these waves in the layer decrease as h^{-4}.

The calculation speed of the numerical implementation of the TBA is high since the wave vectors as well as the amplitudes are analytically expressed (sets of Eqs. (5.105a)–(5.105c) and (5.105a)–(5.110c)) and the boundary conditions are calculated using 2×2 matrices. The devia-

[6] Unfortunately, no computer will ever be rapid enough for infinite matrices. Therefore we have to optimize our programs or algorithms, or find a physically approved approximation.

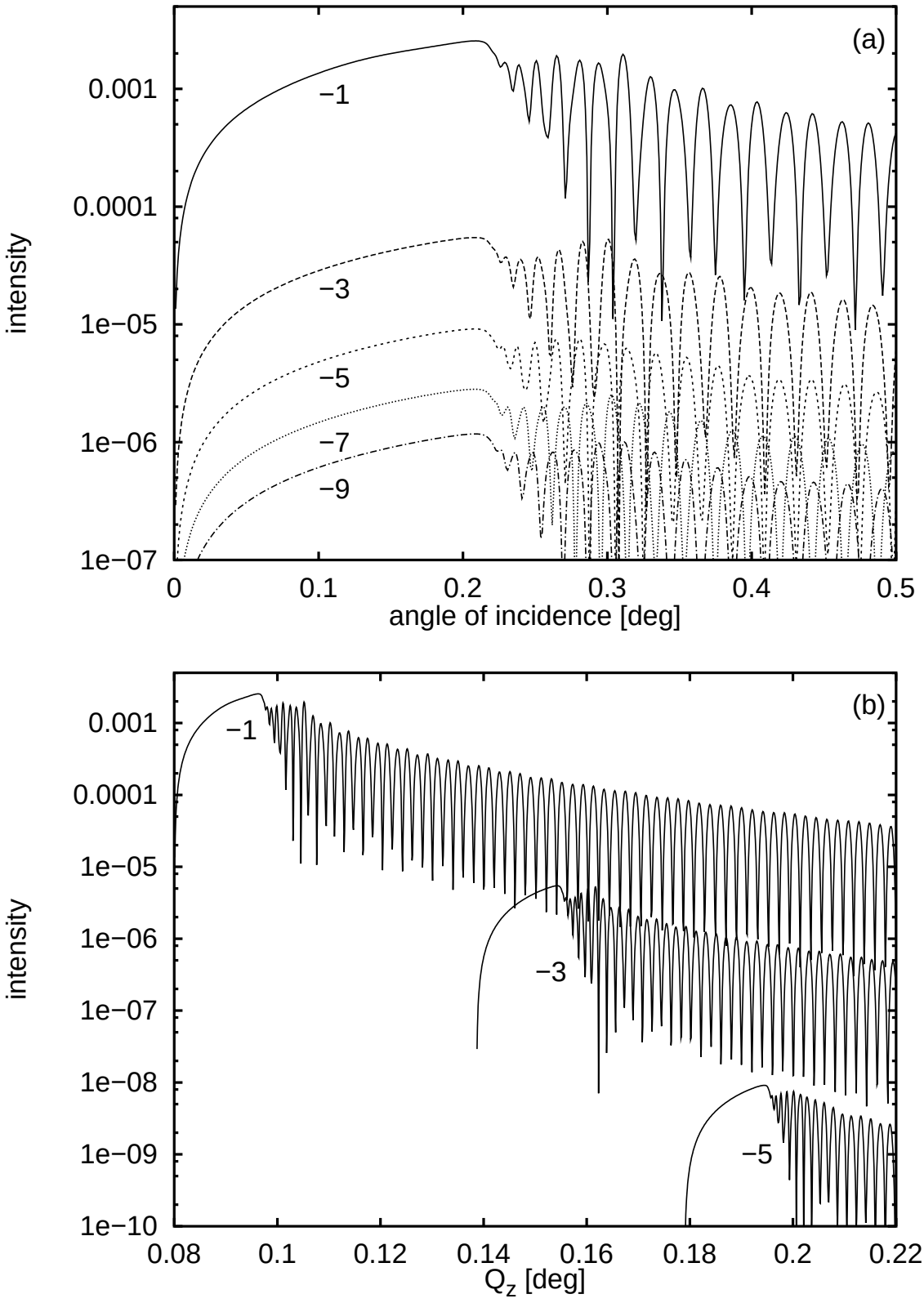

Figure 5.13. Calculations by the dynamical theory, multiple-beam approximation and the DWBA give the same intensity of the odd truncation rods for the discussed surface grating and the coplanar scattering geometry. (a) The graph of the TRs –1, –3, –5, –7 and –9 (diffracted intensity vs. angle of incidence) for the region around the critical angles. (b) The graph of the TRs –1, –3 and –5 (shifted down by 0, 1 and 3 decades, respectively), the intensity being plotted vs. the perpendicular wave vector transfer Q_z.

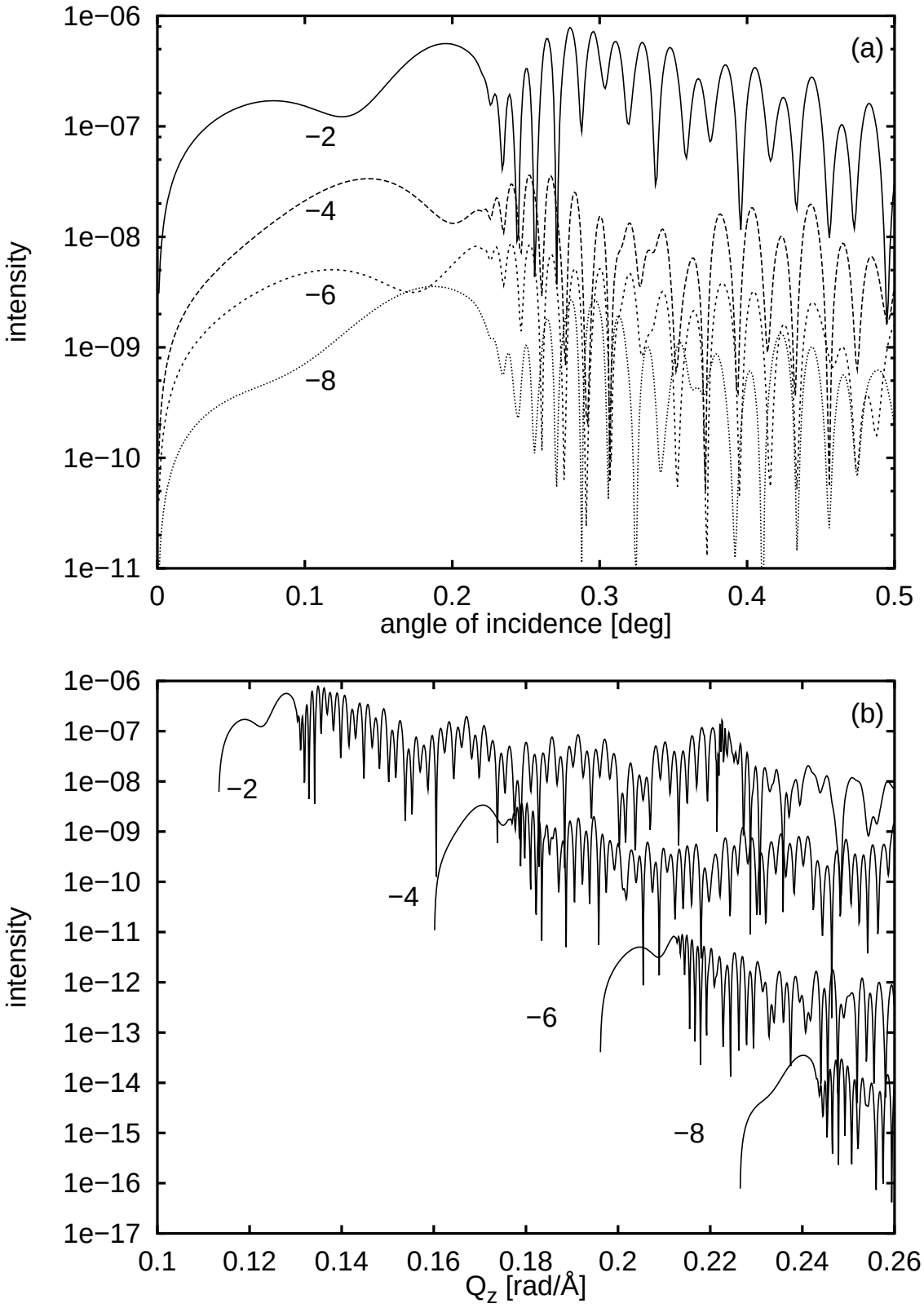

Figure 5.14. The kinematically forbidden even order truncation rods $-2, -4, -6, -8$ calculated by the dynamical theory. At least the third-order multiple-beam approximation of the dynamical theory has to be used to produce the profiles with a sufficient precision. The two-beam approximation, the DWBA of the first order and the kinematical theory give zero reflectivity of even TRs for a grating with $\Gamma = 0.5$. (a) Diffracted intensity vs. the angle of incidence around the critical angle. (b) Intensity plotted vs. the perpendicular wave vector transfer Q_z. The curves of the TRs –2, –4 and –6 are shifted down by 1, 3 and 5 decades, respectively.

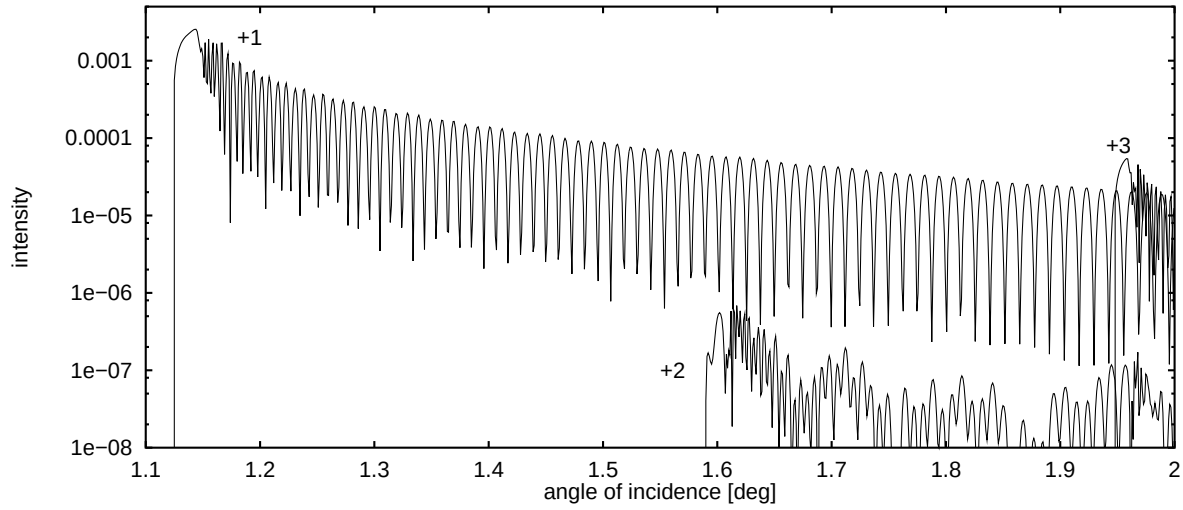

Figure 5.15. Intensity of the positive truncation rods +1, +2 and +3 (dynamical calculation).

tions of the wave vector components with respect to the kinematically calculated ones (including refraction)

$$k_{z0} - \kappa_0 = \frac{k_{z0}^2 - \kappa_{z0}^2}{k_{z0} + \kappa_{z0}} = \frac{K^4 \chi_h^2}{h(2k_x + h)(k_{z0} + \kappa_{z0})} \approx \frac{K^4 \chi_h^2}{k_x h \kappa_{z0}} \approx \frac{K^4 \chi_a^2}{k_x h^3 d^2 \kappa_{0z}} \approx \frac{d\,|\chi_a|^2}{\lambda^2 m^3 \sin\omega} \tag{5.115}$$

are of the order of 10^{-5}. Thus we can conclude that the wave vectors, resulting from the eigenvalue solution, correspond to those calculated "kinematically with the refraction correction", κ_{0z} and κ_{hz}. Further this proved that the eigenstates of the DWBA, which we have chosen according to the virtual planar multilayer, are suitable.

The intensity of the odd order TRs are shown in Fig. 5.13, of the even order TRs in Fig. 5.14. The intensity profiles of the TR –1 calculated either by the TBA (dynamical interaction between TR –1 and TR 0), or as a multiple-beam scattering among TRs –1,0,+1 (TR +1 is evanescent in the plotted region) slightly differ, Fig. 5.16. This shows that the TR +1 influences the intensity of TR –1 for the angle of incidence around the critical angles, so that the interaction with the TR +1 is important. However, we can see that the differences are very small: the curves of both calculations are shifted not more than 0.002° (value of a very good experimental precision), whereas the maximal difference in the intensities is lower than 4%. For angles of incidence below the critical angle of the averaged medium (0.219°) as well as for angles of incidence much larger than the critical angle of the wires (0.309°) both curves coincide. The same behaviour can be found on the intensity profiles of the other odd TRs too, Fig. 5.16.

Therefore there are two scattering regions on each odd TR (see the graphical representation in Fig. 5.12): the multiple-scattering region for the angle of incidence between the critical angles, and the single-scattering region elsewhere. The value of $w_h(0)$ for the TRs ± 1 is 0.012, which slightly exceeds the threshold for the validity of the TBA (5.113). This demonstrates that the condition of the validity of the TBA (5.113) is an approximation only: this condition considers the scattering between the TRs inside a structured layer, but not the enhancement of the transmission function at the critical angles.

The value of w_h (5.109), which determines the "size" of the multiple-scattering region depends on $\chi_0 d/\lambda$. Therefore we find many samples for which the multiple-scattering region can be neglected. This is e.g., the case of the 1.3 μm InP/GaInP MLG measured for the wavelength 0.7114 Å (Sec. 5.7) because of wavelength dependence of the susceptibility $\chi_0 \sim \lambda^2$.

However, we already stated that TBA cannot be used if χ_h is zero (or very close to zero compared to χ_1), i.e., for even TRs in the considered example. These truncation rods are

"kinematically forbidden". This happens because the contributions of the scattering from the primary beam (proportional to E_0) to TR h is weighted by χ_h. If we want to avoid the use of the full dynamical calculation, we have to find a multiple-beam approximation of a sufficient order whose diffraction curve would correspond to the dynamical curve. In the case of the considered surface grating we have found numerically that approximation of the third order, i.e., 14-beam approximation, can be used instead of the full dynamical calculation.

Distorted-wave Born approximation

The distorted-wave Born approximation is a perturbation method. We used the DWBA of the first order and we derived the formula (5.59) for the intensity of the beam corresponding to the TR m. Each structured layer contributes to the amplitude of the scattered wave by a sum of four scattering processes, describing the interaction between the transmitted and reflected incident and diffracted beams, Fig. 5.7. The magnitude of those four contributions for the TR -1 is plotted in Fig. 5.17. The strongest contribution is that of the T_1T_2 process. In the case of the negative TRs, the scattering process R_1T_2 influences the reflectivity around the critical angle because of the maximum of T_2 at the critical angle. The other two processes, R_2T_1 and R_1R_2, are of small amplitude and their contributions to the scattered intensity are negligible. For positive truncation rods, the contributions of R_1T_2 and R_2T_1 change their roles.

The final formula (5.59) of the DWBA calculation gives a clear description of the features on the diffraction curve. Since the scattering process T_1T_2 between the incident-transmitted and diffracted-reflected waves mostly prevails (the reflectivity amplitudes are small: $T_1, T_2 \gg R_1, R_2$), the intensity profile is determined mainly by this primary scattering process. The dependence of T_1 and T_2 on the angle of incidence gives rise to the increase of the scattered intensity at the critical angle (of the averaged grating—given by the choice of the ideal potential), Fig. 3.10. This region corresponds to the so-called Yoneda wings in the diffuse scattering [Yon63]. The oscillations on the truncations rods are caused by the oscillating term $[\exp(-iq_{z0}t) - 1]/(-iq_{z0})$ in Eq. (5.59).

Approximating $|T_1T_2| \approx 1$ for large angles of incidence, the equivalence of the DWBA (5.59) and the two-beam approximation (5.110c) for large angles of incidence can be analytically demonstrated. Consequently, the numerical simulations show that the TBA slightly differs with respect to the DWBA and to the dynamical theory in the region of the critical angles. The differences between the TBA, DWBA and the dynamical theory increases for large period gratings. The numerical calculation shows that the DWBA can be accurately applied for a GaAs surface grating up to the period of 2 μm, where from the multiple-scattering features start to be important. Fig. 5.18 shows what is the difference between the calculation by the DWBA and by the multiple scattering among TRs –3, ... ,+3 for a GaAs grating with the period of 5 μm.

Further, we find that homogeneous layers do not contribute to the intensity of the diffracted waves by a matrix element, only by influencing the amplitudes T and R.

Finally we should note that we used the DWBA of the first order, where only the single scattering process from the incident to the diffracted eigenstates is involved. The amplitude of the diffracted wave of the primary scattering process is proportional to χ_h. Similarly to the two-beam approximation, distorted-wave Born approximation of the first order cannot be used for calculating the intensity of the kinematically forbidden TRs with zero χ_h. This can be overcome by applying the DWBA of a higher order. The DWBA of the second order would be sufficient for determining the intensity of the kinematically forbidden TRs, because they are excited through scattering from the other strong TRs.

The main objection in the literature against the usage of DWBA for the calculation of the reflectivity from gratings was that this perturbing potential is large. This objection is natural if the DWBA is applied for the diffuse scattering calculations in which case it is shown that DWBA breaks down for larger roughnesses (above $\gtrsim$ 20 Å). However, near a rough interface the scattered wavefield is "random", therefore the eigenvectors taken from the laterally averaged multilayer differ strongly from the actual wavefield and their usage in the DWBA is no more

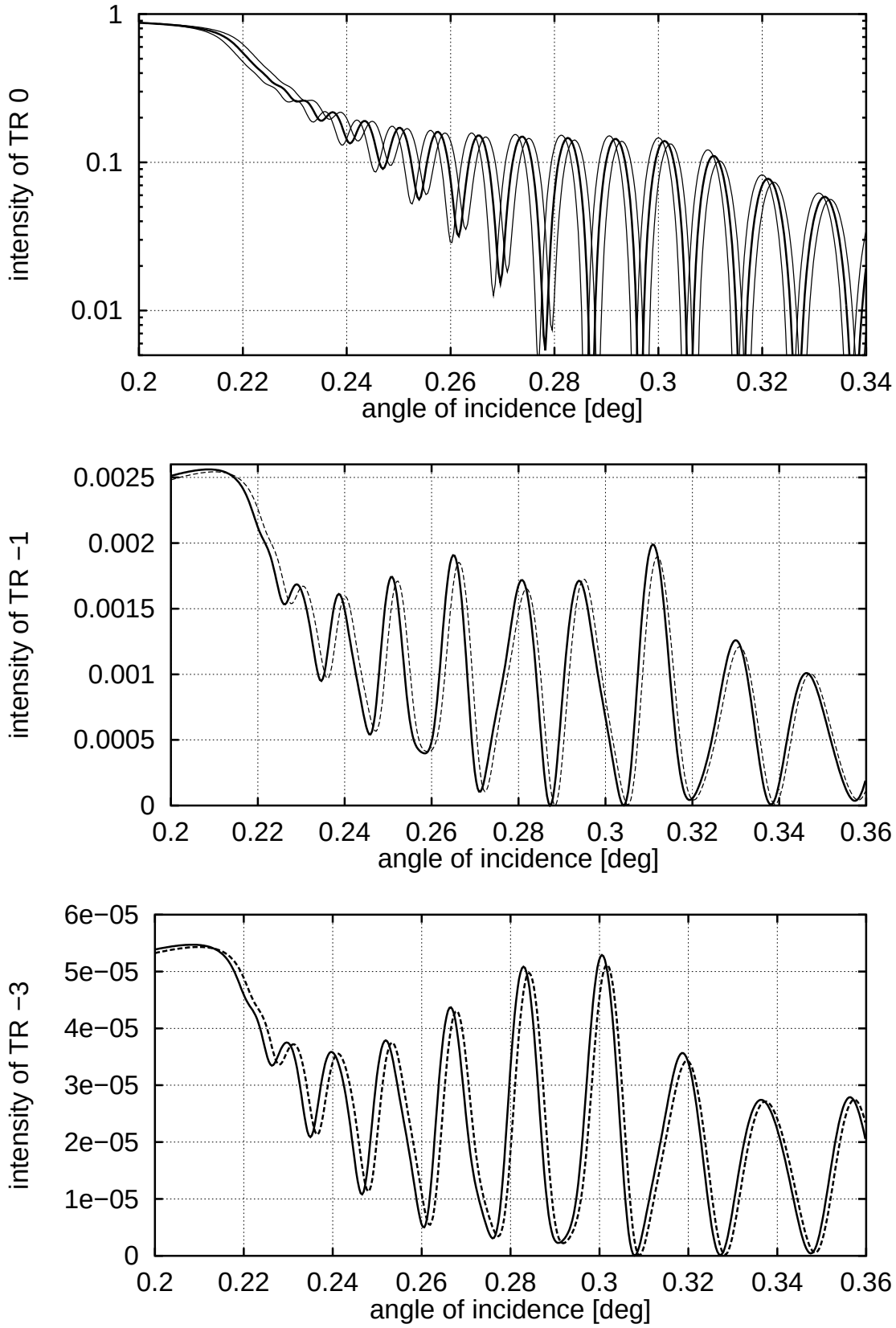

Figure 5.16. Intensity of the TRs 0 (up), –1 (middle) and –3 (down) in the multiple-scattering region around the critical angles. [1] TR 0 calculated dynamically as the interaction between the TRs 0 and +1 (thin right-hand curve), between –1 and 0 (thin left-hand curve) and –1,0,+1 (or more TRs) as the thick middle curve. [2] Intensity of the TR –1 (–3) calculated as the interaction of the TRs –1 and 0 (–3, ... ,0), the dotted curve, and as the interaction of the TRs –1 ... +1 (–3, ... ,–1 or more TRs) as the solid curve, which also coincides with the DWBA calculation. Note the scale of the graph: the angular shift of the curves is smaller than 0.002°.

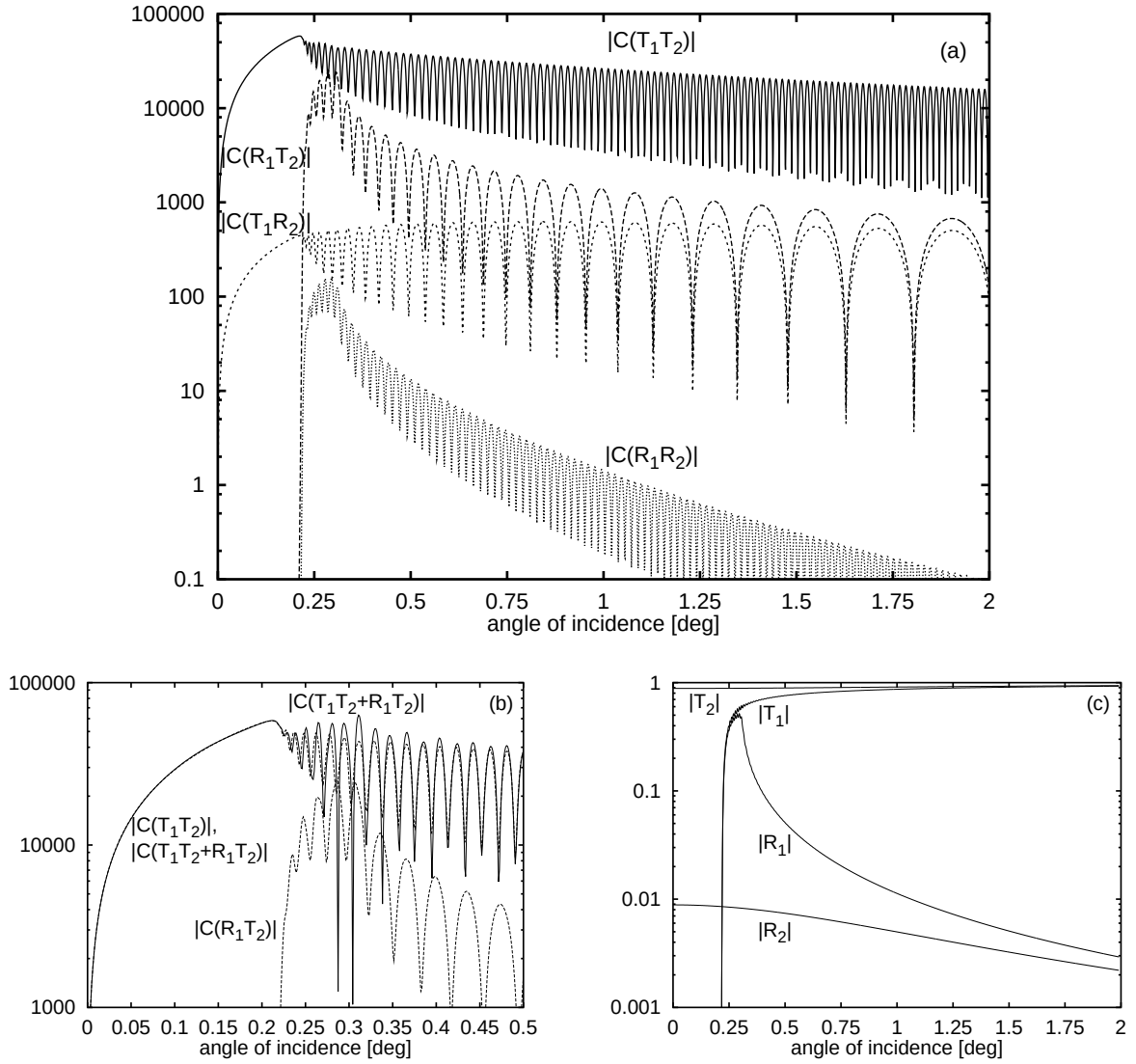

Figure 5.17. The DWBA calculation and the contribution of the four scattering processes to the intensity of the truncation rod –1. (a) Contribution of the additive terms of T_1T_2, T_1R_2, R_1T_2 and R_1R_2, see (5.58)–(5.59). The region around the critical angle of the averaged layer is enlarged in figure (b). The contributions denote the respective terms in (5.56) and in their counterparts in (5.58) and (5.59). $C(T_1T_2)$ represents the term $T_1T_2\,\tilde{\Omega}_{a1}(-\boldsymbol{q}_1)$, etc. The contribution of the process R_1T_2 on the total sum is significant and therefore the "semi-kinematical" calculation (i.e. the calculation using the T_1T_2 term only, see (5.62)) is not sufficient. Figure (c) shows the absolute values of the amplitudes T_1, R_1, T_2, and R_2 at the lower interface of the grating.

appropriate. In the present case of perfect grating structures it shows that the eigenstates of a virtual planar multilayer with laterally averaged potential is a very good choice and therefore the DWBA gives correct results even though the perturbing potential acts in large grating volume (we recall that the grating layer thickness is 3000 Å).

Kinematical theory

We have shown that the kinematical theory without the restriction to the Fraunhofer approximation can qualitatively explain some features of the reflectivity from multilayer gratings. The kinematical diffraction integral is equivalent to the first Born approximation with the eigenstates given by the vacuum plane waves (cf. the DWBA treated above, where the base states are wavefields of the averaged ML). Since the refraction effects are not involved in this theory,

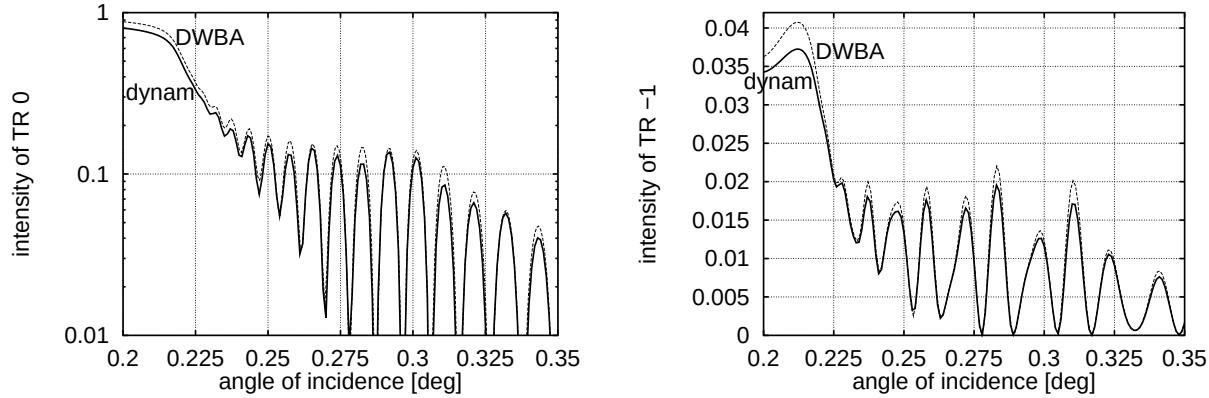

Figure 5.18. Calculation of the TR 0 (left) and the TR −1 (right) for a GaAs surface grating with the period $d = 5$ μm, wavelength $\lambda = 1.54$ Å, by means of the dynamical theory (full curve) and by means of the DWBA (dashed curve).

it cannot explain quantitatively the intensity profile for angles of incidence comparable to the critical angles of the grating materials.

For angles of incidence much greater than the critical angles, the influence of the reflection at interfaces plays a smaller role: the elements of the matrix of generalized Fresnel coefficients (5.99) approach the kinematically calculated Fresnel diffraction coefficients (5.28). The period of the oscillations on a truncation rod approaches that calculated dynamically for larger angles of incidence, Fig. 5.19.

Similarly to the other single-scattering theories, the kinematical theory cannot calculate the intensity of the kinematically forbidden even-order TRs of the discussed surface grating.

Nevertheless, from the approach used by the kinematical theory we get a simple overview of the scattering phenomena. Namely, the Ewald construction, shown in Fig. 5.5, is of general importance. Further, the scattered amplitude is proportional to the Fourier transform (in the $\hat{z}$ direction) of the (lateral) Fourier coefficient of the susceptibility χ_h, which gives a good estimate where to expect the peak positions—and this is what the grating formula is about.

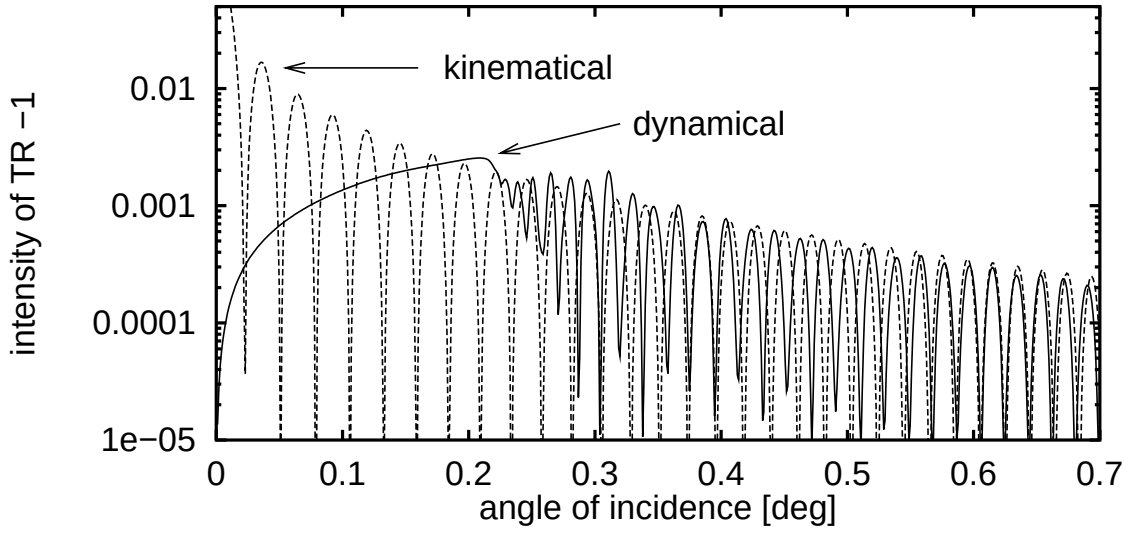

Figure 5.19. Comparison of the kinematical and the dynamical calculation of the truncation rod −1.

5.7.2 Specular reflectivity

So far we discussed the intensity of the diffracted waves. Now let us concentrate on the specular intensity, which is the intensity profile along the zeroth truncation rod (TR 0). The specular reflectivity curve of the considered surface grating is presented in Figs. 5.20 and 5.21.

The curves calculated by the dynamical theory, multiple-beam approximations and DWBA coincide, except for a narrow *dynamical region* on the DWBA curve, which we are going to explain in more details below. They are identical to the reflectivity curve for an averaged layer (with $\delta = \frac{1}{2}\delta_{\mathrm{GaAs}}$) on the substrate as calculated by the dynamical theory of reflectivity from planar multilayers, Ch. 3.

The *dynamical theory* in the one-beam case ($\mathcal{D} = 1$) calculates the scattering only as the propagation of the pair consisting of the incident transmitted and reflected waves. The transmitted and reflected waves in each layer are coupled at interfaces and the corresponding matrix elements depend on the averaged susceptibility χ_0. Therefore this leads to results identical to the dynamical X-ray reflectivity from an averaged planar multilayer (Sec. 3.4.4 and 3.4.5). This is also the result of the DWBA calculation because of the choice of the eigenstates.

Using the full dynamical theory for MLGs, thus the case when $\mathcal{D} > 1$ and (lateral) diffractions by $h \neq 0$ occur, the other TRs are interacting with the TR 0. In Fig. 5.16 we can see that the interaction with both the TRs ± 1 has to be taken into account even when the TR +1 is evanescent in the region $\omega < 1.12^\circ$. This again recalls that the contributions of the wavefields (eigenvectors of the dispersion relation) of opposite TRs cancel each other. However, the specular curves coming from the interaction between TRs 0 and 1, and TRs 0 and –1 differ (Fig. 5.16) because the wavefield diffracted in the grating has to come out through the interfaces, and both diffracted-reflected waves of TRs ± 1 make different angles with the interfaces, which changes their reflection and transmission functions (the generalized Fresnel coefficients).

Another dynamical region of multiple scattering is found near the angle of incidence at which the wavefield of the TR +1 becomes real (this is schematically shown by circles in Fig. 5.8). In this case the diffracted-transmitted wave has a maximum and it can eventually influence the specular beam by taking some of its energy away, cf. the transmission function T_1T_2 in the DWBA. We can see in Fig. 5.21 that only the TR +1 is so strong near the critical angle of its outgoing beam that it enhances and modulates the specular reflectivity curve profile. We can find this feature in the dynamical theories, including TBA, in which the interaction between

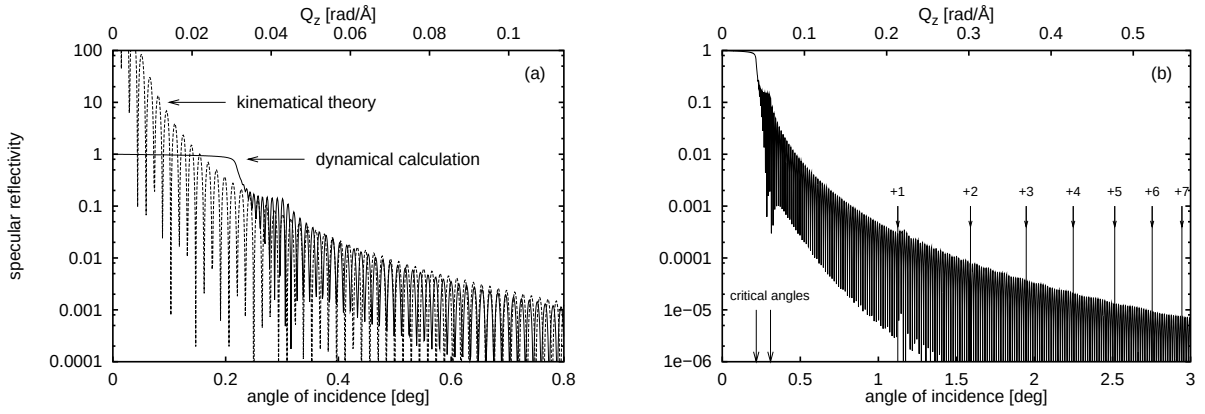

Figure 5.20. The specular reflectivity curves (the main truncation rod) of the discussed GaAs surface grating (period 8000 Å, $\Gamma = 0.5$, thickness 3000 Å; wavelength 1.54 Å). (a) Comparison of the dynamical and the kinematical calculations. (b) Specular curve calculated by the dynamical theory in large angular region. This figure illustrates the fall-down of the intensity of the specular curve and its intensity at the angles at which the positive truncation rods arise (denoted by the enumerated arrows); cf. Fig. 5.22 too. The critical angles of the GaAs material and of the averaged medium are shown by arrows.

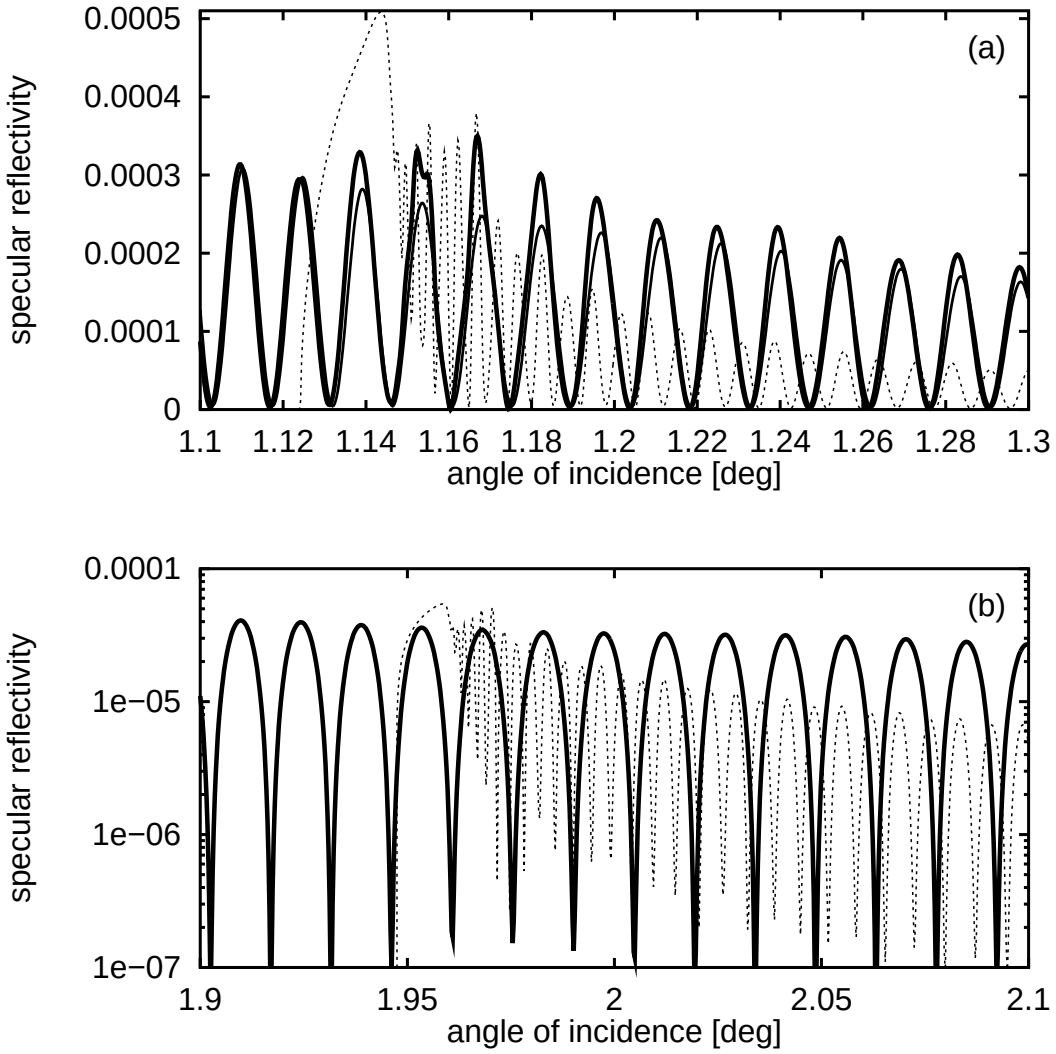

Figure 5.21. The specular reflectivity curves of the discussed GaAs surface grating. (a) Region of the specular reflectivity curve (the upper thick curve) near the angle of incidence where the first truncation rod (TR +1) appears (the wavefield of TR +1 becomes real). The intensity of the TR +1 (shifted down 5-times and represented by the dashed curve) is strong in the region of the maximum of the transmission function and it takes away energy from the incident transmitted beam, which influences the intensity of the specularly reflected beam. The lower thick curve is the dynamical calculation without the interaction with the first TR. (b) Same as (a), but for the third truncation rod (TR +3). Its intensity (dashed curve) is low compared to the intensity of the incident transmitted beam. Therefore it does not influence the other truncation rods nor the specular one (the thick curve).

TR 0 and TR +1 is involved in the calculation. However, the calculations which do not take the interaction between these two TRs into account (i.e., DWBA and the dynamical theory without TR +1 [7]), lead to the reflectivity curve of the averaged planar multilayer. In the region far from this narrow "dynamical" region the reflectivity curve coincides perfectly with that calculated according to the formulae in Sec. 3.4.5 for the averaged multilayer. We note that this dynamical effect diminishes when the grating side walls are rough (Sec. 5.9.1) so that the amplitude of the TR +1 is reduced.

[7] I have already noted that in my program for the numerical simulation of the dynamical theory the TRs dynamically interacting can be arbitrary chosen. For example, we can calculate the dynamical theory using all available TRs, only non-positive or non-negative TRs, or a subset of them. The "dynamical theory without TR +1" means the dynamical calculation considering many TRs except for the specified TR +1.

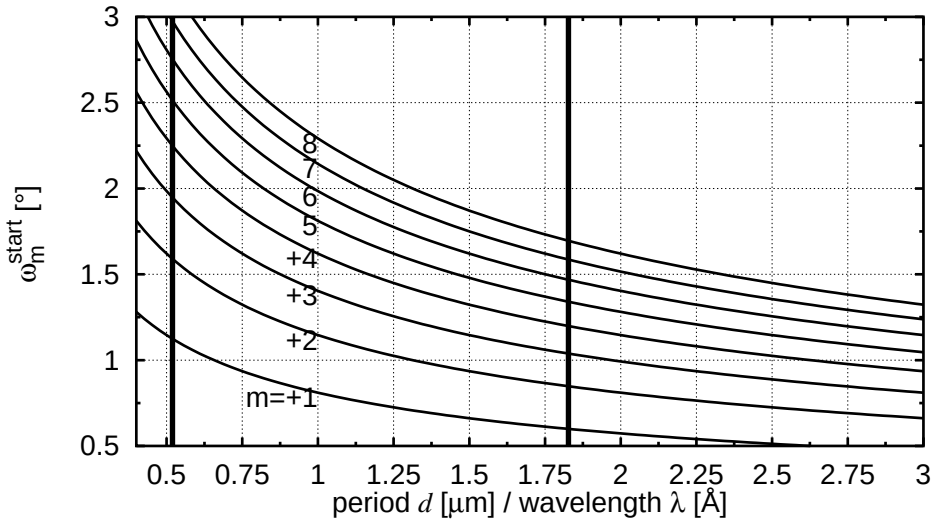

Figure 5.22. Dependence of the angle of incidence $\omega_m^{start} = \sqrt{2m/(d/\lambda)}$, see Sec. 2.3, at which the positive truncation rods +1, ... ,+8 arise, with respect to the ratio of the period d and the wavelength λ. The bold vertical bar on the left-hand side represents the conditions of the discussed SG ($d = 0.8$ μm, $\lambda = 1.54$ Å), that on the right-hand side the conditions of the measured MLG ($d = 1.3$ μm, $\lambda = 0.7114$ Å).

Further, it has been shown by the two-beam approximation that the amplitudes of the diffracted waves are of the order of χ_h/h, Eq. (5.110c). For X-rays the sum of the contributions of the $h \neq 0$ TR is small (except for the TR +1) thus the influence of the total (integrated) non-specular reflectivity on the specular reflectivity amplitude is negligible if the amplitude of the stronges TR is negligible too (i.e., out of the region where the TR +1 is strong).

Let us note that the diffracted TRs make much more impact on the TR 0 profile if they are closer together (in reciprocal space), i.e., for grating period much larger than the discussed one, or when the effective grating period is enlarged by the azimuthal rotation, which is the subject of the treatment in the following section. Further, in visible light optics the susceptibilities χ_h are not small (the index of refraction is substantionally greater than unity) and the specular reflectivity is changed substantially.

For short period gratings the DWBA calculation accurately coincides with the multiple-beam dynamical approximation (the effect of the "effective" field of the TRs). For large period gratings, the multiple-scattering effect plays an important role. The specular reflectivity curve of a GaAs surface grating is well approximated up to a period of 2 μm (for the wavelength 1.54 Å), the differences become important for a period of 5 μm, which is shown in Fig. 5.18.

The reflectivity curve calculated by the *kinematical theory* shows exactly the same behaviour as that discussed for non-specular scans and for the specular reflectivity from planar multilayers, page 42. This we have demonstrated by comparing the "interface" Fresnel coefficients (3.114) and (5.28) for $h = 0$. Therefore we briefly summarize the main features: the intensity, given by (5.36) is inversely proportional to K_z^2 (since $h = 0$), and therefore it diverges around the zero angle of incidence. There is no region of total external reflection—this effect has been already attributed to the choice of the vacuum base states. The refraction corrections to the wave vector in the averaged medium k_z calculated by the dynamical theories become small for large angles of incidence and the dynamical Fresnel coefficients approach their kinematical limit, therefore the dynamical curve approaches the kinematical one.

5.7.3 Azimuthal angle dependence

Up to now we discussed the reflectivity from a grating in the geometry where the incident beam was perpendicular to the wires. When we rotate the sample about its surface normal (azimuthal scan ϕ), the effective period changes as $d(\phi) = d/\cos\phi$, see Fig. 5.4(a). According

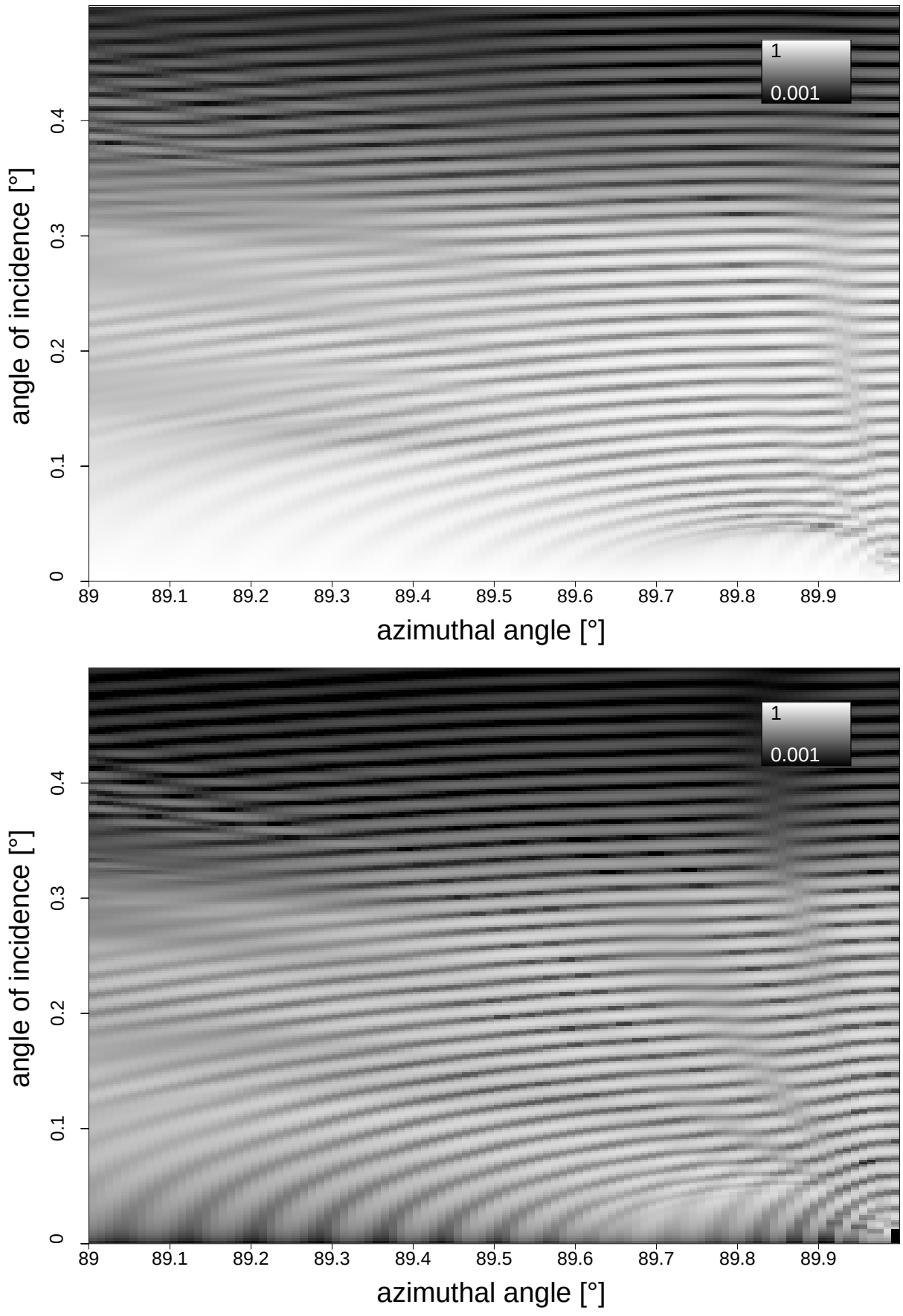

Figure 5.23. Map (azimuthal angle vs. angle of incidence) of intensity of the specular truncation rod (upper map) and of TR –1 (lower map).

to Fig. 5.4(b)–(d), we can see that the sample's reciprocal lattice rotates in reciprocal space and the scattering is non-coplanar, but it still preserves its forward-scattering character (the "Laue case"). We have found that the dynamical theory is well adapted for the case $K_x \gg h$, and we determined a condition for applying the two-beam approximation. From this it follows that the multiple-beam interaction among TRs becomes important for a grating with a large period as well as for a rotated short period grating with larger effective period.

In this section we briefly discuss the case when the incident beam is nearly parallel to the wires, i.e., the azimuthal angle ϕ is near to 90°. From this follows that the $\hat{\boldsymbol{x}}$ component of the incident wave vector $K_x \approx K\cos\phi$, defined by expression (2.1a), is smaller than the lowest order reciprocal vector of the grating h_1.

We calculated numerically the intensity distribution for the surface grating treated in this discussion. Maps of the intensity dependence on the azimuthal and incidence angles for TRs 0 and −1 are shown in Fig. 5.23. For the calculation of these TRs, we have found that for a precision better than 10^{-3} at least the 11-beam dynamical theory, i.e., calculation including dynamical scattering among TRs –5, ... ,+5, has to be used. For calculating the intensity of even order TRs ±2, at least the 15-beam dynamical theory (TRs –7, ... ,+7) is necessary. Let us note that the angular separation of the diffracted waves of two neighbouring TRs is at about 0.01°.

The diffracted waves in this scattering geometry are strong and the scattering has to be calculated dynamically, i.e., as a multiple interaction among many TRs. This need for the multiple-scattering interaction coincides with the condition of the validity of the two-beam approximation (see Sec. 5.6.4 and Eqs. (5.113) vs. (5.111)).

The necessity of the multiple-beam dynamical interaction can be understood from the 2d reciprocal space construction in Fig. 5.4(d). If we enlarge this 2d picture into the true 3d reciprocal space by adding the Q_z axis perpendicular to the paper sheet, then the grating TRs are perpendicular to the paper sheet and they cut the Ewald sphere of the incident wave in points whose Q_z coordinates are very close for the neighbouring TRs. In the real space representation, all the diffracted waves are confined in the grating wires and in the grooves between them, since they make an angle of incidence with the side walls smaller than the critical angle.

5.8 Other grating structures

Up to now we were concerned with discussion of the reflectivity from rectangular periodic gratings. This section we devote to the treatment of scattering by other types of lateral gratings, namely rectangular quasiperiodic gratings and trapezoidal periodic gratings.

5.8.1 Quasiperiodic gratings

Our previous discussion has been focused on scattering by a laterally periodic grating, which represents an artificial 1d crystal with periodic lattice. Now let us treat the reflectivity pattern from a grating with lateral quasiperiodic lattice we have proposed earlier [Mik95]. As a particular example we suppose a (lateral) Fibonacci lattice introduced in Sec. 3.6.2. A sketch of a lateral Fibonacci grating is shown in Fig. 5.24(a).

In Sec. 3.6.2 we discussed the reflectivity from a Fibonacci multilayer grown in direction $\hat{\boldsymbol{z}}$. We used the general properties of the Fibonacci lattice, namely its discrete Fourier transform with the peak positions described by two integers and filling densely the whole 1d reciprocal space. These results can be applied directly also for the present case of a Fibonacci grating, i.e., the Fibonacci lattice in the $\hat{\boldsymbol{x}}$ direction where the wires a, b are positioned according to the Fibonacci sequence. Figure 5.24(b) shows the reciprocal space of this structure. It consists of an infinite number of truncation rods which are enumerated by two integers p, q. A truncation rod (p, q) resides at lateral position $\boldsymbol{h}_{pq} = \frac{2\pi}{d}(p + q\tau)\hat{\boldsymbol{x}}$, where the lattice period is $d = d_a + \tau d_b$. Since the golden mean τ is an irrational number (p. 46), the truncation rods are found in every point of the axis Q_x.

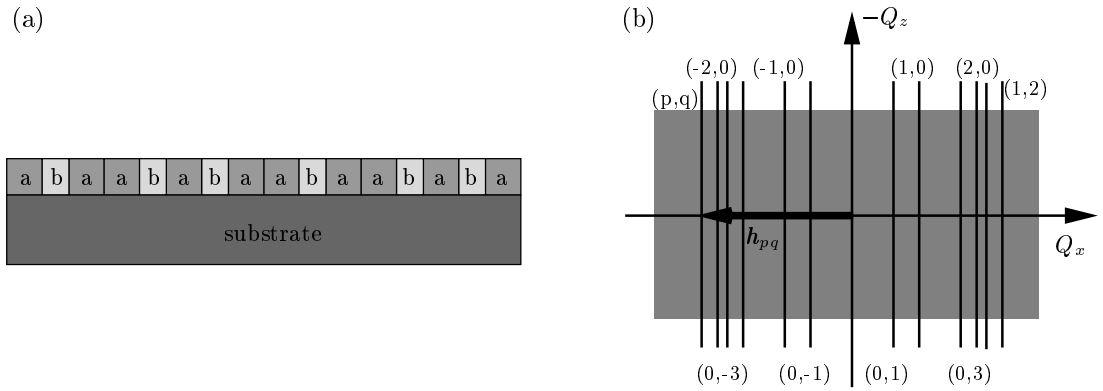

Figure 5.24. (a) A sketch of a Fibonacci grating. (b) Its reciprocal space is a set of truncation rods whose position $\boldsymbol{h}_{pq} = \frac{2\pi}{d}(p + q\tau)\hat{\boldsymbol{x}}$ *are determined by two integers* p, q*. Because the golden mean* τ *is an irrational number, a truncation rod is found in every point of the axis* Q_x*.*

In the calculation of the intensity of the scattered waves, we proceed similarly to our approach of periodic gratings. The only difference (cf. Sec. 5.3) is that the Fourier coefficients are indexed by h_{pq} instead of the equidistant h_m. Then all the calculations by the kinematical theory, distorted-wave Born approximation, dynamical theory and the two-beam approximation can be used without any change, just using h_{pq} instead of h_m and $\chi_{h_{pq}}$ instead of χ_{h_m}. Some "implementational" problems could be encountered in the dynamical theory, since the matrices would be infinite because the Ewald sphere crosses an infinite number of TRs. However, from the Fourier transform of the Fibonacci sequence [SL87] we know that the largest Fourier components are those with small p, q (cf. Fig. 3.12) and therefore most of the TRs will be of very low intensity. For the same reason, there would be only few truncation rods distinguished on an experimental ω-scan.

We have shown earlier that the amplitude of a wave scattered by $\boldsymbol{Q}$ calculated by the kinematical theory, distorted-wave Born approximation and the two-beam approximation is proportional to the modulus of the Fourier transform of the susceptibility, $E_h \sim \chi_h(\boldsymbol{q}_-) \sim \chi(\boldsymbol{q})$, where $\boldsymbol{q}_{\parallel} = \boldsymbol{h}$.[8] Thus for establishing the general properties of a reflectivity map (we mean the truncation rod positions and the peak positions, i.e., the "grating formula") of a grating with any structure we can use the Fourier transform approach used in the kinematical theory of X-ray diffraction.[9] Let us suppose a grating where the material b is vacuum, and the wires of the material a are layers of a multilayer. The susceptibility of the grating can be split into the susceptibility of the multilayer χ_{ML}, shape function of one wire Ω_{a1} and the distribution function of the wires $\chi_d(x) = \sum_n \delta(x - x_n)$. Here x_n is the position of the nth wire (it can be a periodic, quasiperiodic or any other sequence). The susceptibility of the grating is given by the convolution

$$\chi_{\mathrm{grating}}(\boldsymbol{r}) = \Omega_a(x, z) \cdot \chi_{\mathrm{ML}}(\boldsymbol{r}) = [\Omega_{\mathrm{a1}}(x, z) \cdot \chi_{\mathrm{ML}}(\boldsymbol{r})] \otimes \chi_d(x) \ . \tag{5.116}$$

The scattered amplitude is proportional to its Fourier transform (denoted by the star)

$$\chi^*_{\mathrm{grating}}(\boldsymbol{q}) = [\Omega^*_{\mathrm{a1}}(q_x, q_z) \otimes \chi^*_{\mathrm{ML}}(\boldsymbol{q})] \cdot \chi^*_d(q_x) \ . \tag{5.117}$$

According to the rule for the wire distribution, the intensity in the q_x direction in reciprocal space is modified. We can see that the Fourier transform of the wire distribution is *discrete* and therefore it determines the lateral positions $q_{x\boldsymbol{m}}$ of the truncation rods—they are found

[8] In the kinematical theory, $\boldsymbol{q}$ is the vacuum wave vector transfer $\boldsymbol{Q}$. In the DWBA it is the wave vector transfer of a particular scattering process, cf. (5.56).

[9] The kinematical theory of X-ray diffraction shows that the diffracted amplitude is proportional to the Fourier transform of the electron density. The Fourier transforms of the electron density $\rho_{\boldsymbol{h}}$ and of the susceptibility $\chi(\boldsymbol{h})$ are proportional [AKK+74].

in the discrete maxima $q_{x\boldsymbol{m}}$ of the Fourier transform $\chi_d^*(q_x)$. The Fourier transform of the susceptibility profile of the multilayer in the $\hat{\boldsymbol{z}}$ direction determines the positions of the maxima along q_z. The Fourier transform $\chi_{\mathrm{ML}}^*(\boldsymbol{q})$ of the profile of one wire Ω_{a1}^* determines the modulation (an envelope function) of the scattered amplitude and it may lead to extinction of some TRs, thus the dynamical calculation has to be involved. This we have shown earlier on the particular case of a surface grating with $\Gamma = 0.5$.

From this discussion a prediction of the structure of the reflectivity map of any grating sample can be predicted. For example, a Fibonacci grating etched into a Fibonacci multilayer will exhibit a quasiperiodic arrangement of truncation rods along q_x and quasiperiodically arranged maxima along q_z; in a rough approximation the scattered map will be the product of figures 5.24(b) and 3.12. However, to our knowledge such a sample has not been produced until now.

5.8.2 Trapezoidal gratings

So far we have discussed the scattering from gratings with rectangular wire shapes, Fig. 5.2(c). Let us now briefly discuss how to calculate reflection by gratings with other wire shapes, notably with trapezoidal shapes, Fig. 5.2(d).

The gratings with non-rectangular shapes have been treated by different methods. The integral formulae for Maystre's coefficients B_m [May84] have been applied by Tolan *et al.* [TPBK95] to calculate the scattering amplitude by a trapezoidal surface grating. Nevière [Nev94] used the differential matrix method for the calculation of the reflectivity by a grating with triangular wire shapes.

In the present work, the kinematical theory and the DWBA have been formulated in such a way that it is easy to deal with any grating shape. In the kinematical theory, the reflectivity is given by the integral (5.21) which calculates the Fourier transform of the Fourier coefficient $\chi_h(z)$ along the vertical direction $\hat{\boldsymbol{z}}$. We already provided the formula for the rectangular grating (5.25), and the generalization for other grating shapes is straightforward.

The DWBA calculation is easy as well, because the perturbing potential (5.42) is conveniently described by means of the grating shape function $\Omega_a(\boldsymbol{r})$, Fig. 5.2(b). The specular reflectivity from rectangular wires was found to correspond to the reflectivity of the averaged multilayer, Eq. (5.54), because of the choice of the ideal potential. The reflectivity of a grating with another shape is modified by additive terms proportional to the Fourier transform of the wire shape profile, Eq. (5.55). The profiles of the non-zero truncation rods (5.58) contain directly the Fourier transforms of the wire shape function, which are weighted by the amplitudes $T_1T_2, T_1R_2, \ldots$ of the four scattering processes acting in the DWBA of the first order.

Within the dynamical matrix method presented, we can employ the wire shape by the usual approach of calculating the reflectivity from a layer with varying refractive index. We cut the grating into thin (virtual) layers, Fig. 5.25, approximate the trapezoidal shape in each layer by a rectangular shape, and apply the dynamical calculation for such a multilayer grating. Then the transfer matrix of the trapezoidal grating (5.85) will be approximated by the product of the transfer matrices of the virtual layers, $\mathcal{M}^{(2)} = \prod_l M^{(2),l}$, and we expect this product will converge to the transfer matrix of the trapezoidal grating calculated by the differential method. Consequently, this stratifying method will take into account the averaged vertical profile of the index of refraction as well as the varying ratio $\Gamma(z) = d_a(a)/d$, whereas the effect of the slopes of the side walls is neglected. We expect that the slope of the side walls plays a negligible role, because the waves propagating in the grating fall on the side walls under very large angle (with respect to the critical angle), and therefore their refraction on these walls can be neglected (the kinematical limit).

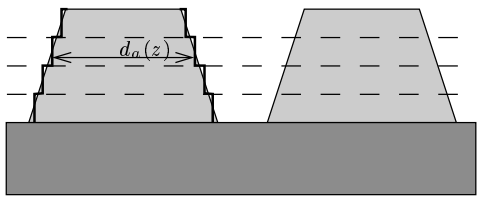

Figure 5.25.

This extension of the dynamical theory for trapezoidal shapes seems to be a good approximation for large slopes (20°–90°), which are present in common MLGs. This approximation could be tested by comparing it to the calculation by the differential method.

Further, this method of virtual layers can be used also in the DWBA to compare the precision of the calculation of the perturbation in the averaged wavefield of the whole trapezoidal grating to the calculation of the sum of the perturbations in the smaller trapezoids of virtual layers.

5.9 Rough gratings

In the previous part we dealt with scattering by perfect multilayer gratings. We have supposed that the grating period is constant all over the sample and that the boundaries separating the different materials are perfectly flat. In this section we will have a look how the structural imperfections of a grating influence the scattered intensity.

Obviously, the grating imperfections can be of two types: macroscopic and microscopic. The main macroscopic imperfection is a fluctuation of the grating period d over the sample area. However, when the mask for the etching of the grating structure is fabricated by means of an optical method (i.e., by optical holography), then the wire period is given by the wavelength used and consequently it is constant over the sample surface. Therefore we will further deal with two microscopic imperfections: rough side walls and rough lateral interfaces.

We will calculate the influence on coherent scattering and we will not deal with the incoherent (diffuse) part. Namely, we do not calculate the profile of ω-scans or 2θ-scans. We suppose that there are only coherent truncation rods, enlarged by the instrumental function.

5.9.1 Rough side walls

Let us suppose that the side walls, i.e., the walls separating the materials a and b in each layer, are rough. In this section we make the calculation for a single structured layer, therefore we will further omit the layer indices. The positions of the side walls of the nth wire are $nd \pm d_a/2 + U(\boldsymbol{r})$, where the displacement U is a random quantity. The theories we used earlier for the calculation of the scattered intensity make use of the Fourier coefficients of the susceptibility (5.3) or of the shape function of the material a (5.5). In the present case of a rough MLG, we use the averaged values $\langle \chi_h \rangle$ and $\langle \Omega_{ah} \rangle$ instead. This is because we have shown that in the single-scattering theories the reflectivity amplitude is proportional to these Fourier coefficients. For the fully dynamical theory, this seems to be a reasonable approximation.

The zeroth Fourier component of the susceptibility is its averaged value in the layer, therefore it does not change in the presence of rough side walls.

The averaging of the Fourier components Ω_{ah} for $h \neq 0$ gives

$$\begin{aligned} \langle \Omega_{ah} \rangle &= \left\langle \frac{1}{d} \int_{-d_a/2+U}^{d_a/2+U} dx\, e^{-ihx} \right\rangle = \frac{1}{d} \frac{\left[e^{-ihd_a/2} \left\langle e^{-ihU} \right\rangle - e^{ihd_a/2} \left\langle e^{-ihU} \right\rangle \right]}{-ih} \\ &= \frac{d_a}{d} \operatorname{sinc} \frac{d_a h}{d} \left\langle e^{-ihU} \right\rangle = \Omega_{ah}^{\mathrm{id}} \left\langle e^{-ihU} \right\rangle . \end{aligned} \tag{5.118}$$

We denoted the Fourier transform of the shape function on the undisturbed system by $\Omega_{ah}^{\mathrm{id}}$. We assume a gaussian distribution function of the side wall roughness characterized by the root mean square roughness σ_w. The updated Fourier coefficients are

$$\begin{aligned} \langle \chi_h \rangle &= \chi_h^{\mathrm{id}}\, e^{-h^2\sigma_w^2/2} \\ \langle \Omega_{ah} \rangle &= \Omega_{ah}^{\mathrm{id}}\, e^{-h^2\sigma_w^2/2} . \end{aligned} \tag{5.119}$$

We can see that the rough side walls diminish the intensity of the non-zero truncation rods. In the single-scattering approximation the amplitude of the diffracted wave of the truncation rod h decreases by a constant value $e^{-h^2\sigma_w^2/2}$ which makes the higher-order truncation rods less

observable. However, in order to achieve a noticeable decrease of the intensity, the factor $h\sigma_w$ should be at about unity and therefore $\sigma_w \gtrsim d/4$. For a realistic example of a grating with the periodicity of 1 μm it means that the intensity of the first TR is changed noticeable for a roughness of several hundreds of Ångstroms.

5.9.2 Rough interfaces

Let us consider the roughness of the interfaces separating adjacent layers of a MLG. We will proceed similarly to the approach used in the calculation of the specular reflectivity from a rough planar multilayer, and we use both the dynamical (Sec. 4.3.1) and kinematical (Sec. 4.3.2) theories.

We describe each rough interface (Sec. 4.2.1) by the displacement $U_j(\boldsymbol{r})$, see (4.1). We suppose a unique probability distribution function over the interface, which means that we do not distinguish between possibly different statistical properties of the interfaces on top of the a and b materials. Therefore we characterize the roughness of an interface j by a single root mean square roughness σ_j and not by means of two separate roughnesses (e.g., σ_{aj}, σ_{bj}).

Rough interfaces and the dynamical matrix theory

The rough interfaces cause layer thickness fluctuations which influence the phase terms (5.83)–(5.84) of the propagation matrices $\mathcal{Q}^{(j)}$ (5.82). According to relations (4.22)–(4.24), the phase matrix becomes random

$$\mathcal{Q}^{(j)}(\boldsymbol{r}_\parallel) = \mathcal{U}_{j-1}(-k_z^{(j)}, \boldsymbol{r}_\parallel)\, \mathcal{Q}^{(j)}(k_z^{(j)}) \mathcal{U}_j(k_z^{(j)}, \boldsymbol{r}_\parallel) \tag{5.120}$$

$$\mathcal{U}_j(k_z, \boldsymbol{r}_\parallel) \equiv \begin{pmatrix} \mathcal{U}^{(j)+}(k_z, \boldsymbol{r}_\parallel) & 0 \\ 0 & \mathcal{U}^{(j)-}(k_z, \boldsymbol{r}_\parallel) \end{pmatrix} . \tag{5.121}$$

Here $\mathcal{U}^{(j)\pm}(k_z, \boldsymbol{r}_\parallel)$ are the diagonal matrices with the diagonal vector

$$\left(e^{\mp i k_{1,z}^{(j)} U_j(\boldsymbol{r}_\parallel)}, e^{\mp i k_{2,z}^{(j)} U_j(\boldsymbol{r}_\parallel)}, \ldots, e^{\mp i k_{\mathcal{D},z}^{(j)} U_j(\boldsymbol{r}_\parallel)} \right) \tag{5.122}$$

for structured layers, and similarly for homogeneous layers.

The amplitude of the reflected waves is given by (5.87), which has to be averaged over the interface displacements. We employ the approximation (cf. (4.27))

$$\left\langle \vec{R}^v \right\rangle = \left\langle \hat{\mathrm{M}}_{21} \cdot \hat{\mathrm{M}}_{11}^{-1} \cdot \vec{T}^v \right\rangle \approx \left\langle \hat{\mathrm{M}}_{21} \right\rangle \cdot \left(\left\langle \hat{\mathrm{M}}_{11} \right\rangle \right)^{-1} \cdot \vec{T}^v . \tag{5.123}$$

In the present formalism we use the same notation as in the dynamical theory of reflection from planar multilayers, therefore we can directly apply the reordering of the matrix sequence according to (4.25). Then the averaged transfer matrix of the whole multilayer reads (cf. (4.29))

$$\langle \mathcal{M}(\boldsymbol{r}_\parallel) \rangle = \prod_{j=1}^{N} \langle \mathcal{N}_j(\boldsymbol{r}_\parallel) \rangle = \prod_{j=1}^{N} \langle \mathcal{P}_{j,j+1}(\boldsymbol{r}_\parallel) \rangle\, \mathcal{Q}^{(j+1)} . \tag{5.124}$$

We rename the ideal matrices $\mathcal{P}_{j,j+1}$ in (5.93) to $\mathcal{P}^{\mathrm{id}}_{j,j+1}$ and put

$$\mathcal{P}_{j,j+1}(\boldsymbol{r}_\parallel) \equiv \mathcal{U}_j(k_z^{(j)}, \boldsymbol{r}_\parallel)\, \mathcal{P}^{\mathrm{id}}_{j,j+1}\, \mathcal{U}_j(-k_z^{(j+1)}, \boldsymbol{r}_\parallel) . \tag{5.125}$$

Averaging the boundary matrix is straightforward. It leads to the form where the elements of the ideal matrix are multiplied by the characteristic function of the probability distribution χ_{U_j} (as usual, we use the gaussian distribution function (4.7))

$$\left\langle \mathcal{P}_{j,j+1}(\boldsymbol{r}_\parallel) \right\rangle = \begin{pmatrix} \left[\tau^{\mathrm{id}}_{j,mn}\, \chi_{U_j}(\ \ k_{z,m}^{(j)} - k_{z,n}^{(j+1)}) \right] & \left[\rho^{\mathrm{id}}_{j,mn}\, \chi_{U_j}(k_{z,m}^{(j)} + k_{z,n}^{(j+1)}) \right] \\ \left[\rho^{\mathrm{id}}_{j,mn}\, \chi_{U_j}(-k_{z,m}^{(j)} - k_{z,n}^{(j+1)}) \right] & \left[\tau^{\mathrm{id}}_{j,mn}\, \chi_{U_j}(k_{z,m}^{(j+1)} - k_{z,n}^{(j)}) \right] \end{pmatrix} . \tag{5.126}$$

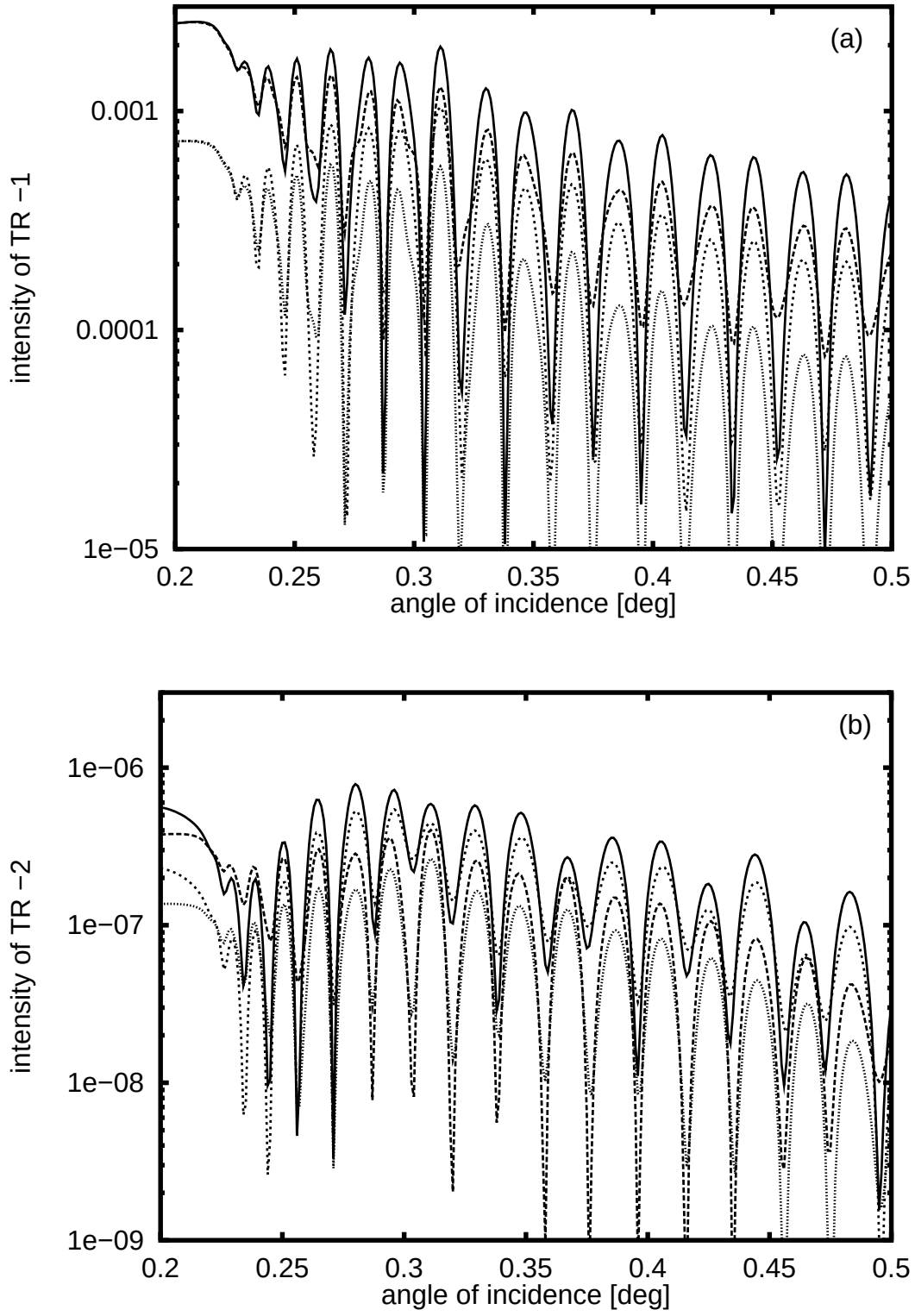

Figure 5.26. Intensity of (a) the odd truncation rod –1 and (b) the even truncation rod –2 (b) of the surface grating according to Sec. 5.7 having rough interfaces. (a) Intensity of TR –1. From the upper to the lower curve: without roughness, interface roughness 12 Å, surface roughness 12 Å, both roughnesses 12 Å. (b) Intensity of the TR –2. From the upper to the lower curve: without roughness, surface roughness 12 Å, interface roughness 12 Å, both roughnesses 12 Å. The explanation of the opposite order of the curves corresponding to the surface and interfaces roughnesses with respect to their order in the odd TR –1 is given in the text.

This relation is analogous to (4.30). However, in the present case the matrices $\hat{\tau}_j^{\rm id}, \hat{\rho}_j^{\rm id}$ are not diagonal and an analog of some "corrected Fresnel coefficients", as it is possible in (4.32), does not exist except for an interface between two homogeneous layers.

We explain the roughness influence in the following way. Rough interfaces change the intensity profile along the Q_z-direction. From the last matrix relation we deduce that the transmission coefficients lying on the diagonal τ_{mm} are not substantionally influenced, since $k_m^{(j)} \approx k_m^{(j+1)}$ for larger angles. The damping of the off-diagonal terms τ_{mn}, $m \neq n$, depends on the "vertical distance" of the wave vectors $|k_{z,m} - k_{z,n}|$. The damping of the reflectivity elements ρ_{mn} is much stronger, since the decrease is given by a static Debye-Waller-like factor in the argument of the vertical wave vector transfer $|k_{z,m} + k_{z,n}|^2$.

Numerical calculation of the specular reflectivity shows that it behaves similarly to the specular reflection from rough laterally averaged planar multilayers. For a simple case of a surface grating the surface and interface roughness acts as shown in Fig. 4.3(a). Numerical results demonstrating the influence of the roughness on the diffracted intensity are shown in Fig. 5.26 for the surface grating discussed in Sec. 5.7. We can see that the diffraction curves are sensitive to a roughness of several Angstroms, as in the case of the reflectivity curves of planar multilayers.

Let us discuss the order of the curves for rough and flat surface/interface, i.e. what is the intensity for a given angle of incidence depending on the roughness of different interfaces. For *the odd TR –1* their order is as that of the specular reflectivity, Fig. 5.26, because the odd TRs are excited by the direct scattering process from the TR 0. Larger surfaces roughness decreases the fall-down of the intensity of TR –1. Larger interface roughness decreases the amplitude of the wavefield of TR –1 confined in the layer, therefore it decreases the amplitude of the oscillations. The order of the intensities for both roughness combinations is *opposite* for the *even TR –2*. This is because the diffracted wavefield of an even TR is excited by a double-scattering process inside the layer. The diffracted-reflected wave of the TR –2 coming from the interior of the layer is less reflected back if the surface roughness is large, and therefore its intensity is higher. The diffracted-reflected wave of TR –2 falling on the bottom side of the flat surface is considerably reflected back for an incidence angle below the critical angle and therefore the intensity measured above the surface is smaller.

Rough interfaces and the kinematical theory

The position $z(\boldsymbol{r})$ of a rough interface is random (4.1), and therefore Eq. (5.27) has to be averaged

$$\begin{aligned} \langle E_h(\boldsymbol{r})\rangle &= \left\langle E_0 \sum_{j=1}^{N} \mathfrak{r}_{h,j}^{\rm kin}\; e^{-iQ_{hz}z_{j+1}(\boldsymbol{r})} \right\rangle \\ &= E_0 \sum_{j=1}^{N} \left\langle \mathfrak{r}_{h,j}^{\rm kin}(\boldsymbol{r}) \right\rangle\; e^{-iQ_{hz}z_{j+1}} \ . \end{aligned} \tag{5.127}$$

The Fresnel reflection coefficient of kinematical diffraction corrected for the roughness of an interface j is

$$\left\langle \mathfrak{r}_{h,j}^{\rm kin}(\boldsymbol{r}) \right\rangle = \mathfrak{r}_{h,j}^{\rm kin}(\boldsymbol{r}) \cdot \left\langle e^{-iQ_{hz}U_j(\boldsymbol{r})} \right\rangle = \mathfrak{r}_{h,j}^{\rm kin} \cdot \chi_{U_j}(Q_{hz}) \ . \tag{5.128}$$

For the gaussian probability distribution function (4.7) we get explicitly

$$\left\langle \mathfrak{r}_{h,j}^{\rm kin}(\boldsymbol{r}) \right\rangle = \mathfrak{r}_{h,j}^{\rm kin}\; e^{-Q_{hz}^2\sigma_j^2/2} \ . \tag{5.129}$$

Similarly to the specular reflectivity from rough planar multilayers (Eqs. (4.35) and (4.36)) we get the kinematical damping factor depending on the $\hat{\boldsymbol{z}}$ component of the vacuum scattering

vector (Debye-Waller form of the diminution). This is different from the dynamical theory where the correction depends on the $\hat{z}$ components of the wave vectors in both neighbouring layers, Eq. (5.126) vs. (4.33). The different behaviour of MLG interface roughness as calculated by the dynamical and kinematical theories is therefore similar to that shown in figure 4.3.

This kinematical damping factor is similar to that empirically assumed by Erko *et al.* [EVV+93]

$$I_h = I_0 \cdot e^{-K^2\sigma^2 \sin^2\theta} \tag{5.130}$$

for I_0 calculated dynamically. They characterized the grating by a single effective roughness σ and used an effective wave vector transfer $K \sin\theta$ instead of the scattering wave vector Q_{hz}.

5.10 Experiment

In this section we present the reflectivity measurement on a multilayer grating whose structure is presented in Fig. 5.27. There are three and a half periods of the bilayer $Ga_{0.47}In_{0.53}As$ (nominal thickness 500 Å) and InP (nominal thickness 300 Å) grown on a InP substrate. The uppermost period is etched. This creates a bilayer grating sitting on multilayer with two and a half periods.

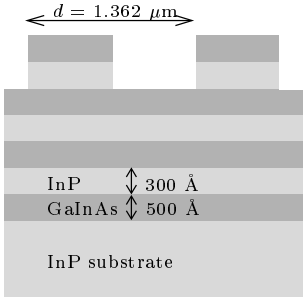

Figure 5.27. Schematical drawing of the sample RG505B4.

We performed the reflectivity measurement of this sample at the Optics Beamline D5 in the E.S.R.F. (European Synchrotron Radiation Facility, Grenoble), using a high-resolution triple-axis diffractometer, Fig. 5.28. The radiation was monochromatized by a single-reflection on a Si(111) crystal positioned on the first goniometer. The sample was mounted on the second independent goniometer. The intensity of the scattered radiation was measured by a scintillation counter mounted after a Si(111) analyzer crystal, both placed on the third independent goniometer. The angle of incidence ω was changed by simple rotation. For measuring the outgoing radiation at certain scattering angle 2θ, a more complicated movement was needed. Firstly, the analyzer crystal as well as the detector had to be rotated. Because of the distance between the second and third goniometers and the finite size of the analyzer crystal, the whole third goniometer had to be moved so that the measured scattered beam always arrived at the analyzer crystal. And finally, the beam between the sample and the analyzer had to pass through a slit, employed in order to discriminate the analyzer streak. Therefore the arm carrying the slit and a lead tube (to avoid the diffuse scattering from the air) had to be moved as well. In order to make the whole movement automatically, we wrote several macros for the `spec` software running the whole measurement. We implemented the macros in very convenient way, so that we could measure in any

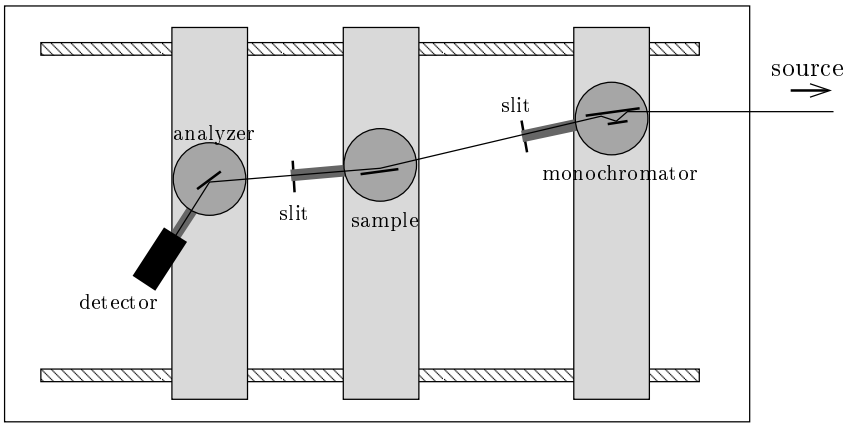

Figure 5.28. A sketch of the diffractometer at the Optics Beamline at the E.S.R.F.

given point in reciprocal space, or perform any reciprocal space scan. The tests showed very good mechanical precision of the whole equipment.

The sample was mounted with its surface vertical, and the incident wave was perpendicular to the wires. Table 5.1 contains the lattice parameters of the compounds and the index of refraction and the critical angle for the wavelength $\lambda = 0.7114$ Å used.

Table 5.1. Lattice parameters and refractive indices for the wavelength 0.7114 Å.

material	lattice parameter	$\delta = 1 - n = -\chi/2$	critical angle θ_C
InP	5.8688 Å	$2.837 \cdot 10^{-6} + i\,6.311 \cdot 10^{-8}$	0.1365°
$Ga_{0.47}In_{0.53}As$	5.8680 Å	$3.284 \cdot 10^{-6} + i\,1.554 \cdot 10^{-7}$	0.1468°

Firstly, the ω-scans have been measured in order to find the positions of the truncation rods. We could resolve the specular truncation rod and the ± 1 truncation rods, Fig. 5.29. From the angular positions of the ± 1 TR peaks we calculate the reciprocal space positions of these truncation rods

$$Q_x^{\pm 1} = \pm \frac{2\pi}{0.7114 \text{ Å}} (\cos 0.595^\circ - \cos 0.105^\circ) = \pm 4.61 \cdot 10^{-4} \text{ Å}^{-1} \tag{5.131}$$

with the precision of $\pm 2 \cdot 10^{-6}$ Å^{-1}. From this follows the grating period

$$d = 2\pi / |Q_x^{\pm 1}| = (1.362 \pm 0.005)\ \mu\text{m}. \tag{5.132}$$

We can see that the truncation rods are very thin in the ω-direction. The full width at half-maximum (FWHM) is 0.006°, which can be verified by calculating the resolution function of the triple-axis diffractometer [HM96]. Thus for measuring the intensity along the "top" of the truncation rod we needed the precision of 0.001°. Therefore we studied the truncation rods by measuring a narrow mapping around them: at each theoretical position (Q_x, Q_z) on the TR we made a small ω-scan and we have taken the maximal intensity of this scan.

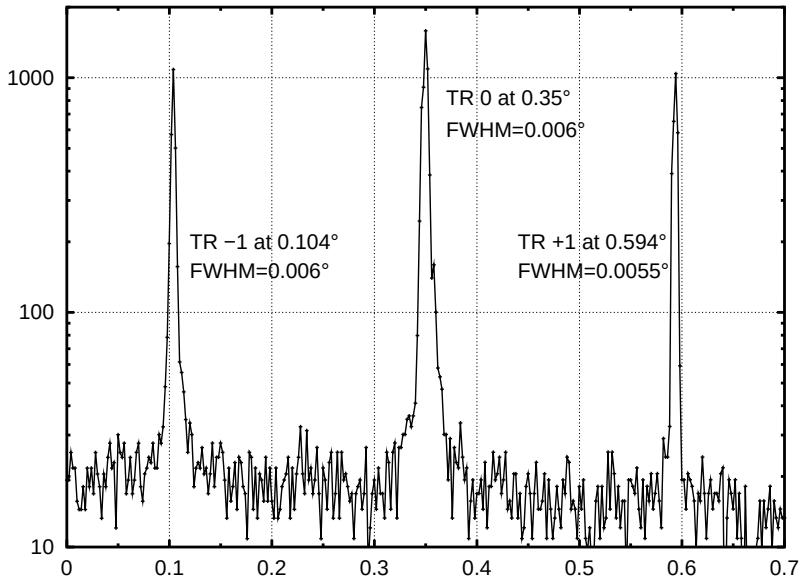

Figure 5.29. ω-scan for $2\theta = 0.7^\circ$ of the sample RG505B4 which cuts the truncation rods –1, 0 and +1.

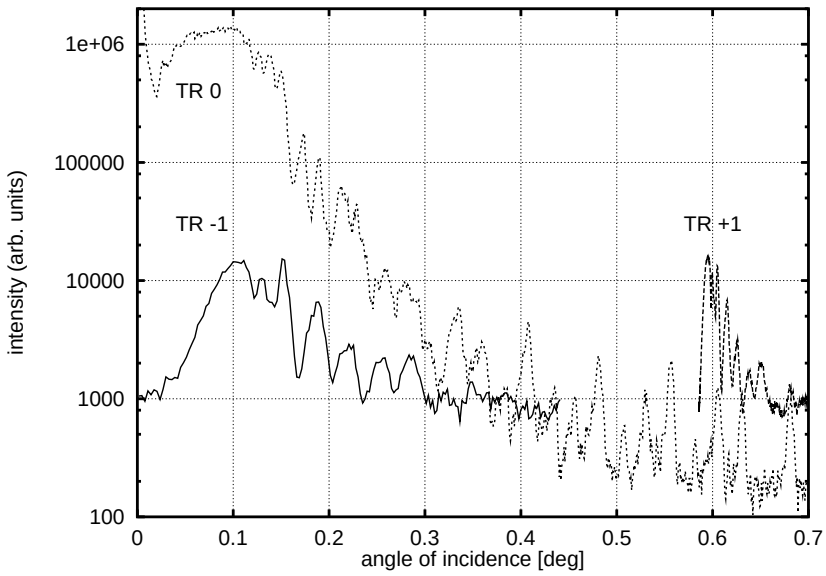

Figure 5.30. Intensity of the measured truncation rods –1, 0 and +1 vs. the angle of incidence.

The measured intensity of truncation rods vs. the angle of incidence is shown in Fig. 5.30. If we plot the TRs as Q_z-scans, then the curves of the opposite TRs ± 1 will coincide (within the experimental precision).

We have theoretically investigated the influence of the dynamical effects of multiple scattering on the sample reflectivity, using firstly the nominal structural parameters of the measured MLG and later the fitted values. We have found that the multiple and single scattering calculations (i.e., the dynamical theory, TBA and DWBA) provide the same curves except in a small region around the critical angles on the specular scans, where TBA slightly differs (with a precision better than 10^{-2}) from the other calculations. Thus it was possible to fit the experimental curves by using any of these theories.

Consequently, we fit the specular curve Fig. 5.31, just as a specular reflectivity curve from a laterally averaged multilayer and the intensity of the TR +1 Fig. 5.32 by the dynamical theory with roughness. We have got a qualitative coincidence of the measured and simulated curves. The peak positions are well estimated, differences are in the intensities of some peaks. Because

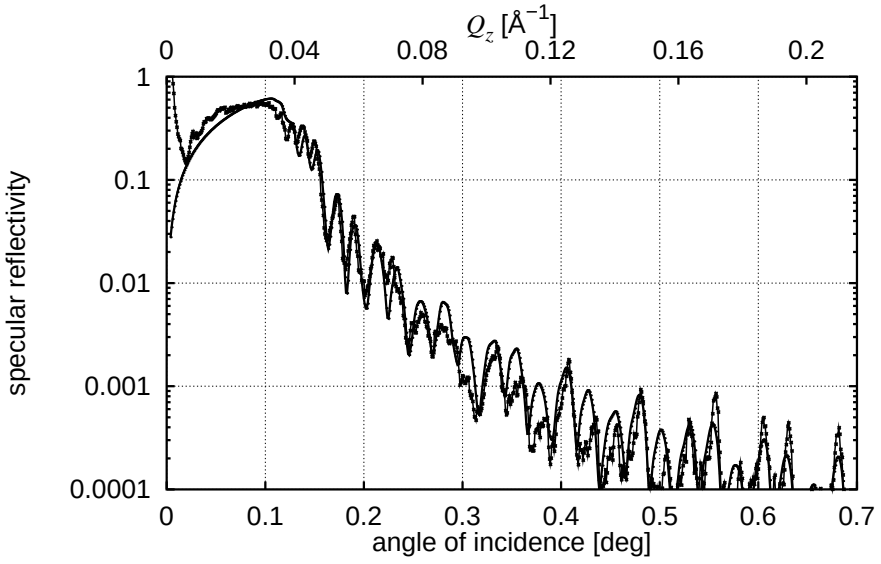

Figure 5.31. Fit of the specular scan of the sample RG505B4.

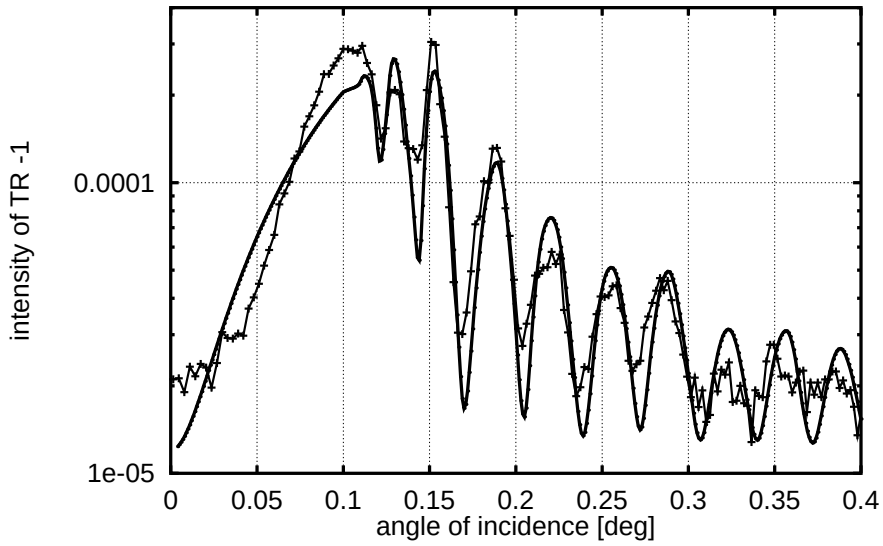

Figure 5.32. Fit of the intensity of the truncation rod +1 of the sample RG505B4.

of the complex structure of the multilayered grating sample, it is not so easy to find a "perfect" fit as we have shown earlier for planar multilayers.

The values of the structural parameters obtained from both fits are the following. The layer thicknesses were found very close to the nominal values: $t_{\mathrm{InP}} = (290 \pm 8)$ Å and $t_{\mathrm{GaInAs}} = (503 \pm 8)$ Å. The estimated interface roughnesses were (5 ± 3) Å. The ratio of the wire width and the grating period $\Gamma = d_A/d = 0.66 \pm 0.03$.

The coincidence of the data fitted by both the specular and diffracted truncation rods verified that the fitted parameters from both fits are consistent. If this were not the case, it would mean that these structural parameters correspond to a false "local minimum" on the surface of fitted parameters and the fit should be remade.

It has been found earlier in X-ray diffraction that the etched grating acts as a transmission grating [GBM+93, BG95] for the scattering from the multilayer below the etched part. Therefore we numerically examined the influence of the multilayer below the grating on the intensity of the truncation rods. We have found that the presence of the ML affects considerably the specular curve—the specular curve is sensitive to all layers in a multilayer. Further, the ML below the grating increases the second peak behind the Yoneda-like wing on the TRs ± 1 with respect to a grating without the underlying multilayer. Increased number of periods of this ML does not influence the diffracted wavefield in the MLG substantially due to the extinction in the first two bilayers below the grating, and therefore the intensity of non-zero TRs is not sensitive for more than two periods of the underlying multilayer for these angles of incidence.

Further we found that the intensity of the truncation rod is not sensitive to the roughness of the grating side-walls below several hundreds of Ångstroms. In order to be sensitive to this roughness, we would have to measure the scattered intensity in the geometry where the incident beam is parallel to the wires. In this case the scattering is no more coplanar and it requires another experimental arrangement. The measurement in this scattering geometry is promising and it will be studied in the future.

5.11 Conclusion

Different theories for the calculation of the X-ray reflection from multilayered gratings have been dealt with in this chapter. Since their formulae have been presented and thoughtfully discussed, I enclosed a "road-map", Fig. 5.33, which presents schematically an overview of the propagation of the approximations in the discussed theories. I hope the reader will enjoy it more than another textual summary.

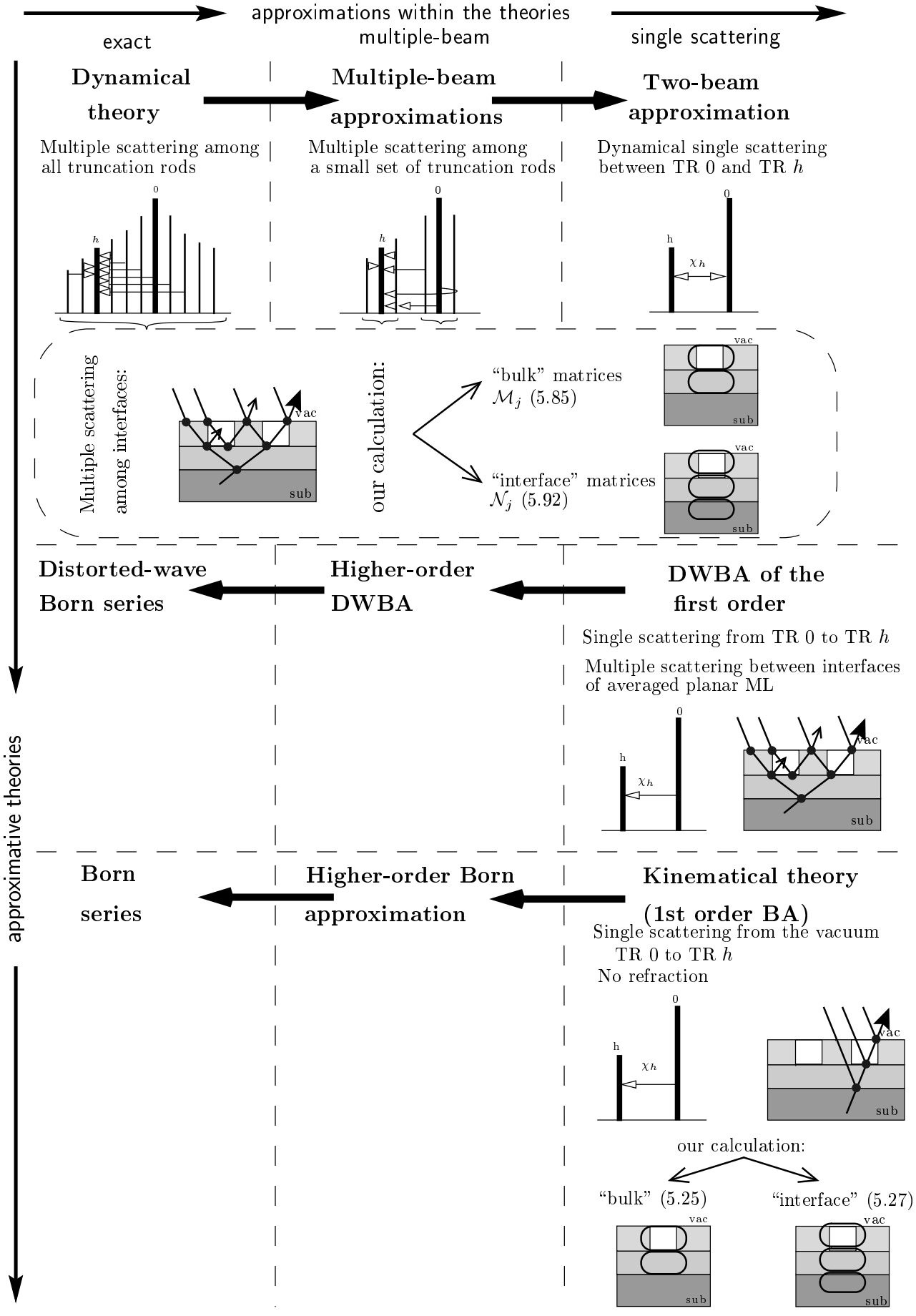

Figure 5.33. A "road-map" of the theories and their approximations for calculating the X-ray reflection from multilayer gratings.

Chapter 6

Conclusion

Conclusion

Dans ma thèse, j'ai traité la théorie de la réflectivité des rayons X et je l'ai appliquée à l'étude de multicouches de plusieurs types :

1. multicouches planaires avec diverses séquences d'empilement (monocouche, périodique, quasipériodique),
2. multicouches rugueuses,
3. réseaux de multicouches (multicouche avec une structure latérale).

Le but de ma thèse était de développer et de présenter plusieurs théories dans un formalisme unique tout en les raccordant aux théories de diffraction des rayons X. Les théories que j'ai discutées sont :

1. la théorie cinématique,
2. l'approximation de l'onde déformée de Born,
3. la théorie dynamique,
4. diverses approximations de la théorie dynamique (approximation à une réflexion unique, approximation à deux ondes et approximation à diffusion multiple).

Ces théories ont été comparées à la fois par leurs expressions analytiques et par des simulations numériques. J'ai décrit les régions où elles sont en bon accord et celles où elles diffèrent.

De plus, j'ai démontré l'utilité des simulations numériques pour l'ajustement des mesures expérimentales. Ceci m'a permis de déterminer les paramètres structuraux des échantillons étudiés dans les laboratoires.

La première partie de la thèse a été consacrée à la représentation de la diffusion dans l'espace réciproque. J'ai décrit les relations entre les mouvements angulaires expérimentaux et les balayages correspondant dans l'espace réciproque. J'ai appliqué ces formules dans la programmation des mouvements des moteurs des goniomètres utilisés au synchrotron.

Ensuite, j'ai analysé la *réflectivité spéculaire* sur des *multicouches planaires*. Tout d'abord j'ai formulé la théorie cinématique. J'ai calculé l'intégrale de diffraction par la méthode de la phase stationnaire, dont la validité n'est pas limitée à la première zone de Fresnel, contrairement à l'approximation de Fraunhofer couramment employée dans les traitements cinématiques. J'ai formulé la théorie dynamique habituelle de la réflectivité et j'en ai déduit l'approximation de la réflexion unique. J'ai comparé les coefficients de Fresnel dynamiques et cinématiques.

La théorie cinématique et l'approximation de la réflexion unique étaient utilisées avec succès pour le calcul de la réflectivité par une *multicouche quasipériodique de Fibonacci*. En appliquant les théorèmes fondamentaux de la physique des quasicristaux, j'ai montré que la courbe de réflectivité présente une autosimilarité et que deux entiers sont nécessaires pour décrire les positions des pics.

J'ai aussi analysé la réflectivité spéculaire et non spéculaire des rayons X sur des *multicouches rugueuses*. J'ai utilisé les propriétés statistiques d'interfaces aléatoirement rugueuses pour calculer la réflectivité avec les théories cinématique et dynamique. J'ai appliqué ces simulations lors de l'ajustement avec les courbes expérimentales obtenues sur des multicouches "sandwich" ou périodiques. J'ai traité brièvement le processus de la diffusion diffuse sur des multicouches rugueuses et j'ai utilisé l'approximation de l'onde déformée de Born (DWBA) pour faire une

analyse quantitative. J'ai présenté les principaux caractères de la diffusion diffuse incohérente sur une carte des mesures effectuées sur une multicouche périodique.

L'essentiel de ce travail concerne la réflexion des rayons X sur des *réseaux de multicouches*. J'ai résolu ce problème en utilisant chacune des trois théories : *la théorie cinématique*, *l'approximation de l'onde déformée de Born* et la *théorie dynamique* rigoureuse. La théorie dynamique a été traitée dans le cadre de la méthode modale à valeurs propres dans un formalisme matriciel. Comme cas limite de la théorie à une seule diffusion, j'ai formulé et discuté de façon approfondie l'approximation à *deux ondes*. La théorie cinématique a été traitée par la méthode de la phase stationnaire.

Ces trois théories ont été formulées dans un seul formalisme général. Ceci facilite leur discussion et leur comparaison. Cela me permet de généraliser les coefficients de Fresnel impliqués dans la réflexion spéculaire conventionelle sur des multicouches planaires au cas de la diffraction latérale. Dans la théorie cinématique, on exprime ces coefficients de réflexion de Fresnel selon la diffraction cinématique, tandis que, dans la théorie dynamique, la "matrice d'interface" de ces coefficients a été généralisée. De plus, j'ai montré que le formalisme utilisé dans toutes ces théories est valable non seulement pour les réseaux périodiques, mais aussi pour le calcul de la réflexion sur des réseaux plus compliqués tels les réseaux quasipériodiques de Fibonacci.

Mon intérêt s'est porté principalement sur les réseaux à courte période (environ 1 μm) mais j'ai aussi discuté brièvement des réseaux à plus grande période. La discussion détaillée a été faite sur un réseau de surface (SG pour surface grating) de période $d = 8000$ Å avec un rapport fil/période du réseau égal à 1/2 ; la longueur d'onde utilisée était 1.54 Å. En gardant ces valeurs en mémoire, j'ai comparé ces théories aussi bien analytiquement que numériquement. Le traitement proposé m'a permis de séparer les effets de la diffusion unique de ceux de la diffusion multiple :

- Les régions à diffusion unique ("two-truncation rod" regions) ont été déterminées comme étant celles où les calculs par la théorie dynamique, l'approximation à deux ondes et DWBA coincident :
  - la plus grande partie du profil des fortes tiges de troncature (truncation rods), interdites cinématiquement pour des angles d'incidence éloignés des angles critiques des matériaux des réseaux,
  - la totalité du profil des fortes tiges de troncature autorisées cinématiquement pour un réseau remplissant les conditions de validité de l'approximation à deux ondes (cas du réseau mesuré),
  - la plus grande partie du profil des fortes tiges de troncature calculé par DWBA.

- Les cas fortement dynamiques où on doit considérer la diffusion multiple parmi les nombreuses tiges de troncature et où les théories de diffusion unique font défaut :
  - le profil d'intensité des faibles tiges de troncature, interdites cinématiquement (tiges de troncature diffractées d'ordre pair),
  - l'intensité diffusée dans la géométrie où le faisceau incident devient parallèle aux fils.

- Les régions de diffusion multiple, où les théories de diffusion unique donnent toujours des résultats approximatifs et où on doit tenir compte de l'intéraction multiple entre plusieurs tiges de troncature :
  - près de l'angle d'incidence pour lequel le champ d'onde de la première tige de troncature devient réel,
  - pour les tiges de troncature fortes dans la région des angles critiques calculés avec l'approximation à deux ondes.

Le principal avantage de la présente approche est la représentation des régions de validité des approximations de diffusion unique (théorie cinématique, DWBA et l'approximation à deux ondes). J'ai démontré que dans l'approximation à deux ondes et dans DWBA, l'amplitude diffusée dans un processus de diffusion primaire (la diffusion simple entre l'onde incidente transmise et l'onde diffractée et réfléchie) est proportionnelle à la transformée de Fourier de la susceptibilité.

Cette proportionnalité a aussi été le résultat du traitement par la théorie cinématique. Cependant cette théorie, équivalente à la première approximation de Born, ne tient pas compte de l'effet de la réfraction qui est d'importance primordiale dans la réflectivité des rayons X.

La DWBA employée au premier ordre tient compte de la réfraction aussi bien que des principaux caractères de la théorie dynamique. Cette DWBA a été trouvée adaptée au calcul de l'intensité des tiges de troncature non interdites et mesurables, ce qui accrédite la légitimité de la méthode DWBA pour les réseaux comme exemple de "rugosité énorme". Ceci confirme l'utilité potentielle de cette méthode pour étudier la diffusion par des couches désordonnées (par exemple des couches en îlots). De plus, j'ai analysé les régions où les effets dynamiques de la diffusion multiple l'emportent et où la théorie dynamique complète de DWBA d'ordre supérieur doit être utilisée.

De manière à introduire dans les calculs les imperfections structurales existant dans des réseaux de multicouches, j'ai étudié également la diffusion par des *réseaux de multicouches rugueuses*. J'ai considéré à la fois la rugosité de côté des fils des réseaux et la rugosité d'interface dans la théorie dynamique de formalisme matriciel et dans la théorie cinématique ; la généralisation de la rugosité dans DWBA est alors directe.

Dans la théorie dynamique, j'ai trouvé que les éléments de la "matrice d'interface" doivent être multipliés par la fonction caractéristique de la distribution de la probabilité de la rugosité d'interface. Ceci est similaire aux "matrices d'interface" des coefficients de Fresnel introduites pour les multicouches planaires.

Dans la théorie cinématique, la rugosité d'interface agit comme le facteur d'atténuation cinématique de Debye-Waller sur les coefficients de Fresnel de la diffraction cinématique. Les formules analytiques déduites permettent de prévoir l'influence de la rugosité sur l'intensité diffusée ce qui a été vérifié par simulation numérique. La rugosité des côtés a été introduite dans l'approximation de processus de diffusion simple en faisant la moyenne latéralement des coefficients de Fourier de la susceptibilité.

Enfin, j'ai utilisé les simulations numériques pour l'ajustement des paramètres structuraux d'un réseau de multicouche InP/GaInAs partiellement gravé.

Perspectives scientifiques des méthodes de réflexion des rayons X. La technique de la réflexion des rayons X est de nos jours utilisée fréquemment et avec succès pour la caractérisation structurale de différentes sortes d'échantillons en multicouches. Les investigations récentes par XRR ont eu lieu dans les domaines suivants :

- les fonctions de corrélation d'interface dans des échantillons avec différents types d'interfaces aléatoires,
- les multicouches avec des interfaces en terrasses, obtenues par exemple lors de la croissance sur des substrats inclinés,
- des échantillons avec une structure latérale :
  - avec une structure presque parfaite (réseaux de multicouches, fils et points quantiques),

  - avec de grandes imperfections, tels les échantillons avec des couches discontinues en îlots.

En particulier, je propose d'étudier, par la réflectivité des rayons X, les réseaux de multicouches qui ont fait l'objet d'un grand intérêt dans ce travail :

- La discussion a ici montré le degré de validité et les limites de DWBA au premier ordre. De manière à élargir l'application de DWBA aux régions où les effets de la diffusion multiple l'emportent (tiges de troncature interdites cinématiquement), cette méthode peut être étendue au deuxième ordre.
- La DWBA pourrait être employée pour calculer la diffusion diffuse incohérente sur des réseaux imparfaits en utilisant soit
  - les états propres d'une multicouche planaire moyennée latéralement, dans la limite des régions de validité discutées dans ce travail,
  - les états propres donnés par la théorie dynamique.
- La technique de la réflectivité non coplanaire peut permettre l'accès à la partie de l'espace réciproque non accessible dans la réflectivité coplanaire. La théorie dynamique modale des valeurs propres, présentée ici, permet de traiter la diffusion non coplanaire. Cependant, la cohérence entre la théorie modale d'approche des valeurs propres et la méthode de couplage pour le cas fortement dynamique quand l'onde incidente devient parallèle aux fils, n'a pas encore été théoriquement confirmée.

Conclusion

In my thesis I have dealt with the theory of the X-ray reflectivity. I have applied it to the study of the following types of multilayered samples:

1. planar multilayers with various stacking sequences (single layer, periodic, quasiperiodic),
2. rough multilayers, and
3. multilayer gratings (multilayers with a lateral structure).

My aim was to develop and present several theories together using one unified formalism while pointing out the links with the X-ray diffraction theories. The theories discussed are:

1. the kinematical theory,
2. the distorted-wave Born approximation,
3. the dynamical theory, and
4. various approximations of the dynamical theory (single-reflection approximation, two-beam and multiple-beam approximations).

These theories have been compared by their analytical expressions as well as by numerical simulations. I discussed their regions of good coincidence as well as their differences.

Further, I demonstrated the use of numerical simulations to fit measured data. This allowed me to reveal structural parameters of the samples we analyzed in our laboratories.

The first part of the thesis has been devoted to the representation of scattering in *reciprocal space*. Here, the relations between the angular movements during an experiment and the appropriate scans in reciprocal space have been described. These formulae have been applied by programming the motor movements of the goniometers for synchrotron measurements.

Further I discussed the *specular reflectivity* from *planar multilayers*. Firstly, the kinematical theory has been formulated. I calculated its diffraction integral by the stationary-phase method, whose validity is not restricted to the first Fresnel zone contrary to the Fraunhofer approximation mostly employed in calculating the kinematical treatments. Further, the usual dynamical theory of reflectivity has been formulated, from which I derived the single-reflection approximation. Dynamical and kinematical Fresnel coefficients have been compared.

The kinematical theory and the single-reflection approximations were successful especially for the calculation of the reflectivity pattern of a quasiperiodic *Fibonacci multilayer*. By applying the fundamental theorems from the physics of quasicrystals I have shown that the reflectivity curve exhibits a self-similarity and two integers are needed to describe the peak positions.

Furthermore, specular and non-specular X-ray reflection from *rough multilayers* has been discussed. The statistical properties of randomly rough interfaces have been employed in the specular reflectivity from both the kinematical and dynamical theories. I applied the simulations in fitting the experimental curves for sandwich multilayers and periodic multilayers. Further diffuse scattering from rough multilayers has been briefly discussed and the distorted-wave Born approximation (DWBA) employed for quantitative analysis. I presented the main features of incoherent diffuse scattering on a measured map from a periodic multilayer.

The main contribution of this work treats X-ray reflection from *multilayer gratings*. I solved this problem using the *kinematical theory*, the *distorted-wave Born approximation* and the rigorous *dynamical theory*. The dynamical theory has been treated in the framework of the matrix modal eigenvalue method. The multiple-beam approximations have been derived from the dynamical theory. As a limiting case of a single-scattering theory I formulated and thoroughly

discussed the *two-beam approximation*. The kinematical theory was treated by the stationary phase method.

All three theories have been formulated within one general formalism. This made their discussion and comparison easier and transparent. It allowed me to generalize the Fresnel coefficients involved in conventional specular X-ray reflection from planar multilayers for the lateral diffraction case. In the kinematical theory, they were expressed by Fresnel reflection coefficients of kinematical diffraction, whereas in the dynamical theory the "interface" matrix of Fresnel coefficients has been generalized. Further I have shown that the formalism used in all the theories is suitable not only for periodic gratings, but also for calculating the reflection from more complicated quasiperiodic Fibonacci gratings.

My main interest has been devoted to *short period gratings* (period $d \approx 1$ μm) and wavelengths around 1 Å, but also larger period gratings have been briefly discussed. A detailed discussion was performed for a short period surface grating (SG, $d = 8000$ Å) with the wire to period ratio one half and for a wavelength of 1.54 Å. The theories have been compared analytically as well as numerically bearing these values in mind. The proposed treatment enabled me to separate the *single scattering* and the *multiple (dynamical) scattering* effects.

- The single-scattering ("two-truncation rod" scattering) regions, where the calculation by the dynamical theory, two-beam approximation and the DWBA coincide, were determined:
  - most of the profile of the strong truncation rods (kinematically non-forbidden) for angles of incidence outside the critical angles of the grating materials (the discussed SG),
  - the whole profile of the strong truncation rods for a grating fulfilling the conditions of validity of the two-beam approximation (the measured multilayer grating),
  - most of the profile of the strong truncation rods calculated by the DWBA.
- Strongly dynamical cases, where multiple-beam scattering among many truncation rods has to be involved and where the single-scattering theories fail:
  - the intensity profile of the weak, kinematically forbidden truncation rods (non-zero even order truncation rods for the discussed SG),
  - the intensity scattered in the grazing incidence geometry where the incident beam falls parallel to the wires.
- Multiple scattering regions, where the single-scattering theories give still approximate results and where the multiple interaction between several truncation rods has to be considered:
  - near to the angle of incidence for which the wavefield of the TR +1 becomes real,
  - in the region of the critical angles for the strong truncation rods and the calculation by the two-beam approximation.

The main advantage of the presented approach is the presentation of the regions of validity of the single-scattering approximations (kinematical theory, DWBA and the two-beam approximation). I demonstrated that within the two-beam approximation and the DWBA the scattered amplitude of the primary scattering process (the single scattering between the incidence-transmitted and the diffracted-reflected waves) is proportional to the Fourier transform of the susceptibility χ_h.

This proportionality was also the result of the treatment by the kinematical theory. However, this theory, equivalent to the first Born approximation, does not include the effect of refraction, which is of major importance in X-ray reflectivity.

The first order DWBA employed includes the refraction as well as the main features of the dynamical theory except for a small known region of strong interaction with TR +1. This DWBA has been found adequate for calculating the intensity of the measurable non-forbidden truncation rods, which confirms the legitimacy of the DWBA for gratings as an example of a "big

roughness". This confirms the potential usability of this method for the studies of scattering by randomly structured layers (e.g., island-layer structures). In addition, I discussed the regions where the dynamical effects of multiple scattering prevail and where the full dynamical theory or the DWBA of higher order have to be employed.

In order to include the structural imperfections of real multilayer gratings into the calculation, I studied scattering from *rough multilayer gratings* too. I have considered both the "side wall" roughness of the grating shape and "interface" roughness into the matrix dynamical formalisms as well as into the kinematical theory, from which the generalization of the roughness into the DWBA is straightforward.

In the dynamical theory, I have found that the elements of the "interface" matrix have to be multiplied by the characteristic function of the interface roughness probability distribution. This is similar to the "interface" matrices of Fresnel coefficients introduced for planar multilayers.

In the kinematical theory, the interface roughness acts as the kinematical Debye-Waller damping factor on the Fresnel coefficients of kinematical diffraction. The derived analytical formulae allowed the roughness influence on the scattered intensity to be predicted, which was verified by the numerical simulation. The side wall roughness was introduced under the approximation of single-scattering processes by averaging laterally the Fourier coefficients of the susceptibility.

Finally, the numerical simulations have been applied to fit the structural parameters of a partially etched InP/GaInAs multilayer grating.

The scientific perspectives of the X-ray reflection methods. X-ray reflection is nowadays frequently and successfully applied to the structural studies of different kinds of multilayered samples. Topics of recent investigations by this technique are:

- interface correlation functions of samples with different types of random interfaces,
- multilayers with terraced interfaces, e.g., multilayers grown on miscut substrates,
- laterally structured samples
  - with nearly perfect structure (multilayer gratings, quantum wires and dots),
  - with large imperfections, like the samples with non-continuous island-like layers.

In particular, we propose the following studies of the X-ray reflectivity from multilayer gratings, to which a great deal of this report has been devoted to.

- The discussion here has shown the degree of validity and the limits of the first order DWBA. In order to extend the application of the DWBA also for the regions of prevailing effects of multiple scattering (the kinematically forbidden truncation rods), this method could be expanded into the second order.
- The DWBA could be advantageously used to calculate the incoherent diffuse scattering from imperfect gratings, using either
  - the eigenstates of a laterally averaged planar multilayer with the restriction to the regions of validity discussed in this work,
  - the eigenstates given by the dynamical theory.
- The non-coplanar reflectivity technique can overcome the limitation of the accessible reciprocal space for the coplanar reflectivity. The presented matrix dynamical theory using the modal eigenvalue approach has been shown to cope with the non-coplanar scattering. However, the consistency of the eigenvalue and the point matching approaches for the strongly dynamical case when the incident wave falls parallel to the wires has not yet been theoretically confirmed.

Bibliography

[AAS84] P.A. Aleksandrov, A.M. Afanasev, and S.A. Stepanov, Asymmetry factor in diffraction of x-rays in conditions of total external reflection, *Sov. Phys. Cryst.* **29**, 119 (1984).

[Ab50] F. Abèles, Recherche sur la propagation des ondes électromagnétique sinusoïdales dans les milieux stratifiés, *Ann. Phys. Fr.* **127**, 597 (1950).

[AEM92] V.V. Aristov, A.I. Erko, and V.V. Martynov, Dynamic x-ray diffraction by a multilayer mirror modulated with a transverse acoustic wave, *X-ray Sci. Technol.* **3**, 211 (1992).

[AG95] F. Axel and D. Gratias. *Beyond Quasicrystals.* Les Editions de Physique, 1995.

[AK83] L.A. Apresjan and J.A. Kravcov. *Teorija perenosu izlucenija.* Nauka, Moscow, 1983.

[AKK+74] L.V. Azaroff, R. Kaplow, N. Kato, R.J. Weiss, A.J.C. Wilson, and R.A. Young. *X-ray diffraction.* McGraw-Hill, New York, 1974.

[AM76] N.W. Ashcroft and N.D. Mermin. *Solid State Physics.* Saunders College Publishing, 1976.

[AM90] A.M. Afanasev and O.G. Melikyan, A modified dynamical theory of x-ray diffraction in extremely asymmetric schemes, *phys. stat. sol. (a)* **122**, 459 (1990).

[ASB+94] J.M. André, A. Sammar, S. Bac, M. Ouahabi, M. Idir, G. Soullié, and R. Barchewitz, Recent advances in etched multilayer x-ray optics, *J. Phys. III France* **4**, 1659 (1994).

[AT94] F. Axel and H. Terauchi, High-resolution x-ray diffraction spectra of Thue-Morse GaAs-AlAs heterostructures, *Phys. Rev. Lett.* **73**, 1308 (1994).

[Bar89] T.W. Barbee, Combined microstructure x-ray optics, *Rev. Sci. Instrum.* **60**, 1588 (1989).

[BdB86] M. Brunel and F. de Bergevin, Diffraction d'un faisceau de rayons X en incidence très rasante, *Acta Cryst. B* **42**, 299 (1986).

[BG95] G.T. Baumbach and M. Gailhanou, X-ray diffraction from epitaxial multilayered surface gratings, *J. Phys. D* **28**, 2321 (1995).

[BHL86] W.J. Bartels, J. Hornstra, and D.J.W. Lobeek, X-ray diffraction of multilayers and superlattices, *Acta Cryst. A* **42**, 539 (1986).

[Bru86] M. Brunel, Fluorescence X en incidence rasante : application au trace des profils d'implantation, *Acta Cryst. A* **42**, 304 (1986).

[BS63] P. Beckmann and A. Spizzichino. *The Scattering of Electromagnetic Waves From Rough Surfaces.* Pergamon, New York, 1963.

[BTPH95] G.T. Baumbach, S. Tixier, U. Pietsch, and V. Holý, Grazing incidence diffraction from multilayers, *Phys. Rev.* **B51**, 16848 (1995).

[BTS+95] S. Bac, P. Troussel, A. Sammar, P. Guerin, F.-R. Ladan, J.-M.André, D. Schirmann, and R. Barchewitz, Theoretical and experimental investigation of x-ray diffraction by a lamellar multilayer amplitude grating, *X-ray Sci. Technol.* **5**, 161 (1995).

[BW70] J.B. Bindell and N. Wainfan, The non-specular scattering of x-rays from thin films, *J. Appl. Cryst.* **3**, 503 (1970).

[BW93] M. Born and E. Wolf. *Principles of Optics.* Pergamon Press, 1993.

[CGL+93] N. Cherief, D. Givord, A. Liénard, K. MacKey, O.F.K. Mc Grath, J.P. Rebouillat, F. Robaut, and Y. Souche, Laser ablation deposition and magnetic characterization of metallic thin films based on rare earth and transition metals, *J. Mag. Mag. Mat.* **121**, 94 (1993).

[Cha84] S.L. Chang. *Multiple diffraction of X-rays in crystals.* Springer Verlag, 1984.

[CJK92] D.W. Cruickshank, H.J. Juretschke, and N. Kato. *P.P. Ewald and his Dynamical Theory of X-Ray.* Oxford University Press, 1992.

[CN76] P. Croce and L. Névot, Etude des couches minces et des surfaces par réflexion rasante, spéculaire ou diffuse, de rayons X, *Revue Phys. Appl.* **11**, 113 (1976).

[Cow75] J. M. Cowley. *Diffraction Physics.* North-Holland, Amsterdam, 1975.

[Dav69] A.S. Davydov. *Quantum Mechanics.* Pergamon Press, 1969.

[DB92a] J. Daillant and O. Bélorgey, Surface scattering of x-rays in thin films. Part I. Theoretical treatment, *J. Chem. Phys.* **97**, 5824 (1992).

[DB92b] J. Daillant and O. Bélorgey, Surface scattering of x-rays in thin films. Part II. Experiments on thin soap films, *J. Chem. Phys.* **97**, 5837 (1992).

[dB94] D.K.G. de Boer, Influence of the roughness profile on the specular reflectivity of x-rays and neutrons, *Phys. Rev.* **B49**, 5817 (1994).

[dB95] D.K.G. de Boer, X-ray reflection and transmission by rough surfaces, *Phys. Rev.* **B51**, 5297 (1995).

[dBLH94] D.K.G. de Boer, A.J.G. Leenaers, and W.W. Van Den Hoogenhof, Influence of roughness profile on reflectivity and angle-dependent x-ray fluorescence, *J. Phys. III France* **4**, 1559 (1994).

[dBLW95] D.K.G. de Boer, A.J.G. Leenaers, and R.M. Wolf, X-ray reflectometry from samples with rough interfaces: an oxidic-multilayer study, *J. Phys. D* **27**, A227 (1995).

[Dos87] H. Dosch, Evanescent absorption in kinematic surface Bragg diffraction, *Phys. Rev.* **B35**, 2137 (1987).

[Els86] V. Elser, The diffraction pattern from projected structures, *Acta Cryst. A* **42**, 36 (1986).

[Erk90] A.I. Erko, Synthesized Bragg-Fresnel multilayer optics, *X-ray Sci. Technol.* **2**, 297 (1990).

[EVV+93] A.I. Erko, B. Vidal, P. Vincent, Yu.A. Agafonov, V.V. Martynov, D.V. Roschupkin, and M. Brunel, Multilayer gratings efficiency: numerical and physical experiments, *Nucl. Instr. and Meth. A* **333**, 599 (1993).

[Fey64] R.P. Feynman. *Feynman Lectures In Physics.* Addison-Wesley, 1964.

[GBM+93] M. Gailhanou, T. Baumbach, U. Marti, P.C. Silva, F.K. Reinhart, and M. Ilegems, X-ray diffraction reciprocal space mapping of a GaAs surface grating, *Appl. Phys. Lett.* **62**, 1623 (1993).

[GR63] I.S. Gradstejn and I.M. Rizhik. *Tablicy integralov, sum, rjadov i proizvedenij.* Gasud. izd. fiz.-mat. lit., Moscow, 1963.

[Gra94] O.F.K. Mc Grath. *Structural and magnetic properties of epitaxial W/Fe/W and Gd/Fe films grown by pulsed laser deposition.* PhD thesis, Université Joseph Fourier, 1994.

[GRC+94] O.F.K. Mc Grath, F. Robaut, N. Cherief, A. Lienard, M. Brunel, and D. Givord, Epitaxial growth of W(110) on Al_2O_3 $(11\bar{2}0)$ by pulsed laser deposition, *J. Cryst. Growth* **135**, 6291 (1994).

[Gui63] A. Guinier. *X-ray diffraction.* W.H. Freeman and comp., San Francisco and London, 1963.

[GVS93] A. Gibaud, G. Vignaud, and S.K. Sinha, The correction of geometrical factors in the analysis of x-ray reflectivity, *Acta Cryst. A* **49**, 642 (1993).

[Hö33] H. Hönl, Zur dispersionstheorie der röntgenstrahlen, *Z. Physik* **84**, 1 (1933).

[Hä76] J. Härtwig, X-ray diffraction in an extremely asymmetric Laue case, *phys. stat. sol. (a)* **37**, 417 (1976).

[HB94] V. Holý and T. Baumbach, Nonspecular x-ray reflection from rough multilayers, *Phys. Rev.* **B49**, 10668 (1994).

[HBB95] V. Holý, G.T. Baumbach, and M. Bessière, Interface roughness in surface-sensitive x-ray methods, *J. Phys. D* **28**, A220 (1995).

[HGD93] B. L. Henke, E.M. Gullikson, and J.C. Davis, X-ray interactions: photoabsorption, scattering, transmission, and reflection at E =50–30,000 eV, Z =1–92, *Atomic Data and Nuclear Data Tables* **54**, 181 (1993).

[HKA+93] V. Holý, J. Kuběna, E. Abramof, K. Lischka, A. Pesek, and E. Koppensteiner, X-ray double and triple crystal diffractometry of mosaic structure in heteroepitaxial layers, *J. Appl. Phys.* **74**, 1736 (1993).

[HKO+93] V. Holý, J. Kuběna, I. Ohlídal, K. Lischka, and W. Plotz, X-ray reflection from rough layered systems, *Phys. Rev.* **B47**, 15896 (1993).

[HM96] V. Holý and P. Mikulík. Theoretical description of multiple crystal arrangements. In *Proceedings of the 23rd course of the International School of Crystallography: "X-ray and neutron dynamical diffraction: theory and applications"*. Plenum Press, 1996.

[HNCM88] H.R. Höche, J. Nieber, M. Clausnitzer, and G. Materlik, Modification of specularly reflected x-ray intensity by grazing incidence coplanar Bragg-case diffraction, *phys. stat. sol. (a)* **105**, 3 (1988).

[Hol96] V. Holý. *High-resolution x-ray diffractometry of thin layers – theoretical aspects.* Masaryk University, Brno, 1996.

[HTK+93] V. Holý, L. Tapfer, E. Koppensteiner, G. Bauer, H. Lage, O. Brandt, and K. Ploog, Triple crystal x-ray diffractometry of periodic arrays of semiconductor quantum wires, *Appl. Phys. Lett.* **63**, 3140 (1993).

[Jan92] C. Janot. *Quasicrystals. A primer.* Oxford Science Publishing, 1992.

[JMP92] X. Jiang, T.H. Metzger, and J. Peisl, Nonspecular x-ray scattering from the amorphous state in W/C multilayers, *Appl. Phys. Lett.* **61**, 904 (1992).

[Kie31] H. Kiessig, *Ann. Phys.* **5**, 715 (1931).

[KLC+96] K. Krastev, F. LeGuern, K. Coat, R. Barchwitz, J.-M. André, M.F. Ravet, E. Cambril, F. Rousseaux, and P. Davi, Spectral sampling of a soft x-ray rube emission by a lamellar multilayer grating in standard and conical mountings, *Nucl. Instr. and Meth. A* **368**, 533 (1996).

[Kni76] Z. Knittl. *Optics of Thin Films.* Wiley, London, 1976.

[Kol94] M. Kolář, High-resolution x-ray diffraction spectra of Thue-Morse GaAs-AlAs heterostructures, *Phys. Rev. Lett.* **73**, 1307 (1994).

[Kor91] J.B. Kortright, Nonspecular x-ray scattering from multilayer structures, *J. Appl. Phys.* **70**, 3620 (1991).

[LC84] C.S. Lent and P.I. Cohen, Diffraction from stepped surfaces. I. Reversible surfaces, *Surf. Sci.* **139**, 121 (1984).

[LG85] Ki-Tung Lee and T.F. George, Theoretical study of laser-induced surface excitations on a grating, *Phys. Rev.* **B31**, 5106 (1985).

[LMD96] O. Litzman, P. Mikulík, and P. Dub, Multiple diffraction of particles by a system of point scatterers as an exactly soluble problem using the Ewald concept, *J. Phys. (UK)* **8**, 4709 (1996).

[LS84] D. Levine and P.J. Steinhardt, Quasicrystals: a new class of ordered structures, *Phys. Rev. Lett.* **53**, 2477 (1984).

[LS86] D. Levine and P.J. Steinhardt, Quasicrystals, *Phys. Rev.* **B34**, 596 (1986).

[Man82] B.B. Mandelbrodt. *The Fractal Geometry of Nature.* Freeman, New York, 1982.

[May84] D. Maystre. Rigorous vector theories of diffraction gratings. In E. Wolf, editor, *Progress in Optics XXI.* North-Holland, Amsterdam, 1984.

[MBC+85] R. Merlin, K. Bajema, R. Clarke, F.Y. Juang, and P.K. Bhattacharya, Quasiperiodic GaAs-AlAs heterostructures, *Phys. Rev. Lett.* **A 55**, 1768 (1985).

[MEC79] W.C. Marra, P. Eisenberger, and A.Y. Cho, X-ray total-external-reflection-Bragg diffraction: A structural study of the GaAs–Al interface, *J. Appl. Phys.* **50**, 6927 (1979).

[MHKP95] P. Mikulík, V. Holý, J. Kuběna, and K. Ploog, X-ray diffraction on Fibonacci superlattices, *Acta Cryst. A* **51**, 825 (1995).

[Mik93a] P. Mikulík. *Diploma thesis: Diffraction on quasiperiodic superlattices.* Masaryk University, Brno, 1993. (in Czech).

[Mik93b] P. Mikulík. *Diploma thesis: La caractérisation du système épitaxial tungstène/saphir par la diffusion des rayons X.* Université Joseph Fourier, Grenoble, 1993. (in French and in English).

[Mik95] P. Mikulík. *Scattering on aperiodic superlattices.* In F. Axel and D. Gratias, editors, *Beyond Quasicrystals*, page 229. Les Editions de Physique, 1995. Course 9.

[MVV+94] V. Martynov, B. Vidal, P. Vincent, M. Brunel, D.V. Roschupkin, Yu. Agafonov, A. Erko, and A. Yuakshin, Comparison of modal and differential methods for multilayer gratings, *Nucl. Instr. and Meth. A* **339**, 617 (1994).

[Nev94] M. Nevière, Bragg-Fresnel multilayer gratings: electromagnetic theory, *J. Opt. Soc. Am. A* **11**, 1835 (1994).

[oC92] The International Union of Crystallography. *International Tables for X-Ray Crystallography.* Kluwer Academic Publisher, 1974, 1992.

[Par54] L.G. Parratt, Surface studies of solids by total reflection of x-rays, *Phys. Rev.* **B95**, 359 (1954).

[PBMM94] U. Pietsch, T. Barberka, W. Mahler, and T.H. Metzger, X-ray diffuse scattering from lead stearate multilayers, *Thin Solid Films* **247**, 230 (1994).

[PC93] A.P. Payne and B.M. Clemens, Influence of roughness distributions and correlations on x-ray diffraction from superlattices, *Phys. Rev.* **B47**, 2289 (1993).

[PCA95] J. Peyrière, E. Cockayne, and F. Axel, Line-shape analysis of high-resolution x-ray diffraction spectra of finite size Thue-Morse GaAs-AlAs multilayer heterostructures, *J. Phys. I (Paris)* **5**, 111 (1995).

[PdWL+91] E.J. Puik, M.J. Van der Wiel, P. Lambooy, J. Verhoeven, F.E. Christensen, and H.A. Padmore, Characterization of a multilayer coated laminar reflection grating at $\lambda = 0.154$ nm, *X-ray Sci. Technol.* **3**, 19 (1991).

[Pin78] Z.G. Pinsker. *Dynamical scattering of X-rays in crystals.* Springer, Berlin, 1978.

[PSKL93] Y.H. Phang, D.E. Savage, R. Kariotis, and M.G. Lagally, X-ray diffraction measurement of partially correlated interfacial roughness in multilayers, *J. Appl. Phys.* **74**, 3181 (1993).

[Pyn92] R. Pynn, Neutron scattering by rough surfaces at grazing incidence, *Phys. Rev.* **B45**, 602 (1992).

[Ray07] Rayleigh, On the dynamical theory of gratings, *Proc. Royal Soc. A* **79**, 399-416 (1907).

[RMC+95] F. Robaut, P. Mikulík, N. Cherief, O.F.K. Mc Grath, D. Givord, T. Baumbach, and J.Y. Veuillen, Epitaxial growth and characterization of $Y_2Co_{17}(0001)$ thin films deposited on W(110), *J. Appl. Phys.* **78**, 997 (1995).

[Rob95] F. Robaut. *Elaboration par dépôt laser pulsé et caractérisation de couches minces épitaxiées de métaux de terres rares et de composés intermétalliques terre rare–cobalt.* PhD thesis, Université Joseph Fourier, 1995.

[RP90] H. Rhan and U. Pietsch, Grazing incidence diffraction of x-rays on semiconductor heterostructures: application of the integral mode, *Z. Phys. B* **80**, 347 (1990).

[SA93] A. Sammar and J.-M. André, Dynamical theory of stratified Fresnel linear zone plates, *J. Opt. Soc. Am. A* **10**, 2324 (1993).

[Sch68] L.I. Schiff. *Quantum Mechanics.* McGraw-Hill, New York, 1968.

[Sea89] V.F. Sears. *Neutron Optics.* Oxford University Press, 1989.

[SJMP91] A. Sammar, J.-M.André, and B. Pardo, Diffraction and scattering by lamellar amplitude multilayer gratings in the X–UV region, *Optics Communications* **86**, 245 (1991).

[SL87] P.J. Steinhardt and D. Levine. *The Physics of Quasicrystals.* World Scientific Publishing, 1987.

[SMP94] T. Salditt, T.H. Metzger, and J. Peisl, Kinetic roughness of amorphous multilayers studied by diffuse x-ray scattering, *Phys. Rev. Lett.* **73**, 2229 (1994).

[SMPJ94] T. Salditt, T.H. Metzger, J. Peisl, and X. Jiang, Diffuse x-ray scattering of amorphous multilayers, *J. Phys. III France* **4**, 1573 (1994).

[SPB95] S.A. Stepanov, U. Pietsch, and G.T. Baumbach, A matrix approach to x-ray grazing-incidence diffraction in multilayers, *Z. Phys. B* **96**, 341 (1995).

[Spe81] V.S. Speriosu, Kinematical x-ray diffractin in nonuniform crystalline films: strain and damage distributions in ion-implanted garnets, *J. Appl. Phys.* **52**, 6094 (1981).

[Spi93] W. Spirkl, Parameter fitting in grazing incidence x-ray reflectometry, *J. Appl. Phys.* **74**, 1776 (1993).

[SSGS88] S.K. Sinha, E.B. Sirota, S. Garoff, and H.B. Stanley, X-ray and neutron scattering from rough surfaces, *Phys. Rev.* **B38**, 2297 (1988).

[SSHO92] M.K. Sanyal, S.K. Sinha, K.G. Huang, and B.M. Ocko, X-ray scattering study of capillary-wave fluctuations at a liquid surface, *Phys. Rev. Lett.* **66**, 628 (1992).

[SSK93] E. Spiller, D. Stearns, and M. Krumrey, Multilayered mirrors: Interfacial roughness, scattering, and image quality, *J. Appl. Phys.* **74**, 107 (1993).

[Ste89] D.G. Stearns, The scattering of x-rays from nonideal multilayer structures, *J. Appl. Phys.* **65**, 491 (1989).

[Tak69] S. Takagi, A dynamical theory of diffraction for a distorted crystal, *J. Phys. Soc. Jap.* **26**, 1239 (1969).

[Tau64] D. Taupin, *Bull. Soc. Fr. Mineral. Crystallogr.* **87**, 469 (1964).

[TKB+92] M. Tolan, G. König, L. Brügemann, W. Press, F. Brinkop, and J.P. Kotthaus, X-ray diffraction from laterally structured surfaces: Total external reflection and grating truncation rods, *Europhys. Lett.* **20**, 223 (1992).

[TKO+90] H. Terauchi, K. Kamigaki, T. Okutani, Y. Nishihata, H. Kasatani, H. Kasano, K. Sakaue, H. Kato, and N. Sano, Synchrotron x-ray diffraction study of third-order Fibonacci lattices, *J. Phys. Soc. Jap.* **59**, 405 (1990).

[TMC+86] J. Todd, R. Merlin, R. Clarke, K.M. Mohanty, and J.D. Axe, Synchrotron x-ray study of a Fibonacci superlattice, *Phys. Rev. Lett.* **57**, 1157 (1986).

[TPBK94] M. Tolan, W. Press, F. Brinkop, and J.P. Kotthaus, X-ray diffraction from laterally structured surfaces: Crystal truncation rods, *J. Appl. Phys.* **75**, 7761 (1994).

[TPBK95] M. Tolan, W. Press, F. Brinkop, and J.P. Kotthaus, X-ray diffraction from laterally structured surfaces: Total external reflection, *Phys. Rev.* **B51**, 2239 (1995).

[TRL+92a] L. Tapfer, G. C. La Rocca, H. Lage, O. Brandt, D. Heitmann, and K. Ploog, X-ray diffraction study of corrugated semiconductor surfaces, quantum wires and quantum boxes, *Appl. Surf. Sci.* **60**, 517 (1992).

[TRL+92b] L. Tapfer, G. C. La Rocca, H. Lage, R. Cingolani, P. Grambow, A. Fischer, D. Heitmann, and K. Ploog, Observation and analysis of quantum wire structures by high-resolution x-ray diffraction, *Surf. Sci.* **267**, 227 (1992).

[TVS+95] M. Tolan, G. Vacca, S.K. Sinha, Z. Li, M. Rafailovich, J. Sokolov, H. Lorenz, and J.P. Kotthaus, X-ray diffraction from mesoscopic system: thin films on 'rough' surfaces, *J. Phys. D* **28**, A231 (1995).

[Vin82] G.H. Vineyard, Grazing-incidence diffraction and the distorted-wave approximatin for the study of surfaces, *Phys. Rev.* **B26**, 4146 (1982).

[VV84] B. Vidal and P. Vincent, Metallic multilayers for x-rays using classical thin-film theory, *Appl. Opt.* **23**, 1794 (1984).

[WB88] P. Wong and A.J. Bray, Scattering by rough surfaces, *Phys. Rev.* **B37**, 7751 (1988).

[WV91] C. Weisbuch and B. Vinter. *Quantum semiconductor structures: fundamentals and applications.* Academic Press, 1991.

[Yon63] Y. Yoneda, Anomalous surface reflection of x-rays, *Phys. Rev.* **131**, 2010 (1963).

[Zab90] H. Zabel, X-ray and neutron scattering at thin films, *Festkörperprobleme* **30**, 197 (1990).

[ZD85] R.K. Zia and W.J. Dallas, A simple derivation of quasi-crystalline spectra, *J. Phys. A (UK)* **18**, L341 (1985).

Abstract (English)

The X-ray reflection from planar and structured multilayers is presented using different theoretical approaches. The scattering phenomena studied are the specular reflection from planar multilayers with various stacking sequences (single layer, periodic, quasiperiodic), the diffuse scattering from rough multilayers, and the scattering from surface gratings and from multilayer gratings. The theories employed for the calculation are: the kinematical theory, the distorted-wave Born approximation, the dynamical theory and various approximations of the dynamical theory (the single-reflection approximation, the two-beam approximation and the multiple-beam approximation), developed in one unified formalism. This unified formalism enables all these theories to be discussed and compared in a consistent and methodological way. Numerical calculations are applied to fit the experimental curves in order to reveal the structural parameters of miscellaneous types of layered samples.

Abstract (français)

La réfléctivité des rayons X par des multicouches planaires et structurées est présentée en utilisant différentes approches théoriques. Les phènomenes de diffusion étudiés sont : la réfléctivité speculaire par des multicouches planaires ayant diverses séquences d'empilement (monocouche, périodique, quasipériodique), la diffusion diffuse de multicouches rugueuses, et enfin la diffusion par des réseaux de surface et par des réseaux de multicouche. Les théories employées pour les calculs : la théorie cinématique, l'approximation de l'onde déformée de Born, la théorie dynamique, et plusieurs approximations de la théorie dynamique (approximation à une réflexion unique, approximation à deux ondes et approximation à diffusion multiple), sont développées dans un formalisme unique. Ce formalisme permet de discuter et de comparer toutes les théories d'une manière solide et méthodologique. Les calcules numérique sont appliqués pour l'ajustement des courbes expérimentales pour mettre en évidence les paramètres structuraux des divers systèmes multicouches.

Abstrakt (česky)

Rentgenová reflektivita rovinných a strukturovaných multivrstev je prezentována za použití různých teoretických postupů. Diskutovány jsou následující typy rozptylu: spekulární reflektivita rovinnými multivrstvami s různou sekvencí vrstev (monovrstva, periodická či kvaziperiodická posloupnost vrstev), difuzní rozptyl od drsných multivrstev, a konečně rozptyl vrstevnatými mřížkami. Teorie použité při výpočtech — kinematická teorie, Bornova aproximace porušených vln, dynamická teorie, a různé aproximace dynamické teorie (aproximace jediného odrazu, dvouvlnná aproximace a aproximace vícenásobného rozptylu) — byly vyvinuty v jednotném formalismu. Tento formalismus umožňuje diskutovat a porovnat všechny tyto teorie v jednotném a metodologickém stylu. Numerické výpočty byly použity při simulování experimentálních křivek pro nafitování strukturních parametrů vzorků.